Aims and Scope

The Journal of Electromagnetic Engineering and Science (**JEES**) is an official English-language journal of the Korean Institute of Electromagnetic and Science (**KIEES**). This journal was launched in 2001 and has been published bimonthly since 2021. It is currently registered with the National Research Foundation of Korea and also indexed in Scopus, CrossRef, EBSCO, DOI/ Crossref, Google Scholar, and Web of Science Core Collection as Science Citation Index Expanded (SCIE) journal. The objective of **JEES** is to publish academic as well as industrial research results and discoveries in electromagnetic engineering and science. The particular scope of the journal includes electromagnetic field theory and its applications; high frequency components, circuits, and systems; antennas; electromagnetic wave environments; and relevant industrial developments. In addition to the regular stream of contributed papers, the journal occasionally publishes special issues on specific topics of current interest, to promote a focused coverage of the selected topics. In addition, **JEES** regularly posts invited review papers by leading researchers in the relevant fields, which will provide an overview of various subjects from their own perspectives. The editors of **JEES** are aware of the importance of rapid publication for the delivery of new research results to its readers with minimum delay, and fully recognize the need for a short turnaround time. Manuscripts submitted to **JEES** take about 3–5 months from the initial submission to publication. This rapid process applies to all three types of manuscripts that **JEES** publishes: regular papers, letters, and invited papers. The publication of submitted manuscripts is subject to blind peer review, and the final decision by the Editor-in-Chief is regularly made based on three reviews from experts in the relevant area. This journal actively promotes research in electromagnetic wave-related engineering and sciences, and its ultimate aim is to benefit the global electromagnetic engineering and science community.

Subscription Information

JEES is published bimonthly in January, March, May, July, September, and November. Full text PDF files are available at the official website (https://www.jees.kr).

The annual subscription rates for this journal are USD 230 for organization members, USD 55 for Full members, USD 37 for associate members, and USD 28 for student members.

REGULAR PAPERS

LETTER

ISAR Image Registration Based on Line Features

Linhua Wu[1] ⓘ · Lizhi Zhao[1,*] ⓘ · Junling Wang[2,*] ⓘ · Jiaoyang Su[1] ⓘ · Weijun Cheng[1] ⓘ

Abstract

Inverse synthetic aperture radar (ISAR) image registration enables the analysis of target dynamics by comparing registered images from different viewpoints. However, it faces significant challenges due to various factors, such as the complex scattering characteristics of the target, limited availability of information, and additive noise in ISAR images. This paper proposes a novel ISAR image registration method based on line features. It integrates information from both dominant scatterers and the target's outer contour to detect lines. According to the consistency principles of multiple lines in rotation and translation, line features from different ISAR images are matched. Simultaneously, the results of the feature matching are utilized to guide the parameter configuration for optimizing the image registration process. Comparative experiments illustrate the advantages of the proposed method in both feature extraction and registration feasibility.

Key Words: Feature Detection, Feature Matching, Image Registration, Inverse Synthetic Aperture Radar (ISAR), Line Features.

I. INTRODUCTION

Inverse synthetic aperture radar (ISAR) plays an important role in space target observation and recognition by providing two-dimensional images of targets in all kinds of weather, as well as in day and night conditions [1]. ISAR image registration enables the analysis of target performance and behavior. By comparing the registered images from different views, researchers can monitor changes in the target's structure, track its movements, and study its dynamics. This information is valuable for understanding the target's capabilities, mission objectives, and operational patterns.

There are many methods for optical image registration and synthetic aperture radar image registration, such as normalized cross-correlation (NCC) [2], scale invariant feature transform (SIFT) [3], speeded up robust feature (SURF) [4], and a plethora of emerging deep learning methods [5]. However, it is difficult to migrate these methods directly into the ISAR field due to the different imaging mechanisms and imaging scenarios involved. The main differences can be summarized as follows:

- Limited information in ISAR images: Unlike optical images characterized by rich texture and gradient information and SAR images with richly detailed scenes, ISAR images usually involve several scatterers on a manmade target. In ISAR images, the most significant information is typically related to the brightness or reflectivity of the target, which is represented by the amplitude of the scatterers in an image.

- Low signal-to-noise ratio (SNR) in ISAR images: The complex electromagnetic scattering characteristics of the target, radar system errors, and translation compensation errors involved in practical imaging degrade image quality and reduce image SNR.

Research on ISAR image registration has mainly focused on the processing of three domains: signal, frequency, and image. Kang et al. [6] proposed a method for ISAR image registration in the signal domain, using raw echo data from different receive an-

tennas to estimate the time-varying angular motion and compensate for the jointly translational motion to ultimately align the range and cross-range directions. Tang et al. [7] used the Fourier-Merlin transform to carry out phase conjugate multiplication in the frequency domain based on the Fourier theorem to achieve ISAR image registration. Furthermore, Gao et al. [8] utilized the correlation coefficient as a similarity measure to estimate alignment parameters. Meanwhile, Adel et al. [9] combined SIFT [10] and SURF [11], based on point features, to achieve image registration. However, in these methods, some meaningless noise points are often extracted as feature points, resulting in unstable performance. Since most space targets feature linear structures (e.g., solar panels and rectangular cavities), line features can be used to solve this problem, since they are more reliable and are less affected by the glinting or defocusing caused by scatterers.

There are many ways in which lines can be detected. The Hough transform (HT) [12] is a popular line detection technique that converts image space into parameter space, where lines are represented as points. However, it is computationally expensive and sensitive to parameter settings. Almazan et al. [13] proposed a probabilistic algorithm to detect lines and thereby improve the sensitivity of parameters, but it required large labeled datasets. Line segment detection (LSD) [14] is another commonly used method for line detection that is based on gradient information that does not rely on HT. Line segment merging (LSM) [15] is an upgraded version of the LSD that applies additional post-processing steps to merge overlapping line segments or remove redundant ones. Notably, line detection is often preceded by contour extraction, which helps segment foreground objects from the background, allowing for more accurate and focused line detection. However, the discontinuity and defocusing caused by scatterers in ISAR images may lead to the extraction of only a coarse contour, which can in turn degrade the performance of the line detection algorithm and lead to large errors in the registration results.

This study proposes a line feature-based ISAR image registration method that exhibits enhanced robustness against image degradation caused by noise, secondary reflections, and system errors. The proposed registration process involves line feature detection, feature matching, and parameter estimation. In particular, feature matching is accomplished by utilizing the spatial relations of line features between the reference image and the sensed image. Furthermore, the registration parameters are estimated by minimizing the sum of the Euclidean distances between the line features. Additionally, the accuracy of line detection in the LSM is improved by employing relevant techniques, such as image enhancement, contour extraction, and scatterer fitting. Moreover, the efficiency of parameter estimation is optimized by implementing the Snake Optimization (SO) [16] algorithm, which dynamically adjusts its search strategy and

parameters, demonstrating solid capabilities in global exploration, robustness, and adaptability.

The remainder of this paper is organized as follows: Section II analyses the transform model for ISAR images from different perspectives, Section III introduces the proposed line feature detection and matching method, Section IV demonstrates the parameter estimation process of the ISAR image registration method, Section V provides the different experimental results to validate the efficacy of the proposed method, and Section VI presents the conclusions of this study.

II. Registration Model of ISAR Image Sequences

This section of the study uses a monostatic scenario as a reference point to analyze the relationship between the different viewpoints of ISAR images.

The ISAR imaging geometry is depicted in Fig. 1, where T_{UVW} represents the inertial coordinate system and $T_{X_kY_kZ_k}$ is the imaging coordinate system at the k-th moment. Furthermore, X_k and Y_k represent the Doppler and range axes of imaging, respectively. Z_k is the normal vector of the imaging plane and e_{los} stands for the unit vector from the radar to the target. Notably, the relative motion of the targets with respect to the radar can be divided into translation and rotation. Translation must be compensated for before azimuth compression [17], while rotation is usually retained for ISAR imaging. Assuming ω_{los} represents the line of sight (LOS) rotation and ω_{tar} refers to the target self-rotation, the effective rotation vector can be formulated as:

$$\omega = e_{los} \times [(\omega_{tar} + \omega_{los}) \times e_{los}]. \qquad (1)$$

Furthermore, assuming translation compensation [18] is complete, the target motion can be considered equivalent to an ideal turntable model at a coherent processing time, as shown in Fig. 2.
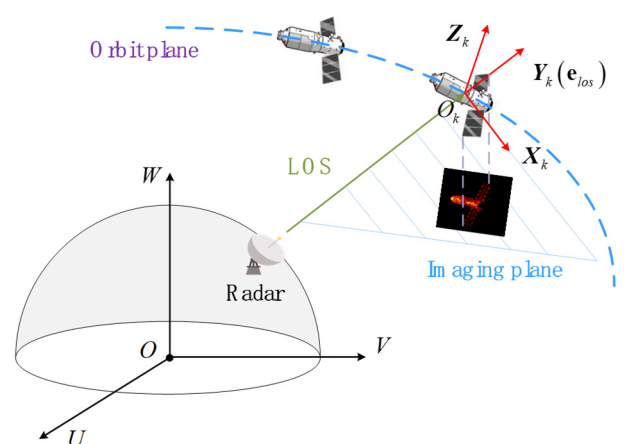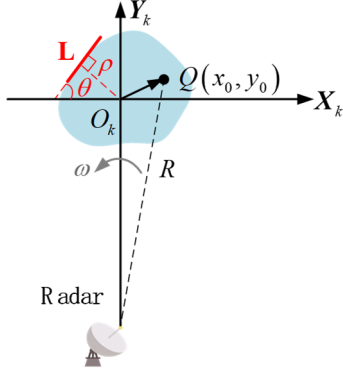

Fig. 1. ISAR imaging geometry.

Fig. 2. An ideal turntable model.

On considering the coordinates of scatterer Q on the target at the initial time as (x_0, y_0) and the range of the target center as R_{O_k}, the instantaneous distance of Q from the radar can be approximated as:

$$R(t) \approx -y_0\cos(\omega t) + x_0\sin(\omega t) + R_{O_k}. \quad (2)$$

Here, c denotes the speed of light, B is the bandwidth, ω refers to the effective target speed, and the coherent processing time is t_{obs}. Furthermore, the range resolution is $\eta_r = c/2B$ and the azimuth resolution is $\eta_a = \lambda/2\omega t_{obs}$. According to the range-Doppler image algorithm, the position of Q relative to the center of the ISAR image can be obtained as follows:

$$Y(t) = -\frac{R(t) - R_{O_k}}{\eta_r}, \quad (3)$$

$$X(t) = \frac{1}{\eta_a}\frac{dR(t)}{dt}. \quad (4)$$

Substituting Eq. (2) into Eqs. (3) and (4), the coordinates of Q in the image can be rewritten in the form of the following matrix:

$$\begin{bmatrix} X(t) \\ Y(t) \end{bmatrix} = \underbrace{\begin{bmatrix} \cos(\omega t) & -\sin(\omega t) \\ \sin(\omega t) & \cos(\omega t) \end{bmatrix}}_{R} \begin{bmatrix} x_0/\eta_a \\ y_0/\eta_r \end{bmatrix}. \quad (5)$$

Furthermore, on considering the image I_1 corresponding to t_1 as the sensed image, and the image I_2 corresponding to t_2 as the reference image, the position relationship of scatterer Q in these two images can be expressed as:

$$\begin{bmatrix} X(t_2) \\ Y(t_2) \end{bmatrix} = R(t_2)R^{-1}(t_1)\begin{bmatrix} X(t_1) \\ Y(t_1) \end{bmatrix} = \begin{bmatrix} \cos\gamma & -\sin\gamma \\ \sin\gamma & \cos\gamma \end{bmatrix}\begin{bmatrix} X(t_1) \\ Y(t_1) \end{bmatrix}, \quad (6)$$

where $\gamma = \omega(t_2 - t_1)$.

However, offsets between images might still remain because of the errors introduced during the delay and the compensation process [19]. Therefore, supposing that the relative offset vector of the centers is $p = [a, b]$, the transformation matrix can be expressed as:

$$\begin{bmatrix} X(t_2) \\ Y(t_2) \\ 1 \end{bmatrix} = \begin{bmatrix} \cos\gamma & -\sin\gamma & a \\ \sin\gamma & \cos\gamma & b \\ 0 & 0 & 1 \end{bmatrix}\begin{bmatrix} X(t_1) \\ Y(t_1) \\ 1 \end{bmatrix} = \begin{bmatrix} R_\gamma & p \\ 0 & 1 \end{bmatrix}\begin{bmatrix} X(t_1) \\ Y(t_1) \\ 1 \end{bmatrix}. \quad (7)$$

The relationship between the same lines in the two images can be obtained in the same way. In this context, it is worth noting that, due to target scattering properties, noise, and low image quality, it is difficult to accurately determine the length of the lines. To address this, the direction angle and the vertical distance from the origin of the image to the line were utilized to describe a line, namely $L = [\rho, \theta]$, as shown in Fig. 2. Therefore, the position vector, which indicates the vertical distance vector from O_k to line L, can be formulated as:

$$r = [-\rho\sin\theta \quad \rho\cos\theta]^T. \quad (8)$$

Notably, the direction vector of line L is:

$$n = [\cos\theta \quad \sin\theta]^T. \quad (9)$$

Therefore, the relationship between line L in the two images can be expressed as follows:

$$\begin{bmatrix} r_2 - p \\ n_2 \end{bmatrix}^T = R_\gamma \begin{bmatrix} r_1 \\ n_1 \end{bmatrix}^T, \quad (10)$$

where r_1 and n_1 represent the position vector and direction vector in image I_1, respectively, while r_2 and n_2 denote the position and direction vectors in image I_2.

III. LINE FEATURE DETECTION AND MATCHING

ISAR images are collections of points, with the edge of the images being discontinuous. As a result, traditional automatic feature extraction methods present considerable challenges for ISAR images. In this section, the LSM algorithm is improved upon to extract line features from ISAR images, thus aiding in the subsequent image registration process.

1. Image Preprocessing

Preprocessing, such as image enhancement and edge detection, is often necessary to improve the robustness of line detection.

Considering that ISAR images are characterized by the presence of several strong scatterers, the weak scatterers in the images may become less distinguishable. To address this issue, the contrast of the ISAR images used in this study was adjusted to en-

hance the visibility of weak scatterers, thereby preserving more target details. In addition, morphological image processing methods [20, 21] were implemented to connect adjacent points and obtain a complete contour. Finally, the outer contour [22] was extracted utilizing a typical edge detection operator, Canny [23].

Although the outer contour exhibited gaps or deviations from the natural target boundary, possibly resulting from the alterations caused in the target's area during the dilatation process, it was still able to offer valuable indications regarding the spatial position of the lines.

2. Line Detection

LSM is well known for its efficiency and accuracy. The LSM process primarily comprises scale-space analysis, gradient calculation, line support region estimation, line validation, line pruning, and line mergence. Notably, the possibility of LSM will be further investigated in the experimental section of this study. In this paper, the outer contour image was used as the input for the LSM to extract coarse line features $L = [\rho, \theta]$.

In this context, it should be noted that during the course of this process, the outer contour errors were transmitted into the line errors. For example, the LSM result presented in Fig. 3 exhibits a gap between the LSM results and the natural edge of the target. To address this problem, the CLEAN technique [24] was employed to pick up dominant scatterers from the entire image and filter the scatterers located close to $L = [\rho, \theta]$. Following this, the discrete scatterers were fitted to improve the accuracy of the LSM results. The following is a detailed description of the process adopted in this study for filtering scatterers and calculating line parameters.

Assuming $P_j(x_j, y_j)$ is the j-th dominant scatterer of the target and $L_h = [\rho_h, \theta_h]$ is the h-th line feature, the distance between P_j and L_h can be estimated using the following equation:

$$d_{j,h} = \frac{|\tan(\theta_h)x_j - y_j + \rho_h\sqrt{1 + \tan^2(\theta_n)}|}{\sqrt{1 + \tan^2(\theta_h)}}. \quad (11)$$

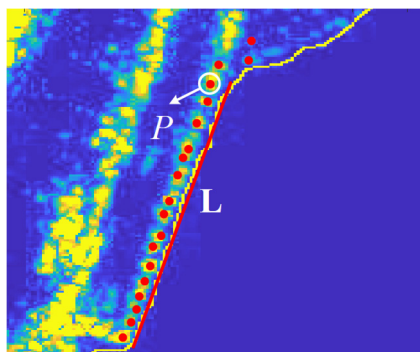To calculate the distance between scatterer P_j and the other lines,

Fig. 3. LSM results.

and obtain an H-dimensional vector, $d_j = [d_{j,1}, d_{j,2}, \dots, d_{j,H}]$, where H denotes the number of lines. Subsequently, the association of P_j with a specific line can be determined based on an appropriate threshold $\varepsilon_d = \sigma|\eta_1 - \eta_2|$, where η_1 and η_2 are the dilation parameters involved in image preprocessing. Notably, σ can adjust the threshold value to affect the sensitivity of the association. If $\min(d_j) \leq \varepsilon_d$, P_j is considered to belong to the associated line, or it is excluded otherwise. Notably, the index of $\min(d_j)$ represents the line located closest to P_j.

After classification, the dominant scatterers in the same group can be linearly fitted. Assuming there are W points in the h-th group, with each point e represented as (x_w, y_w), the corresponding coefficient matrix after fitting will be:

$$F_h = \begin{bmatrix} \sum x_w^2 & \sum x_w \\ \sum x_w & W \end{bmatrix}^{-1} \begin{bmatrix} \sum x_w y_w \\ \sum y_w \end{bmatrix}. \quad (12)$$

Subsequently, the fitted line $L_h = [\tilde{\rho}_h, \tilde{\theta}_h]$ can be obtained. Furthermore, the parameters $\tilde{\rho}_h$ and $\tilde{\theta}_h$ can be formulated as:

$$\tilde{\rho}_h = \frac{|y_j - F_h(1)x_j - F_h(2)|}{\sqrt{1 + [F_h(1)]^2}}, \quad (13)$$

$$\tilde{\theta}_h = \arctan[F_h(1)]. \quad (14)$$

3. Line Feature Matching

In image registration, establishing a corresponding relationship between line features is a primary task. For this purpose, the current study implemented a novel feature matching strategy to identify corresponding lines between two images based on geometric constraints. The initial stage of this feature matching process involved grouping based on angle information, while subsequent stages focused on matching the lines within the same group by ensuring consistency in the distance between them. The details of this process are as follows:

Step I: Categorize the lines with similar orientations into groups based on their angle parameters θ. For instance, assume that I_1 (the sensed image) and I_2 (the reference image) are divided into M and N groups.

Step II: Calculate the average angle of each group to attain $\bar{\theta}_m$, where $m \in [1, 2, \dots, M]$.

Step III: Calculate the angle difference $\Delta\bar{\theta}_{m,n} = |\bar{\theta}_m - \bar{\theta}_n|$ between each group of I_1 and I_2. Store $\Delta\bar{\theta}_{m,n}$ in a $M \times N$ matrix G_θ.

Step IV: Analyze the statistical properties of G_θ and identify the correct match with the highest vote rate by applying a clustering algorithm. Then identify the approximate rotation parameter γ_0.

Step V: Rotate I_1 using γ_0 as $\tilde{I}_1$.

Step VI: Determine the intersection point of any two lines in the same image. Assuming $q_{i,j}$ is the intersection point of L_i and L_j, the coordinates $(X_{q_{i,j}}, Y_{q_{i,j}})$ of $q_{i,j}$ can be calculated as follows:

$$X_{a_{i,j}} = \frac{-\rho_j \sqrt{1 + \tan^2(\theta_j)} + \rho_i \sqrt{1 + \tan^2(\theta_i)}}{\tan(\theta_j) - \tan(\theta_i)}, \tag{15}$$

$$Y_{a_{i,j}} = \frac{\rho_i \tan(\theta_j)\sqrt{1 + \tan^2(\theta_i)} - \rho_j \tan(\theta_i)\sqrt{1 + \tan^2(\theta_j)}}{\tan(\theta_j) - \tan(\theta_i)}. \tag{16}$$

Remove any intersection points falling beyond the range of image I_1 and store the remaining intersection points in the set Q_1. Similarly, generate Q_2 for image I_2.

Step VII: Choose one point from each point set (Q_1 and Q_2) to calculate the distance vector formed by the two points. Record the distance vectors to create a matrix G_q while iterating through all the intersection points.

Step VIII: Perform cluster analysis on the distance vectors in G_q to identify the most frequent occurrences, ultimately completing the line matching.

After correctly matching the intersection points, the average distance vector of the intersection point pairs can be approximated as the translation vector $p_0 = [a_0, b_0]$ between two images.

The key steps of the feature matching process are presented in the flowchart depicted in Fig. 4.

IV. PARAMETER ESTIMATION BASED ON LINE FEATURES

This section presents the results achieved using the SO algorithm to estimate the image registration parameters. Taking γ_0 as the initial rotation angle and $p_0 = [a_0, b_0]$ as the initial translation vector, the angle, range, and cross-range offset can be defined as $\Delta\gamma$, Δa, and Δb. Therefore, the refined values can be considered as follows:

$$\begin{cases} \hat{a} = a_0 + \Delta a \\ \hat{b} = b_0 + \Delta b. \\ \hat{\gamma} = \gamma_0 + \Delta\gamma \end{cases} \tag{17}$$

Furthermore, by substituting Eq. (17) into Eq. (10), the transformed line feature of L_h can be formulated as:

$$\hat{\theta}_{h,1} = \tilde{\theta}_{h,1} + \hat{\gamma}, \tag{18}$$

$$\hat{\rho}_{h,1}(\hat{\gamma}, \hat{a}, \hat{b}) = \sqrt{\tilde{\rho}_{h,1}^2 + \hat{a}^2 + \hat{b}^2 + 2\tilde{\rho}_{h,1}(\hat{b}\sin\hat{\theta}_{h,1} + \hat{a}\cos\hat{\theta}_{h,1})}, \tag{19}$$
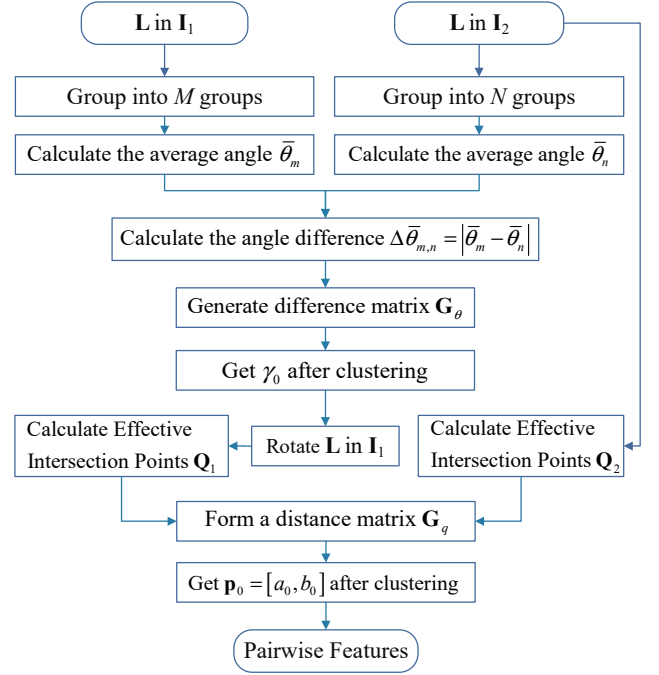
Fig. 4. Flowchart for feature matching.

where $\hat{\theta}_{h,1}$ represent the angle of the h-th line in I_1 after transformation and $\hat{\rho}_{h,1}$ denotes the distance from the origin to the h-th line. Consequently, the new position vector $\hat{r}_{h,1}$ of h-th line in I_1 can be obtained.

The cost function is crucial for an optimization algorithm that guides optimization processes. In this study, the sum of the Euclidean distance between the position vectors of the lines was utilized as the cost function to measure the degree of image alignment. Therefore, assuming there are H_m pairwise line features, the cost function can be expressed as follows:

$$f(\hat{\gamma}, \hat{a}, \hat{b}) = \sum_{h}^{H_m} |\hat{r}_{h,1} - r_{h,2}|. \tag{20}$$

Notably, a minimum value of the cost function indicates that the two concerned images are well aligned. To improve efficiency, this study used SO to calculate the optimal solution for γ, a, and b.

V. EXPERIMENTS

To validate the superiority of the proposed method, different experiments were performed in three parts. The first part is concerned with proving the effectiveness of the proposed ISAR image registration method for simulated ISAR images, while the second part presents comparisons of the accuracy of different feature detection, optimization, and registration methods for ISAR applications using real measured images. In the last part, the robustness of the proposed method is analyzed through error analysis.

1. Effectiveness Validation

To validate the effectiveness of the proposed method, a number of experiments were carried out on simulated ISAR images, with the space target being RADARSAT-2, whose three-dimensional model is available in [25], as depicted in Fig. 5. The radar was set at Beijing (39.9 N, 116.4 E, 0 m), and the satellite two-line orbital element parameters were based on a set of public data available in the public satellite database [26]. The simulated images were generated using the range-Doppler algorithm. The main parameters of the ISAR imaging radar are listed in Table 1.

Two specific imaging times were selected from the observation views, as shown in Fig. 6. The ISAR images corresponding to the two views are presented in Fig. 7. In this context, it should be emphasized that the rectangular solar panels in both images are projected as lines, displaying limited information. Additionally, the reference image depicts an occurrence in which a solar panel obstructs the SAR antenna.

The line results detected by the proposed extraction method are depicted in Fig. 8, while the specific parameters of each line are listed in Table 2.
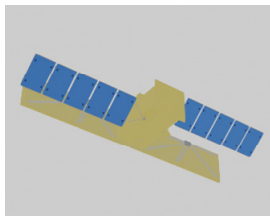

Fig. 5. Three-dimensional model of RADARSAT-2.

Table 1. Optimized dimensions of the 1 × 4 array

Parameter	Value
Bandwidth	1.25 GHz
Center frequency	10 GHz
Range resolution	0.12 m
Cross-range resolution	0.12 m
Pulse repetition frequency	100 Hz
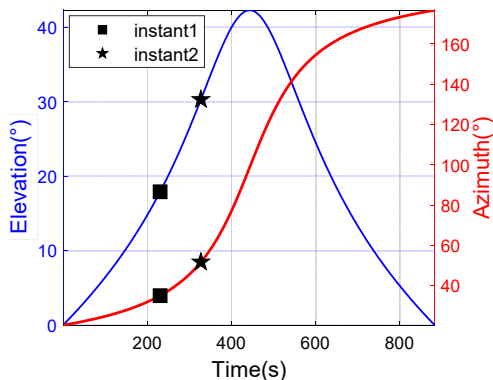
Fig. 6. The corresponding LOS parameters.
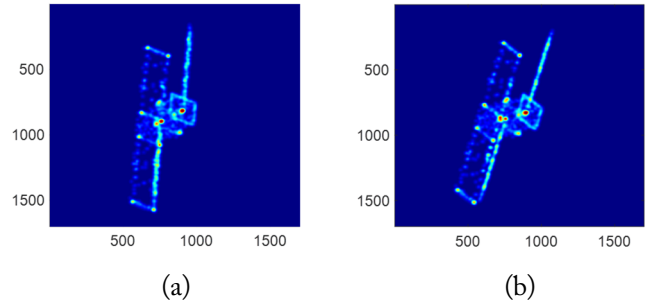
Fig. 7. Simulated ISAR images of RADARSAT-2: (a) reference image and (b) sensed image.
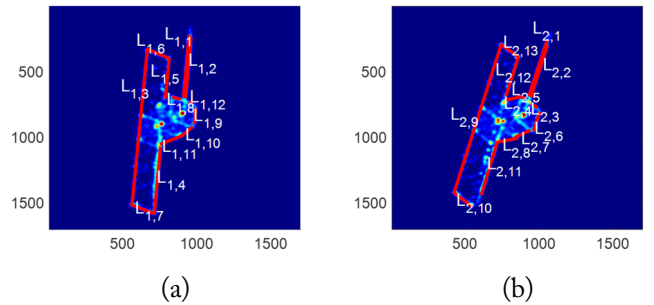
Fig. 8. Feature extraction results from the contours: (a) reference image and (b) sensed image.

Table 2. Details of the extracted lines

h	Reference image		Registration image	
	$\hat{\theta}_{h,1}$ (°)	$\hat{\rho}_{h,1}$ (pixel)	$\hat{\theta}_{h,2}$ (°)	$\hat{\rho}_{h,2}$ (pixel)
1	−86.4261	916.0495	−73.6682	1,057.3776
2	−86.4796	930.1488	−74.1118	1,058.9111
3	−86.9952	576.8552	37.2110	920.3972
4	−86.2272	728.5355	−13.2725	925.9346
5	−85.8718	792.2517	35.4692	862.7557
6	24.8210	647.9276	−73.5892	1,013.8455
7	22.2410	486.4924	−26.6260	972.5338
8	18.1381	791.7010	−11.1237	935.7176
9	−86.3520	991.4765	−74.1940	730.6426
10	−41.8396	908.5218	40.8972	864.1083
11	−25.0343	792.1271	−74.9215	862.7557
12	24.0169	913.0905	−74.0297	1,013.8455
13	–	–	38.8298	730.3151

After feature matching, 12 association pairs were obtained—$L_{1,1}L_{2,1}$, $L_{1,2}L_{2,2}$, $L_{1,3}L_{2,9}$, $L_{1,4}L_{2,11}$, $L_{1,5}L_{2,12}$, $L_{1,6}L_{2,13}$, $L_{1,7}L_{2,10}$, $L_{1,8}L_{2,5}$, $L_{1,9}L_{2,6}$, $L_{1,10}L_{2,7}$, $L_{1,11}L_{2,8}$, and $L_{1,12}L_{2,3}$. Despite some obvious occlusions, the line features could be correctly matched. Most importantly, feature matching yielded the following rough register parameters: $a_0 = 0.6438$, $b_0 = 0.3985$, and $\gamma_0 = -11.5629°$.

In subsequent optimization algorithms, the search range of Δa and Δb were set to $[-100,100]$, while $\Delta\gamma$ was set to $[-3,3]$. Table 3 lists the estimated register parameters, while Fig. 9 depicts the registration results obtained by overlaying the two images—the one before and the one after registration. It is observed that although the main body and the solar panel are well aligned, the SAR antenna presents an alignment error caused by a projection difference between the two imaging planes.

2. Comparison Experiments

Comparison experiments were conducted using real measured ISAR images obtained from the laboratory's official website [27] (@ Fraunhofer FHR). The experiments were carried out in a Windows 10 Professional environment using Intel Core i7-1165G7 processors with 2.80 GHz speed and 16.0 GB RAM, while the codes were implemented in MATLAB R2021a.

2.1 Comparison of line feature extraction methods

The line detection results had a significant effect on the accuracy of the image registration. In particular, the results of three

Table 3. Registration results of the simulated images

Parameter	True value	Estimated value	Error
a (pixel)	10	10.1273	0.1273
b (pixel)	10	10.2250	0.2250
γ (°)	-12	-11.9074	-0.0926

(a)   (b)
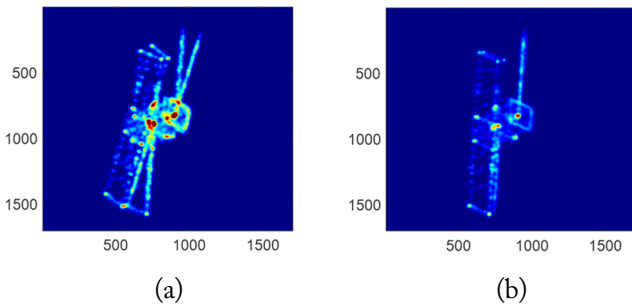
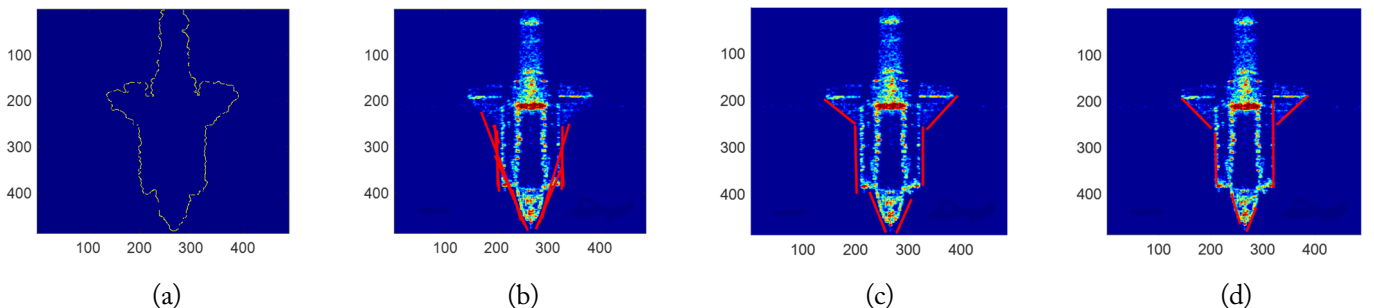Fig. 9. Comparison of overlapped simulated images before and after registration: (a) initial and (b) register.

different line detection methods were compared based on the outer contour of the real measured ISAR images shown in Fig. 10(a). The line features extracted by conducting HT and LSM are presented in Fig. 10(c) and 10(b), respectively, in which the parameters of the distance merge while the shortest length limit of a line is the same. Notably, the HT results show more than two lines near certain areas. In both results, the lines do not fit the actual edges of the target, indicating failed ISAR image registration. In contrast, the result obtained using the proposed line detection method, presented in Fig. 10(d), shows that the line features align well with the target boundary, highlighting that it is more suitable and effective than both HT and LSM.

2.2 Comparison of optimization algorithms

An experiment was conducted to compare the efficiency of particle swarm optimization (PSO) [28] and SO under the same configuration. The iterate time was set to 200, and the parameters related to the learning rate in the SO and PSO were reduced to 0.6 times.

Fig. 11(a) shows the cost function value for each iteration. It can be observed that the PSO quickly converges to reach a local optimum. Additionally, the variation curves of the absolute register errors in terms of the number of iterations during the iterative process are shown in Fig. 11(b), 11(c), and 11(d). It is evident that the parameter estimation accuracy of the SO is better than that of the PSO. Furthermore, the time consumption of PSO and SO was 0.0488 seconds and 0.0324 seconds, respectively.

2.3 Comparison of different registration methods

To verify the superiority of the proposed method, real measured ISAR images featuring the same target were first obtained. Subsequently, the results of the proposed method were compared with those obtained using SIFT and artificial bee colony by carrying out normalized cross correlation (ABC-NCC) [29], with mutual information (MI) [30], normalized image correlation (NIC), and algorithm runtime as the performance indicators. The results are listed in Table 4, while the two overlapped images generated by the experiment are depict-

(a)   (b)   (c)   (d)

Fig. 10. Comparison of different line extraction methods: (a) outer contour, (b) HT, (c) LSM, and (d) the proposed method.
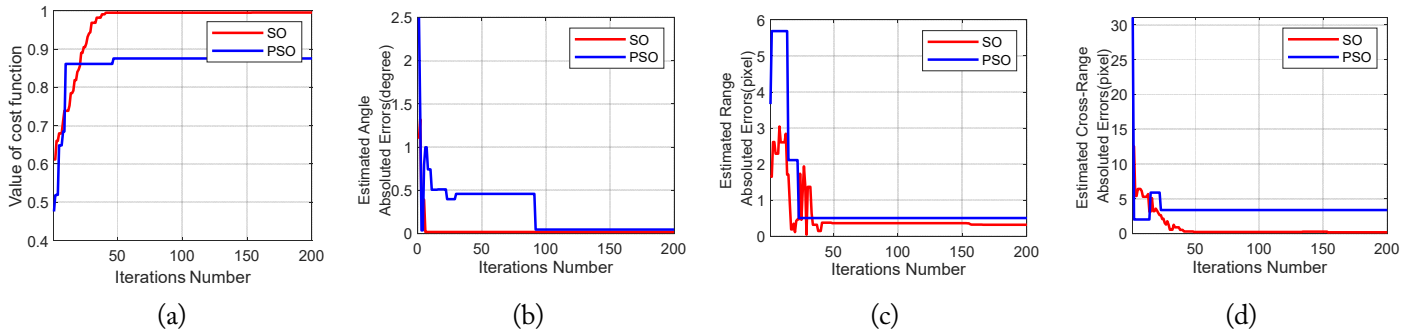
Fig. 11. Comparison of the optimization algorithm results: (a) cost function, (b) angle errors, (c) range errors, and (d) cross-range errors.

Table 4. Comparison of the proposed method with the different registration methods applied to real measured images of the spacecraft

Method	SIFT	ABC-NCC	Proposed method
a (pixel)	121.0021	4.2485	4.0324
b (pixel)	119.9711	2.9892	3.7270
γ (°)	-13.6137	-15.1116	-15.0958
MI	0.0399	0.3364	0.3370
NIC	0.0916	0.7481	0.7449
Time (s)	15.4480	45.9330	10.3697

ed in Fig. 12. It is evident that the proposed method is both fast and accurate. Fig. 12(d) shows that the main body in the image obtained using the proposed method almost overlaps with the real measured one, although the tail is displaced due to secondary reflections.

Moreover, a different space object was also employed for image registration. The estimated register parameters are listed in Table 5, and the two overlapped images are presented in Fig. 13. It can be observed that the image produced by the proposed registration process successfully aligns with the target solar panel and accurately captures the change in the position of the SAR antenna.

3. Robustness Analysis

To further analyze the robustness of the proposed method, 1,000 Monte Carlo simulations were conducted using different SNRs. Under the same scatterer model and mapping parameters, the SNR range was set as 10–30 dB, while the step size was considered 2 dB. Fig. 14(a), 14(c), and 14(e) present the mean error (ME) of the range offset, cross-range offset, and rotation of the images at different SNRs, respectively. Furthermore, Fig. 14(b), 14(d), and 14(f) present the root mean square error (RMSE) of the range offset, cross-range offset, and rotation, respectively. The results show that the proposed method is more robust than SIFT and ABC-NCC, especially with regard to the rotation angle estimation, which reached the order of 0.001. In

Table 5. Comparison with the different registration methods applied to real measured images of ENVISAT

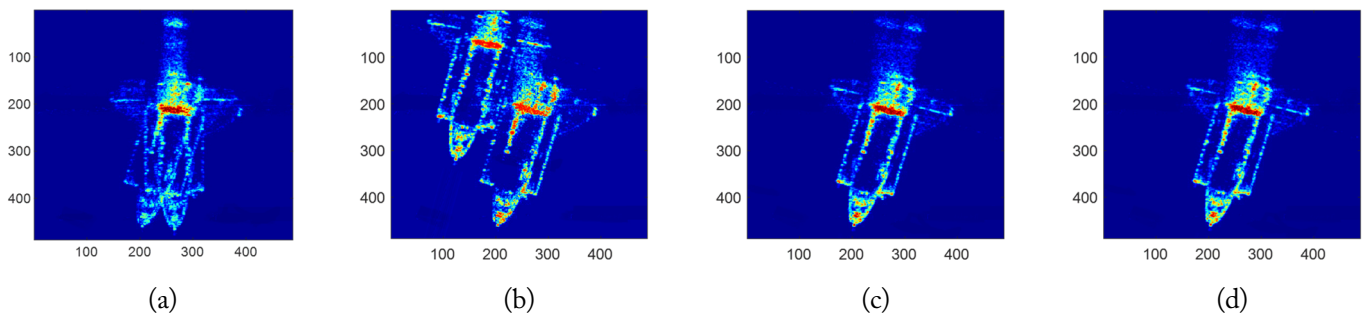| Method	SIFT	ABC-NCC	Proposed method
a (pixel)	-114.0813	-61.2005	-53.8905
b (pixel)	420.1666	35.9135	79.0147
γ (°)	-16.6820	-12.4281	-16.9270
MI	0.0376	0.2970	0.2748
NIC	0.0040	0.6446	0.4810
Time (s)	59.7761	69.0775	18.1011

Fig. 12. Comparison of different methods for registering real measured images of the spacecraft: (a) initial, (b) SIFT, (c) ABC-NCC, and (d) the proposed method.
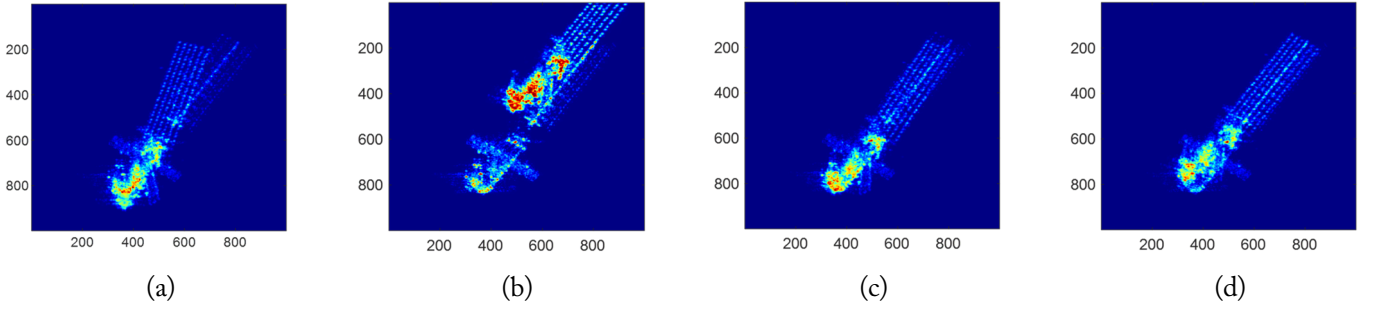
Fig. 13. Comparison of different methods for registering real measured images of ENVISAT: (a) initial, (b) SIFT, (c) ABC-NCC, and (d) the proposed method.
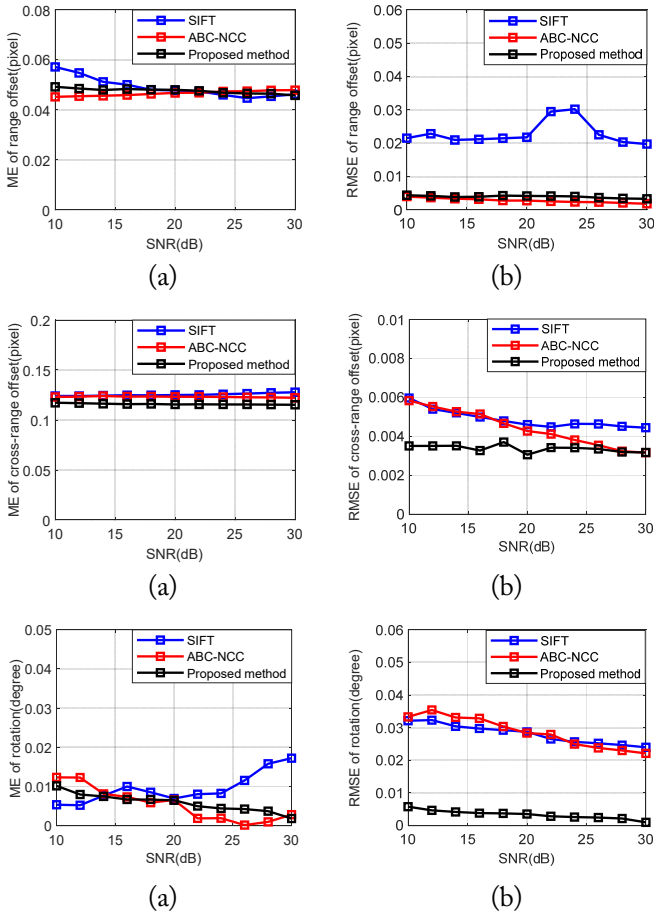

Fig. 14. Estimation errors of the simulation parameters at different SNRs: (a) ME of range offset, (b) RSME of range offset, (c) ME of cross-range offset, (d) RSME of cross-range offset, (e) ME of rotation angle, and (f) RSME of rotation angle.

fact, the main reason for the large errors observed in SIFT or ABC-NCC was that they were based on point or area features, while the ISAR images were noisy and sparse.

VI. CONCLUSION

In this paper, a line features-based ISAR image registry method is proposed. First, a transformation model that incorporated both translational and rotational components was built, after which the traditional LSM was initially applied to detect the rough line features of the target contour. Subsequently, scatterers located in close proximity to the rough line features were fitted to refine and adjust the line features. The pairwise correspondence between the lines was examined using their spatial relations. Finally, considering the sum of the Euclidean distances between the lines as the cost function, the SO algorithm was employed to obtain precise parameters for ISAR image registration. The experimental results confirmed the effectiveness of the proposed algorithm in the ISAR image registration of different targets. Compared to existing methods, the proposed line features exhibited stronger robustness against noise and changes in image, as well as higher uniqueness and stability in matching, thereby improving the accuracy of the registration algorithms.

REFERENCES

[1] A. Orlova, R. Nogueira, and P. Chimenti, "The present and future of the space sector: a business ecosystem approach," *Space Policy*, vol. 52, article no. 101374, 2020. https://doi.org/10.1016/j.spacepol.2020.101374

[2] M. Arar, Y. Ginger, D. Danon, A. H. Bermano, and D. Cohen-Or, "Unsupervised multi-modal image registration via geometry preserving image-to-image translation," in *Proceedings of the IEEE/CVF Conference on Computer Vision and Pattern Recognition*, Seattle, WA, USA, 2020, pp. 13407-13416.

[3] Q. Yu, D. Ni, Y. Jiang, Y. Yan, J. An, and T. Sun, "Universal SAR and optical image registration via a novel SIFT framework based on nonlinear diffusion and a polar spatial-frequency descriptor," *ISPRS Journal of Photogrammetry and Remote Sensing*, vol. 171, pp. 1-17, 2021. https://doi.org/10.1016/j.isprsjprs.2020.10.019

[4] T. Zhang, R. Zhao, and Z. Chen, "Application of migration image registration algorithm based on improved SURF in re-

mote sensing image mosaic," *IEEE Access*, vol. 8, pp. 163637-163645, 2020. https://doi.org/10.1109/ACCESS.2020.3020808

[5] H. Zhang, W. Ni, W. Yan, D. Xiang, J. Wu, X. Yang, and H. Bian, "Registration of multimodal remote sensing image based on deep fully convolutional neural network," *IEEE Journal of Selected Topics in Applied Earth Observations and Remote Sensing*, vol. 12, no. 8, pp. 3028-3042, 2019. https://doi.org/10.1109/JSTARS.2019.2916560

[6] B. S. Kang, K. Lee, and K. T. Kim, "Image registration for 3-D interferometric-ISAR imaging through joint-channel phase difference functions," *IEEE Transactions on Aerospace and Electronic Systems*, vol. 57, no. 1, pp. 22-38, 2021. https://doi.org/10.1109/TAES.2020.3021108

[7] W. Tang, F. Jia, and X. Wang, "Image Large rotation and scale estimation using the Gabor filter," *Electronics*, vol. 11, no. 21, article no. 3471, 2022. https://doi.org/10.3390/electronics11213471

[8] Q. Gao, X. Wei, Z. N. Wang, and D. T. Na, "An imaging processing method for linear array ISAR based on image entropy," *Applied Mechanics and Materials*, vol. 128-129, pp. 525-529, 2012. https://doi.org/10.4028/www.scientific.net/AMM.128-129.525

[9] E. Adel, M. Elmogy, and H. Elbakry, "Image stitching based on feature extraction techniques: a survey," *International Journal of Computer Applications*, vol. 99, no. 6, pp. 1-8, 2014.

[10] F. Bellavia and C. Colombo, "Is there anything new to say about SIFT matching?," *International Journal of Computer Vision*, vol. 128, pp. 1847-1866, 2020. https://doi.org/10.1007/s11263-020-01297-z

[11] Y. D. Pranata, K. C. Wang, J. C. Wang, I. Idram, J. Y. Lai, J. W. Liu, and I. H. Hsieh, "Deep learning and SURF for automated classification and detection of calcaneus fractures in CT images," *Computer Methods and Programs in Biomedicine*, vol. 171, pp. 27-37, 2019. https://doi.org/10.1016/j.cmpb.2019.02.006

[12] Y. Zou, J. Tian, G. Jin, and Y. Zhang, "MTRC-tolerated multi-target imaging based on 3D Hough transform and non-equal sampling sparse solution," *Remote Sensing*, vol. 13, no. 19, article no. 3817, 2021. https://doi.org/10.3390/rs13193817

[13] E. J. Almazan, R. Tal, Y. Qian, and J. H. Elder, "MCMLSD: a dynamic programming approach to line segment detection," in *Proceedings of the IEEE Conference on Computer Vision and Pattern Recognition*, Honolulu, HI, USA, 2017, pp. 2031-2039. https://doi.org/10.1109/CVPR.2017.620

[14] J. Tian, S. Liu, X. Zhong, and J. Zeng, "LSD-based adaptive lane detection and tracking for ADAS in structured road environment," *Soft Computing*, vol. 25, pp. 5709-5722, 2021. https://doi.org/10.1007/s00500-020-05566-4

[15] M. Chen, S. Yan, R. Qin, X. Zhao, T. Fang, Q. Zhu, and X. Ge, "Hierarchical line segment matching for wide-baseline images via exploiting viewpoint robust local structure and geometric constraints," *ISPRS Journal of Photogrammetry and Remote Sensing*, vol. 181, pp. 48-66, 2021. https://doi.org/10.1016/j.isprsjprs.2021.09.002

[16] F. A. Hashim and A. G. Hussien, "Snake optimizer: a novel meta-heuristic optimization algorithm," *Knowledge-Based Systems*, vol. 242, article no. 108320, 2022. https://doi.org/10.1016/j.knosys.2022.108320

[17] Y. Wang, Y. Shu, X. Yang, M. Zhou, and Z. Tian, "Recent progress of ISAR imaging algorithms," in *Communications, Signal Processing, and Systems*. Singapore: Springer, 2020, pp. 1418-1421. https://doi.org/10.1007/978-981-15-8411-4_188

[18] L. Yang, M. Xing, L. Zhang, G. C. Sun, Y. Gao, Z. Zhang, and Z. Bao, "Integration of rotation estimation and high-order compensation for ultrahigh-resolution microwave photonic ISAR imagery," *IEEE Transactions on Geoscience and Remote Sensing*, vol. 59, no. 3, pp. 2095-2115, 2021. https://doi.org/10.1109/TGRS.2020.2994337

[19] P. Zhou, G. Zhang, and W. Yang, "A review of ISAR imaging technology," in *Proceedings of 2020 IEEE International Conference on Information Technology, Big Data and Artificial Intelligence (ICIBA)*, Chongqing, China, 2020, pp. 664-668. https://doi.org/10.1109/ICIBA50161.2020.9277180

[20] R. Soundrapandiyan, S. C. Satapathy, P. V. S. S. R. Chandra Mouli, and N. G. Nhu, "A comprehensive survey on image enhancement techniques with special emphasis on infrared images," *Multimedia Tools and Applications*, vol. 81, pp. 9045-9077, 2022. https://doi.org/10.1007/s11042-021-11250-y

[21] F. Samadi, G. Akbarizadeh, and H. Kaabi, "Change detection in SAR images using deep belief network: a new training approach based on morphological images," *IET Image Processing*, vol. 13, no. 12, pp. 2255-2264, 2019. https://doi.org/10.1049/iet-ipr.2018.6248

[22] J. Liang, C. Fan, S. Hou, C. Shen, Y. Huang, and S. Yu, "GaitEdge: beyond plain end-to-end gait recognition for better practicality," in *Computer Vision – ECCV 2022*. Cham, Switzerland: Springer, 2022, pp. 375-390. https://doi.org/10.1007/978-3-031-20065-6_22

[23] D. Dhillon and R. Chouhan, "Enhanced edge detection using SR-guided threshold maneuvering and window mapping: handling broken edges and noisy structures in canny edges," *IEEE Access*, vol. 10, pp. 11191-11205, 2022. https://doi.org/10.1109/ACCESS.2022.3145428

[24] X. Zhang, J. Cui, J. Wang, C. Sun, Z. Zhu, F. Wang, and Y. Ma, "Parametric scatterer extraction method for space-target inverse synthetic aperture radar image CLEAN," *IET Radar, Sonar & Navigation*, vol. 17, no. 5, pp. 899-915, 2023. https://doi.org/10.1049/rsn2.12386

[25] National Aeronautics and Space Administration, "NASA 3D Resources," c2023 [Online]. Available: https://

nasa3d.arc.nasa.gov.

[26] "The public satellite database," c2024 [Online]. Available: https://www.n2yo.com.

[27] Fraunhofer, "Allen Erwartungen zum Trotz," c2021 [Online]. Available: https://www.fhr.fraunhofer.de/de/bereiche/Radar-zur-Weltraumlageerfassung-RWL/Allen-Erwartungen-zum-Trotz-JB2021.html.

[28] A. Pradhan, S. K. Bisoy, and A. Das, "A survey on PSO based meta-heuristic scheduling mechanism in cloud computing environment," *Journal of King Saud University-Computer and Information Sciences*, vol. 34, no. 8, pp. 4888-4901, 2022. https://doi.org/10.1016/j.jksuci.2021.01.003

[29] A. Banharnsakun, "Feature point matching based on ABC-NCC algorithm," *Evolving Systems*, vol. 9, pp. 71-80, 2018. https://doi.org/10.1007/s12530-017-9183-y

[30] Z. Peng, W. Huang, M. Luo, Q. Zheng, Y. Rong, T. Xu, and J. Huang, "Graph representation learning via graphical mutual information maximization," in *Proceedings of The Web Conference 2020*, Taipei, Taiwan, 2020, pp. 259-270. https://doi.org/10.1145/3366423.3380112

Linhua Wu

https://orcid.org/0009-0006-0790-0556

was born in 1999. She received her B.E. degree from Hubei University of Economics, Wuhan, China, in 2021. Currently, she is an M.E. candidate at the School of Information Engineering, Minzu University of China. Her current research interests include ISAR image processing and computer architecture.

Jiaoyang Su

https://orcid.org/0009-0008-7626-0577

was born in 1988. He received his B.E. degree from Minzu University of China in 2011 and his M.E. degree from Beijing Institute of Technology in 2013. Currently, he is an engineer at Minzu University of China, Beijing, China. His research interests include computer architecture and signal processing.

Lizhi Zhao

https://orcid.org/0000-0001-7216-9014

was born in 1986. She received her B.E. degree from Hebei University of Technology in 2008 and her Ph.D. degree from Beijing Institute of Technology in 2015. She was a joint training student at the University of Pisa in 2013. Currently, she is a lecture at Minzu University of China, Beijing, China. Her research interests include radar imaging and bistatic radar signal processing.

Weijun Cheng

https://orcid.org/0000-0003-1432-4324

received his M.S. degree in electronics and control engineering from the China University of Mining and Technology, Beijing, China, in 1998, and his Ph.D. degree in telecommunications engineering from Beijing University of Posts and Telecommunications, Beijing, China, in 2004. He was a postdoctoral research fellow in electronics engineering from 2005 to 2007 at Peking University, Beijing, China. From 2017 to 2018, he was a visiting scholar at the School of Electrical, Computer, and Energy Engineering in Arizona State University, AZ, USA, along with Professor Junshan Zhang. Currently, he is an associate professor at the School of Information Engineering, Minzu University of China, Beijing, China. His research interests are wireless communication theory and AI in IoT.

Junling Wang

https://orcid.org/0000-0001-7158-0688

received his B.E. and M.E. degrees from China University of Petroleum, Qingdao, China, in 2005 and 2008, respectively. In 2013, he received his Ph.D. degree from the Beijing Institute of Technology (BIT). He was an exchange student in the Department of Signal Theory and Communications, Universitat Politecnica de Catalunya, in 2010. Since 2013, he has been working in the School of Information and Electronics, BIT, Beijing, China, where he is currently an associate professor. His current research interests include satellite detection and imaging as well as radar signal processing.

Detection of Buried Nonlinear Targets Using DORT

Young Jin Song ⓘ · Sun K. Hong* ⓘ

Abstract

Ground-penetrating radars (GPR) based on a variety of techniques have been proposed to improve the performance of buried target (e.g., landmines, threat devices) detection. However, the small radar cross section (RCS) of small electronic devices poses difficulties for target detection, especially when they are buried in lossy and inhomogeneous media. This paper presents a novel buried nonlinear target detection method based on the decomposition of the time-reversal operator (DORT) that uses a multistatic system to overcome the limitations of conventional GPR. Using harmonic radar, which detects the harmonic responses scattered from electronic devices, and DORT processing, which enables focusing/imaging of the detected target, the detection performance is verified by conducting simulation and measurements. The overall results demonstrate that the proposed method achieves accurate detection of buried targets with small RCS.

Key Words: Buried Targets, DORT, Ground-Penetrating Radars, Harmonic Radars, Nonlinear Detection.

I. INTRODUCTION

Buried target detection and imaging have been topics of interest for various military and security applications. In particular, ground-penetrating radars (GPR) have proven to be useful in detecting landmines and threat devices buried in the ground [1–5]. Unlike targets in free space, buried targets are typically immersed in dielectric media, which are often lossy and inhomogeneous. Moreover, the occurrence of coupling between unwanted objects or multiple scatterers adds further complexity, rendering the detection of buried targets difficult. As a result, various techniques have been proposed to improve the performance of buried target detection and GPR [6–13].

Even when using advanced processing techniques, targets with a small radar cross section (RCS), especially when they are buried, are difficult to detect. Notably, buried threat devices, such as improvised explosive devices (IEDs) and bombs, often comprise non-metallic materials, thereby producing small RCS.

However, many such devices contain small electronic components that are largely used to control detonation, among other functions. In this context, by utilizing nonlinear detection, the difficulty of detecting small RCS buried targets can possibly be alleviated. In other words, taking advantage of the nonlinear characteristics of the semiconductor junctions in electronics, harmonic radar can be implemented to detect the harmonic responses scattered from these "nonlinear targets" with mall RCS, which are otherwise difficult to detect [14–17]. Since harmonic radars are designed to only receive nonlinear (harmonic) responses from targets, linear responses (clutter and other unwanted signals) are inherently suppressed. Such properties of harmonic radars are well suited for improving the performance of buried target detection, i.e., detecting targets containing small electronic devices.

When detecting buried targets, a multistatic system can be used to effectively improve detection accuracy, as it can appropriately deal with weak target signals in a lossy medium [3, 18–

21]. Using signal processing algorithms, the signals collected by an antenna array in a multistatic manner can be used to provide images of targets. In particular, the decomposition of the time-reversal operator (DORT) technique has been widely used in various detection scenarios using an array-based system [22–32]. DORT allows for the separation of multiple detected targets through the eigenvalue decomposition (EVD) of the time-reversal operator in the multistatic response matrix, thus providing the information necessary for selective focusing/imaging of each detected target. For this reason, DORT has been used for the detection and imaging of multiple buried targets [23, 25, 27, 31]. Recently, the use of DORT for nonlinear target detection has also been proposed [28, 30, 32], which demonstrated the accurate detection of nonlinear targets in the presence of linear scatters. However, the use of DORT-based techniques for buried nonlinear target detection has yet to be reported.

The reported capabilities of DORT for detecting buried and nonlinear targets make it a suitable candidate for buried nonlinear target detection. Therefore, this paper proposes and demonstrates array-based buried nonlinear (harmonic) target detection using DORT. The performance of the proposed approach was verified through numerical simulations and measurements of various test cases involving buried nonlinear targets.

II. PROPOSED APPROACH

A general scenario of the proposed approach for the detection of buried nonlinear targets is illustrated in Fig. 1, where it is considered that both linear and nonlinear targets may exist in a buried environment. An antenna array is used to generate multistatic responses from the probed environment, which are then processed using DORT for the detection and focusing/imaging of the targets. Here, the antenna array can be configured into a monostatic array, where the same array is used to transmit (Tx) and receive (Rx) signals, or a bistatic array, where separate Tx and Rx arrays are used.

DORT is an array-based detection processing technique that separates detected targets and extracts information on their lo-

Fig. 1. Buried nonlinear target detection using an array-based system and DORT.

catio'ns in terms of their eigenvalues and the corresponding eigenvectors through EVD [22]. In the case of an array with N elements, the time-domain monostatic/bistatic responses collectively make up an $N \times N$ multistatic matrix $M(t)$. Each matrix element of $M(t)$, namely $m_{i,j}(t)$, represents the response between the jth Tx and i^{th} Rx antenna element pair. Therefore, in the presence of P scatterers, $m_{i,j}(t)$ can be expressed in terms of the scattered response from the pth scatterer, $s_{p,j}(t)$, and the Green's function between the scatterer and the ith receive antenna, $g_{i,p}(t)$. This can be expressed as follows:

$$m_{i,j}(t) = \sum_{p=1}^{P} s_{p,j}(t) * g_{i,p}(t), \tag{1}$$

where * denotes convolution. To account for the responses from both linear and nonlinear targets, $s_{p,j}(t)$ can be expressed using a power series, as follows:

$$s_{p,j}(t) = \sum_{k=1}^{\infty} c_k \left[f(t) * g_{p,j}(t) \right]^k, \tag{2}$$

where $f(t)$ is the transmit pulse and $g_{p,j}(t)$ represents the Green's function between the pth scatter and j^{th} Tx antenna. For linear targets, scattering only occurs in the fundamental band of $f(t)$, which means that c_k is nonzero only for $k = 1$. In contrast, in the case of nonlinear targets, the scattered responses contain the harmonic bands of $f(t)$, resulting in nonzero c_k for all values of k. Here, we are only interested in receiving the nonlinear responses in the second harmonic band, that is, only the portion of $m_{i,j}(t)$ corresponding to $k = 2$, namely $m_{i,j}^h(t)$, will be received and processed. Therefore, by receiving and processing only the second harmonic content, the linear responses (clutter) are inherently suppressed.

DORT processing can then be applied to $M^h(\omega)$, which refers to the frequency domain version of $M^h(t)$. The time-reversal operator $T(\omega)$ can be defined as follows:

$$T(\omega) = M^h(\omega)M^{h\dagger}(\omega), \tag{3}$$

where † denotes the Hermitian conjugate corresponding to the time reversal in the frequency domain. The eigenvalues and eigenvectors can be extracted through EVD of $T(\omega)$ which can be expressed as:

$$T(\omega) = U(\omega)\Lambda(\omega)U^{\dagger}(\omega), \tag{4}$$

where $\Lambda(\omega)$ is a diagonal matrix containing the eigenvalues λ_n and $U(\omega)$ is a unitary matrix containing the eigenvectors. Ideally, each nonzero eigenvalue should correspond to each detected nonlinear target, while the associated eigenvectors should
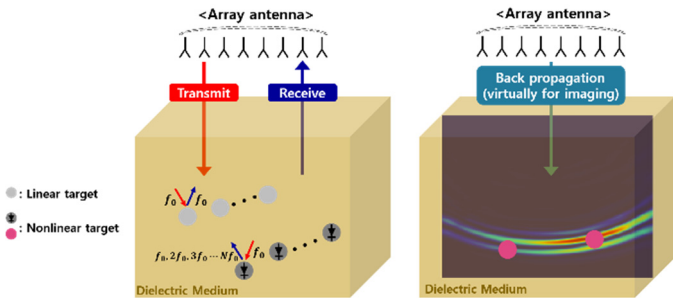
represent the phase-conjugated Green's functions between the array elements and target. This implies that the detected targets and their information can be separated in terms of their eigenstructure. The EVD of $T(\omega)$ can be done by means of the singular value decomposition of $M^h(\omega)$, since $T(\omega)$ is a Hermitian matrix [28].

Once the detected targets are separated by implementing EVD, a set of signals that can be backpropagated for selective focusing (imaging) of each target can be determined. Therefore, for the ith target, the backpropagation signals can be represented as follows:

$$k_n(\omega) = \sigma_n(\omega)v_n(\omega), \qquad (5)$$

where $\sigma_n(\omega)$ is the singular value $(\sigma_n^2 = \lambda_n)$ and $v_n(\omega)$ is the eigenvector. Therefore, each element of $k_n(\omega)$ corresponds to the signal fed into the array elements for selective focusing on the nth target. Subsequently, by taking the inverse Fourier transform of Eq. (5) (over the second harmonic band), the time-domain backpropagation signals, $k_n(t)$, can be obtained, which can then be virtually fed into the antenna array to generate focused waves at the location of the corresponding target.

In the following sections, the detection and location of buried nonlinear targets utilizing the aforementioned approach are demonstrated through numerical simulation and measurements.

III. NUMERICAL SIMULATIONS AND MEASUREMENTS

To validate the proposed approach, a buried nonlinear target detection environment was set up, as shown in Fig. 2, comprising an acrylic box (30 cm × 30 cm × 30 cm) filled with dry sand ($\varepsilon_r = 3$), and two separate antenna arrays for Tx and Rx. For the transmit signal, a Gaussian pulse with a center frequency of 3.1 GHz and a bandwidth of 200 MHz was used. The array elements were antipodal Vivaldi antennas (40 mm × 60 mm × 1.6 mm), as shown in Fig. 3(a). The reflection coefficient of the Vivaldi antenna is shown in Fig. 3(b), where the impedance bandwidth covers both the fundamental and second harmonic bands. The spacing of the array elements was set to $0.81\lambda_h$, with λ_h being the wavelength at 6.2 GHz (2nd harmonic) in the sand. This spacing was determined by accounting for the transmit and receive frequencies—3.1 GHz and 6.2 GHz, respectively—as well as the potential presence of grating lobes and mutual coupling between the Tx and Rx arrays [28]. A planar bowtie structure (22.6 mm × 26 mm × 1.2 mm) was used to represent the linear and nonlinear targets, where a resistor and Schottky diode were used as their terminations, respectively. Since the purpose of this experiment was to demonstrate the feasibility of the proposed approach, a canonical shape, such as bowtie, that allows for sufficient scattering over a wide bandwidth, including the fundamental and second harmonic bands, was considered to be a good choice for the test target.

The performance of the proposed approach in the aforementioned test environment was examined by carrying out numerical simulation and measurements. The numerical simulation was performed using SEMCAD X [33]. The measurement setup is depicted in Fig. 2. On the Tx-end, a high-speed arbitrary waveform generator is used as the signal source, followed by a power amplifier. In addition, a band pass filter (3–3.2 GHz) is connected to suppress any self-generated harmonics occurring before transmitting through the Tx antenna. On the Rx-end, a band pass filter (5.6–7.0 GHz) is placed behind the Rx antenna, followed by a low noise amplifier to effectively amplify the received target harmonic responses for an oscilloscope to directly sample and capture them for signal processing. Measurements were performed for each Tx–Rx element pair to collect each $m_{i,j}^h(t)$ at a time, which were then arranged into $M^h(t)$ in the processing. The power level of the transmit pulse was set to 0.5 W (27 dBm). For nonlinear target detection, it is important to use sufficient transmit power to excite harmonic responses from nonlinear targets. The nonlinear detection range
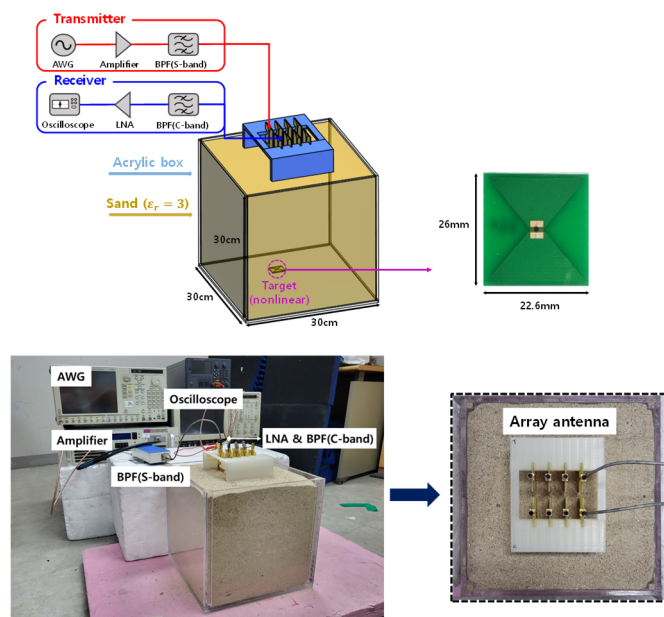

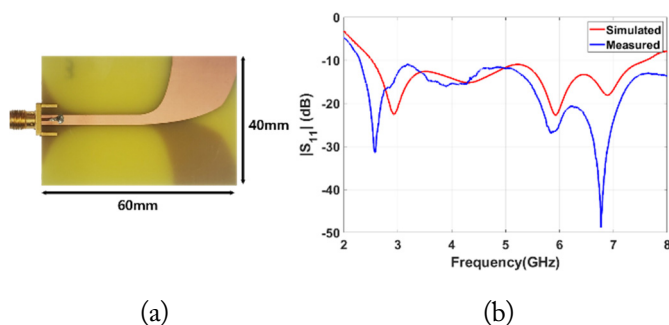Fig. 2. Block diagram and experimental setup for buried nonlinear target detection.

Fig. 3. (a) Fabricated Vivaldi antenna and (b) reflection coefficient ($|S_{11}|$) of the Vivaldi antenna.

is determined by the parameters, such as the transmit power and nonlinear RCS, that constitute the nonlinear radar equation, the details of which can be found in [15, 17].

Fig. 4 illustrates three representative target configurations— Case 1 involves a single buried nonlinear target, Case 2 involves linear and nonlinear buried targets, and Case 3 involves two nonlinear buried targets.

For Case 1, as shown in Fig. 4(a), a single nonlinear target was placed 25 cm below the surface, slightly to the right of the center. Based on the results of the DORT processing, the extracted eigenvalues from the simulated and measured data are shown in Fig. 5(a) and 5(b), respectively. The presence of the nonlinear target is confirmed by the dominant eigenvalue $\lambda_1(\omega)$ in the second harmonic band, which can be verified in Fig. 5 for both the simulation and measurement. Fig. 6(a) and 6(b) show the imaging/focusing results for the simulated and measured cases, respectively. The backpropagation signals are generated using $v_1(\omega)$ and $\sigma_1(\omega)$, based on Eq. (5). Note that the backpropagated waves are virtually generated using the numerical model in SEMCAD X for both cases. The images in Fig. 6 correspond to the time instance at which the backpropagated waves focus on the location of the nonlinear target, indicating that the nonlinear target is properly detected and located using the DORT processing.

For Case 2, a nonlinear target was buried 25 cm below the surface, slightly to the right of the center, while a linear target was placed 23.5 cm below the surface, slightly to the left of the center.

Fig. 7(a) and 7(b) show the extracted eigenvalues from the simulated and measured data, respectively. Even in the presence of the linear target, only one dominant eigenvalue could be extracted in the second harmonic band, indicating that only the nonlinear target was detected as a result of harmonic detection since the linear target did not generate any harmonics. The imaging/focusing results for the simulated and measured cases are shown in Fig. 8(a) and 8(b), respectively. It is evident that the nonlinear target is properly detected and located even in the presence of a linear target nearby.

For Case 3, the same target locations as those in Case 2 were retained, but both targets were nonlinear targets. The extracted eigenvalues from the simulated and measured data are shown in Fig. 9(a) and 9(b), respectively. The presence of two nonlinear targets was confirmed by two significant eigenvalues, $\lambda_1(\omega)$ and $\lambda_2(\omega)$, appearing in the second harmonic band, indicating that both nonlinear targets were properly detected and separated in the eigenstructure. The backpropagation signals for each target were then generated using $v_1(\omega)$ and $v_2(\omega)$, as well as the corresponding $\sigma_1(\omega)$ and $\sigma_2(\omega)$. The selective focusing/imaging results of each nonlinear target are shown in Fig. 10. For each target, focusing of the backpropagated waves takes place at the target location, with the simulated and measured results in close agreement. This verifies that multiple buried nonlinear targets can be properly detected, separated and selectively located, using DORT.
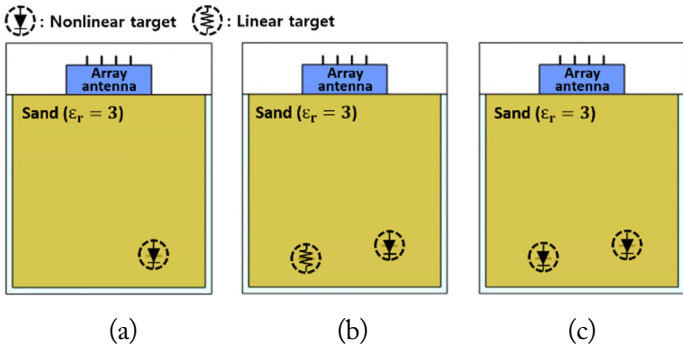

Fig. 4. The three representative buried target cases tested: (a) Case 1, single nonlinear target, (b) Case 2, a nonlinear target and a linear target, and (c) Case 3, two nonlinear targets.
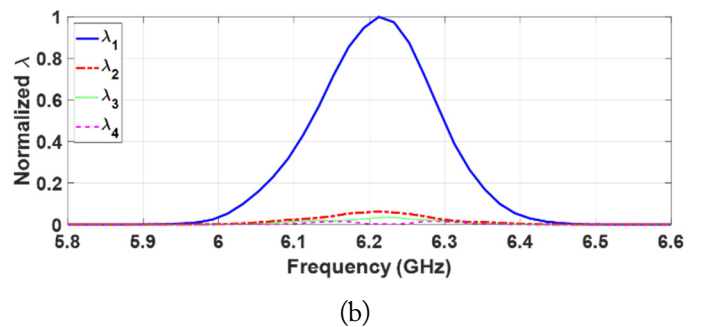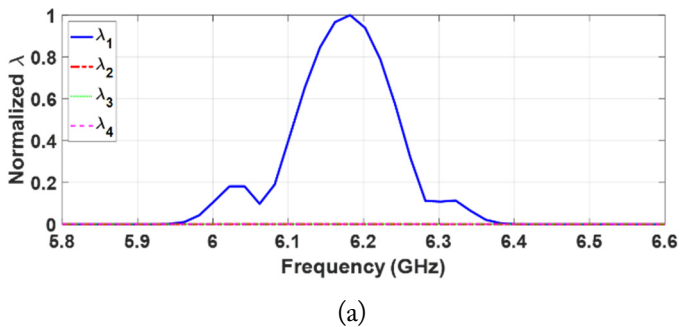

Fig. 6. Backpropagation (imaging/focusing) results for the detected nonlinear target in Case 1 on using (a) the simulated and (b) measured data.

Fig. 5. Extracted eigenvalues for Case 1 from (a) simulated data and (b) measured data.

(a)

(b)

Fig. 7. Extracted eigenvalues for Case 2 from (a) simulated data and (b) measured data.

(a)

(b)

Fig. 8. Backpropagation (imaging/focusing) results for the detected nonlinear target in Case 2 on using (a) the simulated and (b) measured data.

IV. Effects of Target Orientation

The simulated and measured results described in the previous section were obtained with the array antenna and the bowtie target facing each other directly. To test the effects of target orientation on detection performance, simulation was conducted by rotating the target about its center from 0° to 90°, as shown in Fig. 11(a). The imaging/focusing results for the four simulated cases, as shown in Fig. 11(b), highlight that the backpropagated waves remain properly focused on the location of the nonlinear target even when the array antenna and target do not face each other directly. This is primarily due to the bowtie structure exhibiting an omnidirectional pattern, which minimizes the influence of the target orientation. However, in practical

(a)

(b)

Fig. 9. Extracted eigenvalues for Case 3 from (a) simulated data and (b) measured data.

(a)

(b)

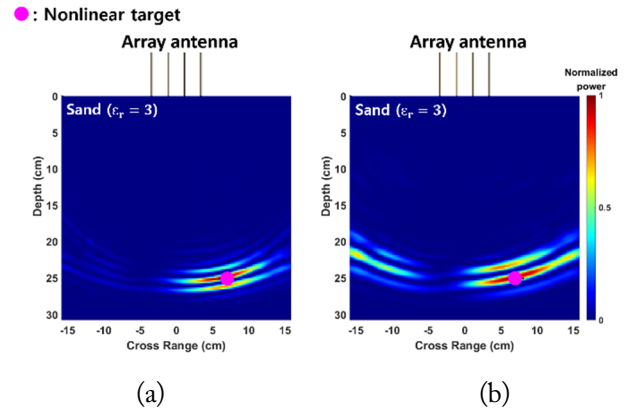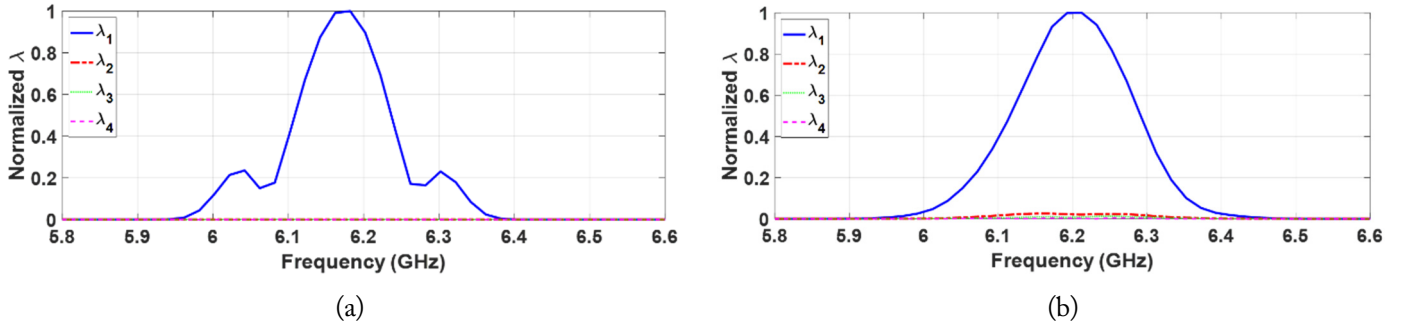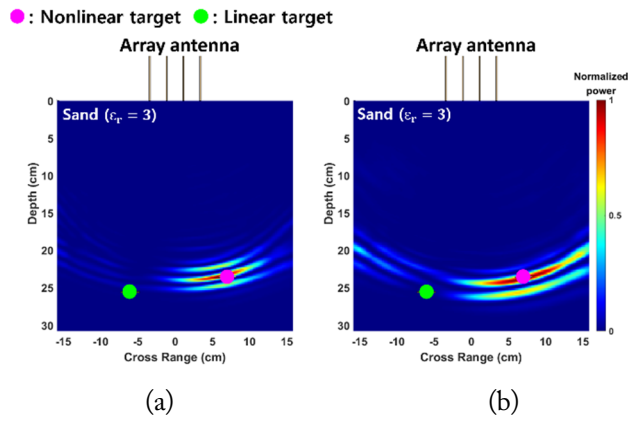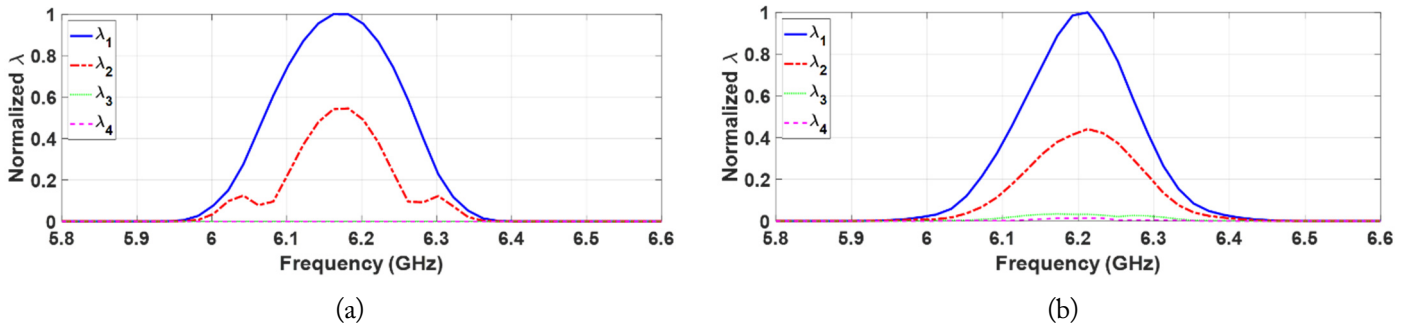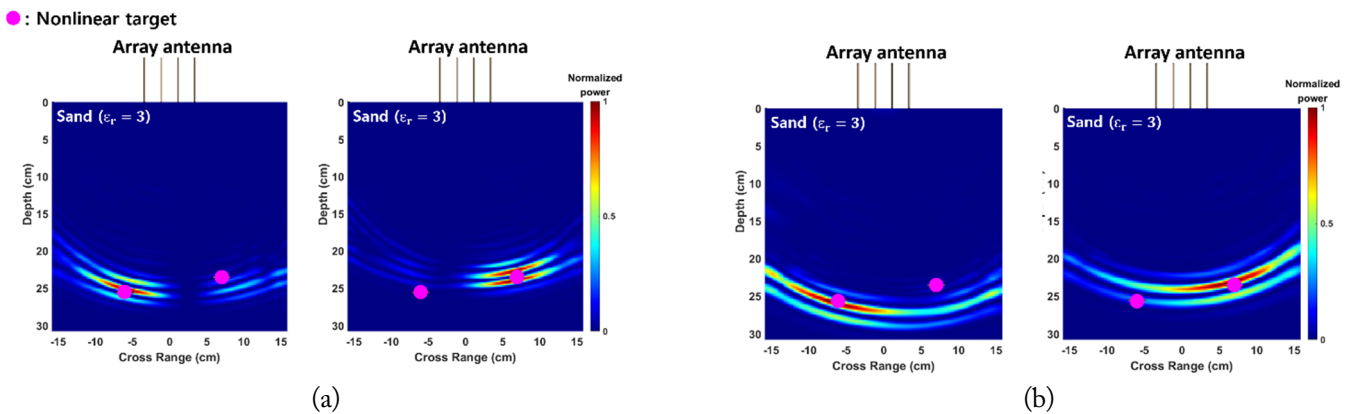Fig. 10. Backpropagation (imaging/focusing) results for the detected nonlinear target in Case 3 on using (a) the simulated and (b) measured data. Note that backpropagation was performed for each of the two detected nonlinear targets.
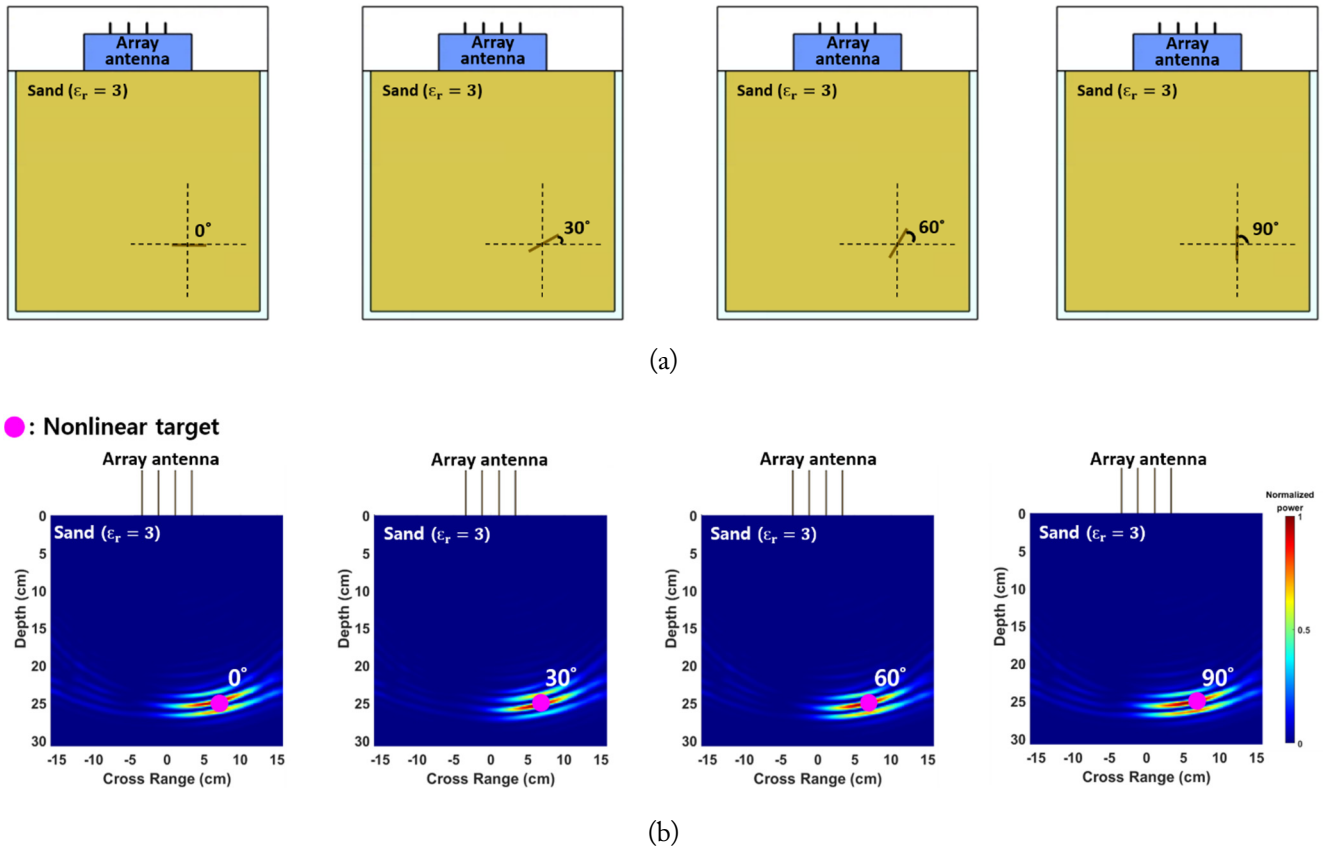
(a)

(b)

Fig. 11. (a) Four buried single nonlinear target cases for examining the influence of target orientation and (b) backpropagation (imaging/focusing) results for the detected nonlinear target in each case.

scenarios in which realistic targets may be various electronic devices exhibiting more angle-dependent scattering patterns, a detailed analysis on the influence of target orientations would be important for accurately predicting the detection performance of the proposed approach.

V. Conclusion

This paper proposes and validates the application of harmonic detection and DORT processing for detecting buried nonlinear targets. Through simulation and measurements in a test environment, the detection and location of buried nonlinear targets were verified for various configurations, demonstrating the feasibility of the proposed approach for detecting buried small electronic devices, which are typically difficult to detect. The results of this study merit further investigation into the proposed technique, which holds good potential for application in areas where the detection of small buried nonlinear devices is crucial, such as security, military and biomedical applications.

References

[1] P. Chaturvedi and R. G. Plumb, "Electromagnetic imaging of underground targets using constrained optimization," *IEEE Transactions on Geoscience and Remote Sensing*, vol. 60, no. 8, pp. 551-561, 1995. https://doi.org/10.1109/36.387572

[2] S. Lambot, E. C. Slob, I. van den Bosch, B. Stockbroeckx, and M. Vanclooster, "Modeling of ground-penetrating radar for accurate characterization of subsurface electric properties," *IEEE Transactions on Geoscience and Remote Sensing*, vol. 42, no. 11, pp. 2555-2568, 2004. https://doi.org/10.1109/TGRS.2004.834800

[3] T. Counts, A. C. Gurbuz, W. R. Scott, J. H. McClellan, and K. Kim, "Multistatic ground-penetrating radar experiments," *IEEE Transactions on Geoscience and Remote Sensing*, vol. 45, no. 8, pp. 2544-255, 2007. https://doi.org/10.1109/TGRS.2007.900677

[4] L. Li, A. E. C. Tan, K. Jhamb, and K. Rambabu, "Buried object characterization using ultra-wideband ground penetrating radar," *IEEE Transactions on Microwave Theory and Techniques*, vol. 60, no. 8, pp. 2654-2664, 2012. https://doi.org/10.1109/TMTT.2012.2198235

[5] A. Gharamohammadi, F. Behnia, and R. Amiri, "Imaging based on correlation function for buried objects identification," *IEEE Sensors Journal*, vol. 18, no. 18, pp. 7407-7413, 2018. https://doi.org/10.1109/JSEN.2018.2859170

[6] A. Van Der Merwe and I. J. Gupta, "A novel signal processing technique for clutter reduction in GPR measurements of small, shallow land mines," *IEEE Transactions on Geoscience and Remote Sensing*, vol. 38, no. 6, pp. 2627-2637, 2000. https://doi.org/10.1109/36.885209

[7] U. Boniger and J. Tronicke, "Subsurface utility extraction and characterization: combining GPR symmetry and polarization attributes," *IEEE Transactions on Geoscience and Remote Sensing*, vol. 50, no. 3, pp. 736-746, 2012. https://doi.org/10.1109/TGRS.2011.2163413

[8] R. Solimene, A. Cuccaro, A. Dell'Aversano, I. Catapano, and F. Soldovieri, "Ground clutter removal in GPR surveys," *IEEE Journal of Selected Topics in Applied Earth Observations and Remote Sensing*, vol. 7, no. 3, pp. 792-798, 2014. https://doi.org/10.1109/JSTARS.2013.2287016

[9] K. R. Krueger, J. H. McClellan, and W. R. Scott, "Efficient algorithm design for GPR imaging of landmines," *IEEE Transactions on Geoscience and Remote Sensing*, vol. 53, no. 7, pp. 4010-4021, 2015. https://doi.org/10.1109/TGRS.2015.2388786

[10] J. Xiao and L. Liu, "Suppression of clutters caused by periodic scatterers in GPR profiles with multibandpass filtering for NDT&E imaging enhancement," *IEEE Journal of Selected Topics in Applied Earth Observations and Remote Sensing*, vol. 10, no. 10, pp. 4273-4279, 2017. https://doi.org/10.1109/JSTARS.2017.2752163

[11] M. Moalla, H. Frigui, A. Karem, and A. Bouzid, "Application of convolutional and recurrent neural networks for buried threat detection using ground penetrating radar data," *IEEE Transactions on Geoscience and Remote Sensing*, vol. 58, no. 10, pp. 7022-7034, 2020. https://doi.org/10.1109/TGRS.2020.2978763

[12] D. Kumlu and I. Erer, "GPR clutter reduction by robust orthonormal subspace learning," *IEEE Access*, vol. 8, pp. 74145-74156, 2020. https://doi.org/10.1109/ACCESS.2020.2988333

[13] D. Kumlu, "GPR image recovery effect on faster R-CNN-based buried target detection," *Journal of Electromagnetic Engineering and Science*, vol. 22, no. 5, pp. 591-598, 2022. https://doi.org/10.26866/jees.2022.5.r.127

[14] R. O. Hstger, "Harmonic radar systems for near-ground in-foliage nonlinear scatterers," *IEEE Transactions on Aerospace and Electronic Systems*, vol. 12, no. 2, pp. 230-245, 1976. https://doi.org/10.1109/TAES.1976.308301

[15] G. J. Mazzaro, A. F. Martone, and D. M. McNamara, "Detection of RF electronics by multitone harmonic radar," *IEEE Transactions on Aerospace and Electronic Systems*, vol. 50, no. 1, pp. 477-490, 2014. https://doi.org/10.1109/TAES.2013.120798

[16] A. Mishra and C. Li, "A review: recent progress in the design and development of nonlinear radars," *Remote Sensing*, vol. 13, no. 24, article no. 4982, 2021. https://doi.org/10.3390/rs13244982

[17] S. Y. Oh, K. H. Cha, H. Hong, H. Park, and S. K. Hong, "Measurement of nonlinear RCS of electronic targets for nonlinear detection," *Journal of Electromagnetic Engineering and Science*, vol. 22, no. 4, pp. 447-451, 2022. https://doi.org/10.26866/jees.2022.4.r.108

[18] A. J. Devaney, "Time reversal imaging of obscured targets from multistatic data," *IEEE Transactions on Antennas and Propagation*, vol. 53, no. 5, pp. 1600-1610, 2005. https://doi.org/10.1109/TAP.2005.846723

[19] Y. Xie, B. Guo, L. Xu, J. Li, and P. Stoica, "Multistatic adaptive microwave imaging for early breast cancer detection," *IEEE Transactions on Biomedical Engineering*, vol. 53, no. 8, pp. 1647-1657, 2006. https://doi.org/10.1109/TBME.2006.878058

[20] M. Ambrosanio, M. T. Bevacqua, T. Isernia, and V. Pascazio, "Performance analysis of tomographic methods against experimental contactless multistatic ground penetrating radar," *IEEE Journal of Selected Topics in Applied Earth Observations and Remote Sensing*, vol. 14, pp. 1171-1183, 2020. https://doi.org/10.1109/JSTARS.2020.3034996

[21] A. Aljurbua and K. Sarabandi, "Detection and localization of buried pipelines using a 3-D multistatic imaging radar," *IEEE Transactions on Geoscience and Remote Sensing*, vol. 60, article no. 2003710, 2021. https://doi.org/10.1109/TGRS.2021.3131913

[22] C. Prada and M. Fink, "Eigenmodes of the time reversal operator: a solution to selective focusing in multiple-target media," *Wave Motion*, vol. 20, no. 2, pp. 151-163, 1994. https://doi.org/10.1016/0165-2125(94)90039-6

[23] G. Micolau, M. Saillard, and P. Borderies, "DORT method as applied to ultrawideband signals for detection of buried objects," *IEEE Transactions on Geoscience and Remote Sensing*, vol. 41, no. 8, pp. 1813-1820, 2003. https://doi.org/10.1109/TGRS.2003.814139

[24] J. L. Robert, M. Burcher, C. Cohen-Bacrie, and M. Fink, "Time reversal operator decomposition with focused transmission and robustness to speckle noise: application to microcalcification detection," *The Journal of the Acoustical Society of America*, vol. 119, no. 6, pp. 3848-3859, 2006. https://doi.org/10.1121/1.2190163

[25] M. E. Yavuz and F. L. Teixeira, "Full time-domain DORT for ultrawideband electromagnetic fields in dispersive, random inhomogeneous media," *IEEE Transactions on Antennas and Propagation*, vol. 54, no. 8, pp. 2305-2315, 2006. https://doi.org/10.1109/TAP.2006.879196

[26] M. E. Yavuz and F. L. Teixeira, "Ultrawideband microwave sensing and imaging using time-reversal techniques: a review," *Remote Sensing*, vol. 1, no. 3, pp. 466-495, 2009. https://doi.org/10.3390/rs1030466

[27] T. Zhang, P. C. Chaumet, E. Mudry, A. Sentenac, and K. Belkebir, "Electromagnetic wave imaging of targets buried in a cluttered medium using a hybrid inversion-DORT meth-

od," *Inverse Problems*, vol. 28, no. 12, article no. 125008, 2012. https://doi.org/10.1088/0266-5611/28/12/125008

[28] J. M. Faia, Y. He, H. S. Park, E. Wheeler, and S. K. Hong, "Detection and location of nonlinear scatterers using DORT applied with pulse inversion," *Progress in Electromagnetics Research Letters*, vol. 80, pp. 101-108, 2018. https://doi.org/10.2528/PIERL18092605

[29] S. K. Hong, "Effects of target resonances on ultrawideband-DORT," *Journal of Electromagnetic Waves and Applications*, vol. 32, no. 13, pp. 1710-1732, 2018. https://doi.org/10.1080/09205071.2018.1467284

[30] S. K. Hong and H. S. Park, "Embedded resonances for discrimination of multiple passive nonlinear targets applicable to

DORT," *Progress in Electromagnetics Research M*, vol. 81, pp. 31-42, 2019. http://dx.doi.org/10.2528/PIERM19021703

[31] D. H. Chambers, "Application of DORT to multistatic GPR data," in *SPIE Defense and Commercial Sensing*, Anaheim, CA, USA, 2020 [Online]. Available: https://www.osti.gov/servlets/purl/1634895.

[32] K. Cha, H. S. Park, and S. K. Hong, "Nonlinear through-the-wall detection using DORT applied with LFM pulses," *IEEE Antennas and Wireless Propagation Letters*, vol. 22, no. 6, pp. 1331-1335, 2023. https://doi.org/10.1109/LAWP.2023.3241637

[33] SPEAG, "SEMCAD X," 2018 [Online]. Available: http://speag.swiss/products/semcad/overview/.

Young Jin Song

https://orcid.org/0009-0008-7330-8483

received his B.S. degree in electronic engineering from Soongsil University, Seoul, South Korea, in 2022, and is currently pursuing his combined M.S./Ph.D. degree in electronic engineering at Soongsil University. His research interests include nonlinear radars and wireless power transfer.

Sun K. Hong

https://orcid.org/0000-0002-3794-3171

received his B.S. degree in electrical engineering from the University of Maryland, College Park, MD, USA, in 2005, and his M.S. and Ph.D. degrees in electrical engineering from Virginia Tech, Blacksburg, VA, USA, in 2008 and 2012, respectively. From 2005 to 2015, he was a research engineer with the U.S. Naval Research Laboratory, Washington, DC, USA, where he was involved in research related to time-domain techniques in electromagnetics, nonlinear electromagnetic interaction, radars, electro-magnetic scattering, high power microwave (HPM) applications, and antennas. From 2015 to 2017, he was an assistant professor in the Department of Electrical and Computer Engineering, Rose-Hulman Institute of Technology, Terre Haute, IN, USA. Since 2017, he has been with Soongsil University, Seoul, South Korea, where he is currently an associate professor at the School of Electronic Engineering. His current research interests include wave-front control techniques, wireless power transfer, EM waves in complex propagation environments, detection of nonlinear devices, radars, high-power electromagnetics, and antennas.

Design of a Compact Log Periodic Dipole Array Antenna for Broadband and High-Power Beam Synthesis Using Superposition

Changhyeon Im[1] ◐ · Sangwoon Youn[1] ◐ · Tae Heung Lim[2] ◐ · Hosung Choo[1,*] ◐

Abstract

This paper investigates various array beam shapes for high-power electronic warfare applications using an actual broadband array antenna. For use in a limited mounting space, a compact printed log periodic dipole array (LPDA) operating over a wide bandwidth is designed. The LPDA is then extended to an 8 × 1 array, with active element patterns (AEPs) obtained through simulation and measurement. Beam synthesis is performed by the superposition of several array patterns, which involves adjusting the weight of each AEP. To derive a synthesized array beam shape that is similar to the guided mask, the Taylor window weighting method is applied to each array pattern. Finally, beam synthesis for the flat-top beam, cosecant-squared beam, and iso-flux beam is performed using Taylor window-weighted AEPs, and the results are compared with those of beam shapes using ideal isotropic patterns. The results demonstrate that various beam shapes can be achieved for high-power electronic warfare applications using the AEPs of an actual array antenna.

Key Words: Active Element Patterns (AEPs), Beam Synthesis, Broadband, Log Periodic Dipole Array (LPDA).

I. Introduction

In the field of electronic warfare, the use of various array antenna systems capable of beamforming over a wide bandwidth using high-power radiation has been gradually increasing [1–3]. Such systems are often necessary in critical electronic warfare systems, such as high-power jammers, long-range radars, and target direction-finding systems, which play key roles in establishing a superior electromagnetic spectrum environment [4–6]. For example, broadband jammers used in avionics warfare typically operate within the frequency range of 1–18 GHz, while long-range radars used in ground stations function within the

2–4 GHz range [7]. Furthermore, direction-finding systems for detecting unauthorized transmitters often operate in the 1–40 GHz range. Since these high-power broadband systems are usually mounted on an aircraft, vehicle, or ground base station, which offers limited mounting space, a small-sized array antenna that satisfies wide bandwidth operations is required. Various types of broadband antennas, such as a ridged horn, an antipodal Vivaldi, and a log periodic dipole array (LPDA), have been extensively studied for use in these systems [8, 9]. Furthermore, in terms of power efficiency, an array antenna system that can form various shapes of beam patterns by adjusting the magnitude and phase of individual antenna elements is crucial [5, 10–15].

Therefore, beam synthesis studies have been conducted primarily for wireless communication and wireless power transmission applications [16, 17]. Recently, it has been applied to specific electronic warfare situations. For example, a flat-top beam can be used to uniformly transmit signals to a number of systems, cosecant-squared beams can be employed for air-to-ground scanning, and an iso-flux beam can be used at high altitudes to transmit uniform power to the ground. However, most studies have yielded only theoretical beam synthesis results, assuming that the array elements are ideal isotropic sources. In actual array antennas, each antenna element has different radiation patterns with mutual couplings. As a result, unexpected performance degradations, such as phase changes in antenna ports, reduction of radiation gain, and distortion in the radiation pattern, are observed in many cases. These problems also lead to distorted or unintended results pertaining to synthesized array beam shapes. Therefore, it is necessary to identify and study methods that can help obtain various beam shapes for specific purposes by accounting for the different radiation patterns and mutual couplings of each array element.

In this paper, various array beam shapes for high-power electronic warfare applications are derived using an actual broadband array antenna. For high-power arrays to be applied in a limited mounting space, a compact printed LPDA operating over a wide bandwidth is designed. To confirm the broadband characteristics of the designed antenna, the LPDA is fabricated, and its antenna performances, such as reflection coefficients and radiation patterns, are measured in a full anechoic chamber. The LPDA is then extended to an 8 × 1 array, and the active element patterns (AEPs) of the individual elements, considering their mutual couplings, are obtained by conducting measurements as well as simulations. Following this, after adjusting the weights of each AEP, beam synthesis within the guided mask is performed

by the superposition of several array patterns with different steering angles and amplitudes. To derive synthesized array beam shapes that closely resemble the guided mask, the Taylor window weighting method is applied to each array pattern. Finally, beam synthesis for a flat-top beam, a cosecant-squared beam, and an iso-flux beam is performed using the Taylor window-weighted AEPs. The results are then compared with those of the beam shapes using ideal isotropic patterns, ultimately demonstrating that various beam shapes for high-power electronic warfare, such as the flat-top beam, the cosecant-squared beam, and the iso-flux beam, can be achieved using the AEPs of the actual array antenna.

II. DESIGN AND MEASUREMENT OF THE BROADBAND LPDA AND ITS ARRAY

1. Broadband LDPA

Fig. 1 presents the geometry of the proposed compact LPDA for high-power broadband beamforming applications. The LPDA element was optimized to satisfy broadband characteristics operating within the 2–5 GHz range and boresight gain of more than 3 dBi for high-power beamforming systems, which typically allow limited antenna mounting space. The optimized antenna was printed on an FR-4 substrate (ε_r = 4.3, $\tan\delta$ = 0.018) to minimize the dimensions of length l_s, width w_s, and thickness t_s, as shown in Fig. 1(a)–1(c). In the LPDA design, a total of 13 dipole elements were employed to realize high directivity and broadband characteristics, which would help attain the various beam shapes required in electronic warfare systems. Each dipole element was designed considering a geometric ratio τ and an apex angle α, as expressed using equations as follows:
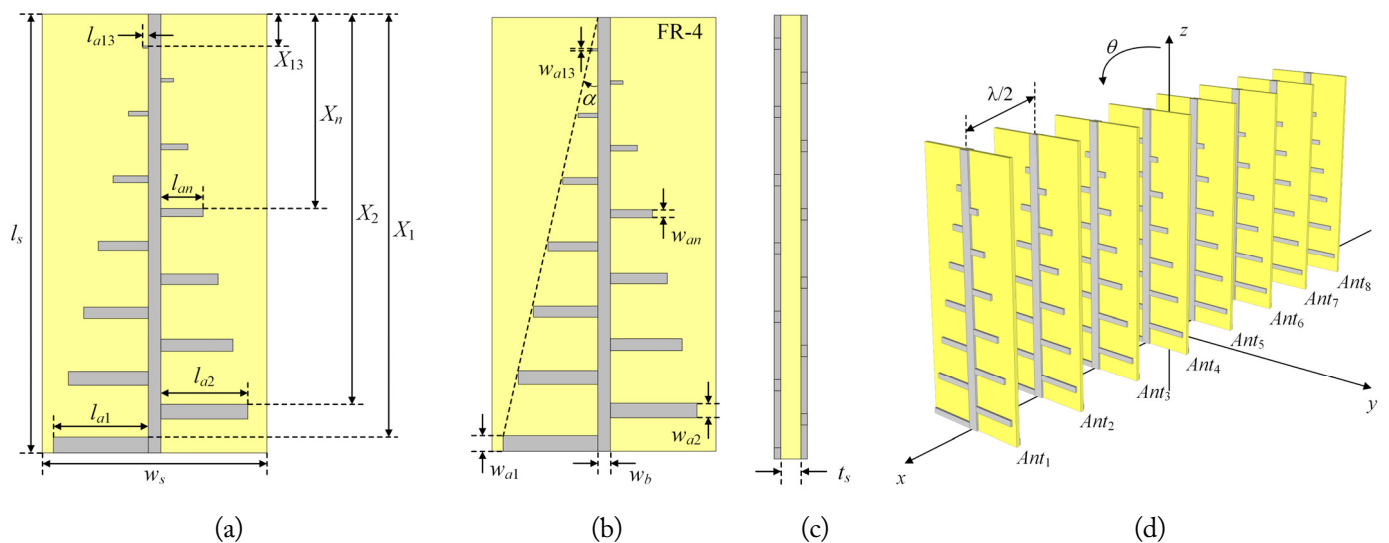

Fig. 1. Geometry of the proposed antenna: (a) top view, (b) bottom view, (c) side view, and (d) isometric view of the array antenna.

$$\tau = \frac{l_{a(n+1)}}{l_{an}} = \frac{X_{n+1}}{X_n}, \qquad (1)$$

$$\alpha = \tan^{-1}\left(\frac{l_{an}}{X_n}\right). \qquad (2)$$

As shown in Fig. 1(a) and 1(b), the geometric parameters of length l_{a1} and width w_{a1} of the longest element determined the lowest operating frequency to be 2 GHz. Subsequently, the other elements were sequentially designed with regard to the geometric ratio τ. Notably, l_{an} refers to the length of the nth dipole element, while the length of the $(n+1)^{\text{th}}$ element can be given by $\tau \cdot l_{an}$. The position parameter X_n was then calculated in the same way. Meanwhile, the length l_{a13} and width w_{a13} at position X_{13} were designed to cover the highest operating frequency of 5 GHz. Furthermore, the relation between the length l_{an} and location X_n of the dipoles was determined by the apex angle α in Fig. 1(b). The boom located at the center of the substrate was designed to feed the dipole elements with a width of w_b and length of l_s. Notably, the dimensions of an LPDA, as determined by the two design factors (τ and α), have a significant impact on broadband impedance-matching characteristics. The optimized design parameters, the detailed values of which are listed in Table 1, were obtained using the CST Studio Suite EM simulation software (http://www.cst.com). The single LPDA element was then extended to an 8 × 1 linear array configuration, maintaining array spacing of $\lambda/2$ at 4 GHz to synthesize various beams for electronic warfare purposes, as shown in Fig. 1(d). It is quite obvious that array antennas equipped with a large number of elements have an advantage in beam synthesis due to the narrow half-power beam width (HPBW) of the array pattern [18–21]. However, there are some disadvantages as well—the array system should be bulky and heavy. To compensate for these disadvantages, this study derived the beam synthesis performance using only eight elements of the LPDA that exhibited high gain and broadband characteristics.

Fig. 2(a) presents a photograph of the fabricated single LPDA, which shows that the proposed antenna is directly fed by an SMA connector at the top of the boom. Fig. 2(b) illustrates the extended 8 × 1 array in the x-axis, along with the proposed LPDA. The eight array elements were fixed at exact positions by a multi-layered, lightweight Styrofoam jig. Fig. 3 presents the reflection coefficients with regard to the LPDA boom width w_b. It is observed that when w_b is 4 mm, the reflection is less than −10 dB in the 1.7–5 GHz range.

2. LDPA Array

Fig. 4 presents the measured and simulated active reflection coefficients (ARCs) of Ant_5 (the center element) of the proposed compact printed LPDA array. The measured ARCs show broad-

Table 1. Design parameters of the proposed antenna

Parameter	Value	Parameter	Value
l_s	124 mm	w_b	4 mm
w_s	72 mm	t_s	1.6 mm
l_{a1}	29 mm	w_{a1}	6 mm
l_{a2}	23.73 mm	w_{a2}	4.98 mm
l_{a3}	19.36 mm	w_{a3}	4.13 mm
l_{a4}	15.73 mm	w_{a4}	3.43 mm
l_{a5}	12.71 mm	w_{a5}	2.85 mm
l_{a6}	10.21 mm	w_{a6}	2.36 mm
l_{a7}	8.14 mm	w_{a7}	1.96 mm
l_{a8}	6.41 mm	w_{a8}	1.63 mm
l_{a9}	4.98 mm	w_{a9}	1.35 mm
l_{a10}	3.80 mm	w_{a10}	1.12 mm
l_{a11}	2.81 mm	w_{a11}	0.93 mm
l_{a12}	1.99 mm	w_{a12}	0.77 mm
l_{a13}	1.31 mm	w_{a13}	0.64 mm
X_1	118 mm	X_8	29.83 mm
X_2	97.43 mm	X_9	24.25 mm
X_3	80.36 mm	X_{10}	19.62 mm
X_4	66.19 mm	X_{11}	15.77 mm
X_5	54.42 mm	X_{12}	12.58 mm
X_6	44.66 mm	X_{13}	9.93 mm
X_7	36.56 mm	τ	0.83
α	0.25 rad	−	−

band characteristics of less than −10 dB within the 2.2–5 GHz range (fractional bandwidth of 93.3%), which agrees well with the simulation results. Furthermore, although a slight change in the reflection coefficient was observed due to mutual coupling changes when using the array antenna for the various beam synthesis estimations, no significant change could be identified. Therefore, the designed LPDA can be employed for high-power beamforming in electronic warfare systems with a wide bandwidth. Fig. 5 shows the results of mutual coupling between Ant_5 and the other elements. Furthermore, mutual couplings with Ant_1, Ant_2, Ant_3, and Ant_4 were measured. Notably, the mutual coupling with Ant_4 (the nearest element) was less than −10 dB between 1 GHz and 5 GHz. Fig. 6 presents the measured and simulated boresight gains of the 8 × 1 array antenna. The solid line indicates the simulation results, while the "×" markers represent the measurement results. It is observed that the measured boresight gains are more than 10 dBi from 2 GHz, with the simulation results showing a similar tendency. Fig. 7(a)–7(f) present the measured and simulated 2D AEPs of Ant_2 and Ant_5 at 2.5
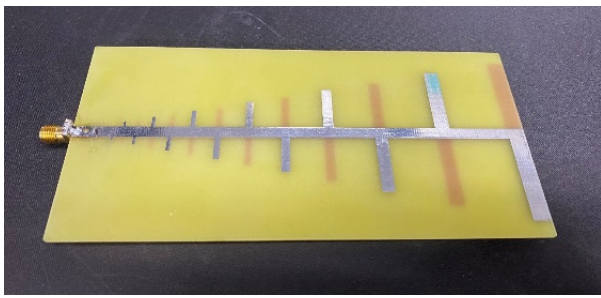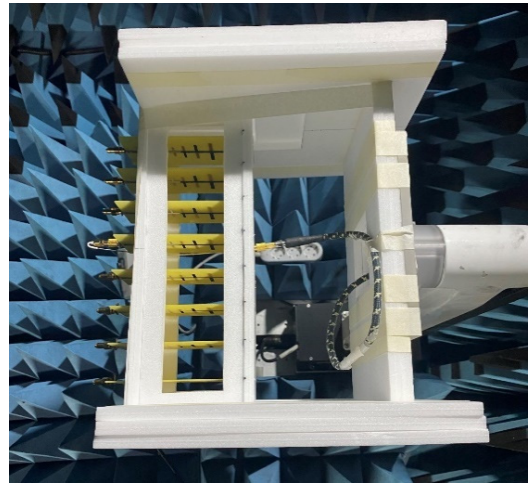
(a)   (b)

Fig. 2. Photographs of the fabricated antenna: (a) single LPDA element and (b) 8 × 1 array configuration.
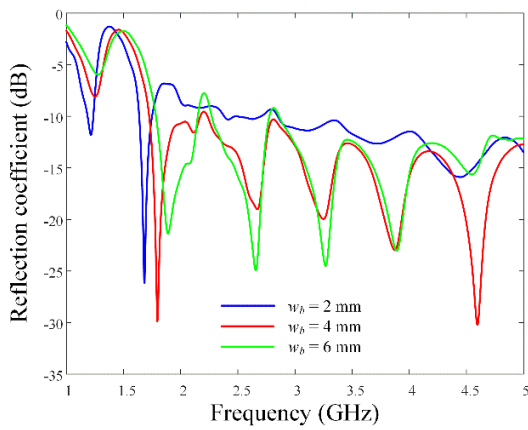

Fig. 3. Reflection coefficients in accordance with parameter w_b.
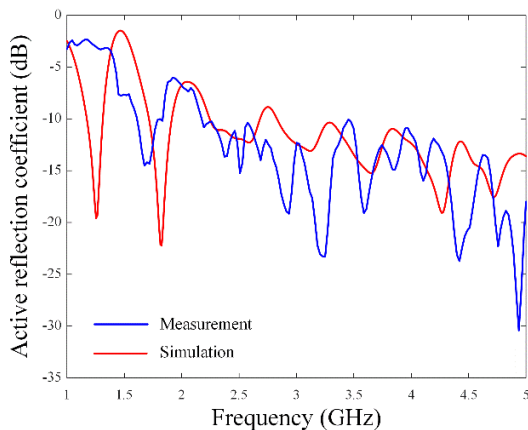
Fig. 4. Measured and simulated ARCs of the Ant_5 element.

Fig. 5. Measured and simulated mutual couplings of the array antenna elements with Ant_5.
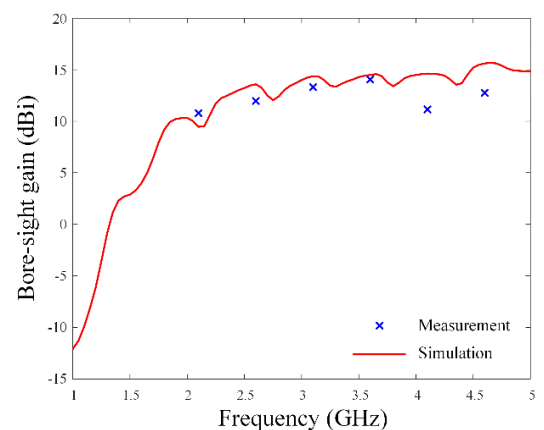
Fig. 6. Measured and simulated boresight gains of the array antenna according to frequency.

GHz, 3.5 GHz, and 4.5 GHz, respectively. As expected, Ant_2, which is located near the edge, has an asymmetric radiation pattern, while Ant_5, located at the center, has a symmetrical beam pattern. At 4.5 GHz, Ant_2 has a maximum gain of 6.3 dBi ($\theta = -56°$), and Ant_5 shows 6.0 dBi ($\theta = -22°$). However, since sig-

nificant distortion is often observed in the patterns of individual elements in actual array antennas, it is necessary to use AEP instead of the ideal isotropic radiation pattern for beam synthesis.
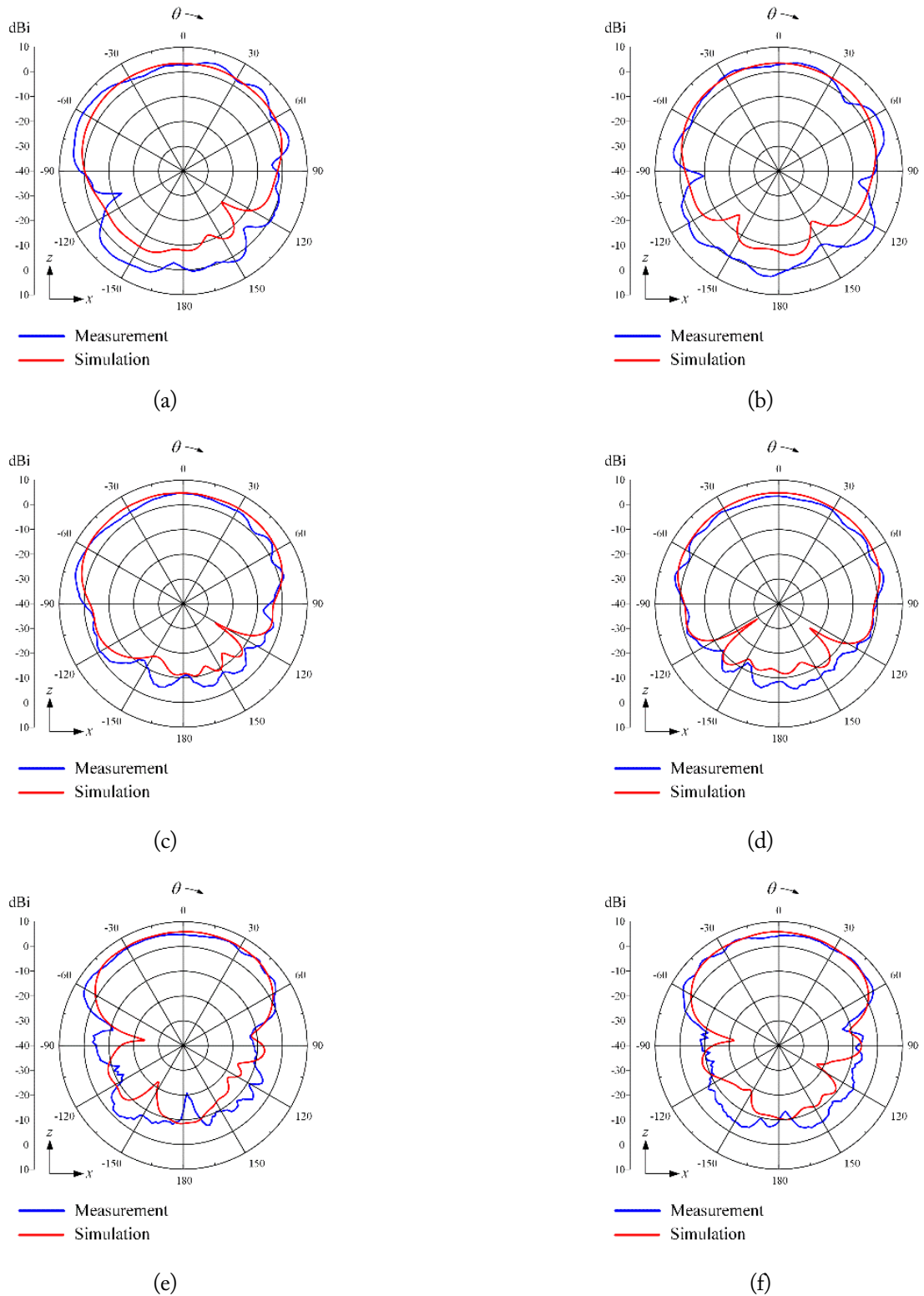
Fig. 7. Measured and simulated AEPs: (a) Ant_2 element at 2.5 GHz, (b) Ant_5 element at 2.5 GHz, (c) Ant_2 element at 3.5 GHz, (d) Ant_5 element at 3.5 GHz, (e) Ant_2 element at 4.5 GHz, and (f) Ant_5 element at 4.5 GHz.
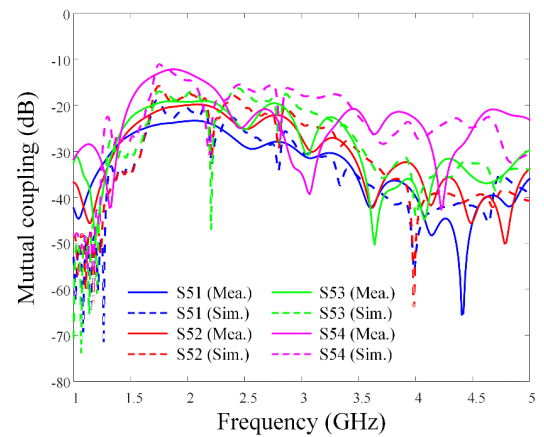
III. BEAM SYNTHESIS USING THE BROADBAND LPDA

Beam synthesis can be conducted through the superposition of several array patterns $b_m f(\theta, \theta_m)$ with different steering angles θ_m and amplitudes b_m, as shown in a equation as follow [12]:

$$F(\theta) = b_1 f(\theta, \theta_1) + b_2 f(\theta, \theta_2) + \cdots + b_m f(\theta, \theta_m) \\ + \cdots + b_{M-1} f(\theta, \theta_{M-1}) + b_M f(\theta, \theta_M), \quad (3)$$

Here, b_m is the required amplitude weighting, and θ_m is the steering angle for each array pattern. For example, when a guide

mask for the desired beam shape is defined in Fig. 8(a), the most appropriate beam pattern can be obtained by the superposition of multiple array patterns. Notably, to derive a synthesized beam shape that closely resembles the guided mask, a narrow HPBW and a low sidelobe level (SLL) is required for each array pattern. Therefore, the Taylor window weighting method is applied to each array pattern to achieve a low SLL using an equation as follow:

$$f(\theta, \theta_m) = \sum_{n-1}^{N} a_n g_n(\theta, \theta_m). \tag{4}$$

Here, a_n represents the weighted amplitude applied to the nth element in the Taylor window, and $g_n(\theta, \theta_m)$ denotes the AEP of the nth element with steering angle θ_m. The array patterns for the designed 8 × 1 array when using Taylor window weighting are shown in Fig. 8(b). The resulting measurements using AEPs exhibited an HPBW of 17.4° and an SLL of 19.4 dB.

Following this, beam synthesis for the flat-top beam, cosecant-squared beam, and iso-flux beam were carried out using Taylor window-weighted array patterns. Notably, the root-mean-square error (RMSE) lies within the range of 0 and 1, meaning that an RMSE of 0.2 indicates an error of 20%, which can be evaluated as a relatively small error. The RMSE was calculated as an evaluation metric to observe the similarity of the beam pattern shape between the measurement results and the guided mask. This can be obtained using an equation as follow:

$$\text{RMSE} = \sqrt{\frac{1}{L} \sum_{\theta=-90°}^{90°} (F(\theta) - G(\theta))^2}. \tag{5}$$

Here, $F(\theta)$ represents the normalized directivity of the synthesized beam, and $G(\theta)$ is the value of the guided mask at angle θ.
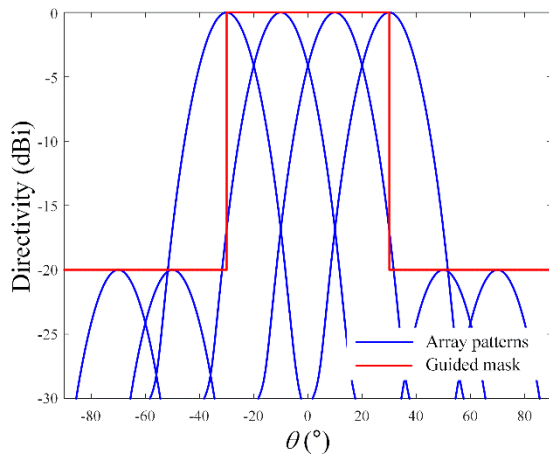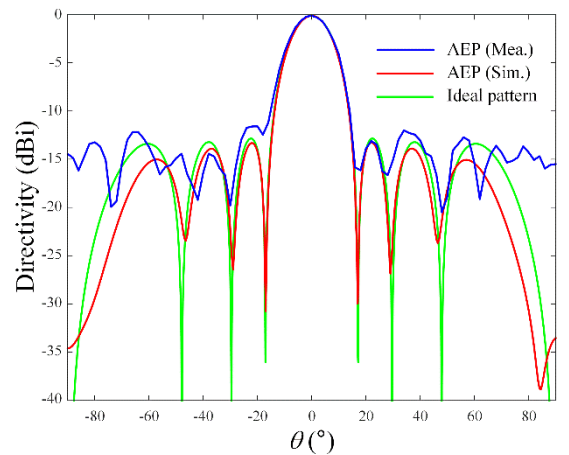
Notably, since there are 91 sampling points (L) between −90° and 90°, the synthesized beam and the guided mask were compared by examining 91 uniformly distributed points between −90° to 90°.

Fig. 9(a) depicts the synthesized flat-top beams, which are generally used for searching and detecting targets at wide scan angles. The goals of the flat-top beam were to achieve a beam-width of 80° (−40 $\leq \theta \leq$ 40° and an SLL of more than 10 dB. Beam synthesis was performed by determining the amplitude b_m when the number of array patterns M was 30. When using the measured AEPs, the results showed a beamwidth of 75° and an RMSE of 0.159 compared to the guided mask.

Fig. 9(b) illustrates the cosecant-squared beam, which is typically used for high-power airborne jamming systems. Similar to the method described previously, the cosecant-squared beam was obtained based on the guided mask ($\csc^2(11.2°)$ at −40° $\leq \theta \leq$ −31.6° and $\csc^2(\theta+40°)$ at −31.6° $\leq \theta \leq$ 40°), resulting in the optimum b_m (M = 30) for the most appropriate synthesized beam. The cosecant-squared beam was set to maintain a difference of 7.27 dB between the maximum and minimum values within 80° of the beamwidth. The results of the cosecant-squared beam showed that the shape attained a maximum directivity of 0 dB at θ = −30° and a reduced directivity of −7.55 dB at θ = 40°, thus achieving an RMSE of 0.167 compared to the guided mask.

Fig. 9(c) presents the results of the iso-flux beam, which is generally used in the earth-observing missions of satellites. Similar to the previous beams, the iso-flux beam was also obtained based on the guided mask ($1.5 \times 10^{-3}\theta^2+1$ at −40° $\leq \theta \leq$ 40°). Its beamwidth was set to 80° and gain difference was set to 5.4 dB. When using the measured AEPs, the iso-flux beam exhibited right-side peak directivity at θ = 32° and left-side peak at θ = −32°. In the boresight direction (θ = 0°), a low directivity of −3.57 dB was observed, and an RMSE of 0.162 was obtained compared to the guided mask.

(a)

(b)

Fig. 8. Beam synthesis using Taylor window-weighted array patterns: (a) superposition of array patterns for beam synthesis and (b) Taylor window-weighted array patterns.
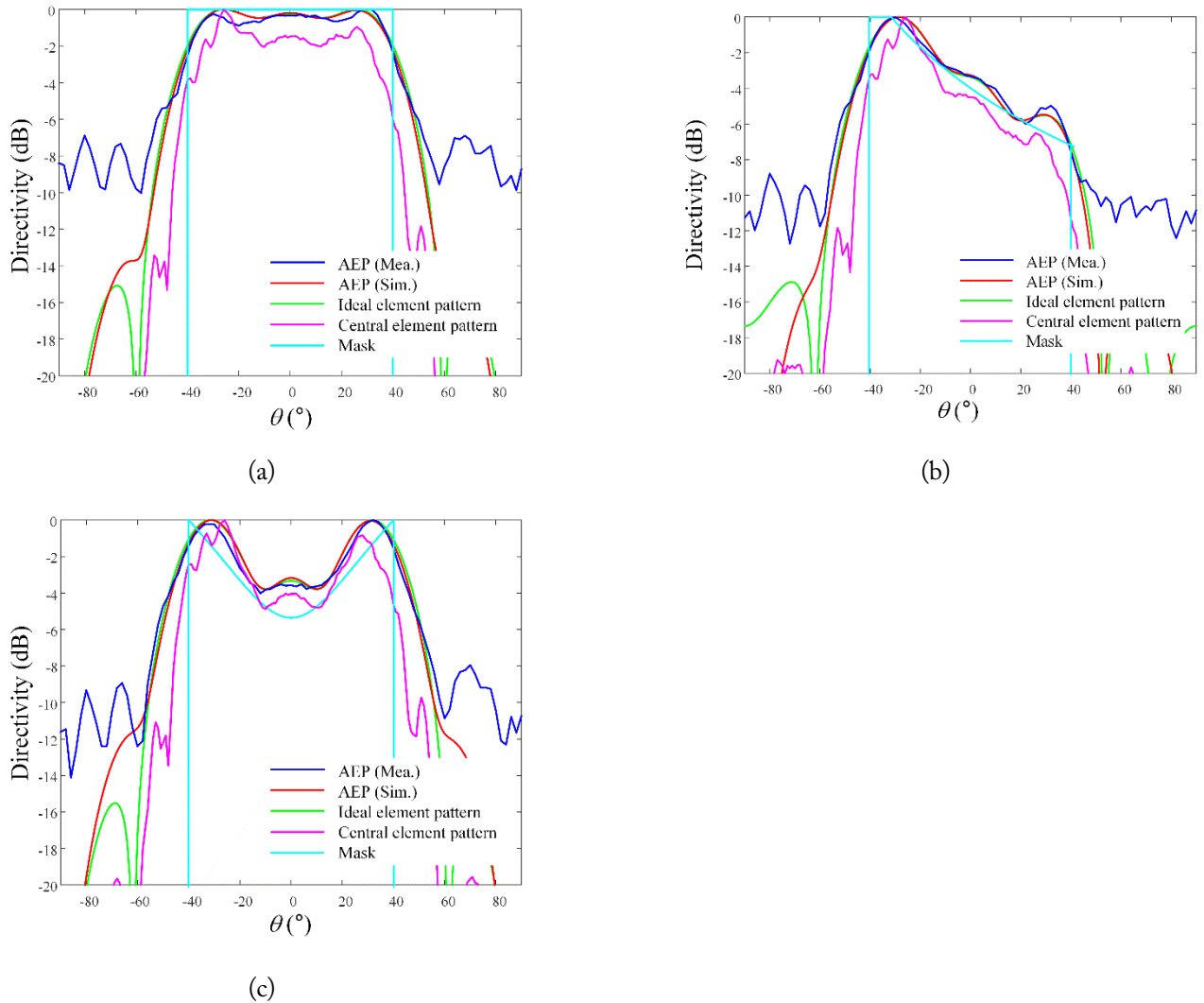
(a)

(b)

(c)

Fig. 9. Synthesized beam patterns using measured and simulated active element patterns of the designed LPDA: (a) flat-top beam pattern, (b) cosecant-squared beam pattern, and (c) iso-flux beam pattern.

This study used a different number of M based on the shape of the synthesized beam. Notably, an inadequate number of M results in multiple nulls in the synthesized beam, whereas an excessive number of M increases the SLL of the beam. Therefore, an appropriate value of M should be used to derive the beam that best resembles the shape of the mask. The results of this study confirm that various beam shapes for high-power electronic warfare applications can be achieved using the AEPs of the designed LPDA. To compare the similarities between the measurement and simulation results, the RMSEs obtained with regard to the guided masks are listed in Table 2. It is evident that the measurement results of the synthesized beams are similar to the simulation results at $-40° \leq \theta \leq 40°$, as indicated by the low RMSEs. However, a relatively high difference was observed in the case of SLLs. These differences may be attributed to the fact that measurement results usually show degraded performance compared to theoretical simulation results due to various reasons, such as measurement conditions, fabrication errors, and

Table 2. RMSEs of the synthesized beam patterns

Beam shape	Measurement	Simulation	Ideal pattern
Flat-top beam	0.159	0.145	0.081
Cosecant-squared beam	0.167	0.168	0.239
Iso-flux beam	0.162	0.198	0.184

cable loss [22, 23]. In particular, since SLLs are more sensitive to errors, they exhibit greater degradation. Moreover, the performance degradation observed in the measurement can occur when the fabricated antenna is applied to the system. Therefore, when conducting beam synthesis research, it is crucial to confirm performance through fabrication.

IV. CONCLUSION

In this paper, various beam shapes for high-power electronic warfare applications were derived using an actual broadband

array antenna. Specifically, a compact printed LPDA with broadband characteristics was fabricated and measured for use in a limited mounting space. Subsequently, the LPDA was extended to an 8 × 1 linear array, while AEPs were obtained through measurement and simulation. The measured ARC was less than −10 dB within the 2.2–5 GHz band, while the measured boresight gains were more than 10 dBi from 2 GHz. Furthermore, beam synthesis was performed by the superposition of several array patterns with different steering angles and amplitudes. The flat-top beam achieved a beamwidth of 75° and an RMSE of 0.159. The cosecant-squared beam, which attained maximum directivity at $\theta = -30°$ and a reduced directivity of −7.55 dB at 40° achieved an RMSE of 0.167 compared to the guided mask. In addition, the iso-flux beam obtained an RMSE of 0.162 compared to the guided mask. These results were compared with those of the beam shapes obtained using ideal isotropic patterns, which ultimately confirmed that various beam shapes can be achieved in high-power electronic warfare applications using the actual array antenna.

REFERENCES

[1] X. Chen, T. Shu, K. B. Yu, J. He, and W. Yu, "Joint adaptive beamforming techniques for distributed array radars in multiple mainlobe and sidelobe jammings," *IEEE Antennas and Wireless Propagation Letters*, vol. 19, no. 2, pp. 248-252, 2020. https://doi.org/10.1109/LAWP.2019.2958687

[2] L. Paulsen, T. Hoffmann, C. Fulton, M. Yeary, A. Saunders, D. Thompson, B. Chen, A. Guo, and B. Murmann, "Impact: a low cost, reconfigurable, digital beamforming common module building block for next generation phased arrays," in *Proceedings of SPIE 9479: Open Architecture/Open Business Model Net-Centric Systems and Defense Transformation 2015*. Bellingham, WA: International Society for Optics and Photonics, 2015, pp. 16-30. https://doi.org/10.1117/12.2179712

[3] A. E. Spezio, "Electronic warfare systems," *IEEE Transactions on Microwave Theory and Techniques*, vol. 50, no. 3, pp. 633-644, 2002. https://doi.org/10.1109/22.989948

[4] B. Barshan and B. Eravci, "Automatic radar antenna scan type recognition in electronic warfare," *IEEE Transactions on Aerospace and Electronic Systems*, vol. 48, no. 4, pp. 2908-2931, 2012. https://doi.org/10.1109/TAES.2012.6324669

[5] N. T. Nguyen, R. Sauleau, M. Ettorre, and L. Le Coq, "Focal array fed dielectric lenses: an attractive solution for beam reconfiguration at millimeter waves," *IEEE Transactions on Antennas and Propagation*, vol. 59, no. 6, pp. 2152-2159, 2011. https://doi.org/10.1109/TAP.2011.2144550

[6] Z. Yang, Y. Chen, and S. Yang, "Scanning Radiation pattern synthesis using characteristic mode of airship platform," in *Proceedings of 2021 IEEE International Workshop on Electromagnetics: Applications and Student Innovation Competition (iWEM)*, Guangzhou, China, 2021, pp. 1-3. https://doi.org/10.1109/iWEM53379.2021.9790716

[7] S. K. Biswas and V. Chandrasekar, "Cross-validation of observations between the GPM dual-frequency precipitation radar and ground based dual-polarization radars," *Remote Sensing*, vol. 10, no. 11, article no. 1773, 2018. https://doi.org/10.3390/rs10111773

[8] I. Chiba, Y. Konishi, and T. Nishino, "Progress of phased array systems in Japan," in *Proceedings of 2010 IEEE International Symposium on Phased Array Systems and Technology*, Waltham, MA, USA, 2010, pp. 19-28. https://doi.org/10.1109/ARRAY.2010.5613395

[9] A. Rao, A. Chatterjee, J. Payne, J. Trujillo, M. Blefko, and J. Kmieciak, "Design options for a multi-beam/multi-band airborne antenna," in *Proceedings of 2019 13th European Conference on Antennas and Propagation (EuCAP)*, Krakow, Poland, 2019, pp. 1-4.

[10] Y. Aslan, J. Puskely, A. Roederer, and A. Yarovoy, "Multiple beam synthesis of passively cooled 5G planar arrays using convex optimization," *IEEE Transactions on Antennas and Propagation*, vol. 68, no. 5, pp. 3557-3566, 2020. https://doi.org/10.1109/TAP.2019.2955885

[11] J. Y. Li, Y. X. Qi, and S. G. Zhou, "Shaped beam synthesis based on superposition principle and Taylor method," *IEEE Transactions on Antennas and Propagation*, vol. 65, no. 11, pp. 6157-6160, 2017. https://doi.org/10.1109/TAP.2017.2754468

[12] H. Patidar, V. Maheshwari, R. Kar, P. K. Singh, and V. K. Sahu, "Comparative study of evolutionary algorithms to generate flat-top beam pattern for synthesis of a linear antenna array," *ICTACT Journal on Communication Technology*, vol. 12, no. 3, pp. 2519-2526, 2021.

[13] H. Patidar, G. K. Mahanti, and R. Muralidharan, "Synthesis of flat-top beam pattern of linear antenna arrays with restricted side lobe level, VSWR and independent nulls using Flower Pollination algorithm," *International Journal of Electronics*, vol. 106, no. 12, pp. 1964-1977, 2019. https://doi.org/10.1080/00207217.2019.1636297

[14] S. Dai, M. Li, Q. H. Abbasi, and M. A. Imran, "A zero placement algorithm for synthesis of flat top beam pattern with low sidelobe level," *IEEE Access*, vol. 8, pp. 225935-225944, 2020. https://doi.org/10.1109/ACCESS.2020.3045287

[15] L. F. Yepes, D. H. Covarrubias, M. A. Alonso, and R. Ferrus, "Hybrid sparse linear array synthesis applied to phased antenna arrays," *IEEE Antennas and Wireless Propagation Let-

ters, vol. 13, pp. 185-188, 2014. https://doi.org/10.1109/LAWP.2014.2301012

[16] G. Oliveri, L. Poli, and A. Massa, "Maximum efficiency beam synthesis of radiating planar arrays for wireless power transmission," *IEEE Transactions on Antennas and Propagation*, vol. 61, no. 5, pp. 2490-2499, 2013. https://doi.org/10.1109/TAP.2013.2241714

[17] H. S. Yoon, D. G. Jo, D. I. Kim, and K. W. Choi, "On-off arbitrary beam synthesis and non-interactive beam management for phased antenna array communications," *IEEE Transactions on Vehicular Technology*, vol. 70, no. 6, pp. 5959-5973, 2021. https://doi.org/10.1109/TVT.2021.3078781

[18] J. I. Echeveste, M. A. G. de Aza, and J. Zapata, "Shaped beam synthesis of real antenna arrays via finite-element method, Floquet modal analysis, and convex programming," *IEEE Transactions on Antennas and Propagation*, vol. 64, no. 4, pp. 1279-1286, 2016. https://doi.org/10.1109/TAP.2016.2526038

[19] S. Lei, W. Yang, Z. Lin, Z. He, H. Hu, Z. Zhao, and Y. Bao, "An excitation-DRR control approach for wide-beam power gain pattern synthesis," *Signal Processing*, vol. 204, article no. 108858, 2023. https://doi.org/10.1016/j.sigpro.2022.108858

[20] Z. Lin, H. Hu, S. Lei, R. Li, J. Tian, and B. Chen, "Low-sidelobe shaped-beam pattern synthesis with amplitude constraints," *IEEE Transactions on Antennas and Propagation*, vol. 70, no. 4, pp. 2717-2731, 2022. https://doi.org/10.1109/TAP.2021.3125319

[21] R. Elliott and G. Stern, "A new technique for shaped beam synthesis of equispaced arrays," *IEEE Transactions on Antennas and Propagation*, vol. 32, no. 10, pp. 1129-1133, 1984. https://doi.org/10.1109/TAP.1984.1143216

[22] Y. M. Pan, K. W. Leung, and K. M. Luk, "of the millimeter-wave rectangular dielectric resonator antenna using a higher-order mode," *IEEE Transactions on Antennas and Propagation*, vol. 59, no. 8, pp. 2780-2788, 2011. https://doi.org/10.1109/TAP.2011.2158962

[23] S. G. Zhou, P. Dong, G. L. Huang, and J. Y. Li, "Wideband antenna array with full metal structure and air-filled microstrip feeding network," *IEEE Transactions on Antennas and Propagation*, vol. 65, no. 6, pp. 3041-3048, 2017. https://doi.org/10.1109/TAP.2017.2681319

Changhyeon Im

https://orcid.org/0000-0002-8973-4398

received his B.S. degree in electronic and electrical engineering from Hongik University, Seoul, South Korea, in 2021, where he is currently pursuing his Ph.D. in electronic and electrical engineering. His research interests include mesh reflector antennas, 5G applications, wireless power transfer, and ultra-wideband antennas.

Tae Heung Lim

https://orcid.org/0000-0001-7968-1272

received the B.S., M.S., and Ph.D degrees in electronic and electrical engineering from Hongik University, Seoul, South Korea, in 2016, 2018, and 2022, respectively. He was a Postdoctoral Researcher in Ulsan National Institute of Science and Technology (UNIST) in 2022. He was a Senior Researcher with the Agency for Defense Development, Daejon, South Korea in 2023. He is currently an assistant professor with the School of Electronic Engineering, Kumoh National Institute of Technology. His research interests include space surveillance radar, 6G system antennas, sea-based radar, high-power array antennas, adaptive beamforming, and wave propagations for radar applications.

Sangwoon Youn

https://orcid.org/0000-0003-1437-8445

received his B.S. and M.S. degrees in electronic and electrical engineering from Hongik University, Seoul, South Korea, in 2019 and 2021, respectively, where he is currently pursuing a Ph.D. in electronic and electrical engineering. His research interests include EMI and EMC, wave propagation, UWB antennas, 5G applications, and direction-finding and anti-jamming systems.

Hosung Choo

https://orcid.org/0000-0002-8409-6964

received his B.S. degree in radio science and engineering from Hanyang University, Seoul, South Korea, in 1998, and his M.S. and Ph.D. degrees in electrical and computer engineering from the University of Texas at Austin in 2000 and 2003, respectively. In September 2003, he joined the School of Electronic and Electrical Engineering, Hongik University, Seoul, where he is currently a professor. His principal areas of research include electrically small antennas for wireless communications, reader and tag antennas for RFID, on-glass and conformal antennas for vehicles and aircrafts, and array antennas for GPS applications.

Broadband Transmit/Receive Switch for 3T and 7T Magnetic Resonance Imaging

Ashraf Abuelhaija[1],* · Gameel Saleh[2] · Sanaa Salama[3] · Mohammed Hamdan[1]

Abstract

This article presents a transmit/receive switch that utilizes a broadband microstripline hybrid coupler. The proposed switch is suitable for application in both 3T and 7T magnetic resonance imaging. It operates within three frequency ranges, covering well-known X-atomic nuclei, such as ^{1}H, ^{13}C, ^{19}F, ^{23}Na, and ^{31}P, at both 3T and 7T magnetic field strengths. For the 7T application, the switch simultaneously covers the corresponding X-atomic nuclei frequencies within two bands. However, for the 3T application, tuning is required to cover the corresponding X-atomic nuclei frequencies, particularly those below 60 MHz. The microstripline trace widths of the proposed switch were designed to prevent excessive temperature increases when exposed to 1 kW power of radio frequency pulses. The characteristics of the switch were obtained using the Momentum tool—an electromagnetic simulator supported by ADS software. The proposed switch was fabricated, with its measurement verification results demonstrating favorable return loss (>10 dB), high isolation (>40 dB), and low insertion loss (<0.8 dB) at all operating frequencies.

Key Words: Broadband, Hybrid Coupler, Magnetic Resonance Imaging, Microstripline, PIN Diode.

I. INTRODUCTION

Magnetic resonance spectroscopy holds great promise in clinical neurological practice. It measures the concentrations of specific chemicals in the body to help diagnose diseases in the brain and other cancerous tissues. Cancerous tissues are often characterized by metabolic alterations. Notably, ^{13}C magnetic resonance imaging (MRI) examines variations in the metabolism of organic molecules. These changes in biochemical processes serve as a marker for the presence of certain disorders, including prostate cancer, brain tumors, diabetes, lung injury, neuroinflammation, inflammatory arthritis, cardiovascular disease, and cardiac metabolism [1]. Specifically, brain tumors are commonly detected by ^{31}P MRI scanner assessments of phosphorous composition and cellular energy [2]. Likewise, breast cancer can be diagnosed by ^{23}Na MRI, which detects changes in ion homeostasis, since the total concentration of sodium is notably higher in malignant breasts than in healthy tissues. It also allows the visualization of tissue ^{23}Na concentrations for patients with lung cancer [3]. Furthermore, ^{31}P MRI has been found to be feasible for use as a measure of tongue cancer in 7T MRI [4]. Additionally, ^{13}C MRI is suitable both for initial diagnosis and for monitoring the treatment of prostate cancer [5]. In this context, X-nuclei switches and coils enable physicians to study metabolism and measure chemical transformation, since they can help characterize the sophistication of tissues or the chemical consequences of disease progression [6, 7].

The switches used in MRI transmit radio frequency (RF) signals from an RF amplifier to the body through an RF coil, and also receive the signal from the body through the RF coil to then redirect it to the receiver circuit. Single- and multi-tuned switches are used for single- and multi-resonant coils, respectively. Notably, several methods for designing these switches have already been developed, such as trap circuits, positive-intrinsic-negative (PIN) diodes, transistors, and microelectromechanical systems (MEMS). In [8], a PIN diode-based ^{1}H transmit/receive (T/R) switch was introduced, owing to its reliability and linearity, to achieve a reduction in the switching time to 1 microsecond. In [9], a dual-tuned T/R switch capable of handling both ^{1}H and ^{31}P frequencies was engineered specifically for 3T MRI applications. This circuit, which included a linear switch for the ^{1}H coil and a quadrature switch for the ^{31}P coil, employed PIN diodes in conjunction with various other electronic components. Field effective transistor (FET)-based switches have been introduced as another topology and solution for switches in MRI [10–12]. For instance, a depletion-mode gallium nitride (GaN) switch was introduced in [11], while an enhanced-mode GaN (eGaN) FET-based switch was proposed in [12]. These switches have advantages over PIN diode switches in terms of their low DC power and reduced amount of biasing current used. However, FET switches are sensitive to RF power overstress and temperature [11], and they often suffer from lower signal-to-noise ratio (SNR) [12]. To address this, MEMS-based switches were introduced to MRI coils in [13, 14]. Notably, dual-tuned switches based on MEMS and PIN diodes, used along with a dual-tuned ^{1}H/^{19}F coil, were investigated for lung MRI applications [15]. The MEMS switch demonstrated reduced DC switching voltage compared to PIN diodes in a reverse bias state [16].

Microstripline (MSL)-based switches represent a novel switch category whose advantages over conventional couplers lie in their enhanced heat dissipation and ability to manage higher power signals [17]. A compact dual-tuned MSL-based switch designed for a dual-resonant ^{1}H/^{13}C coil was introduced for 7T MRI in [18]. This innovative design accommodated simultaneous dual-frequency signal transmission to and from a dual-resonance RF coil, eliminating the need for tuning during operation. Moreover, in [18], the size of the switch was reduced by 50% compared to the initial ^{1}H MSL-based switch in [17]. In [19], two MSL-based switches were introduced—one to interrogate different X-nuclei (^{1}H, ^{13}C, ^{19}F, ^{23}Na, and ^{31}P) one at a time by tuning, and the second to work as a dual-tuned switch for ^{1}H/^{23}Na MRI applications. Furthermore, a dual-tuned ^{1}H/^{31}P quadrature MSL-based T/R switch for 7T MRI was introduced in [20]. A single ^{1}H MSL-based switch for 7T MRI, bearing a T- and cascaded pi-shape and a realistic MSL trace width, was designed and extensively investigated to specify exact widths without in-creasing the temperature [21]. In [22, 23], two geometries of broadband MSL-based switches were introduced to simultaneously cover the X-nuclei (^{1}H, ^{13}C, ^{19}F, ^{23}Na, and ^{31}P) for 7T MRI without tuning. All of these MSL-based switches demonstrate excellent characteristics, including strong signal matching, high isolation, minimal insertion loss, effective power dissipation, and the capacity to manage high-power signals.

The novelty of this specific switch design lies in its ability to work along with RF coils to cover resonances corresponding to a wide range of X-nuclei for both 3T and 7T MRI. From an economic perspective, such a design does away with the need to use different switches with different coils since the same switch can be used for different MRI machines. This reduces both costs and complexity while also keeping sufficient space to facilitate future designs of multichannel-multi resonant coils that can be used for both 3T and 7T MRI simultaneously.

II. THE PROPOSED BROADBAND T/R SWITCH

1. Overview of the T/R Switch

A T/R switch is considered an important device in an MRI system that utilizes T/R RF coils. In the transmission state, after generating a pulsed RF signal, an RF signal is fed into a power amplifier to amplify it to the necessary level for exciting the intended X-nuclei. Following this, the T/R switch transmits the RF signal to the RF coil. At the reception state, the RF coil delivers the detected signal from the targeted object to the T/R switch, which in turn forwards it to the low-noise amplifier, as shown in Fig. 1.

2. Broadband Hybrid Couplers

Due to growing interest in high-speed wireless communication, the demand for ultra-wideband (UWB) technology and devices has increased manifold. Notably, classical quadrature hybrid couplers demonstrate narrowband characteristics. Therefore, in recent years, several studies and investigations have been conducted on couplers to extend their bandwidths [24–28]. In [24], a two-section wideband hybrid coupler using a short-circuited parallel-coupled 3-line was presented. This coupler exhibited 55% fractional bandwidth (FBW) under specifica-
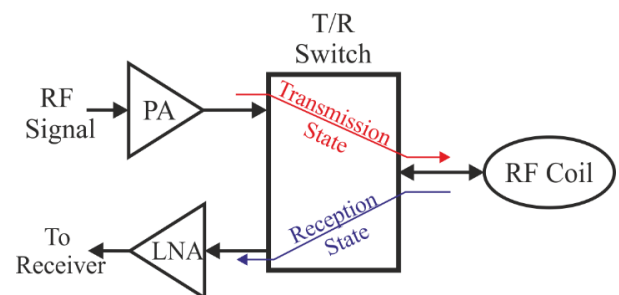

Fig. 1. Simplified diagram of an integrated T/R switch in an MRI system.

tions limited by 1 dB power imbalance, 20.1 dB return loss, 20.8 dB isolation, and 3.2° phase imbalance. In [25], a hybrid coupler using a tandem connection was presented, demonstrating 38% FBW under specifications limited by 0.6 dB power imbalance, 25 dB return loss, and 32 dB isolation. Under the same conditions as the tandem coupler, a UWB hybrid coupler was designed using the tandem connection between two 8.3 dB multi-section couplers [26] to be used in the frequency range from 1 GHz to 10 GHz. It was designed under specifications limited by ±1.5 dB amplitude unbalance, ±7° phase imbalance, and both isolation and return loss of more than 14 dB. In [27], an UWB multilayer 3 dB directional coupler was presented, whose operating frequency extended from 3.1 GHz to 10.6 GHz, with a coupling and insertion loss of 3.4 dB ± 1.1 dB. The isolation and return loss were more than 14 dB. In [28], a 3-dB UWB coupler using multilayer technology, operating between 3.1 and 10.6 GHz, was presented. It was designed under specifications limited by ±1.3 dB amplitude unbalance, 3.5° phase unbalance, 19 dB return loss, and 18 dB isolation.

The broadband 3T and 7T T/R switch proposed in this study can cover frequencies corresponding to the common X-nuclei resonant frequencies at 3T and 7T MRI, summarized in Table 1. While resonances above 61 MHz fall within the two broadbands offered by the switch without the need for tuning, the lower frequencies can be covered after applying the tuning method.

3. Methods and Materials

The 3T and 7T T/R switch presented in this study was designed based on a two-section branch-line hybrid coupler, initially introduced in [29]. Such a coupler is constructed using two sections of transmission lines, consisting of three vertical lines (a, c, a) and four identical horizontal lines (b, b, b, b). These lines share a common vertical line connected to an inverter, as illustrated in Fig. 2. Notably, the quarter-wavelength is the standardized length employed for all the vertical and horizontal lines. In this context, the characteristic impedance of transmission line a can be determined using the formula described in [29].

$$Z_a=(\sqrt{k}+\sqrt{k+1})Z_o. \tag{1}$$

Here, k represents the ratio of the signal power at port 2 (through) to the signal power at port 4 (coupled), and Z_o is the port impedance, which is typically 50 Ω. When k equals 1, the input signal inserted at port 1 is evenly divided between ports 2 and 4, along with a 90° phase shift, resulting in −3 dB quadrature outputs, while port 3 remains isolated. This configuration corresponds to a 90° hybrid coupler. Substituting k with 1 in Eq. (1), Z_a becomes 2.414 times Z_o. Therefore, to calculate the characteristic impedances of transmission lines b and c, the following formula, as described in [29], can be employed:

$$k=\frac{Z_o^2 Z_c^2}{Z_b^4}. \tag{2}$$

On rearranging Eq. (2), the following equation will be obtained:

$$Z_c=\frac{\sqrt{k}Z_b^2}{Z_o}. \tag{3}$$

Assuming Z_b is equal to Z_o, Z_c will also be equal to Z_o. After calculating the characteristic impedances, the following values can be achieved: Z_a = 120.7 Ω and Z_b = Z_c = 50 Ω. The simulated S-parameters of the proposed coupler are depicted in Fig. 3(a). The operational bandwidth, considering a 1 dB magnitude imbalance and a 5° phase imbalance, is determined from Fig. 3(a) and 3(b) as approximately 48.2%. Notably, for practical applications, the hybrid coupler was designed using a Rogers RO4003C substrate with a permittivity of 3.38 and a thickness of 1.52 mm. Fig. 4 depicts the layout of the hybrid coupler in a Momentum electromagnetic simulation, which is supported by ADS software.

The dimensions for each transmission line in Fig. 2 are summarized in Table 2. The operating frequency of the coupler was chosen to be 95 MHz. To reduce the overall area of the coupler, the microstrip lines were designed in a multi-bended manner. Ultimately, the dimensions of the final design were established
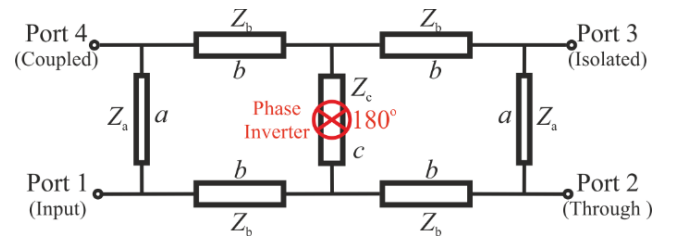
Fig. 2. Schematic diagram of the two-section branch-line hybrid coupler. Adapted from Abuelhaija and Saleh [22].

Table 1. Gyromagnetic ratio and resonant frequency at 3T and 7T for common nuclei

Nucleus	[1]H	[19]F	[31]P	[23]Na	[13]C
Gyromagnetic ratio ($\gamma/2\pi$) in MHz/Tesla	42.58	40.08	17.25	11.27	10.71
Frequency @ 3T in MHz	127.74	120.24	51.75	33.81	32.13
Frequency @ 7T in MHz	298.06	280.56	120.75	78.89	74.97
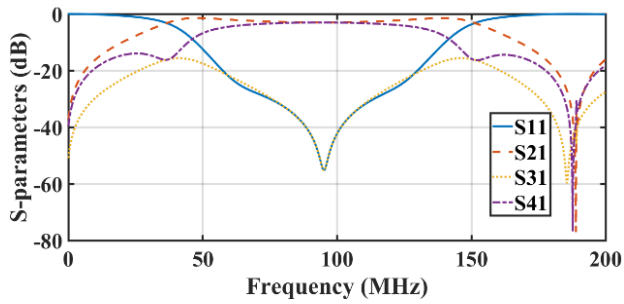
(a)
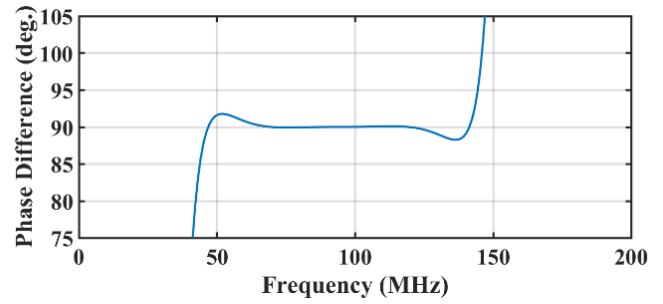
(b)

Fig. 3. (a) Simulated S-parameters of the two-section branch-line hybrid coupler with $k = 1$ and (b) phase difference between the through and coupled ports.

Fig. 4. Layout of the two-section branch-line hybrid coupler.

Table 2. Dimensions of the hybrid coupler microstriplines designed at 95 MHz

	Transmission line					
	a		b		c	
	l_a	W_a	l_b	W_b	l_c	W_c
Dimension (mm)	509	0.53	482.5	3.51	482.5	3.51

as 360 mm × 200 mm, which reduced the size of the coupler by 62.7% in comparison to the coupler without bending.
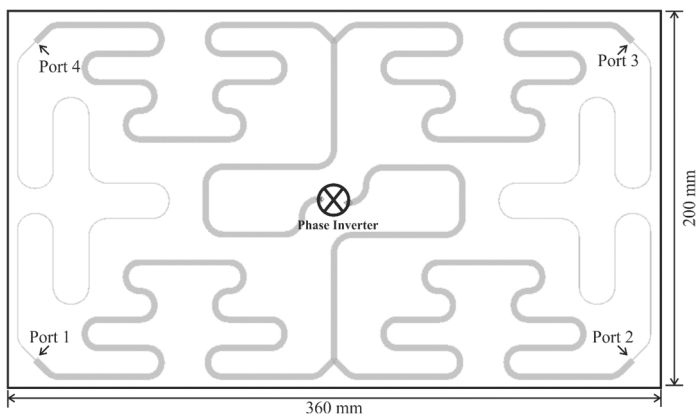
The hybrid coupler assumed a pivotal role in the design of the broadband 3T and 7T T/R switch. As depicted in Fig. 5, the proposed T/R switch comprises two hybrid couplers—while the left coupler is dedicated to the transmission state, both are simultaneously engaged in the reception state. In the transmission state, a pulsed RF signal is fed into port 1 and subsequently forwarded to the RF coil at port 2 after applying forward bias to the PIN diodes. During reception, both PIN diodes are reverse-biased, facilitating the routing of the detected signal from the RF coil to the receiver at port 4. To minimize the overall footprint of the T/R switch, both couplers were positioned in a back-to-back configuration, ensuring a common ground connection. The coupled and through ports of the first coupler were
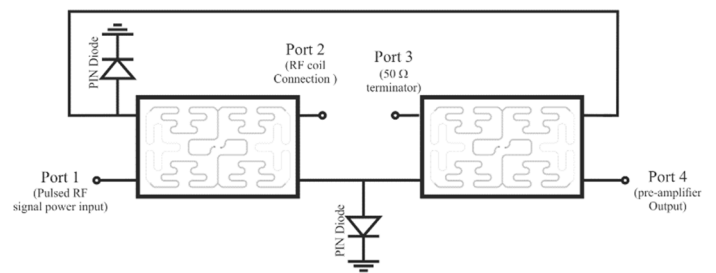

Fig. 5. Two-section branch-line hybrid coupler based broadband T/R switch.

internally connected to the corresponding ports in the second coupler using small connectors. A phase inverter (180° phase shifter) was inserted in the middle of each coupler using a coaxial cable on a crossover configuration.

To cover the frequencies of 7T MRI and the most common X-nuclei resonant frequencies at 3T MRI without the need for tuning, the operating frequency of the couplers was chosen to be 95 MHz. At this frequency, the T/R switch would be able to cover frequencies of X-nuclei that are more than 61 MHz within its two broadbands. The resonance frequencies corresponding to the remaining X-nuclei (such as ^{31}P, [23]Na, and ^{13}C at 3T) for 3T MRI can also be covered by adding a tuning capacitor $C_t = 62$ pF at the terminals of each MSL, as shown in Fig. 6. For the middle MSL c, the quarter-wavelength MSL was split into two-eighth of an MSL, with a phase inverter in between. Each eighth MSL was connected to one tuning capacitor with a value of $2 \times C_t$ from one terminal.

III. SIMULATION RESULTS AND MEASUREMENT VERIFICATION

1. Simulation Results

The S-parameters obtained by conducting EM simulations using the designed hybrid coupler (see Fig. 4) are shown in Fig. 7. The coupler was characterized by two broadbands—the first extended around the fundamental frequency (95 MHz), whereas the second extended around the third odd harmonics (285
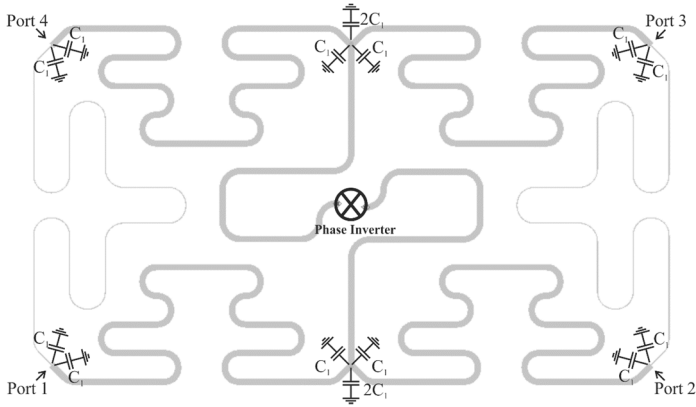
Fig. 6. Layout of the two-section branch-line hybrid coupler with tuning capacitors.

Fig. 7. *S*-parameters for the two-section branch-line hybrid couplers.

Fig. 8. *S*-parameters of the broadband T/R switch in the transmission state.

MHz). The bandwidths of the first and second broadbands fell within the 70–120 MHz and 260–308 MHz ranges, respectively, as calculated based on the following specifications: less than 1 dB magnitude imbalance and less than 5 phase imbalance. Notably, the proposed hybrid coupler demonstrated low return loss ($S_{11} < -25$ dB) and high isolation ($S_{31} < -25$ dB).

The evaluation of the T/R switch equipped with a two-section hybrid coupler was conducted by analyzing the *S*-parameters acquired from the electromagnetic simulations. As depicted in Fig. 8 and Tables 3 and 4, in the transmission state, the T/R switch exhibits commendable performance, characterized by strong matching ($S_{11} < -10$ dB) and minimal insertion loss ($S_{21} > -0.56$ dB) across all X-nuclei frequencies. Further-
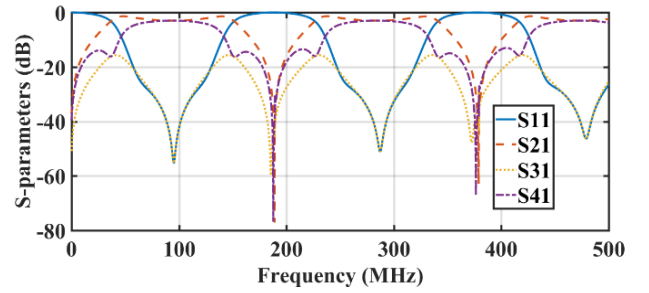
more, substantial isolation ($S_{41} < -44$ dB) between port 1 (the signal generator) and port 4 (the receiver) was achieved. Furthermore, as illustrated in Fig. 9 and Tables 3 and 4, the T/R switch maintains favorable matching ($S_{22} < -23.9$ dB) and low insertion loss ($S_{42} < -0.32$ dB) at all X-nuclei frequencies in the reception state.

Table 3. Simulated *S*-parameters of the broadband T/R switch in the transmission state and reception state at 3T

Atomic nuclei	Frequency (MHz)	Transmission state (dB)			Reception state (dB)		
		S_{11}	S_{21}	S_{41}	S_{22}	S_{12}	S_{42}
^{1}H	127.74	−10.60	−0.56	−44.70	−25.45	−22.36	−0.32
^{19}F	120.24	−20 .17	−0.21	−52.30	−26.87	−23.57	−0.12
^{31}P	51.75	–	–	–	–	–	–
^{23}Na	33.81	–	–	–	–	–	–
^{13}C	32.13	–	–	–	–	–	–

Table 4. Simulated *S*-parameters of the broadband T/R switch in the transmission state and reception state at 7T

Atomic nuclei	Frequency (MHz)	Transmission state (dB)			Reception state (dB)		
		S_{11}	S_{21}	S_{41}	S_{22}	S_{12}	S_{42}
^{1}H	298.06	−43.12	−0.17	−75.50	−28.52	−30.41	−0.02
^{19}F	280.56	−48.00	−0.17	−67.80	−41.25	−33.06	−0.01
^{31}P	120.75	−19.25	−0.21	−51.50	−27.50	−23.48	−0.13
^{23}Na	78.89	−55.40	−0.17	−85.00	−25.32	−25.97	−0.04
^{13}C	74.97	−33.34	−0.17	−63.75	−23.90	−24.35	−0.07

Fig. 8 depicts the two broadbands of the T/R switch in the transmission state. The first band extends from 61.1 MHz to 128.3 MHz, while the second band extends from 250.3 MHz to 317.5 MHz. They were calculated based on specifications of less than 1 dB insertion loss and less than 10 dB return loss. Furthermore, Fig. 9 presents the two broadbands of the T/R switch at the reception state. It is observed that the insertion loss for both bands is less than 0.36 dB, while the return loss is less than 23.5 dB.

To address the remaining X-nuclei frequencies, the hybrid couplers in the T/R switch were tuned using capacitor C_t. During transmission, the T/R switch achieved excellent matching ($S_{11} < -21$ dB) and low insertion loss ($S_{21} > -0.35$ dB) at the remaining X-nuclei frequencies, as seen in Fig. 10 and Table 5. Furthermore, high isolation ($S_{41} < -35.9$ dB) between port 1 (signal generator) and port 4 (receiver) was achieved. In the reception state, the T/R switch maintained strong matching (S_{22}

< -11.1 dB) and low insertion loss ($S_{42} < -0.6$ dB) at these frequencies, as shown in Fig. 11 and Table 5.

2. Measurement Verification

A prototype of the two-section branch-line hybrid coupler was fabricated on a 360 mm × 200 mm Rogers RO4003C substrate with a permittivity of 3.38 and thickness of 1.52 mm, as shown in Fig. 12. The subminiature version A (SMA) connectors for each port were soldered to the bottom of the substrate. The phase inverter (180° phase shifter) in the middle of the coupler was implemented using a very short 50 Ω coaxial cable on a crossover configuration. Notably, while it is possible to add a coaxial cable of any electrical length, even 0°, in simulations, such is not the case in reality—adding a coaxial cable with 0° electrical length is not possible. As a result, in this study, differ-
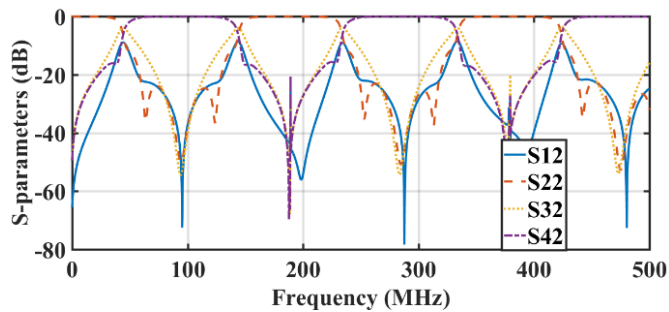
Fig. 9. *S*-parameters of the broadband T/R switch in the reception state.
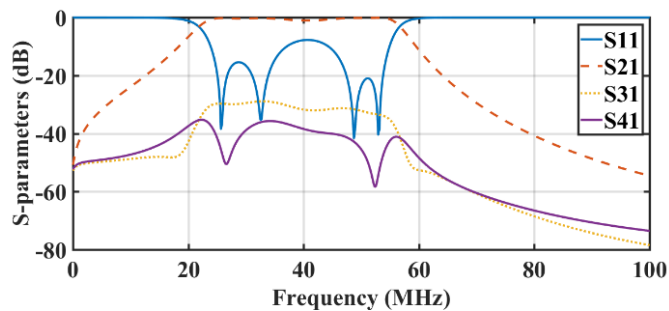
Fig. 10. *S*-parameters of the broadband T/R switch in the transmission state after tuning.
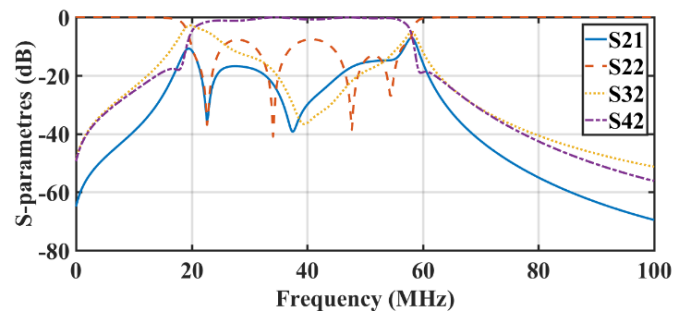
Fig. 11. *S*-parameters of the broadband T/R switch in the reception state after tuning.
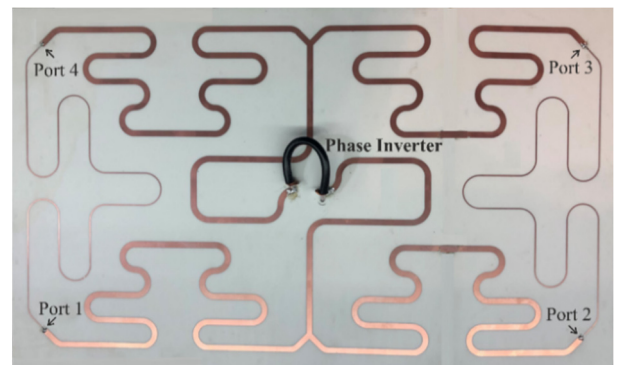
Fig. 12 Prototype of the two-section branch-line hybrid coupler.

Table 5. Simulated *S*-parameters of the broadband T/R switch in the transmission state and reception state at 3T after tuning

Atomic nuclei	Frequency (MHz)	Transmission state (dB)			Reception state (dB)		
		S_{11}	S_{21}	S_{41}	S_{22}	S_{12}	S_{42}
^{1}H	127.74	–	–	–	–	–	–
^{19}F	120.24	–	–	–	–	–	–
^{31}P	51.75	−21.10	−0.24	−48.78	−13.40	−15.25	−0.42
^{23}Na	33.81	−31.36	−0.32	−35.90	−17.55	−20.30	−0.23
^{13}C	32.13	−21.06	−0.35	−37.14	−11.10	−18.25	−0.60

ent coaxial cable lengths were tested to observe their effects. The effect of the electrical length of a coaxial cable (phase inverter) on coupler characteristics is shown in Fig. 13, where it is observed that the higher the electrical length, the lower the phase shift (less than 180°). Notably, this deviation from the 180° phase shift led to increased return loss and reduced bandwidth at the third odd harmonics. Fig. 13 clearly shows that at the acceptable deviation of 10° (θ = 10°), a return loss of less than 10 dB and a bandwidth of at least 90% can be maintained, coinciding with results of the electrical length without a deviation at 180° (θ = 0°). In practice, the physical length of the connected coaxial cable corresponded to a 5° electrical length. Notably, the electrical length was calculated based on the 95 MHz fundamental frequency of the coupler.

The T/R switch was easily fabricated using two hybrid couplers, as shown in Fig. 12. They were connected back to back, so that the ground planes of the two substrates were joined. To examine the internal connections between the couplers corresponding to the connections shown in Fig. 5, two thin wires were inserted through the ground planes. Two PIN diodes were placed on the first coupler at ports 2 and 4 in the same position as the two thin wires.

Fig. 14(a) and 14(b) present the measured and simulated S-parameters of the T/R switch during transmission and reception. In the transmission state, the T/R switch shows excellent matching (S_{11} < −10 dB), low insertion loss (S_{21} > −0.8 dB), and high isolation (S_{41} < −44 dB) between the signal generator (port 1) and the receiver (port 4) across all X-nuclei frequencies. During reception, the T/R switch maintains good matching (S_{22} < −17 dB) and low insertion loss (S_{42} > −0.4 dB) at all X-nuclei frequencies.

Fig. 15(a) and 15(b) present the measured and simulated S-parameters of the T/R switch in the transmission and reception states after using tuning capacitors. They cover the first frequency band required to cover the corresponding X-atomic nuclei frequencies, especially those below 60 MHz. Notably, a good match between the simulation and measurement results is observed.

However, the PIN diodes, lumped elements, transmission lines, biasing network, and Roger's substrate play crucial roles in contributing to the discrepancies between the measurements and simulations observed in Figs. 14 and 15.

IV. DISCUSSION

A comparison of the performance of the proposed 3T–7T T/R switch with that of state-of-the-art switches is reported in Table 6, clearly demonstrating that the proposed T/R switch shows promising performance relative to the other designs. The proposed switch can operate at three wide frequency bands: 25–55 MHz, 61.1–128.3 MHz, and 250.3–317.5 MHz. Comparatively, in [30, 31], the highest operating frequency was limited to 200 MHz. Furthermore, in [17, 32–34], the lowest operating frequencies were above 250 MHz. Therefore, all state-of-the-art

Fig. 13. Simulated (θ = 0°) and measured (θ = 5°, 10°, and 20°): (a) S_{11} and (b) S_{21} parameters for different coaxial cables.

Fig.14. Measured and simulated S-parameters for two-section hybrid couplers-based T/R switch in (a) transmission state and (b) reception state.

Fig. 15. Measured and simulated *S*-parameters for two-section hybrid couplers-based T/R switch in (a) transmission state after tuning and (b) reception state after tuning.
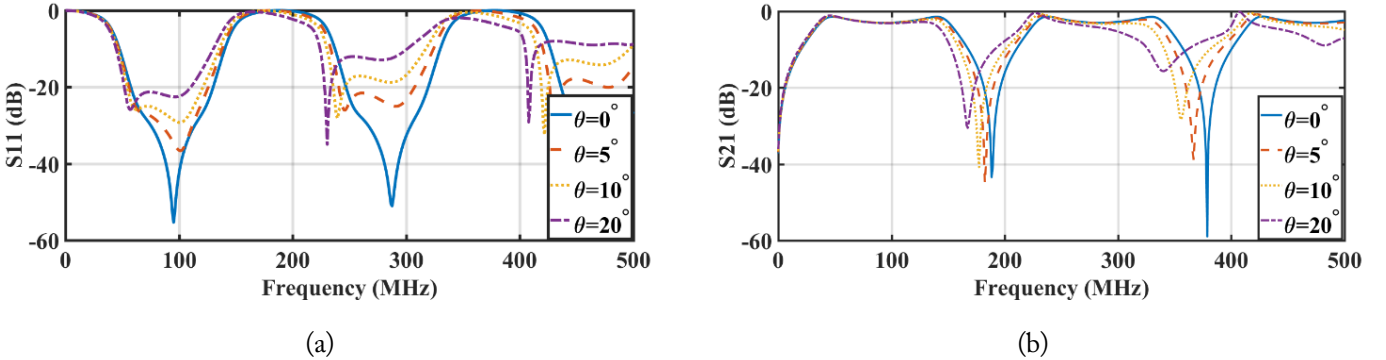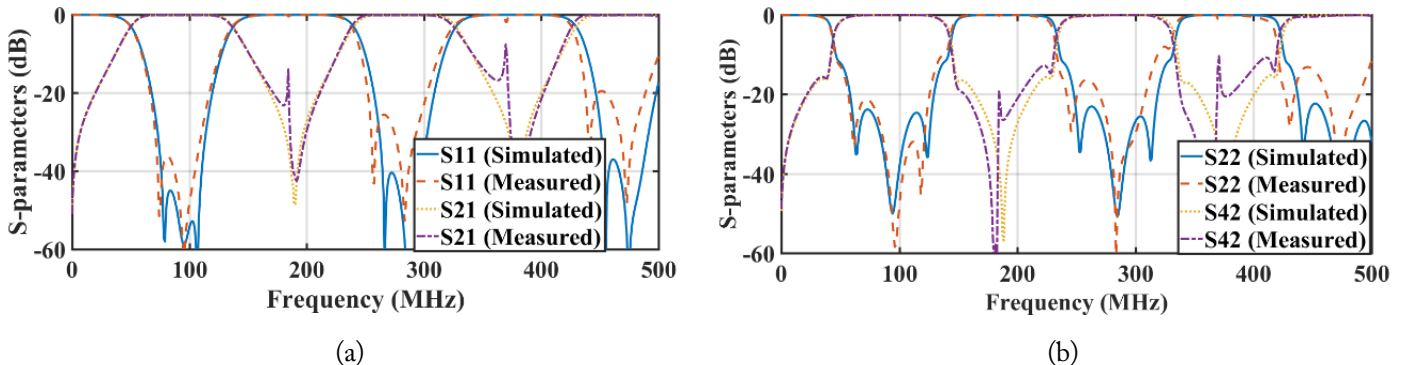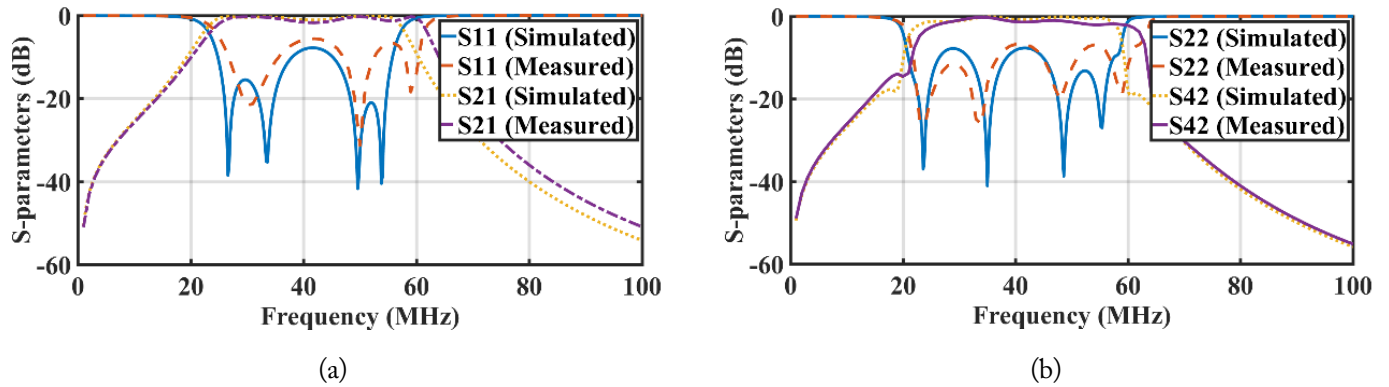
reported switches failed to cover many of the atomic X-nuclei frequencies for 3T and 7T magnetic field strengths. In addition, as shown in Table 6, the proposed switch demonstrates low insertion loss in both the transmission and reception states as compared to the designs reported in [30, 33, 34]. Regarding isolation performance, the designed switch demonstrates high isolation compared to its counterparts reported in [32–34]. Moreover, based on the performance of the proposed switch, it can be used along with both single- and multi-tuned RF coils that resonate within the three broadbands of its operating frequencies. As a result, the scanning process can be conducted without changing the type of RF coil or asking the patient to move. This will not only minimize the number of artifacts used but also reduce the amount of time spent in the scanning process.

V. Conclusion

This work involved designing, simulating, and fabricating a broadband transmit/receive switch for 3T and 7T MRI. ADS software was employed to design the switch, incorporating two hybrid couplers based on the two-section branch-line method, each with specified performance criteria (1 dB magnitude imbalance and 5° phase imbalance). The switch successfully covered various atomic X-nuclei frequencies within its three primary frequency bands (25–55 MHz, 61.1–128.3 MHz, and 250.3–317.5 MHz) at 3T and 7T magnetic field strengths, maintaining excellent return loss (>10 dB) and isolation (>40 dB), as well as low insertion loss (<0.8 dB), at all operating frequencies.

References

[1] Z. J. Wang, M. A. Ohliger, P. E. Larson, J. W. Gordon, R. A.

Table 6. Comparison between this work and the state-of-the-art T/R switches

Study	Frequency range (MHz)	Insertion loss (dB)		Tx-Rx isolation (dB)	Coil port return loss (dB)
		Transmission state	Reception state		
Yuan et al. [32]	250–1,000	0.2–0.56	0.2–0.56	>35	>13
Xiao et al. [30]	0.3–200	0.4–6	0.14–5	62–90	>22.6
Abuelhaija et al. [17]	280–340	<0.3	<0.45	>40	>20.0
Caverly [33]	290–310	1–2	–	12–28	–
Ji et al. [34]	250–350	0.2–2	0.27–2	16–35.7	–
Abou-Khousa and Mustapha [31]	30–200	0.09–0.2	0.11–0.37	63–80	>18
This work	(3 bands) 25–55	0.2–0.8	0.2–0.4	>40	>10
	61.1–128.3				
	250.3–317.5				

"-" indicates that the corresponding result has not been evaluated.

Bok, et al., "Hyperpolarized ^{13}C MRI: state of the art and future directions," *Radiology*, vol. 291, no. 2, pp. 273-284, 2019. https://doi.org/10.1148/radiol.2019182391

[2] S. B. Peter and V. R. Nandhan, "31-Phosphorus magnetic resonance spectroscopy in evaluation of glioma and metastases in 3T MRI," *Indian Journal of Radiology and Imaging*, vol. 31, no. 4, pp. 873-881, 2021. https://doi.org/10.1055/s-0041-1741090

[3] T. Henzler, S. Konstandin, G. Schmid-Bindert, P. Apfaltrer, S. Haneder, F. Wenz, et al., "Imaging of tumor viability in lung cancer: initial results using ^{23}Na-MRI," *RöFo*, vol. 184, no. 4, pp. 340-344, 2012. https://doi.org/10.1055/s-0031-1299277

[4] R. Forner, K. Nam, K. J. de Koning, T. van der Velden, W. van der Kemp, A. Raaijmakers, and D. W. Klomp, "RF coil setup for ^{31}P MRSI in tongue cancer in vivo at 7 T, " *Frontiers in Neurology*, vol. 12, article no. 695202, 2021. https://doi.org/10.3389/fneur.2021.695202

[5] UCH Clinical Trials, "Hyperpolarized Pyruvate (^{13}C) MR imaging in monitoring patients with prostate cancer on active surveillance," 2024 [Online]. Available: https://clinicaltrials.ucbraid.org/trial/NCT03933670.

[6] J. Dai, M. Gosselink, T. A. van der Velden, E. F. Meliado, A. J. E. Raaijmakers, and D. W. J. Klomp, "An RF coil design to enable quintuple nuclear whole-brain MRI," *Magnetic Resonance in Medicine*, vol. 89, no. 5, pp. 2131-2141, 2023. https://doi.org/10.1002/mrm.29577

[7] C. Ianniello, G. Madelin, L. Moy, and R. Brown, "A dual-tuned multichannel bilateral RF coil for ^{1}H/^{23}Na breast MRI at 7 T," *Magnetic Resonance in Medicine*, vol. 82, no. 4, pp. 1566-1575, 2019. https://doi.org/10.1002/mrm.27829

[8] D. O. Brunner, L. Furrer, M. Weiger, W. Baumberger, T. Schmid, J. Reber, et al., "Symmetrically biased T/R switches for NMR and MRI with microsecond dead time," *Journal of Magnetic Resonance*, vol. 263, pp. 147-155, 2016. https://doi.org/10.1016/j.jmr.2015.12.016

[9] B. Thapa, J. Kaggie, N. Sapkota, D. Frank, and E. K. Jeong, "Design and development of a general-purpose transmit/receive (T/R) switch for 3T MRI, compatible for a linear, quadrature and double-tuned RF coil," *Concepts in Magnetic Resonance Part B: Magnetic Resonance Engineering*, vol. 46, no. 2, pp. 56-65, 2016. https://doi.org/10.1002/cmr.b.21321

[10] P. K. Grannell, M. J. Orchard, P. Mansfield, A. N. Garroway, and D. C. Stalker, "A FET analogue switch for pulsed NMR receivers," *Journal of Physics E: Scientific Instruments*, vol. 6, no. 12, article no. 1202, 1973. https://doi.org/10.1088/0022-3735/6/12/020

[11] J. Y. Lu, T. Grafendorfer, T. Zhang, S. Vasanawala, F. Robb, J. M. Pauly, and G. C. Scott, "Depletion-mode GaN HEMT Q-spoil switches for MRI coils," *IEEE Transactions on Medical Imaging*, vol. 35, no. 12, pp. 2558-2567, 2016. https://doi.org/10.1109/TMI.2016.2586053

[12] M. Twieg, M. D. Rooij, and M. A. Griswold, "Enhancement mode GaN on silicon (eGaN FETs) for coil detuning," in *Proceedings of the Joint Annual Meeting ISMRM–ESMRMB*, Milan, Italy, 2014.

[13] M. Fuentes, E. Weber, S. Wilson, B. Li, and S. Crozier, "Micro-electromechanical systems (MEMS) based RF-switches in MRI: a performance study," in *Proceedings of the 18th Annual Meeting of ISMRM*, Stockholm, Sweden, 2010.

[14] S. B. Bulumulla, K. J. Park, E. Fiveland, J. Iannotti, and F. Robb, "MEMS switch integrated radio frequency coils and arrays for magnetic resonance imaging," *Review of Scientific Instruments*, vol. 88, no. 2, article no. 025003, 2017. https://doi.org/10.1063/1.4975181

[15] A. Maunder, M. Rao, F. Robb, and J. Wild, "RF coil design for multinuclear lung MRI of 19F fluorinated gases and 1H using MEMS," in *Proceedings of the 24th Annual Meeting of ISMRM,* Singapore, 2016.

[16] A. Maunder, M. Rao, F. Robb, and J. M. Wild, "Comparison of MEMS switches and PIN diodes for switched dual tuned RF coils," *Magnetic Resonance in Medicine*, vol. 80, no. 4, pp. 1746-1753, 2018. https://doi.org/10.1002/mrm.27156

[17] A. Abuelhaija, G. Saleh, T. Baldawi, and S. Salama, "Symmetrical and asymmetrical microstripline-based transmit/receive switches for 7-Tesla magnetic resonance imaging," *International Journal of Circuit Theory and Applications*, vol. 49, no. 7, pp. 2082-2093, 2021. https://doi.org/10.1002/cta.3013

[18] G. Saleh and A. Abuelhaija, "Dual tuned switch for dual resonance 1H/13C MRI coil," in *Proceedings of 2021 IEEE International IOT, Electronics and Mechatronics Conference (IEMTRONICS)*, Toronto, Canada, 2021, pp. 1-7. https://doi.org/10.1109/IEMTRONICS52119.2021.9422627

[19] A. Abuelhaija, G. Saleh, O. Nashwan, S. Issa, and S. Salama, "Multi-and dual-tuned microstripline-based transmit/receive switch for 7-Tesla magnetic resonance imaging" *International Journal of Imaging Systems and Technology*, vol. 32, no. 2, pp. 590-599, 2022. https://doi.org/10.1002/ima.22634

[20] A. Abuelhaija and G. Saleh, "Dual tuned 1H/31P quadrature microstripline-based transmit/receive switch for 7 Tesla magnetic resonance imaging," *International Journal of Electrical & Computer Engineering*, vol. 12, no. 3, pp. 2177-2183, 2022. https://doi.org/10.11591/ijece.v12i3.pp2177-2183

[21] A. Abuelhaija and G. Saleh, "A pi-shaped compact dual tuned H/23 Na microstripline-based switch for 7-Tesla MRI," *International Journal on Communications Antenna and Propagation*, vol. 11, no. 1, pp. 57-64, 2021. https://doi.org/10.15866/irecap.v11i1.20302

[22] A. Abuelhaija and G. Saleh, "Two-section branch-line hybrid couplers based broadband transmit/receive switch," *International Journal of Electrical and Computer Engineering (IJECE)*, vol. 13, no. 3, pp. 2600-2607, 2023. https://

doi.org/10.11591/ijece.v13i3.pp2600-2607

[23] A. Abuelhaija and G. Saleh, "Broadbands four-branch hybrid coupler-based T/R switch for 7-Tesla magnetic resonance imaging," *International Journal on Communications Antenna and Propagation*, vol. 12, no. 5, pp. 380-384, 2022. https://doi.org/10.15866/irecap.v12i5.22449

[24] H. J. Yoon and B. W. Min, "Two section wideband 90° hybrid coupler using parallel-coupled three-line," *IEEE Microwave and Wireless Components Letters*, vol. 27, no. 6, pp. 548-550, 2017. https://doi.org/10.1109/LMWC.2017.2701304

[25] A. Jain, R. P. Yadav, and S. V. Kulkarni, "Design and development of 2 kW, 3 dB hybrid coupler for the prototype ion cyclotron resonance frequency (ICRF) system," *International Journal of Microwave and Wireless Technologies*, vol. 11, no. 1, pp. 1-6, 2019. https://doi.org/10.1017/S175907871800137X

[26] S. M. H. Javadzadeh, S. M. S. Majedi, and F. Farzaneh, "Broadside coupler channels 1 to 10 GHz," *Microwaves and RF*, vol. 51, no. 1, pp. 68-77, 2012.

[27] M. Leib, D. Mack, F. Thurow, and W. Menzel, "Design of a multilayer ultra-wideband directional coupler," in *Proceedings of the German Microwave Conference*, Hamburg, Germany, 2018, pp. 1-4.

[28] D. N. A. Zaidel, S. K. A. Rahim, N. Seman, C. L. Chew, and N. H. Khamis, "A design of octagon-shaped 3-dB ultra wideband coupler using multilayer technology," *Microwave and Optical Technology Letters*, vol. 55, no. 1, pp. 127-130, 2013. https://doi.org/10.1002/mop.27259

[29] L. Chiu and Q. Xue, "Wideband parallel-strip 90 hybrid coupler with swap," *Electronics Letters*, vol. 44, no. 11, pp. 687-688, 2018. https://doi.org/10.1049/el:20080975

[30] Y. Xiao, Z. Zhao, Z. Qian, and H. Zhou, "A high isolation switching unit for MRI system," *Procedia Engineering*, vol. 7, pp. 265-269, 2010. https://doi.org/10.1016/j.proeng.2010.11.042

[31] M. A. Abou-Khousa and A. A. Mustapha, "Wideband RF transmit-receive switch for multi-nuclei NMR spectrometers," *IEEE Transactions on Circuits and Systems II: Express Briefs*, vol. 69, no. 3, pp. 904-908, 2022. https://doi.org/10.1109/TCSII.2021.3121210

[32] L. Yuan, Z. Wang, W. Wei, and X. Han, "High-frequency broadband RF transmit-receive switch for pulsed magnetic field NMR," *IEEE Transactions on Instrumentation and Measurement*, vol. 72, article no. 6004109, 2023. https://doi.org/10.1109/TIM.2023.3267530

[33] R. H. Caverly, "PIN diode-based transmit-receive switch for 7 T MRI," in *Proceedings of 2016 IEEE Topical Conference on Biomedical Wireless Technologies, Networks, and Sensing Systems (BioWireleSS)*, Austin, TX, USA, 2016, pp. 100-102. https://doi.org/10.1109/BIOWIRELESS.2016.7445574

[34] Y. Ji, W. Hoffmann, M. Pham, A. E. Dunn, H. Han, C. Ozerdem, et al., "High peak and high average radiofrequency power transmit/receive switch for thermal magnetic resonance," *Magnetic Resonance in Medicine*, vol. 80, no. 5, pp. 2246-2255, 2018. https://doi.org/10.1002/mrm.27194

Ashraf Abuelhaija
https://orcid.org/0000-0002-6645-3833

is an associate professor in the Department of Electrical Engineering at Applied Science Private University, Amman, Jordan, from where he received his B.Sc. degree in communications and electronics engineering in 2007. He received his master's degree and Ph.D. in electrical engineering from DuisburgEssen University in 2010 and 2016, respectively. His research interests pertain to the area of antennas and RF technology. From 2012 to 2014, he worked as a research assistant at Erwin L. Hahn Institute for Magnetic Resonance Imaging, Essen. From 2014 to 2016, he was a research assistant at the Department of Microwave and RF Technology at Duisburg-Essen University.

Gameel Saleh
https://orcid.org/0000-0003-1502-3582
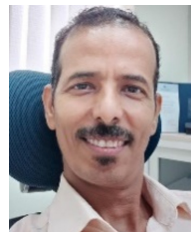
was born in Aden, Yemen. He received his B.Sc. degree in electrical engineering from Aden University, Aden, Yemen, in 2001, and his M.S. degree in electrical engineering from Jordan University of Science and Technology, Irbid, Jordan, in 2008. In 2013, he was awarded a Dr.-Ing (Ph.D.) degree in electrical engineering by Duisburg–Essen University, Duisburg, Germany. From 2014 to 2015, Dr. Saleh worked in the Communication Engineering Department of Aden University. Since 2015, he has been working as an associate professor in the Department of Biomedical Engineering at Imam Abdulrahman Bin Faisal University, Dammam, Saudi Arabia. His current research interests include RF circuits, metamaterials, wearable antennas, and biosensors. Dr. Saleh was a recipient of the German Academic Exchange Service Fellowships in 2006 and 2009.

Sanaa Salama

https://orcid.org/0000-0001-9480-6985

received her B.Sc. degree in Telecommunication Technology from the Arab American University (AAUP), Palestine, in 2006 (excellent evaluation, GPA 3.96/4), and her M.Sc. degree in electrical engineering from the University of Jordan, Jordan, in 2009 (excellent evaluation, GPA 3.83/4). In 2015, she received her Ph.D. degree in electrical engineering from Duisburg-Essen University in Germany. Her research interests include characteristic chassis wave modes, MIMO antenna design, beam-forming antenna array design, reconfigurable antennas, coupling element-based antenna structures, mutual coupling, chassis wave-mode coupling, and port and pattern isolation. Her recent field of research is the design of RF coils for 7 T MRI systems, design of decoupling and matching networks, and the design of implantable antennas for MICS and ISM bands. Since 2015, she has been an assistant professor in the Department of Telecommunication Engineering at AAUP. She has also authored a number of conference and journal papers.

Mohammed Hamdan

https://orcid.org/0000-0001-5320-2931

received his Ph.D. degree in electrical engineering from the University of Southampton, Southampton, UK, in 2019. He received his M.Sc. degree in Energy and Sustainability with Electric Power Engineering from the University of Southampton, UK, in 2014. He received his B.Sc. degree in electrical engineering from Jordan University of Science and Technology, Irbid, Jordan, in 2010. Currently, he is an assistant professor at Applied Science Private University, Jordan. His current research focuses on the impact of renewable technologies on the distribution grid, numerical simulation (FEA), and theoretical analytics (thermal, electrical, and mechanical) of high voltage AC and DC power cables.

Mechanism and Method for Residual Flux Detection of Transformer Cores Based on Different Polarities Response Currents

Cailing Huo[1] ⓘ · Yiming Yang[1,*] ⓘ · Fuyin Ni[1] ⓘ · Qiang Xie[2] ⓘ

Abstract

This paper proposes a residual flux detection method based on the different polarities of response currents. When a positive–negative alternating DC voltage is loaded, the direction of the residual flux can be determined by the difference between the various polarities of the response current waveforms. As a result, residual flux value can be calculated using the empirical formula that relates residual flux to the responce current. In this formula, unknown parameters can be obtained using the field-circuit coupling method. Finally, this paper employs a closed iron core as an example to obtain the corresponding formula and then verifies its accuracy through experiments. The results show that the accuracy of the proposed method is less than 5%, which is higher than that of other existing methods. The method presented in this paper not only accurately detects the residual flux of a transformer but also requires no additional energy from the transformer.

Key Words: Different Polarity Response Currents, Empirical Formula, Power Transformer, Residual Flux.

I. INTRODUCTION

A power transformer is one of the most significant and expensive equipment employed in a power grid. As a result, safe operation of the power transformer is crucial for a power system [1]. Transformer core materials generally feature hysteresis and saturation characteristics [2], due to which an unknown residual flux (RF) may be generated in their iron core after a DC resistance test, a transformation ratio measurement, or a no-load closing operation [3]. If this RF is large, a large amount of inrush current may form when the transformer is turned off, which can lead to winding deformation, current imbalance, and harmonic pollution [4]. Such situations render the transformer

protection function invalid. Therefore, research on RF detection mechanisms and methods has important academic significance for reducing inrush current [5].

At present, an empirical method is often used to estimate magnetic flux, according to which the RF is estimated based on the 0.2–0.7 saturation flux [6–8]. However, this estimation error depends on historical experience, which is not conducive to on-site detection. The second method is the induced voltage method, which is based on the electromagnetic induction law for detecting magnetic flux changes in the magnetic core [9]. It calculates the RF by recording the induced voltage waveform when the transformer is turned off. However, since the RF calculated on starting the transformer is always different from the stabilized RF [10],

the feasibility of this method is limited in practical application. The third method is the pre-magnetization method [11], which involves pre-charging the iron core with a known RF to then use phase-selective closing technology or the demagnetization method to suppress the inrush current. However, this method cannot pre-charge a certain amount of RF in advance for the actual transformer core, which limits its feasibility in practice.

The RF formation process involves complex changes in the magnetic domain structure of ferromagnetic materials [12]. Therefore, some previous studies have also studied indirect detection methods. In [13], RF was measured by analyzing the magnetic leakage around the iron core. Although this method was able to detect RF, it was limited by the influence of different measuring points on the measurement results, ultimately achieving a measurement accuracy as high as 20%. In [14], RF was estimated by analyzing the magnetized inductance. However, its measurement results were limited by the accuracy of the iron core model In addition, an RF detection method based on even the harmonics of the induced voltage is presented in [15], which was able to detect the RF of the current transformer, but its accuracy was limited by the accuracy of the simulation model. In [16], an RF detection method using small loop energy is proposed, but this method ignores the energy change under small RF, thus increasing the error of the extraction relationship. In [17], an RF detection method based on phase difference was analyzed, but the phase difference obtained by this method under different RFs was small, which is not conducive to its detection in practice. Furthermore, [18–20] studied RF detection methods considering transient variables, but the test time of the measured waveform was difficult to extract, rendering the accuracy of the detection results unstable and not conducive to on-site testing. Based on the above research methods, it is evident that there is still no fast and effective RF detection method available.

This paper presents an RF detection method based on the different polarities of response currents to obtain an accurate RF value and polarity. First, when the DC voltage in different directions is loaded in sequenc, the RF detection mechanism is analyzed, and a method for determining the RF direction is proposed. Following this, the relationship between the RF and the response current is established, and the corresponding parameters are obtained by employing the field-circuit coupling method. Finally, an RF test platform for a square core is built to verify the feasibility of the theoretical analysis and the accuracy of the proposed method.

II. DETECTION PRINCIPLE OF RESIDUAL FLUX

The RF formation mechanism based on different magnetized states is depicted in Fig. 1, indicating that when the magnetic field strength H gradually increases to reach its maximum value, the magnetic flux increases along $0ab$. Furthermore, when the external magnetic field disappears at point a or b due to hystere-

sis characteristics, a different RF is generated in the iron core, such as B_r or B_r'. Therefore, it is evident that RF generation is primarily decided by changes in the domain structure at the RF, which can be reflected by changes in the relative differential permeability (μ_{rd}), expressed as follows:

$$\mu_{rd} = \frac{1}{\mu_0} \frac{\Delta B}{\Delta H} \tag{1}$$

where μ_0 is a constant, referring to the vacuum permeability of air, and ΔB and ΔH are the increments of B and H, respectively.

To analyze the variation trend of differential permeability at RF, this paper analyzed the material characteristics of the iron core using the silicon-steel sheets (model B30P105). The hysteresis loop of the core at low frequencies was measured, after which the differential permeability trend caused by saturation to the RF state was analyzed, as shown in Fig. 2. It is observed that when the frequency is 5 Hz, the B_m reaches 1.8 T, while the coercive force H_c is 13 A/m, indicating the difficulty involved in magnetizing the material. Furthermore, when ΔH is greater than 5% of H_c, the difference between the positive relative permeability μ_{rp} and negative relative permeability μ_{rn} is quite obvious. At this juncture, the relationship between μ_{rp} and μ_{rn} can be expressed as follows:
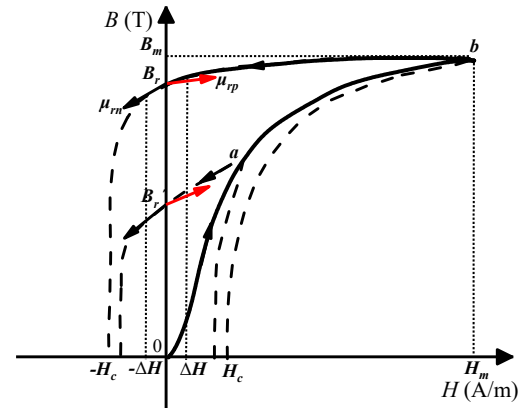

Fig. 1. Formation mechanism of residual flux under different magnetization states.
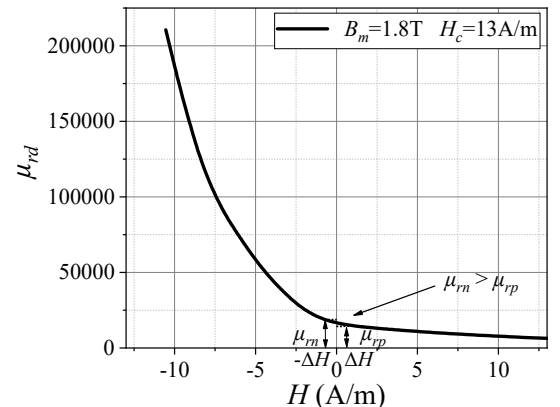

Fig. 2. Variation trend of μ_{rd} caused by saturation to the residual flux state.

$$\mu_{rp} < \mu_{rn}. \tag{2}$$

Based on the above relationship, the RF direction can be judged by comparing μ_{rp} with μ_{rn}. However, measuring μ_{rp} and μ_{rn} is not an easy task, due to the complex changes occurring in the magnetic domain structure. Therefore, it is necessary to analyze an indirect variable that can reflect μ_{rd}. Notably, when a DC voltage is loaded on one side of the winding of a transformer, the quantitative detection of RF can be realized by analyzing the relationship between the response current and the μ_{rd} in the circuit.

After the transformer is turned off, the method proposed in this paper only needs to connect the designed DC measurement circuit to a winding located close to the iron core for response current sensing. Subsequently, by analyzing the relationship between the response current and the RF, quantitative detection of the RF can be realized. Fig. 3 presents the DC detection circuit, where $u_s(t)$ is the DC voltage and R_s denotes the series resistance. In an actual operation, when a transformer is reconnected to the power system, the RF direction remains unknown. To address this issue, the current paper analyzed the relationship between the RF and the response current under different excitation directions of the applied voltage. The main waveforms generated by applying the DC excitation directions are presented in Fig. 4. First, a positive DC voltage with the same polarity as the initial RF density was applied, after which a negative DC voltage was introduced—this waveform is abbreviated as PN. Similarly, a negative DC voltage with a polarity opposite to the initial RF density was applied, after which a positive DC voltage was implemented—this waveform is abbreviated as NP.

As shown in Fig. 4, in the case of PN, when the positive voltage is loaded first at t_1, the positive respond current $i_p(t)$ is generated. When the voltage is removed after t_2, the RF in the iron core becomes a new B_{rp}. Subsequently, when the negative voltage with a polarity opposite to the RF is applied at t_3, a negative respond current $i_n(t)$ is generated. After t_4, when the voltage is removed, the initial RF changes from B_{rp} to B_{rn}. However, in the case of NP, as shown in Fig. 4(b), $i_n(t)$ is produced first and $i_p(t)$ is produced second, due to which the initial RF first changes to B_{rn} and then to B_{rp}. According to Eq. (2), μ_{rp} at RF is less than μ_{rn}, due to which the changes in RF are different in the case of PN and NP. Thus, the waveforms of the measured positive and negative respond current are also different. Consequently, the quantitative detection of the RF was realized by means of this difference.

When a voltage is loaded, the transformer core becomes equivalent to an *RL* series-parallel circuit. Fig. 5 shows an equivalent circuit model for the measurement circuit, where R_s represents the total resistance in the circuit, primarily including the series resistance and winding resistance. Meanwhile, L_{eq} stands for the equivalent magnetized inductance of the iron core,

which is related to the change in magnetic flux. R_{Fe} stands for hysteresis loss in transient processes, also called iron loss resistance. Notably, when the turns of the winding (N), the cross-sectional area S, and the average magnetic circuit length l are known, the magnetization inductance L_{eq} at the RF can be related to the differential permeability μ_{rd}.

According to the magnetic circuit analysis, the relationship between L_{eq} and μ_{rd} can be expressed as:

$$L_{eq} = \frac{N^2 S \mu_0}{l} \mu_{rd}. \tag{3}$$

Furthermore, since the applied excitation is DC excitation, the time constant in the measurement circuit can be expressed as L_{eq}/R. Therefore, the respond current $i(t)$ in the circuit can be formulated as follows:

$$i(t) = I_o\left(1 - e^{-\frac{t}{\frac{1}{R}\frac{N^2 S \mu_0}{l}\mu_{rd}}}\right) = I_o\left(1 - e^{-\frac{t}{k\mu_{rd}}}\right), \tag{4}$$

where R represents the parallel connection between R_{Fe} and R_s. Furthermore, according to Eq. (4), $i_p(t)$ and $i_n(t)$ are represented as follows:
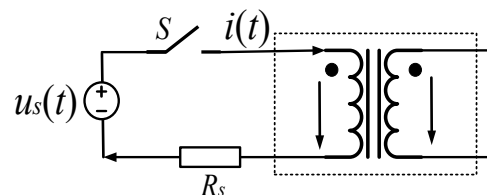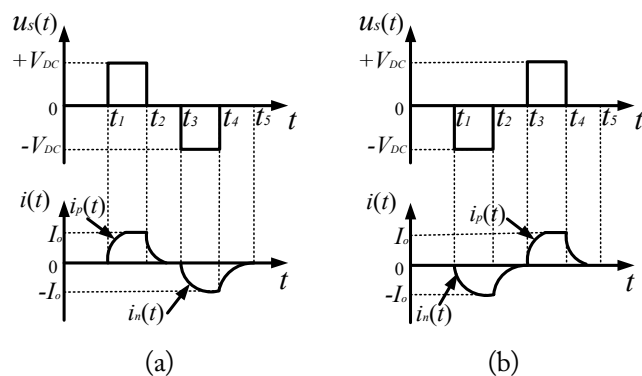

Fig. 3. DC measurement circuit.

(a)　　　　　　　　　(b)

Fig. 4. Main waveforms: (a) PN and (b) NP.
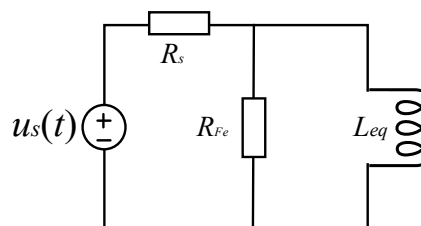

Fig. 5. Equivalent circuit model.

$$\begin{cases} i_p(t) = I_o\left(1 - e^{-\frac{t}{k\mu_{rp}}}\right) \\ i_n(t) = I_o\left(1 - e^{-\frac{t}{k\mu_{rn}}}\right) \end{cases}. \tag{5}$$

Based on Eqs. (2) and (5), the relationship between $i_p(t)$ and $i_n(t)$ can be obtained from the following formula:

$$i_p(t) > i_n(t). \tag{6}$$

Regardless of whether the positive or negative excitation was loaded first, the change rate of $i_p(t)$ was found to be faster than that of $i_n(t)$. Therefore, the RF direction can be judged by comparing the waveforms $i_p(t)$ and $i_n(t)$. Notably, to obtain the relationship between RF and the response current, μ_{rd} can be expressed as follows:

$$\mu_{rd} = -\frac{t_s l R}{N^2 S \mu_0} \frac{1}{\ln\left(1 - \frac{1}{I_o} \cdot i(t_s)\right)}, \tag{7}$$

where t_s is the best measurement time for the respond current. According to Eq. (7), the change in the magnetic domain structure at RF maintains a pertinent relationship with respond current. Therefore, this study proposes a method for calculating the RF by establishing a relationship between B_r and $i(t_s)$. This relationship can be expressed as follows:

$$B_r = f\left(i(t_s)\right) = \frac{a}{\ln\left(1 - 1/I_o \cdot i(t_s)\right)} + b, \tag{8}$$

where a and b are constant coefficients whose values are determined by the finite element method, and I_o represents the current value when the circuit reaches a steady state, which can be expressed as V_{DC}/R.

In the following sections, the field-circuit coupling method is applied to analyze the above relationship, and an experimental verification is carried out.

III. FIELD-CIRCUIT COUPLING ANALYSIS

This paper used the finite element method to extract empirical formulas for calculating RF. First, the iron core was modeled. To simulate the initial RF in the iron core, the hysteresis model of the iron core was used during modeling. In particular, the J-A hysteresis model presented in [21] was employed to simulate the hysteresis characteristics of the iron core and achieve an accurate simulation of its initial RF. The five parameter values of the hysteresis model obtained through parameter identification were $M_s = 1.58 \times 10^6$ A/m, $a = 4.56$ A/m, $alpha = 5.67 \times 10^{-6}$, $k = 8.95$ A/m, and $c = 0.18$. Fig. 6 depicts the research objects selected for this study. As shown, S of the iron core is

0.0016 m^2, l of the iron core is 1.92 m, and N of the measuring winding is 50.

Notably, before DC excitation loading, the initial RF needs to be preset in the core. In this study, the initial RF was simulated by applying a short-term large current to the core. First, a large current was applied to the winding so that the magnetic flux of the core quickly reached its maximum value. Subsequently, the large current was removed, with the static flux in the core being the initial RF of the simulation. As shown in Fig. 6, when the initial RF is 0.845 T, the magnetic flux inside the core is larger than that outside the core. This can be attributed to the shorter magnetic circuit length of the inner side and the smaller magnetic resistance of the core, which makes the magnetic flux larger. The error between the internal and external magnetic flux with regard to the average magnetic flux was less than 0.12%, indicating that the distribution of magnetic flux at the RF was almost uniform.

1. Selection of Independent Variables

Fig. 7 traces the waveforms of the preset current, the loaded DC voltage, the flux density, and the respond current for PN and NP. It is evident that when $i_p(t)$ reaches the steady state (the current value is 0.043 A), $i_n(t)$ has not yet reached the steady state (the current value is 0.029 A). As a result, the value of $i_p(t)$ is greater than that of $i_n(t)$—consistent with the theoretical analysis. Furthermore, Fig. 7 shows that when a positive voltage is applied, the RF change remains within 0.001 T, thus remaining almost unchanged. However, when a negative voltage is applied, the RF change is large than that caused by the positive voltage. This indicates that while $i_n(t)$ is generated at almost the same B_r (0.845 T and 0.846 T), $i_p(t)$ is generated at a different B_r (0.845 T and 0.808 T). Therefore, if $i_p(t)$ is selected to measure the RF in the iron core, a large error may occur in the measurement. However, if $i_n(t)$ is selected, the error would be greatly reduced. Therefore, to improve measurement accuracy, this paper considered $i_n(t)$ as the independent variable for detecting the RF in the iron core.
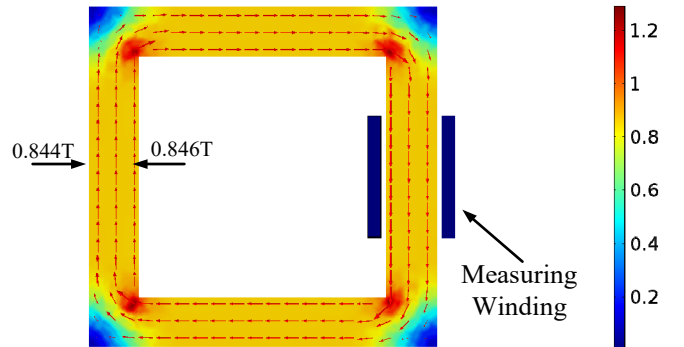

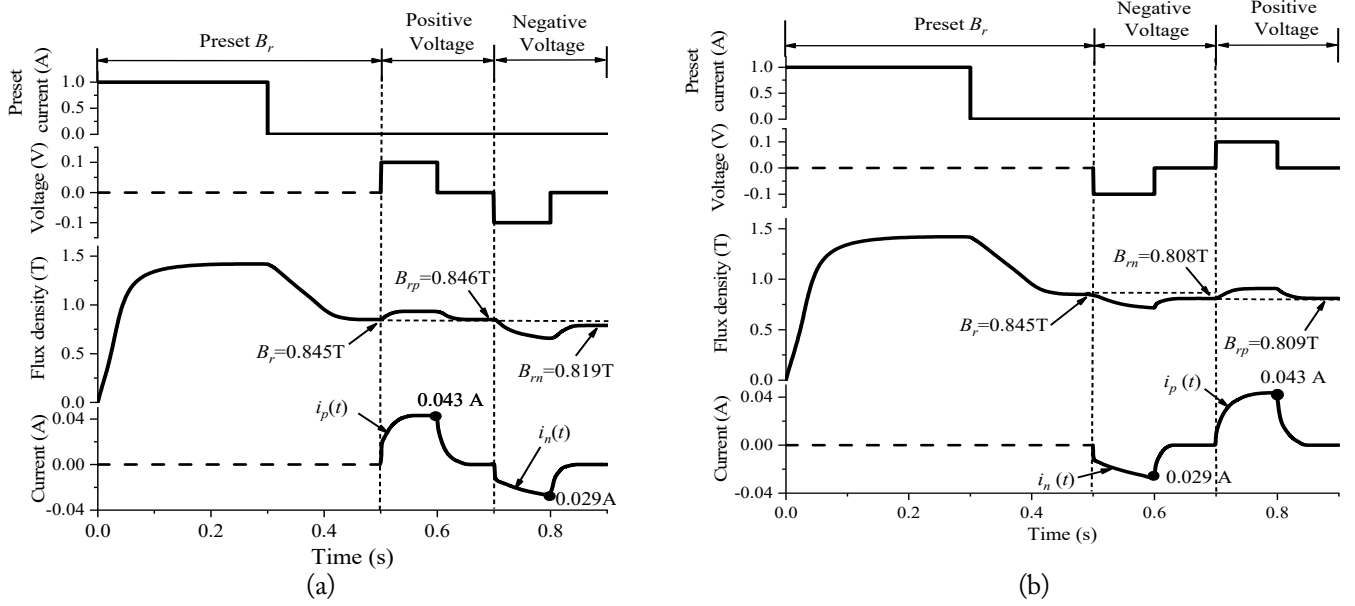Fig. 6. Square iron core model in finite-element method (FEM).

Fig. 7. The main waveforms in the finite-element method (FEM): (a) PN and (b) NP.

2. Selection of Load Voltage

In Fig. 7(a), the initial RF changes from 0.846 T to 0.819 T, with the change rate of negative B_r being 3.19%. Meanwhile, in Fig. 7(b), the initial RF changes from 0.845 T to 0.808 T, with the change rate of negative B_r being 4.38%. This indicates that the influence of negative voltage on RF is relatively obvious in the case of NP. As a result, the maximum range of the applied excitation was obtained by analyzing the RF change rate under NP. Fig. 8 traces the change in trend of negative B_r under NP, where parameter k is the ratio of H_1 $(H_1 = \Delta H)$ to the coercive force H_c, reflecting the influence of the loaded voltage on RF. Notably, when $k > 0.13$, the $B_r\%$ exceeds 5%. Therefore, this study considers the change in B_r to be less than 5% when DC voltage is applied. In addition, when H_1 is not greater than 5% of H_c in Fig. 2, the change in μ_{rp} and μ_{rn} may not be very obvious, which may make it impossible to determine the RF direction. Thus, the value of k is selected as 0.05 to 0.13 of the H_c.

Based on the ampere loop law, the following equation can be formulated:

$$I_o \cdot N = H_1 \cdot l. \tag{9}$$

The applied V_{DC} can be expressed as follows:

$$V_{DC} = \frac{H_1 \cdot l \cdot R}{N}. \tag{10}$$

Therefore, when the range of k $(k = H_1/H_c)$ is from 0.05 to 0.13, the range of the applied V_{DC} can be formulated as follows:

$$\frac{0.05 H_c \cdot l \cdot R}{N} \leq V_{DC} \leq \frac{0.13 H_c \cdot l \cdot R}{N}. \tag{11}$$
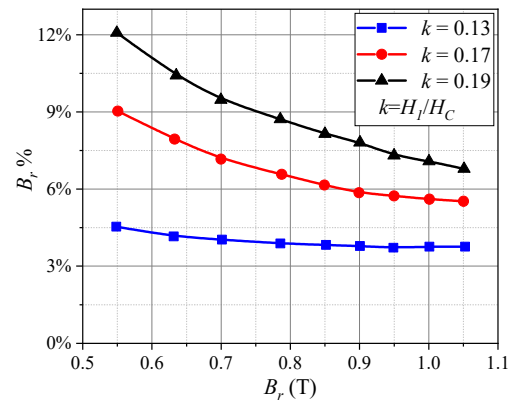
Fig. 8. Change rate of negative B_r at NP.

Furthermore, when the parameters are $N = 50$, $R = 2.32$ Ω, and $H_c = 13$ A/m, the range of the applied V_{DC} can be considered as follows:

$$0.058V \leq V_{DC} \leq 0.151V. \tag{12}$$

3. Determination of Best Measurement Time

According to the determined core material characteristics and external circuit parameters, finite element simulation analysis was carried out to obtain the respongise current under different RFs. Subsequently, the best measurement time for the response current was selected to investigate the relationship between different RFs and the response current.

Fig. 9 shows the waveforms of $i_p(t)$ and $i_n(t)$ at different RFs when the voltage is 0.1 V. It is evident that the current values obtained at different moments are different. This made it necessary to analyze the relationship between the current value at different moments and the RF. As shown in Fig. 10, when the

time is 0.025 seconds, the change in trend of $i_p(t)$ with an increase in RF is different under PN than under NP (Fig. 10(a)). However, when the time is 0.1 seconds, the change trend of $i_n(t)$ is basically the same for the two cases (Fig. 10(b)). This may be attributed to the fact that when positive voltage is applied, the initial RF is different for both cases, whereas when negative voltage is applied, the initial RF remains unchanged. This indicates that, while the generated $i_n(t)$ basically remains the same, $i_p(t)$ is different in the two cases. Therefore, to accurately calculate the RF in different directions, this paper chose $i_n(t)$ as the measurable variable to calculate the RF in the iron core. Furthermore, the best measurement time t_s was selected as 0.1 seconds, indicating the moment when the voltage would be removed. Notably, at this time, the values of $i_n(t)$ calculated from the experiment would be easier to measure and the difference in current values would also be more obvious.

After determining the best measurement time for the re-

sponse current, the empirical formula for calculating RF was obtained by analyzing the relationship between respond current and RF using the data fitting method. Since the basic functional form of the fitting formula had already been determined by drawing on Eq. (8), only the parameter values had to be determined. Therefore, considering that the time is 0.1 seconds, the voltage is 0.1 V, and the total resistance is 2.32 Ω, the relationship between $i_n(t)$ and B_r can be fitted as follows:

$$B_r = \frac{a}{\ln\left(1 - 23.26 \cdot i_n(t_s)\right)} + b. \tag{13}$$

Here, the values for a and b were obtained by the data fitting method as 0.67 and 1.45, respectively.

IV. EXPERIMENTAL VALIDATION

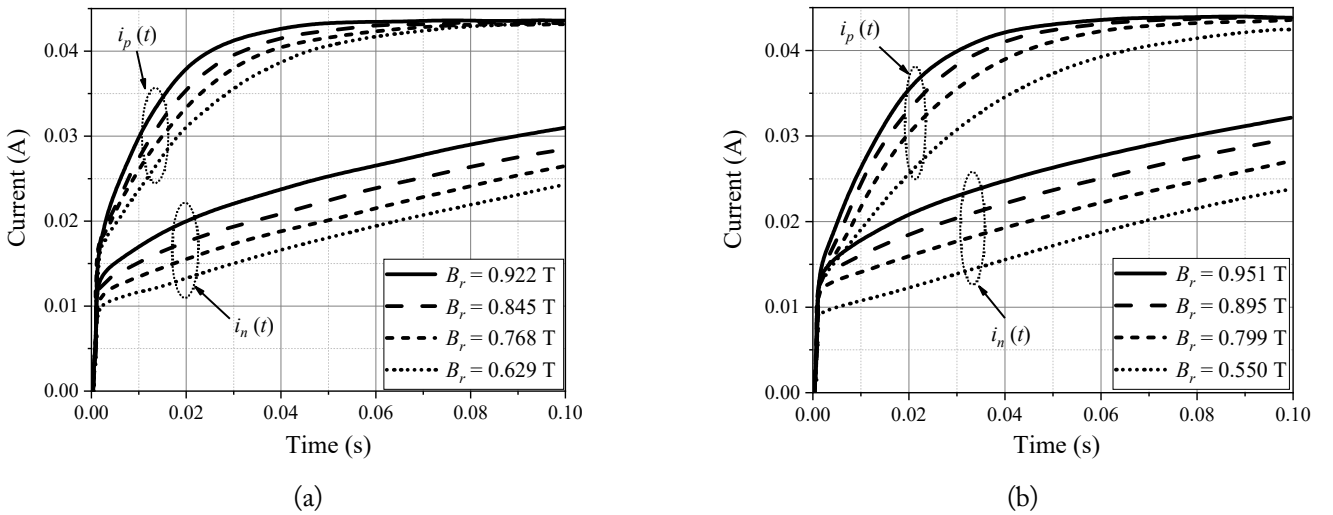An RF detection platform comprising a square iron core was

Fig. 9. Waveforms of $i_\mathrm{p}(t)$ and $i_\mathrm{n}(t)$ at different residual fluxes: (a) PN and (b) NP.
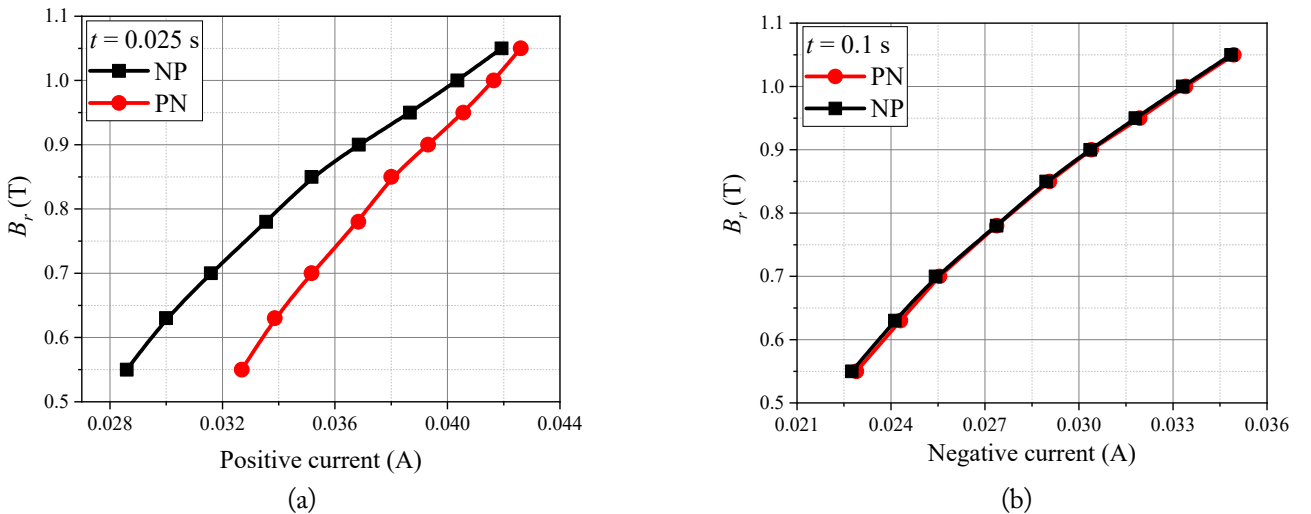

Fig. 10. (a) Relationship between positive respond current and B_r at $t = 0.025$ seconds and (b) relationship between negative respond current and B_r at $t = 0.1$ seconds.

built to verify the feasibility of the theoretical analysis and the accuracy of the proposed method. Fig. 11 shows a photograph of the experimental platform, where the tested core ("1") is composed of Baosteel B30P105 silicon steel sheets. The material type was kept consistent with the simulation to ensure the accuracy of the test results. Furthermore, a signal generator ("2") is employed to generate different square wave voltage signals, which can help realize the control of voltage polarity. A power amplifier ("3") is used to amplify the applied voltage signal, while a switch ("4") is employed to control the turn-on and turn-off actions of the detection circuit. The resistor ("5") is used to block the current. An oscilloscope ("6") is added to observe the flow of the current through the windings ("7"). Furthermore, the high-precision current probe N2782B ("8") is used to acquire current signals since it can realize accurate current detection in the ms or even the μs range. Moreover, Fluxmeter480 ("9") is included in the setup, since it is capable of tracking real-time changes in magnetic flux density, with the measured magnetic flux being the flux based on the voltage integration principle.

The initial RF direction of offline transformers usually remains unknown. At this moment, the same positive voltage as the initial RF polarity can be applied to measure the positive response current $i_+(t)$. Subsequently, when applying negative voltage, the negative current $i_-(t)$ can be measured. Subsequently, if the change rate of the $i_+(t)$ is found to be greater than $i_-(t)$, $i_+(t)$ can be determined to be $i_p(t)$, and $i_-(t)$ as $i_n(t)$,
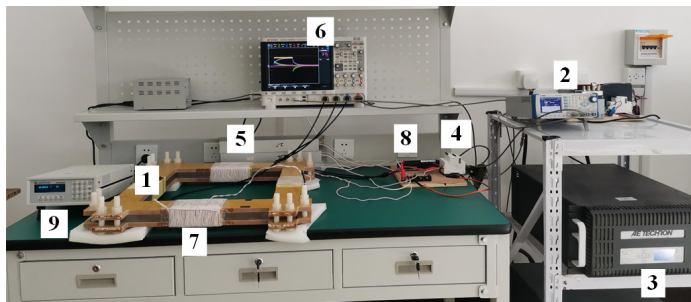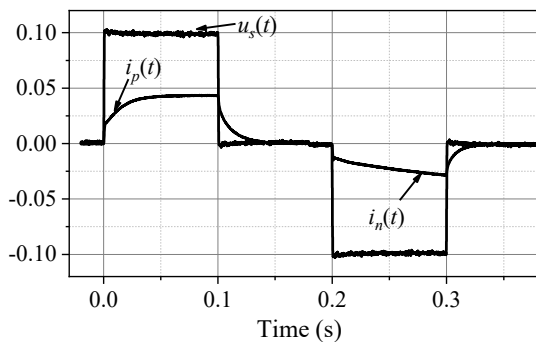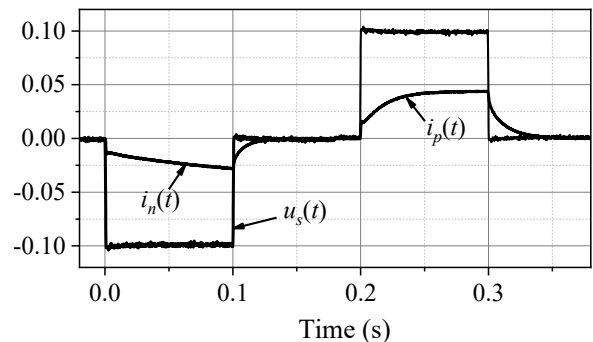
which would prove that the iron core has positive RF. If the opposite result is achieved, the iron core can be presumed to have negative RF. Finally, when $t = t_s$, the value of the negative current can be integrated using Eq. (13) to calculate the RF in the iron core.

Fig. 12 shows the voltage and respond current waveforms when the preset B_r is 0.846 T. This shows that when the positive voltage is loaded, $i_p(t)$ is generated, whereas when the negative voltage is loaded, $i_n(t)$ is generated. Fig. 13 shows the $i_p(t)$ and $i_n(t)$ at different RFs. It is evident that the change rate of $i_p(t)$ is faster than that of $i_n(t)$, as a result of which the iron core is determined to have a positive RF. This conclusion also indicates that $i_p(t)$ represents the positive RF direction and $i_n(t)$ represents the negative RF direction. Furthermore, the above analysis proves the accuracy of the theoretical analysis conducted in this paper.

As shown in Fig. 13, when the time is 0.1 seconds, the voltage is removed. At this time, the negative current was measured to calculate the RF in the iron core. Therefore, when $t_s = 0.1$ seconds, the negative current was measured and then substituted into Eq. (13) to calculate the RF in the iron core, represented as B_{r1}. In the case of PN, as shown in Fig. 13(a), when the preset RF is 0.922 T, the current value reaches 0.0311 A, with the calculated B_{r1} value being 0.929 T. Compared to the preset B_r, the relative error was found to be 0.76%. Meanwhile, in the case of NP, as shown in Fig. 13(b), when the preset B_r is 0.935 T, the calculated B_{r1} value reaches 0.946 T, with the relative error being 1.18%. This indicates that the change rate of RF is greater for NP than for PN. As a result, this paper primarily analyzed the measurement error in the case of NP.

Based on [6–8], RF is usually approximated as 0.2–0.7 times the saturation magnetic density. Since the saturated magnetic density of the iron core material selected for study in this paper was about 1.8 T, the RF detection range was determined to be 0.4 T to 1.2 T. Table 1 shows the experiment results at NP, with B_{r2} indicating the measured RF obtained using the voltage integration method [15, 16]. The relative error between the pre-
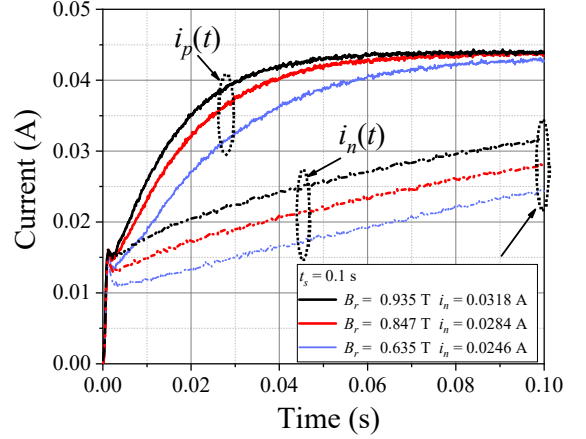

Fig. 11. The experimental platform.

Fig. 12. Waveforms of applied DC voltage and measured current when B_r is 0.846 T: (a) PN and (b) NP.
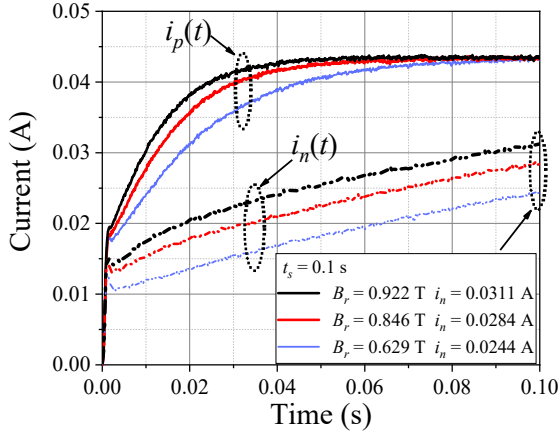
Fig. 13. Waveforms of measured currents at different residual fluxes: (a) PN and (b) NP.

Table 1. Experiment results at NP

| Preset RF (T)	i_n (A)	B_{r1} (T)	B_{r2} (T)	$\varepsilon_1\%$ (%)	$\varepsilon_2\%$ (%)
0.548	0.0229	0.569	0.494	3.87	−9.81
0.635	0.0243	0.646	0.575	1.67	−9.40
0.678	0.0251	0.686	0.619	1.14	−8.77
0.800	0.0272	0.781	0.729	−2.37	−8.88
0.847	0.0285	0.834	0.776	−1.55	−8.42
0.895	0.0298	0.883	0.821	−1.36	−8.24
0.935	0.0316	0.946	0.857	1.12	−8.35
0.961	0.0324	0.970	0.877	0.95	−8.71

set RF and B_{r1} is expressed as $\varepsilon_1\%$, while the relative error between the preset RF and B_{r2} is expressed as $\varepsilon_2\%$. The maximum $\varepsilon_1\%$ is within 5%, which is less than the $\varepsilon_2\%$ obtained using a different preset B_r. This result highlights that the accuracy of the proposed method is higher than that of the voltage integration method.

Fig. 14 presents a comparative analysis of the simulation and experimental results at different RFs. It is observed that the variation trend of the experimental results is largely the same as that of the simulation results. Furthermore, the measurement error indicated that the proposed detection method exhibits a certain feasibility. Compared to existing detection methods [15–20], the proposed method was able to not only judge the RF direction, but also accurately detect the RF value. In addition, since the RF generation mechanism is closely related to variations in the differential permeability at the RF, the differential permeability may be significantly reflected by the measured response current. Furthermore, the proposed method can be applied for RF detection in other power equipment composed of iron cores, indicating its wide applicability.

V. CONCLUSION

In this paper, an indirect RF detection method for power transformer cores is proposed based on the different polarities of
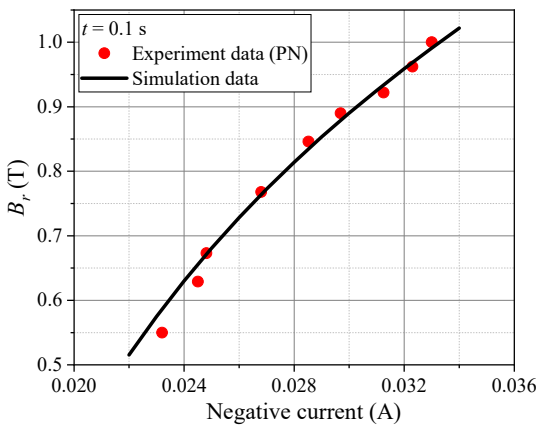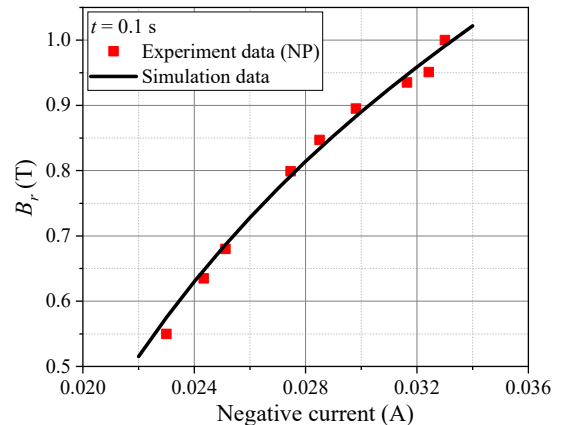
Fig. 14. Comparison of error results: (a) PN and (b) NP.

respond currents. The proposed method was able to accurately identify RF polarity and conduct a quantitative detection of the RF value. In particular, RF polarity was determined by comparing the change rates of different polarities of response currents. Furthermore, the relationship between the RF and the negative response current was constructed using the field-circuit coupling method to realize the quantitative detection of the RF value. The experimental results exhibited an accuracy that reached 5%, which is higher than the accuracy achieved by the existing methods. Notably, since transformer cores composed of different structures use different empirical formulas for RF calculation, their corresponding empirical formulas need to be extracted based on the presented method. The method proposed in this paper can also be applied to detect RF in other power equipment cores characterized by closed magnetic circuit structures.

REFERENCES

[1] Q. Liu, F. Liu, R. Zou, S. Wang, Y. Tian, Y. Wang, L. Yuan, and Y. Li, "A compact-design oriented shipboard power supply system with transformer integrated filtering method," *IEEE Transactions on Power Electronics*, vol. 37, no. 2, pp. 2089-2099, 2022. https://doi.org/10.1109/TPEL.2021.3102938

[2] G. Glazyrin, N. Mitrofanov, A. Rusina, V. Fyodorova, and A. Arestova, "Simulation of transients in an autonomous power system considering the generator and transformer magnetic core saturation," *Energy Reports*, vol. 9(Supplement 1), pp. 444-451, 2023. https://doi.org/10.1016/j.egyr.2022.11.031

[3] S. Sanati and Y. Alinejad-Beromi, "Fast and complete mitigation of residual flux in current transformers suitable for autoreclosing schemes using Jiles-Atherton modeling," *IEEE Transactions on Power Delivery*, vol. 37, no. 2, pp. 765-774, 2022. https://doi.org/10.1109/TPWRD.2021.3070075

[4] S. Afrasiabi, M. Afrasiabi, B. Parang, M. Mohammadi, H. Samet, and T. Dragicevic, "Fast GRNN-based method for distinguishing inrush currents in power transformers," *IEEE Transactions on Industrial Electronics*, vol. 69, no. 8, pp. 8501-8512, 2022. https://doi.org/10.1109/TIE.2021.3109535

[5] E. Hajipour, M. Salehizadeh, M. Vakilian, and M. Sanaye-Pasand, "Residual flux mitigation of protective current transformers used in an autoreclosing scheme," *IEEE Transactions on Power Delivery*, vol. 31, no. 4, pp. 1636-1644, 2016.

https://doi.org/10.1109/TPWRD.2015.2480773

[6] E. Colombo and G. Santagostino, "Results of the inquiries on actual network conditions when switching magnetizing and small inductive currents and on transformer and shunt reactor saturation characteristics," *Electra*, vol. 94, pp. 35-53, 1984.

[7] J. H. Brunke and K. J. Frohlich, "Elimination of transformer inrush currents by controlled switching. I. Theoretical considerations," *IEEE Transactions on Power Delivery*, vol. 16, no. 2, pp. 276-280, 2021. https://doi.org/10.1109/61.915495

[8] Y. F. Wu, H. R. Hu, W. Luo, T. Wang, and L. Ruan, "Research on no-load test of 1,000kV ultra-high voltage transformer," in *Proceedings of the 2011 Asia-Pacific Power and Energy Engineering Conference*, Wuhan, China, 2011, pp. 1-6. https://doi.org/10.1109/APPEEC.2011.5747683

[9] K. Wang, G. Li, S. Zhang, J. Li, J. Liu, X. Wu, H. Yang, and X. Hu, "Research on residual flux characteristics of transformer with single-phase four-limb core under different DC excitation current," in *Proceedings of 2020 IEEE International Conference on High Voltage Engineering and Application (ICHVE)*, Beijing, China, 2020, pp. 1-5. https://doi.org/10.1109/ICHVE49031.2020.9279826

[10] Y. Li, M. Jin, H. Li, G. Li, W. Chen, D. Chen, and J. Xie, "Study on measurement method of remanence of power transformer," *Power System Protection and Control*, vol. 47, no. 15, pp. 102-107, 2019. https://doi.org/10.7667/PSPC20191514

[11] T. Liu, X. Liu, S. Liang, J. Wang, and C. Yao, "Residual flux measuring method on the core of ferromagnetic components based on alternating polarity DC voltage source," *Transactions of China Electrotechnical Society*, vol. 32, no. 13, pp. 137-144, 2017.

[12] M. L. Hodgdon, "Applications of a theory of ferromagnetic hysteresis," *IEEE Transactions on Magnetics*, vol. 24, no. 1, pp. 218-221, 1988. https://doi.org/10.1109/20.43893

[13] D. Cavallera, V. Oiring, J. L. Coulomb, O. Chadebec, B. Caillault, and F. Zgainski, "A new method to evaluate residual flux thanks to leakage flux, application to a transformer," *IEEE Transactions on Magnetics*, vol. 50, no. 2, pp. 1005-1008, 2014. https://doi.org/10.1109/TMAG.2013.2282175

[14] C. Wei, X. Li, M. Yang, Z. Ma, and H. Hou, "Novel remanence determination for power transformers based on magnetizing inductance measurements," *Energies*, vol. 12, no. 24, article no. 4616, 2019. https://doi.org/10.3390/en12244616

[15] T. Zheng and Y. Wang, "Fast and in situ remanent flux detection method for a protection current transformer based on the fluxgate theory," *AIP Advances*, vol. 11, no. 1, article no. 015034, 2021. https://doi.org/10.1063/9.0000140

[16] D. Vulin, K. Milicevic, I. Biondic, and G. Petrovic, "Determining the residual magnetic flux value of a single-phase transformer using a minor hysteresis loop," *IEEE Transactions on Power Delivery*, vol. 36, no. 4, pp. 2066-2074, 2021.

https://doi.org/10.1109/TPWRD.2020.3019407

[17] Y. Ren, Y. Wang, C. Liu, and S. Wu, "A novel method for measuring residual flux density of the single-phase transformer core based on phase difference," *AIP Advances*, vol. 13, no. 2, article no. 025332, 2023. https://doi.org/10.1063/9.0000375

[18] S. Wu, Y. Ren, Y. Wang, C. Huo, and C. Liu, "Residual flux measurement of power transformer based on transient current difference," *IEEE Transactions on Magnetics*, vol. 58, no. 2, article no. 8400405, 2022. https://doi.org/10.1109/TMAG.2021.3082699

[19] C. Huo, Y. Wang, S. Wu, and C. Liu, "Research on residual flux density measurement for single-phase transformer core based on energy changes," *IEEE Transactions on Instrumentation and Measurement*, vol. 70, article no. 6011909, 2021. https://doi.org/10.1109/TIM.2021.3117087

[20] C. Huo, Y. Wang, S. Wu, Y. Yang, and Z. Zhao, "Residual flux density measurement method for transformer core considering relative differential permeability," *EEE Transactions on Magnetics*, vol. 57, no. 2, article no 8400204, 2021. https://doi.org/10.1109/TMAG.2020.3003658

[21] Z. Zhao, Y. Wang, and C. Huo, "Modeling of transformer ring core and residual magnetism measurement," *Electrical Measurement and Instrumentation*, vol. 60, no. 7, pp. 116-121, 2023.

Cailing Huo

https://orcid.org/0000-0001-5480-2007

received her M.E. degree in electrical engineering from Shanghai University of Electric Power, Shanghai, China, in 2015, and her Ph.D. degree in electrical engineering from Hebei University of Technology, Tianjin, China, in 2022. She is currently a lecturer at Jiangsu University of Technology, Jiangsu, China. Her research interests include the testing and elimination of remanence in transformer cores.

Fuyin Ni

https://orcid.org/0000-0003-4208-7928

received his Ph.D. degree in control engineering from Jiangsu University, Jiangsu, China. He is currently a vice professor at Jiangsu University of Technology, China. His research interests include modern power supply technology and distribution generation.

Yiming Yang

https://orcid.org/0000-0003-3181-5061

received his M.E. degree in electrical engineering from Hebei University of Technology, Tianjin, China, in 2021. He is currently a lecturer at Jiangsu University of Technology, Jiangsu, China. His research interests include magnetic materials and the measurement of soft magnetic composites.

Qiang Xie

https://orcid.org/0009-0005-2337-4456

received his M.E. degree in electrical engineering from the China University of Mining and Technology, Xuzhou, China, in 2014 and 2017. He is currently an engineer at the Changzhou Power Supply Branch of State Grid Jiangsu Electric Power Co. Ltd., where he is primarily engaged in the operation and overhaul of high-voltage cables.

Novel Design of a Bandwidth Enhanced and Frequency Reconfigurable, Wearable Antenna for Body Centric Communication

Devendra Kumar[1,*] (ID) · Dhirendra Mathur[2] (ID)

Abstract

This paper proposes a novel design for a frequency reconfigurable and bandwidth-enhanced antenna for use in biomedical telemetry applications. Data pertaining to a patient's body parameters, such as blood pressure, pulse, and temperature, are gathered using sensors and then transmitted to a remote place for monitoring. The proposed antenna is connected to a wearable transmitter, which transfers the body parameter data to a centrally located nearby control unit. The antenna operates in the 5.8 GHz band in single-band mode and in the 4.27 GHz (C band) and 5.8 GHz industrial, scientific, and medical (ISM) bands in dual-band mode. The use of ethylene-vinyl acetate foam as a substrate makes the structure waterproof and ultraviolet resistant. The basic antenna structure equipped with proximity coupling offers a front-to-back ratio (FBR) of 17.62 dB and a bandwidth of 122 MHz. With an additional upper patch and resonant slots, bandwidth enhancement of 82.85% and 11.57% improvement in the FBR are achieved, respectively. Overall, a maximum FBR of 19.66 dB and gain of 5.0 dBi are attained over the resonant frequency. The specific absorption rate is found to be 0.145 W/kg for 10 gram of tissue.

Key Words: Bandwidth, Coupling, Directivity, Radiation, SAR, Wearable.

I. INTRODUCTION

Microstrip patch antennas—widely used due to their low profile, compact size, and conformal design—are highly suitable for wearable applications, such as patient monitoring, sports activities, security, and firefighting. In patient monitoring applications, transmission and reception involving high data rates are necessary for various on-body/off-body devices. However, since microstrip antennas usually have a narrow bandwidth, they are insufficient for use in such wearable applications. Nonetheless, various techniques for bandwidth enhancement have been pro-posed in the literature. For instance, the use of a double U-shaped defective ground structure [1], folded defects [2], and L-shaped defects [3] have all been proposed for bandwidth improvement. Furthermore, stripline and L-shaped probes have been used to feed multilayer structures [4]. Some studies have also employed sequential phase feeding methods for bandwidth enhancement [5, 6]. In addition, using capacitive coupling with a small disc on top offered improvements in bandwidth in [7], while introducing multiple slots on a patch close to the resonant frequency also had the same effect [8, 9]. Similarly, implementing two parasitic patches in the annular area helped improve

bandwidth [10], and so did a coplanar waveguide-fed antenna using modified ground [11]. Other proposed methods for bandwidth improvement include using a vertical coupling-based method with modified ground [12], and employing the dual resonance method using ethylene-vinyl acetate (EVA) foam as substrate [13]. Furthermore, the literature has attempted to improve antenna performance by experimenting with different substrate materials created using EVA foam and plastic polymers [14]. In addition, different techniques for realizing multi-band operations have been explored, such as employing two stacked patches operating at two different frequencies [15], using three independent radiators that are switched using PIN diodes to operate at 1.575 GHz for global positioning systems (GPS) and at the 2.45 GHz and 5.2 GHz industrial, scientific, and medical (ISM) bands [16], and implementing a loop inspired dual/triple band operation that uses switching by PIN diodes for the 4G, 5G, and X bands [17]. In modern wireless applications, the use of reconfigurable antennas is preferred due to their ability to radiate more than one pattern at different frequencies and polarizations. For instance, [18] reported frequency and polarization reconfiguration using PIN switching diodes for L1, worldwide interoperability for microwave access (WiMAX), wireless local area network, and mobile bands. Frequency reconfiguration for multi-bands using microelectromechanical system (MEMS) switches has also been demonstrated in [19, 20]. A liquid dielectric-controlled polarization reconfigurable antenna for radio frequency identification has been proposed in [21], while stub switching by employing PIN diodes has been recommended for frequency reconfigurability in [22]. In addition, a frequency reconfigurable planar inverted-F antenna for GSM 850/900 and UMTS 2100 was presented in [23].

In this work, stacked layers and multiple slots near the resonant frequency are combined to improve the bandwidth of a wearable antenna. The upper patch bearing resonant slots provides the desired bandwidth enhancement. Moreover, low-cost flexible EVA foam material is used as the substrate and copper tape is used as the patch, while frequency reconfigurability is incorporated using a PIN diode. Finally, the antenna structure was tested and validated for wearable applications using an equivalent human body model.

II. ANTENNA DESIGN

The dimensions of the proposed antenna were calculated using standard Eqs. (1)–(3) for microstrip design [24], as noted below:

$$W = \frac{c}{2f_o\sqrt{\frac{\varepsilon_r + 1}{2}}}, \tag{1}$$

$$\varepsilon_{eff} = \frac{\varepsilon_r + 1}{2} + \frac{\varepsilon_r - 1}{2}\left[\frac{1}{\sqrt{1 + 12\left(\frac{h}{w}\right)}}\right], \tag{2}$$

$$L = \frac{c}{2f_o\sqrt{\varepsilon_{eff}}} - 0.824h\left[\frac{(\varepsilon_{eff} + 0.3)\left(\frac{w}{h} + 0.264\right)}{(\varepsilon_{eff} + 0.258)\left(\frac{w}{h} + 0.8\right)}\right], \tag{3}$$

where W is the width of the antenna, L is its length, ε_r indicates the relative permittivity of the substrate, ε_{eff} refers to the effective permittivity, h is the thickness of the substrate, f_o denotes the resonant frequency, and c is the velocity of light.

Notably, the antenna was simulated using the CST Microwave Studio. Its ground plane, created using copper material, had dimensions of 62 mm × 58 mm × 0.05 mm, while the substrate material was EVA foam having a relative permittivity of 1.2, loss tangent of 0.02, and size of 62 mm × 58 mm × 1.65 mm. The patch consisted of a copper tape of size 24.64 mm × 21.33 mm × 0.05 mm. A slot of size 8 mm × 11.66 mm was cut into the patch. Furthermore, a feed line of size 15.3 mm × 3 mm was used to excite the patch. The spacing between the feed and the patch was optimized to 2.5 mm on the left and right sides and 1.7 mm on the top of the feed. The basic antenna design is presented in Fig. 1.

III. EVOLUTION OF ANTENNA DESIGN

The EVA foam substrate (thickness = 1.65 mm) was chosen for the proposed antenna because it is flexible and suitable for wearable applications, owing to its electrical and mechanical properties. First, the basic antenna with an EVA foam substrate of height 1.75 mm was designed for the 5.8 GHz frequency band. Energy was fed into the patch as coupling by the feed line. However, the bandwidth obtained at this frequency was 122 MHz, which is narrow and insufficient for high data rate transmission/reception. Therefore, for bandwidth enhancement,
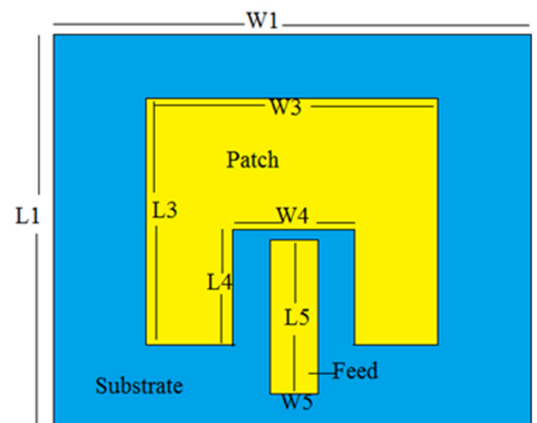

Fig. 1. Geometry of a basic antenna.

another patch was placed onto the first patch. As shown in Fig. 2(a), an upper patch of size 23 mm × 20 mm × 0.05 mm is placed at a height of 8.25 mm from the first patch, with air being the dielectric in the gap. Notably, since the thickness of the upper patch was 0.05 mm, it was difficult to suspend it in air and keep it parallel to the lower patch. Therefore, expanded polyurethane foam with a relative permittivity of $\varepsilon_r = 1$ was used in the air gap to support the upper patch. Consequently, the bandwidth increased to 203 MHz. Furthermore, two slots of equal size (4 mm × 4 mm) were created at the center of the upper patch, as shown in Fig. 2(b), with the spacing between them being 9 mm. The size of the slots and the upper patch were optimized to attain an enhanced bandwidth. Due to the creation of slots on the upper patch, the overall bandwidth in-creased to 223 MHz at a resonant frequency of 5.8 GHz. The flowchart of the entire fabrication process is shown in Fig. 2(c), and the antenna dimensions are noted in Table 1.

IV. RESULTS AND DISCUSSION

1. Antenna without Upper Patch

First, the antenna created using only the first layer of the patch, as shown in Fig. 1, was simulated. The obtained antenna parameters, along with proximity coupling, were $S_{11} = -45$ dB at 5.8 GHz, bandwidth = 122 MHz, directivity = 8.9 dBi in the broadside direction, side lobe level = −14.3 dB, half power beam width (HPBW) = 67.7°, front-to-back ratio = 17.62 dB, and maximum gain over frequency = 4.78 dBi.
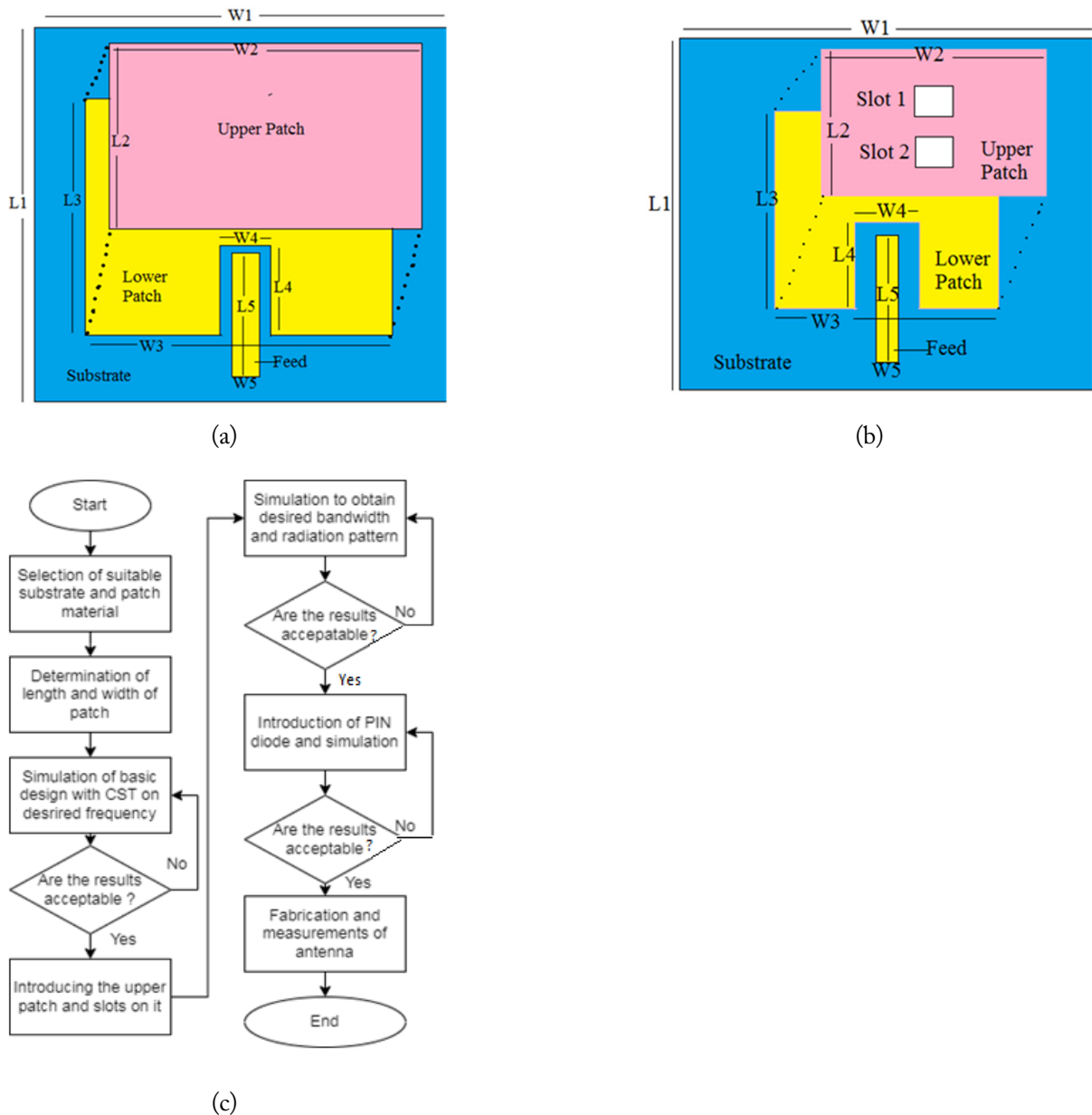

Fig. 2. Geometry of the antenna structure: (a) antenna with upper patch, (b) antenna with slots in the upper patch, and (c) flowchart of the design.

Table 1. Antenna dimensions (unit: mm)

Structure	Length	Width	Thickness
Ground plane	$L_1 = 58$	$W_1 = 62$	0.05
Substrate	$L_1 = 58$	$W_1 = 62$	1.65
Lower patch	$L_3 = 21.33$	$W_3 = 24.64$	0.05
Patch slot	$L_4 = 11.66$	$W_4 = 8$	–
Feed	$L_5 = 15.3$	$W_5 = 3$	0.05
Upper patch	$L_2 = 20$	$W_2 = 23$	0.05
Slots on upper patch	4	4	–

2. Antenna with Upper Patch

To achieve further enhancement in bandwidth, modifications were implemented on the upper patch. Two slots were added to the upper patch, and their locations were optimized to help widen the bandwidth. The parameters obtained for this antenna were $S_{11} = -29$ dB at 5.8 GHz, bandwidth = 223 MHz, far-field directivity = 9.32 dBi, sidelobe level = -13.1 dB, HPBW = 58.7°, maximum gain over frequency = 5.0 dBi, and front-to-back ratio = 19.66 dB. A comparison of the simulated S_{11}, directivity, and gain for all three stages of antenna evolution (basic patch, incorporation of the upper patch, and slots) is illustrated in Fig. 3(a), 3(b), and 3(c), respectively. Notably, a minor tilt in the radiation pattern of the antenna was observed when the upper patch was introduced over the lower patch. This can be attributed to the phase difference between the waves radiated from the two patches—the path length between both patches created the phase difference. The related parameter values are summarized in Table 2. As shown in Fig. 3(d), the bandwidth of the antenna without slots on its upper patch is 203 MHz. Subsequently, upon adding slots onto the upper patch, the bandwidth increased to 223 MHz, as shown in Fig. 3(e).

Measurements were performed using N-5247A vector network analyzer (VNA) from Agilent Technology, the results of which were in good agreement with the simulation results. A comparison of the simulated and measured S_{11} and gain on a single band is shown in Fig. 4(a) and 4(b), respectively. The simulated S_{11} is -29 dB at the center frequency, while the polar gain pattern shows that most of the radiation occurs in the broadside direction, with very low radiation in the backward direction, showing a low level of sidelobes. This type of directional radiation pattern is best suited for body-centric communication. The curves depicted in Fig. 4(c) show simulated directivity of 9.32 dBi, gain from 5.0 dBi to 7.1 dBi, and radiation efficiency from -2.0 dB to -1.5 dB in the operating band. A photograph of the fabricated antenna is presented in Fig. 5. An equivalent electrical circuit diagram of the geometry shown in Fig. 2(b), created using ADS software, is presented in Fig. 6(a). The pass band signifies S_{11} responses below -10 dB at the resonant frequency, while the stop bands signify responses above -10 dB.

To obtain the values of lumped components, first the quality factor was calculated using the bandwidth and resonance frequency. Subsequently, the values of the lumped components were calculated based on basic electrical theory. Notably, the calculated component values satisfied the 5.8 GHz resonant frequency. Furthermore, the S_{11} data generated by CST software were simulated using ADS software to compare the S_{11} values, as shown in Fig. 6(b). It is observed that the S_{11} results produced by ADS are similar to those produced by CST, showing an error of 0.5% in the bandwidth. Therefore, using ADS software, the proposed design was successfully validated.

3. Frequency Reconfigurability

A simple and widely used technique for achieving frequency reconfigurability involves the use of PIN diodes to switch antenna geometry patterns. As shown in Fig. 7(a), a PIN diode is placed between the left edge of the feed line and the patch. The diode can be switched ON/OFF through appropriate biasing, as shown in Table 3. Therefore, when the diode is reverse-biased (Mode-1), the feed line is not directly connected to the patch, and energy is fed as a coupling. The antenna resonates at 5.8 GHz frequency to attain an enhanced bandwidth of 223 MHz. When the diode is forward-biased (Mode-2), the feed line is directly connected to the patch on the left side. The structure is then reconfigured, and the antenna carries out dual-band operations at both the 4.27 GHz and 5.8 GHz frequencies simultaneously.

The PIN diode BAR 64-03W E6327 from Infineon Technology was used in this study. The specifications of this PIN diode are as follows: forward voltage = 0.8–1.1 V, forward current = 10–100 mA, forward resistance = 2.1Ω, reverse-biased capacitance = 0.20 pF, and reverse biased resistance = 3.4 kΩ. The simulated and measured S_{11} in the dual band is presented in Fig. 7(b). The bandwidth attained in the single band (Diode OFF) mode was 223 MHz (5.651–5.874 GHz) at the resonant frequency of 5.8 GHz. In ON mode, the antenna exhibited dual band characteristics, attaining a bandwidth of 110 MHz (4.210–4.320 GHz) at 4.27 GHz (WBAN) and a bandwidth of 105 MHz (5.760–5.865 GHz) at 5.8 GHz (ISM). Although the antenna was primarily designed for the 5.8 GHz band for biomedical applications, the reconfiguration mode enabled an additional band at 4.27 GHz while maintaining the original band at 5.8 GHz with 50% bandwidth. Such dual-band characteristics are useful for short-range communication, since bandwidths of 20/40/80/160 MHz are also adopted for body area network applications. Fig. 7(c) shows that the radiation efficiency is -2.3 dB at 4.27 GHz and -5.0 dB at 5.8 GHz in dual band mode. Furthermore, the VNA measurement setup is shown in Fig. 7(d), while the diode equivalent diagram is presented in Fig. 8. In the forward-biased condition, a resistance of 2.1 Ω and inductance of 1.8 nH formed a series circuit. In reverse-biased conditions, a
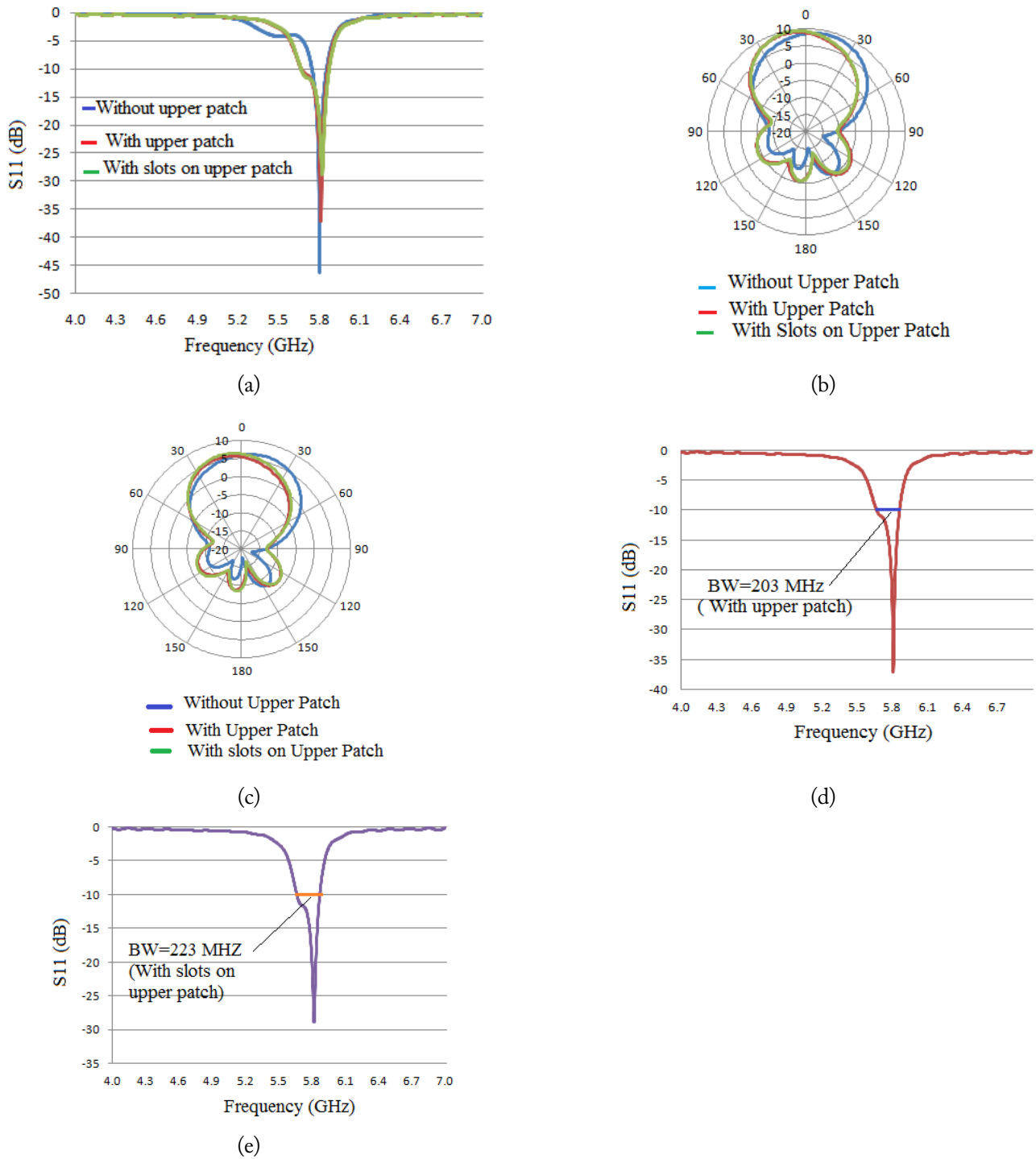
Fig. 3. Antenna parameters: (a) S_{11} (dB), (b) directivity (dBi), (c) gain (dBi), (d) bandwidth with upper patch, and (e) bandwidth with slots on the upper patch.

capacitance of 0.2 pF and resistance of 3.4 kΩ formed a shunt circuit. The phase curves in Fig. 9(a) show that the phase is zero at both resonant frequencies. The Z_{11} (impedance) curve in Fig. 9(b) indicates that the input impedance of the antenna is 51.3 Ω at 4.27 GHz and 5.8 GHz resonant frequencies, which is close to the reference impedance of 50 Ω. The current distribution in the dual-band operation of both patches is shown in Fig. 9(c). The simulated and measured radiation patterns at the dual band frequencies are depicted in Fig. 9(d) and 9(e).

4. Effects of Feed Width Variation

The effects of variations in the width of the feed line on antenna performance are depicted in Fig. 10. It is evident that an increase in the width of the feed line leads to an increase in the gain of the antenna, while the resonant frequency remains constant up to a certain width and then increases sharply. Meanwhile, the directivity increases, exhibiting only slight variations, and the front-to-back ratio remains almost constant, with very slight variations.
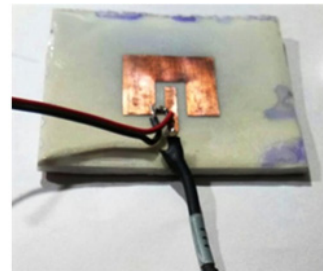
Table 2. Antenna parameters

Antenna parameter	Antenna without upper patch	Antenna with slots on the upper patch
Front-to-back ratio	17.46	19.66
S_{11} (dB)	−45	−29
Gain (dBi)	4.78	5.0
Bandwidth (MHz)	122	223
Directivity (dBi)	8.9	9.32
Sidelobe level (dB)	−14.3	−13.1

## 5. Effects of Ground Plane Size Variation

The results of the simulations conducted on the antenna using different ground plane sizes are shown in Fig. 11. As the ground plane size increases, the bandwidth remains constant, exhibiting only minor variations of 0.86 MHz. Furthermore, the resonant frequency increases to reach a maximum of 10 MHz from 5.8 GHz. Directivity increases at a faster rate initially, but remains almost constant as the ground plane size increases.

A comparison of the current work with previous related research is presented in Table 4, showing the values achieved by each proposed antenna in terms of antenna size, frequency, bandwidth, gain, material, and application in the wireless body area network. Among the reported works, some antenna structures are large, with complex array designs that are able to attain a low percentage of bandwidth enhancement. In contrast, the proposed work achieved a high percentage of bandwidth enhancement and substantial gain using a simple design that is small in size and involves a low-cost, flexible substrate.
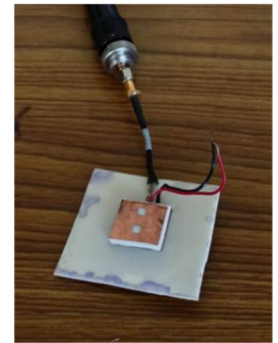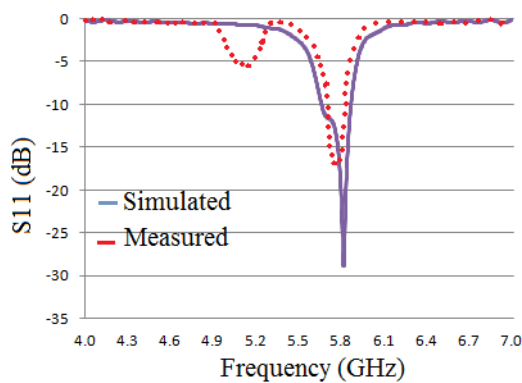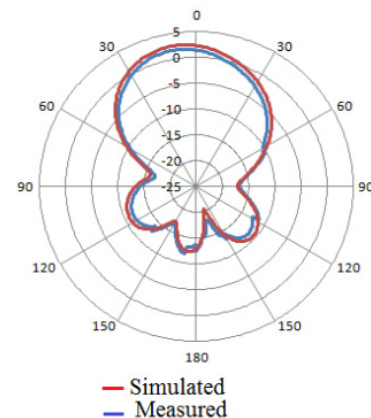

(a)   (b)
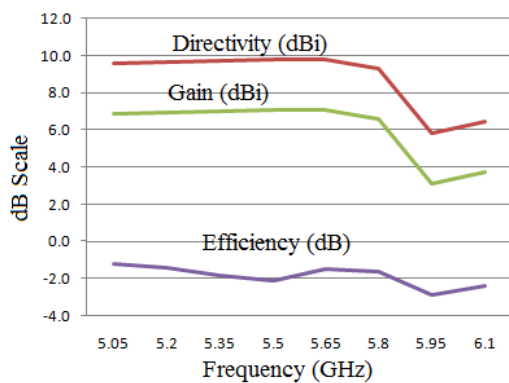
Fig. 5. The fabricated antenna: (a) without upper patch and (b) with upper patch.

(a)

(b)

(c)

Fig. 4. Antenna parameters: (a) simulated and measured S_{11} on single band, (b) polar plot of the simulated and measured gains, and (c) simulated directivity (dBi), gain (dBi), and radiation efficiency (dB).

(a)

(b)
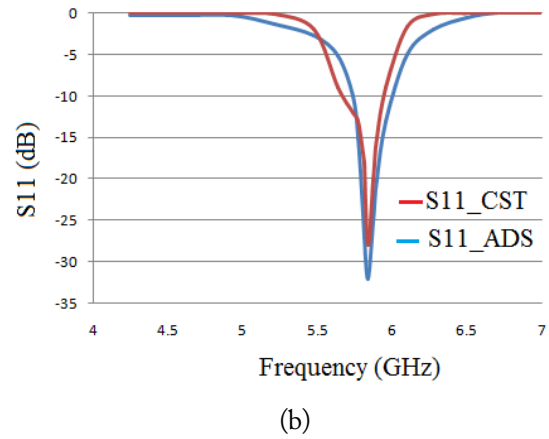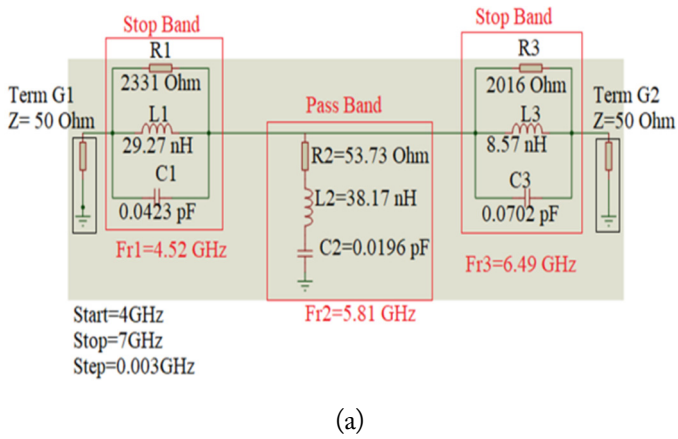
Fig. 6. (a) Equivalent circuit, and (b) comparison of S_{11} between CST and ADS.

(a)

(b)

(c)

(d)
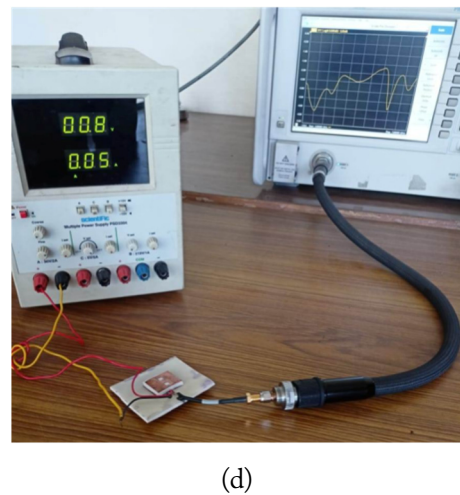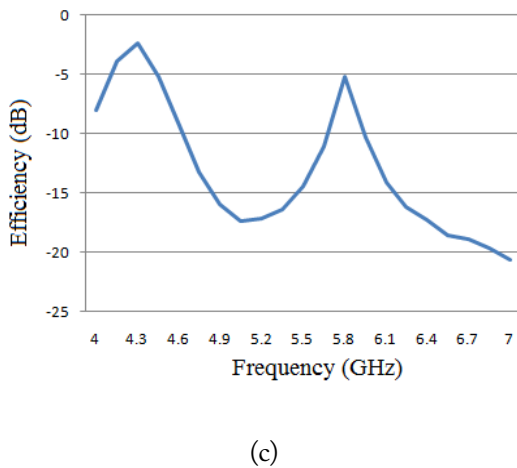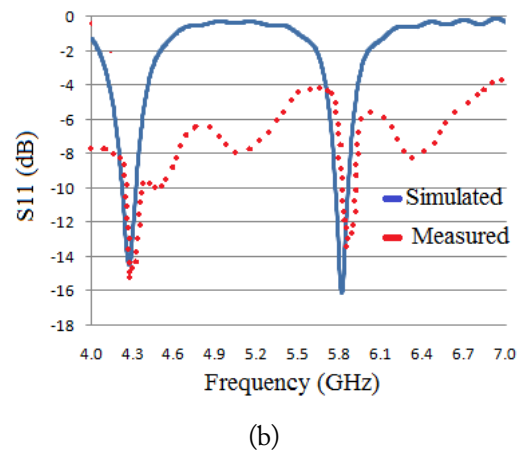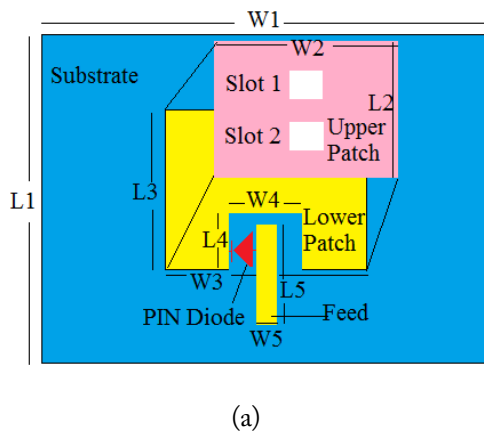
Fig. 7. (a) PIN diode connection, (b) simulated and measured S_{11} in the dual band mode, (c) radiation efficiency in the dual band mode, and (d) VNA measurement setup.

V. SAR Calculation

A wearable antenna is usually used along with on-body devices, which are responsible for establishing communication between the on-body and off-body devices for patient data transmission. For this kind of communication, the radiation pattern must be directional and propagate away from the body. Moreo-

ver, radiation directed toward the body is hazardous and, therefore, must be minimized. The simulated 3-dimensional radiation depicted in Fig. 12(a) shows that the radiated field is in the broadside direction, while minimal radiation is present in the back direction toward the body. Furthermore, to calculate the specific absorption rate (SAR), an equivalent human body model of size 94 mm × 90 mm × 70 mm was considered, as shown in

Table 3. Frequency switching

Mode of operation	State of diode	Resonant frequency (GHz)	S_{11} (dB)	
			Simulated	Measured
Mode-1	OFF	5.80	−29.0	−17.0
Mode-2	ON	4.27	−14.5	−16.0
		5.80	−16.0	−14.0

Fig. 8. Diode equivalent diagram: (a) ON state and (b) OFF state.

(a)

(b)

(c)
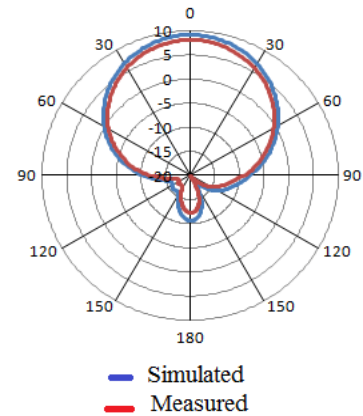
(d)
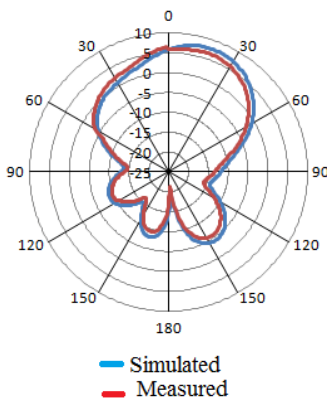
(e)

Fig. 9. Dual band parameters: (a) phase curve, (b) impedance curve, (c) current distribution over patches, (d) radiation pattern at 4.27 GHz, and (e) radiation pattern at 5.8 GHz.
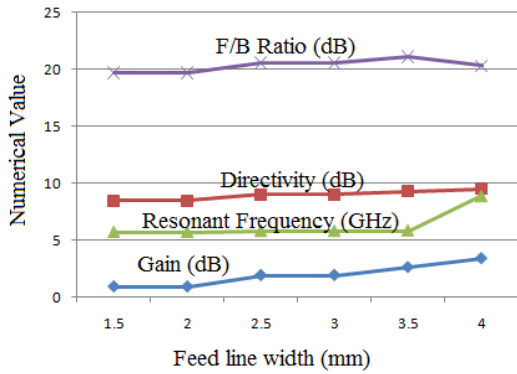
Fig. 10. Effects of feed width variation.
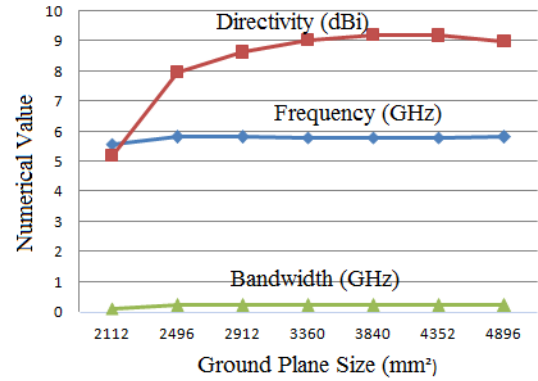
Fig. 11. Effects of ground plane size variation.

Table 4. Comparative study with past research

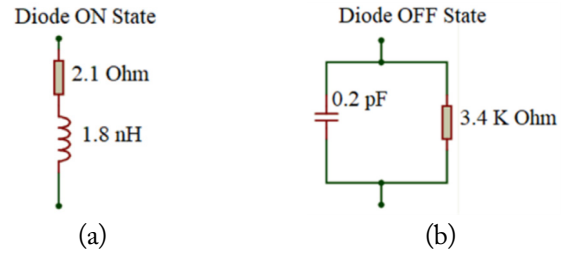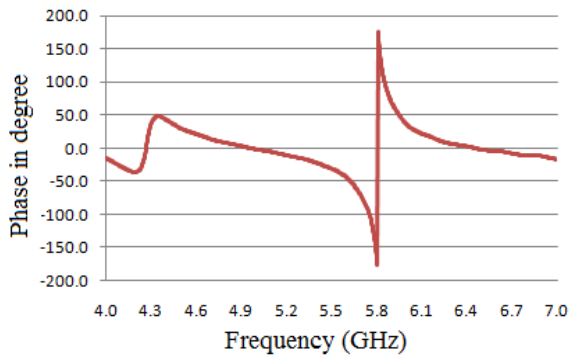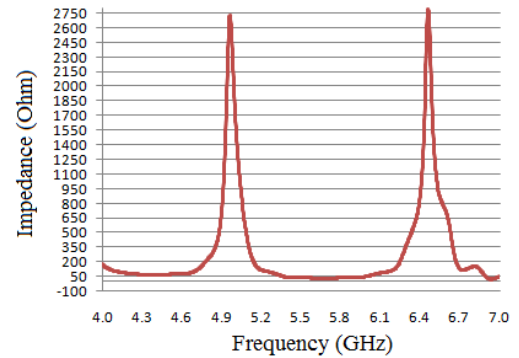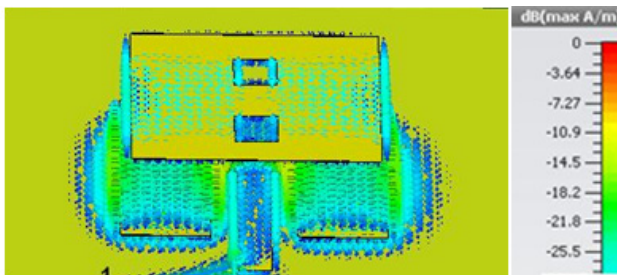| Study	Antenna size, l × b × h (mm)	Resonant frequency (GHz)	Enhancement of bandwidth (%)	Gain (dBi)	Material of substrate	Application bands
Chiang and Tam [1]	98.1 × 60.4 × 15.7	0.790–2.060	112	–	RO4003	GSM
Kumar and Guha [2]	60 × 60 × 1.575	10.00	22	6.9	RT/duroid 5870	–
Chakraborty et al. [3]	17.4 × 14.4 × 1 4 × 4 array	53–71	29	17.1	LTCC	–
Wang et al. [4]	95.54 × 95.54 × 1.89 2 × 2 array	5.2–6.3	12.7	12	Teflon	ISM
Deng et al. [5]	50 × 50 × 1.524 3 × 3 array	5.13–6.24	12.9	9.8	Rogers 5880	ISM
Wu et al. [7]	40 × 40 × 1.6	2.45	6.26	5.32	FR4	ISM
Luzon and Gerasta [8]	80 × 55 × 1.6	1.6	70.8	2.0	FR4	GPS
Munir et al. [9]	150 × 150 × 1.6	3.06	6	2.7	FR4	–
Mao et al [12]	34 × 34 × 1.6	1.8/3.5/5.2/5.8	–	1.7–4.4	FR4	GSM/ISM
Wang et al. [13]	250 × 250 × 8	0.430	5.2	4.36	EVA Foam	–
Sung [15]	50 × 50 × 0.8	2.45/4.27	14.35	3.17/3.83	FR4	ISM
Kanagasabai et al. [16]	26 × 25 × 0.2	1.575/2.45/5.2	1.83–3.17	3.6–4.04	Rogers RO4003	ISM
Rasool et al. [17]	50 × 55 × 1.6	2.21/3.42/4.85/8.02/10.19	–	4.09	FR4	4G, 5G, and X
George and Lili [18]	40 × 40 × 2.5	1.6/2.4/2.5	2.4–3.2	1.96–5.2	Rogers 6010LM	L1/WiMAX/ Sat Com
Hassan et al. [19]	32 × 98 × 1	0.6/1.8/2.4/3.5/5.5	–	5.14	FR4	GSM/ISM/ WiMAX
This work	62 × 58 × 10	4.27/5.8	82.85	5.0–7.1	EVA foam	C and ISM

Fig. 12(b). The thickness of the skin, fat, and muscle layers was 3 mm, 7 mm, and 60 mm, respectively. The dimensions and electrical parameters of the cubic human body model are noted in Table 5 [25]. The antenna was kept 2 mm away from the body model to provide space for wearable clothes. The calculated re-

sults presented in Fig. 12(c) show that the SAR value is 0.145 W/kg for 10 gram of tissue, which is well within the limits of the SAR value (2 W/kg for 10 gram tissue) prescribed by the Federal Communications Commission and the International Commission on Non-Ionizing Radiation Protection [26, 27].

(a)

(b)

(c)
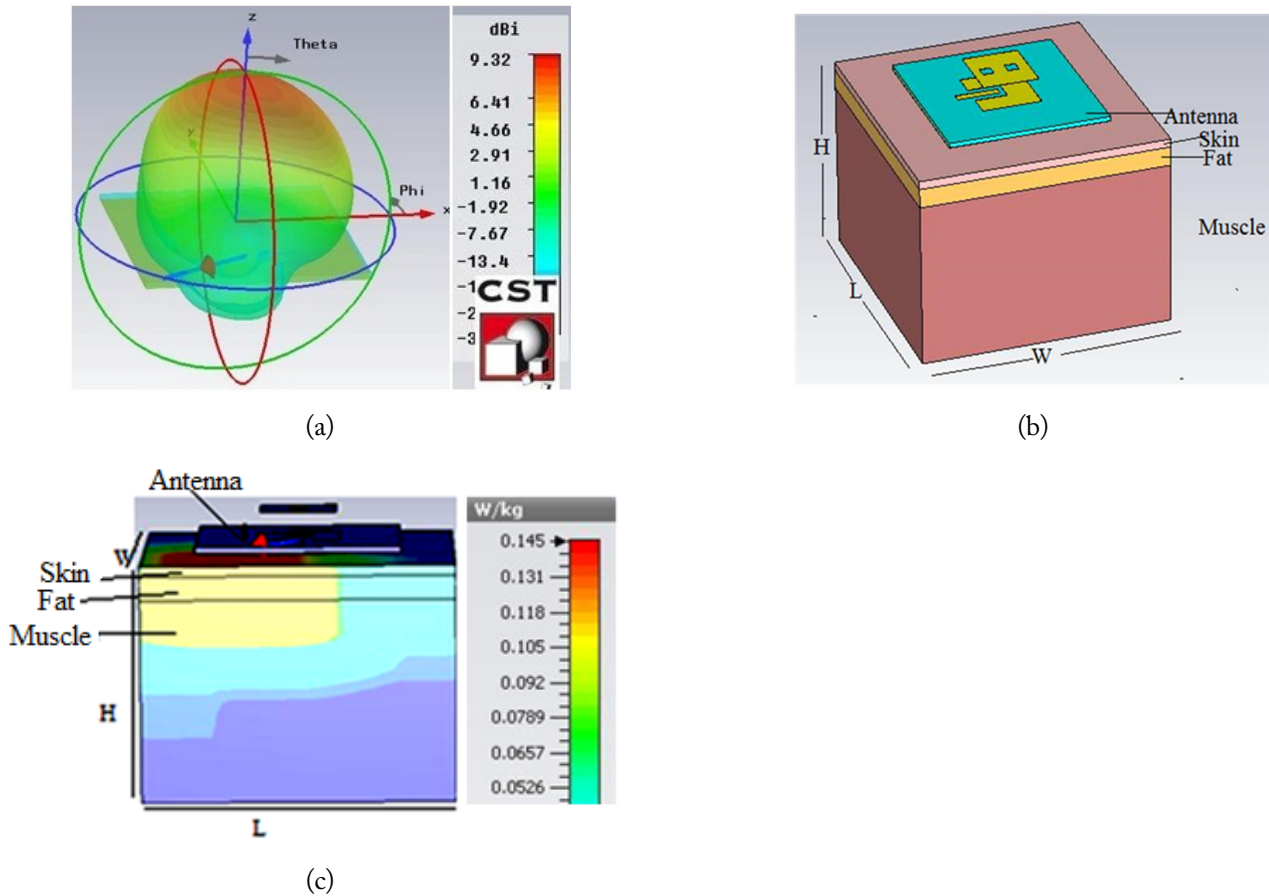
Fig. 12. A 3D radiation and SAR calculation: (a) structure of the transparent 3D radiation pattern, (b) equivalent human body model, and (c) on-body measurement.

Table 5. Dimensions/electrical parameters of the equivalent human body model

Dimensions/electrical parameter	Skin	Fat	Muscle
Length, L (mm)	94	94	94
Width, W (mm)	90	90	90
Height, H (mm)	3	7	60
Relative permittivity	35	4.9	48.5
Conductivity (S/m)	3.7	0.2	4.9
Mass density (kg/m³)	1,090	930	1,050

Furthermore, the back radiation was calculated in accordance with Eq. (4) as the ratio of the radiated power in the back hemisphere from the antenna to the total radiated power, which can be expressed as follows:

$$\text{Back radiation (\%)} = \frac{\int_0^{2\pi}\int_{\pi/2}^{\pi}|E|^2\sin\theta\,d\theta\,d\phi}{\int_0^{2\pi}\int_0^{\pi}|E|^2\sin\theta\,d\theta\,d\phi} \times 100. \quad (4)$$

Here, E is the electric field, θ is a variation of the angle of the electric field in the vertical plane, and ϕ is a variation of the angle of the electric field in the horizontal plane.

VI. BENDING EFFECTS

An equivalent cylindrical structure that accounts for the air gap and the skin layer of the body was created, as shown in Fig. 13(a). The outer cylinder with 2 mm thickness represents the air gap, while the inner cylinder with 3 mm thickness represents the skin layer. The bending effects of the antenna were studied by placing it on the surface of the cylinders with different radii. The results of S_{11} based on the different radii are shown in Fig. 13(b). It was observed that the resonant frequency of the antenna drifted toward the higher side, while the return loss became poorer, as the radius (R) of the cylinder increased. However, no significant effect on the radiation pattern and efficiency of the antenna was observed due to bending.

VII. CONCLUSION

This work proposes a simple design for a low-cost frequency reconfigurable dual-band antenna that can be used to establish wireless connectivity between on-body and off-body devices, enabling data transmission from the patient's body to other remote monitoring places. Substantial gain, bandwidth, and directional radiation patterns are the primary requirements of
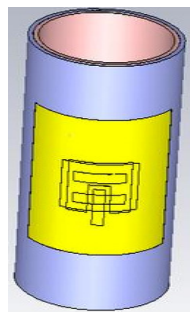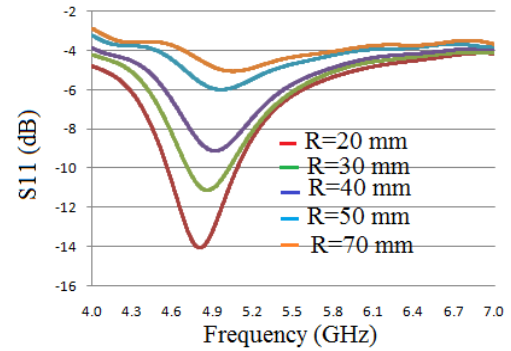
(a) (b)

Fig. 13. Bending effects: (a) cylinder mimicking the air gap and skin layer of the body and (b) S_{11} at different radii.

high-rate data transmissions in biomedical telemetry. Exhibiting enhanced bandwidth and directional radiation, the proposed antenna met all these requirements. Furthermore, the antenna achieved low back radiation toward the body, a high front-to-back ratio, and a very low SAR value, all of which are highly desired parameters for wearable applications. A parametric study was conducted to understand the effects of variation in dimension on the parameters of an antenna. The physical properties of the EVA foam substrate and the stability of the antenna parameters, such as resonant frequency, bandwidth, directivity, and front-to-back ratio, under body loading conditions make it suitable for telemetry applications.

REFERENCES

[1] K. H. Chiang and K. W. Tam, "Microstrip monopole antenna with enhanced bandwidth using defected ground structure," *IEEE Antennas and Wireless Propagation Letters*, vol. 7, pp. 532-535, 2008. https://doi.org/10.1109/LAWP.2008.2005592

[2] C. Kumar and D. Guha, "Defected ground structure (DGS)-integrated rectangular microstrip patch for improved polarisation purity with wide impedance bandwidth," *IET Microwaves, Antennas & Propagation*, vol. 8, no. 8, pp. 589-596, 2014. https://doi.org/10.1049/iet-map.2013.0567

[3] S. Chakraborty, D. Dutta, P. Ghosh, N. Giri, N. Agarwal, M. Gangopadhyay, and M. Chakraborty, "Frequency tuning characteristics & bandwidth enhancement for circular microstrip antenna by integrating L shaped DGS," in *Proceedings of 2020 IEEE International IOT, Electronics and Mechatronics Conference (IEMTRONICS)*, Vancouver, Canada, 2020, pp. 1-7. https://doi.org/10.1109/IEMTRONICS51293.2020.9216423

[4] L. Wang, Y. X. Guo, and W. X. Sheng, "Wideband high-gain 60-GHz LTCC L-probe patch antenna array with a soft surface," *IEEE Transactions on Antennas and Propagation*, vol. 61, no. 4, pp. 1802-1809, 2013. https://doi.org/10.1109/TAP.2012.2220331

[5] C. Deng, Y. Li, Z. Zhang, and Z. Feng, "A wideband sequential-phase fed circularly polarized patch array," *IEEE Transactions on Antennas and Propagation*, vol. 62, no. 7, pp. 3890-3893, 2014. https://doi.org/10.1109/TAP.2014.2321380

[6] K. Ding, C. Gao, D. Qu, and Q. Yin, "Compact broadband circularly polarized antenna with parasitic patches," *IEEE Transactions on Antennas and Propagation*, vol. 65, no. 9, pp. 4854-4857, 2017. https://doi.org/10.1109/TAP.2017.2723938

[7] J. Wu, Y. Yin, Z. Wang, and R. Lian, "Broadband circularly polarized patch antenna with parasitic strips," *IEEE Antennas and Wireless Propagation Letters*, vol. 14, pp. 559-562, 2014. https://doi.org/10.1109/LAWP.2014.2373823

[8] M. A. Luzon and O. J. Gerasta, "Slotted circular polarized rectangular microstrip patch antenna with enhanced bandwidth for wireless communication in 2.45 GHz," in *Proceedings of 2018 IEEE 10th International Conference on Humanoid, Nanotechnology, Information Technology, Communication and Control, Environment and Management (HNICEM)*, Baguio City, Philippines, 2018, pp. 1-6. https://doi.org/10.1109/HNICEM.2018.8666349

[9] A. Munir, G. Petrus, and H. Nusantara, "Multiple slots technique for bandwidth enhancement of microstrip rectangular patch antenna," in *Proceedings of 2013 International Conference on QiR*, Yogyakarta, Indonesia, 2013, pp. 150-154. https://doi.org/10.1109/QiR.2013.6632555

[10] J. F. Lin and Q. X. Chu, "Enhancing bandwidth of CP microstrip antenna by using parasitic patches in annular sector shapes to control electric field components," *IEEE Antennas and Wireless Propagation Letters*, vol. 17, no. 5, pp. 924-927, 2018. https://doi.org/10.1109/LAWP.2018.2825236

[11] T. Li, F. S. Zhang, F. Gao, and Y. L. Guo, "CPW-fed circularly polarized square slot antenna with enhanced bandwidth and reduced size for wideband wireless applications," *Progress In Electromagnetics Research C*, vol. 65, pp. 121-129, 2016. https://doi.org/10.2528/PIERC16050905

[12] C. X. Mao, S. S. Gao, Y. Wang, and J. T. S. Sumantyo, "Compact broadband dual-sense circularly polarized microstrip antenna/array with enhanced isolation," *IEEE Transactions on Antennas and Propagation*, vol. 65, no. 12, pp. 7073-7082,

2017. https://doi.org/10.1109/TAP.2017.2766440

[13] H. Wang, Z. Zhang, Y. Li, and Z. Feng, "A dual-resonant shorted patch antenna for wearable application in 430 MHz band," *IEEE Transactions on Antennas and Propagation*, vol. 61, no. 12, pp. 6195-6200, 2013. https://doi.org/10.1109/TAP.2013.2282044

[14] I. Gil and X. Colom, "Antennas based on low-cost thermoplastic polymer substrates for communication in the industrial, scientific and medical radio band," *Journal of Electromagnetic Waves and Applications*, vol. 33, no. 11, pp. 1486-1502, 2019. https://doi.org/10.1080/09205071.2019.1614485

[15] Y. Sung, "Wideband circularly polarized antenna for dual-band operation," *Microwave and Optical Technology Letters*, vol. 63, no. 1, pp. 286-294, 2021. https://doi.org/10.1002/mop.32576

[16] M. Kanagasabai, P. Sambandam, G. N. A. Mohammed, N. M. Dinesh, M. S. Morais, A. Viswanathan, S. K. Palaniswamy, and A. Shrivastav, "On the design of frequency reconfigurable tri-band miniaturized antenna for WBAN applications," *AEU-International Journal of Electronics and Communications*, vol. 127, article no. 153450, 2020. https://doi.org/10.1016/j.aeue.2020.153450

[17] M. Rasool, A. Khan, F. Bhatti, B. Ijaz, and A. Iftikhar, "A compact circular loop inspired frequency and bandwidth reconfigurable antenna for 4G, 5G, and X-band applications," Radioengineering, vol. 29, no. 3, pp. 471-478, 2020. https://doi.org/10.13164/re.2020.0471

[18] U. George and F. Lili, "A simple frequency and polarization reconfigurable antenna," *Electromagnetics*, vol. 40, no. 6, pp. 435-444, 2020. https://doi.org/10.1080/02726343.2020.1811940

[19] M. M. Hassan, Z. Zahid, A. A. Khan, I. Rashid, A. Rauf, M. Maqsood, and F. A. Bhatti, "Two element MIMO antenna with frequency reconfigurable characteristics utilizing RF MEMS for 5G applications," *Journal of Electromagnetic Waves and Applications*, vol. 34, no. 9, pp. 1210-1224, 2020. https://doi.org/10.1080/09205071.2020.1765883

[20] B. V. S. Sailaja and K. K. Naik, "CPW-fed elliptical shaped patch antenna with RF switches for wireless applications," *Microelectronics Journal*, vol. 111, article no. 105019, 2021. https://doi.org/10.1016/j.mejo.2021.105019

[21] Z. Chen, H. Z. Li, H. Wong, X. Zhang, and T. Yuan, "A circularly-polarized-reconfigurable patch antenna with liquid dielectric," *IEEE Open Journal of Antennas and Propagation*, vol. 2, pp. 396-401, 2021. https://doi.org/10.1109/OJAP.2021.3064996

[22] W. A. Awan, S. I. Naqvi, W. A. E. Ali, N. Hussain, A. Iqbal, H. H. Tran, M. Alibakhshikenari, and E. Limiti, "Design and realization of a frequency reconfigurable antenna with wide, dual, and single-band operations for compact sized wireless applications," *Electronics*, vol. 10, no. 11, article no. 1321, 2021. https://doi.org/10.3390/electronics10111321

[23] A. Ghaffar, A. Altaf, A. Aneja, X. J. Li, S. Khan, N. Alibakhshikenari, F. Flalcone, and E. Limiti, "A frequency reconfigurable compact planar inverted-F antenna for portable devices," *International Journal of Antennas and Propagation*, vol. 2022, article no. 7239608, 2022. https://doi.org/10.1155/2022/7239608

[24] C. A. Balanis, *Antenna Theory: Analysis and Design*, 3rd ed. Hoboken, NJ: John Wiley & Sons, 2005.

[25] L. A. Y. Poffelie, P. J. Soh, S. Yan, and G. A. Vandenbosch, "A high-fidelity all-textile UWB antenna with low back radiation for off-body WBAN applications," *IEEE Transactions on Antennas and Propagation*, vol. 64, no. 2, pp. 757-760, 2016. https://doi.org/10.1109/TAP.2015.2510035

[26] International Commission on Non-Ionizing Radiation Protection, "Guidelines for limiting exposure to time-varying electric, magnetic, and electromagnetic fields (up to 300 GHz)," *Health Physics*, vol. 74, no. 4, pp. 494-522, 1998.

[27] Federal Communications Commission Office of Engineering, and Technology, "Evaluating compliance with FCC guidelines for human exposure to radiofrequency electromagnetic fields," *Supplement C–OET Bulletin 65*, 2001 [Online]. Available: https://transition.fcc.gov/Bureaus/Engineering_Technology/Documents/bulletins/oet65/oet65c.pdf.

Devendra Kumar
https://orcid.org/0000-0002-0016-203X

has been an assistant professor in the Department of Electronics and Communication Engineering, Rustamji Institute of Technology, Gwalior, since 2010. He received his M.Tech. degree from MITS, Gwalior, in 2009. He is currently pursuing his Ph.D. from Rajasthan Technical University, Kota. His areas of interest are microwave antennas, filters, and radars.

Dhirendra Mathur
https://orcid.org/0000-0003-1167-3932

is a professor in the Department of Electronics and Communication Engineering, Rajasthan Technical University, Kota. He received his Ph.D. degree from Malaviya National Institute of Technology, Jaipur. He has published various papers in international journals and conferences. His areas of interest are microwave antennas, filters, and nanotechnology.

LCP-Based Low-Cost Base Station Antenna for 3.7 GHz 5G Band

Youngju Lee[1] ⬤ · Seung-Ho Choi[2] ⬤ · Bum-Hee Lee[2] ⬤ · Jung-Yub Lee[2] ⬤ · Jae Hee Kim[3,*] ⬤

Abstract

This paper presents a large-scale base station antenna assembly structure that is low-cost, reliable, and easy to manufacture. The antenna element is composed of a low-loss liquid crystal polymer based on a plastic molded module and a modified wideband stacked patch antenna. The base station antenna consists of a 4 × 8 antenna module, with each module comprising 3 × 1 subarrays along with dual-polarized antenna elements. The antenna element achieved an efficiency of 91% and an impedance bandwidth of 1.14 GHz within a height of 10 mm at 3.7 GHz. Furthermore, the fabricated array antenna structure was tested and verified to have an effective isotropic radiated power of 75.6 dBm at boresight and a steering range of less than ±60°. Therefore, the proposed structure meets the required antenna and beam-forming performance for commercial 5G active antenna systems.

Key Words: Base-Station Antenna, Liquid Crystal Polymer (LCP), Stacked Patch, 5G.

I. INTRODUCTION

The 5G wireless communication networks are considered suitable candidates for next-generation cellular systems owing to growing traffic in the existing 4G spectrum and demand for high data rates. Recently, 5G commercial services have been deployed in South Korea and the United States. In America, the provision of C-band services at 3.7–3.98 GHz is already underway, beginning with small-cell services in the millimeter wave band. In this context, to ensure a successful network equipment business, high-performance base stations that produce high yields need to be mass-produced at low cost.

For C-band services, massive multi-input multi-output (MIMO) is a major technology that has the potential to improve the reliabilities of data links as well as performances related to the capacity and user experience of 5G-enhanced mobile broadband using hundreds of large antenna arrays in a base station [1]. In particular, MIMO systems apply highly directed radiation beams through adaptive beamforming and signal processing algorithms to different pairs of antennas using active antenna systems (AASs) [2].

Notably, the passive antenna beam patterns in legacy cellular systems are fixed, and they are shaped to transmit signals uniformly within the coverage direction.

In contrast, AASs comprising multiple antenna elements can transmit and receive signals through beams with narrow beamwidths and high gains. In addition, such systems can adjust the amplitude and phase of each transmitted/received radio frequency chain to dynamically control the beam direction toward the location of the desired user, resulting in significant throughput and efficiency improvements [3].

Fig. 1 presents an example of the antenna configuration of an active antenna system for a massive MIMO. In terms of the development cost and angular coverage of the cell, applying independent digital beamforming to every antenna element would be inefficient. Hence, a single transmit/receive chain, including a power amplifier and a low-noise amplifier, is connected to a group of antennas, called a subarray. The subarray consists of three antenna elements, with each antenna element having two polarizations—positive polarization (P pol.), which is tilted by +45° relative to the vertical axis, and negative polarization (N pol.), which is tilted by −45°. Since a signal input is necessary for each polarization, each subarray bears two input ports. Therefore, an entire array antenna comprises multiple subarrays as its array element. In particular, four vertical columns of subarrays and eight horizontal rows of subarrays create the entire array. Fig. 1(b) shows the configuration of a simple radio structure in AASs, which is connected to an antenna. The active antenna system is composed of 64 transceiver chains, each of which should deliver a precise and stable amplitude and phase to the antenna in various environments to create the desired beam-forming pattern. Furthermore, the calibration network serves to calibrate the amplitude and phase of the signal transmitted to the antenna.

In recent years, increasing demand for broadband dual-polarized antennas characterized by a compact and planar configuration has been observed, owing to their low cost, ease of manufacturing, and system integration. To address this demand, many dual-polarized base station antennas have been proposed to achieve broadband and dual-polarization performance, including antennas that involve modifying the dipole structure [4–6] and patch antennas using an L-probe feed and a meander line feed [7–11]. Notably, a double-layered stacked patch antenna has also been proposed in the literature for attaining a broad imped-

ance band and flat gains [12]. Although these antennas exhibit broadband characteristics, they tend to have high antenna height and a mechanically complex structure—features that discourage mass production—since most of them have been produced with a focus on the performance of a single antenna element.

In this regard, liquid crystal polymers (LCPs) with low dielectric constant and low loss tangent have been proposed for use in circuit devices, module packaging, and flexible antenna arrays [13, 14]. Notably, LCPs are attractive materials for use in antennas due to their low water absorption and low dielectric losses.

In this paper, a novel low-profile, broadband, dual-polarized antenna structure is proposed for low cost and easy manufacturing of large-scale AASs for base stations. The proposed antenna is composed of 96 antenna elements with dimensions of 360 mm × 930 mm × 10 mm. Furthermore, a low-loss LCP-based plastic molding substrate is employed to easily fabricate a 3D fixture for the flexible 3D design of the antenna and feed line, as well as to reduce costs for fabricating two subarray-based molding modules compared to the costs involved in using a large-scale printed circuit board (PCB) substrate.

The proposed antenna operated efficiently in the C-band from 3.7 to 3.98 GHz. Furthermore, its performance was verified by comparing simulation results. The verification results confirmed that the novel plastic molding structure proposed in this study can be employed for the mass production of large-scale antennas, thus satisfying the cost reduction requirements as compared to antennas based on PCB.

II. 3 × 1 SUBARRAY ON PLASTIC MOLDED MODULE

A basic plastic molding antenna element for large-scale MIMO systems at 3.7 GHz is presented in Fig. 2. A single
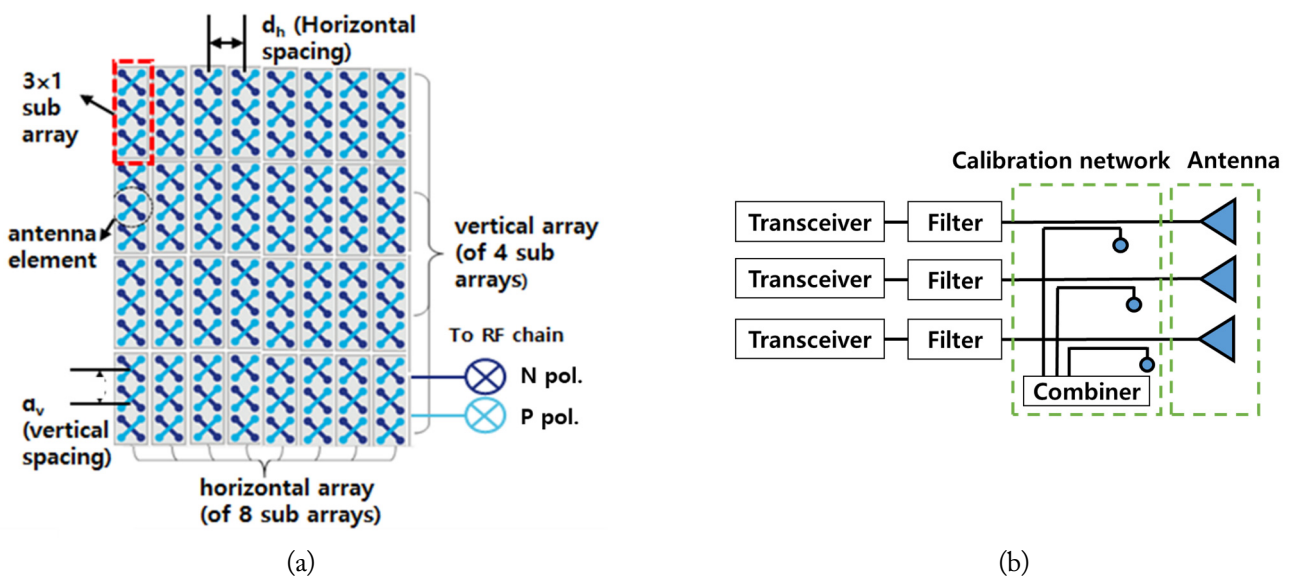

(a)

(b)

Fig. 1. An example of active antenna systems for massive MIMO radio configuration: (a) array antenna and (b) a simple radio structure.

antenna element consists of two stacked patches—a lower patch and an upper patch—that are floated on a plastic molding substrate while maintaining a constant gap between the lower stacked L-shaped coupled feed. The stacked patches were used to obtain a wide impedance bandwidth, which was satisfied when the upper patch was sufficiently floated from the lower patch for loose coupling. Furthermore, two resonant frequencies were placed closely to achieve wideband impedance using a relatively thick antenna.

When the distance between the upper and lower patches was decreased to lower the height of the antenna, strong coupling was observed, resulting in a wider separation between the two resonance frequencies. This led to some frequency regions between the two resonance frequencies failing to meet $S_{11} < -10$ dB. To address this issue, this paper proposes a structure in which a slot is made in the lower patch to reduce coupling while also narrowing the distance between the upper and lower patches. The length and width (w_{up}) of the upper patch in Fig. 2(c) are 26 mm, while those (w_{low}) of the lower patch are 21 mm. Furthermore, the size (w_{slot}) of the hole in the lower patch is 11 mm. The upper patch and lower patch are located 10 mm and 6 mm above the ground, respectively, while the feed is placed 5 mm above the ground. The upper and lower patches are sup-

ported by a plastic mold while also keeping an air gap between the patches. The feed line is raised 12 mm away from the center of the antenna, with the length of the feed line coupled with the lower patch being 5 mm.

The LCP material, which was used as the primary material for constructing the plastic structure, acted as a position fixture, as well as the substrate of the antenna and the feed line. This material was chosen because it allowed relatively easy fabrication of molding for mass production, was characterized by good thermal management in the molding process, and exhibited low loss characteristics for high radio frequency (RF) performance, such as insertion loss and antenna efficiency, as shown in Table 1.

Table 1. Comparison of various types of materials for the molded module

Material	Permittivity	Loss tangent	HDT (°)	Price
DS-7409	3.2	0.0025	400	High
LCP	3.7	0.0023	305	Mid.
PPS	4.1	0.0045	270	Mid.
PC	2.7	0.012	130	Low

LCP = liquid crystal polymer, PPS = polyphenylene sulfide, PC = poly carbonates, HDT = heat deflection temperature.
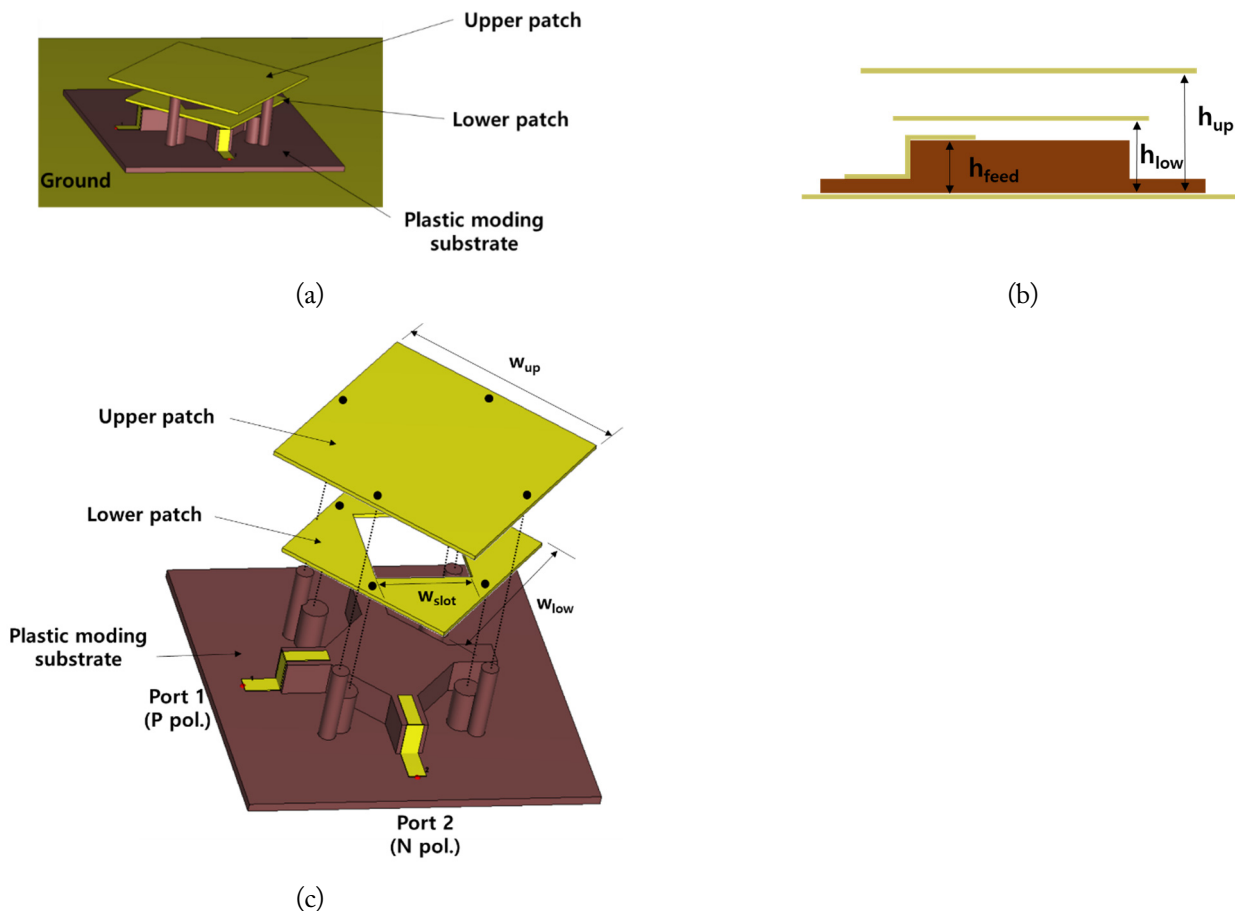

(a)

(b)

(c)

Fig. 2. Structure of the proposed antenna element: (a) 3D view, (b) side view, and (c) each part of the antenna structure.

Furthermore, compared to conventional fabrication processes based on large-scale PCBs for large-sized antennas, the proposed module has a relatively small size and could be repeatedly assembled on the metal ground to from a large-scale antenna.

In the absence of a hole ($w_{slot} = 0$) in the lower patch of the structure depicted in Fig. 2, the input impedance is simulated based on the height of the upper patch. Fig. 3(a) shows a Smith chart, while Fig. 3(b) depicts the magnitude of S_{11} with respect to frequency. It is evident that as the height of the upper patch increases, the coupling between the upper and lower patches decreases, ultimately leading to a reduction in the size of the resonance circle formed on the Smith chart. Additionally, the second resonant frequency declines as the coupling decreases. When the two resonance frequencies are located close to each other, an $S_{11} < -10$ dB is obtained over the entire frequency band. Therefore, although increasing the height of the upper patch is favorable from the perspective of bandwidth, it results in the disadvantage of thickening the antenna.

To reduce coupling without increasing the thickness of the antenna, a hole was introduced in the lower patch. The simulated S_{11} values when using varying hole sizes (w_{slot}) for the same antenna structure as in Fig. 2 are presented in Fig. 4. As shown in Fig. 4(a), an increase in hole size leads to a decrease in coupling, resulting in a smaller resonant circle on the Smith chart. Additionally, Fig. 4(b) shows that the second resonant frequency also declines as the hole size increases. This indicates that the introduction of holes in the lower patch results in reduced coupling with the upper patch without having to increase its height. The shift in the position of the resonance circle on the Smith chart occurs because increasing the hole size in the lower patch leads to a lowering of the patch's resonant frequency. In this context, impedance matching and other related factors can also be optimized by adjusting the length of the L-probe. The S_{11} of the proposed antenna is traced by the blue dash-dotted line in Fig. 4, achieving a 1.14 GHz (3.32–4.46 GHz) impedance bandwidth.

Fig. 5 illustrates the simulated realized gain in terms of different frequencies. Within the impedance bandwidth of 3.32–4.46 GHz, the antenna gain varies between a minimum of 8.1 dBi and a maximum of 9.5 dBi. Moreover, the antenna gain over various frequencies reveals considerable wideband performance for a single element.
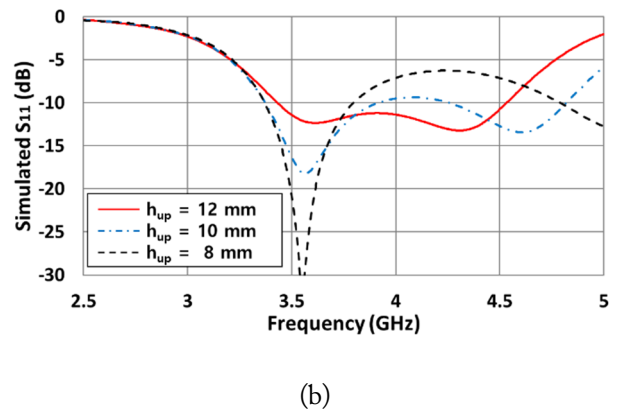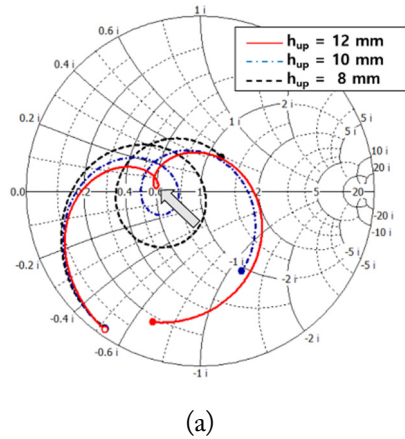

(a) (b)

Fig. 3. Simulated S_{11} of the antenna element for different heights of the upper patch; (a) Smith chart and (b) magnitude in dB.
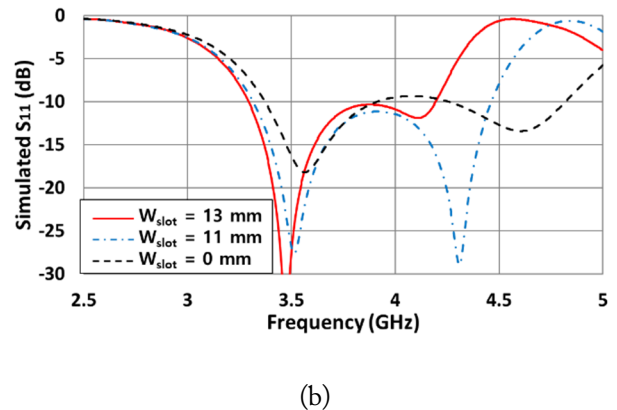

(a) (b)
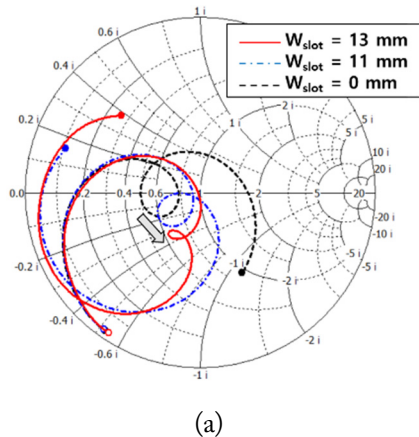
Fig. 4. Simulated S_{11} of the antenna element for different hole sizes of the lower patch; (a) Smith chart and (b) magnitude in dB.
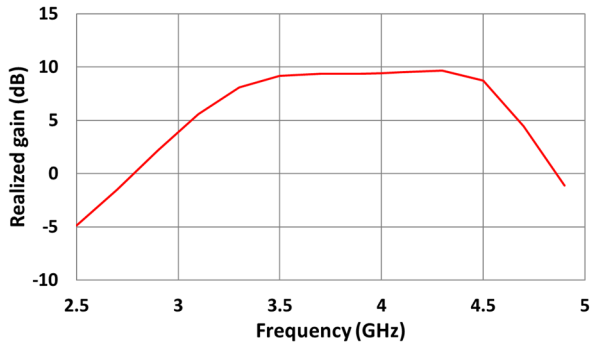
Fig. 5. Simulated realized gain of the antenna element.

To enrich the distribution of the radiated power within the coverage area and to reduce interference from the upper region, a 6° electronically down-tilt beam is required in the vertical direction of the base station antenna. For a 6° down-tilt beam in the vertical direction, the phase difference at each feed network for a subarray should be about 36°. Notably, a 3 × 1 subarray in the vertical direction would be more efficient than using three single antennas for independent digital beamforming and RF chains even the vertical beamforming range of the antenna is limited to a specified range.

When determining the distance between the vertical antennas, the vertical beamforming range and increment of gain should be carefully considered as the main specifications of the active antenna system. For the system proposed in this study, the distance between antennas in the vertical direction was 0.78λ (61 mm) for a vertical scan range of 20° and a gain of approximately 11 dBi. Meanwhile, the distance between antennas in the horizontal direction was 0.54λ (42 mm). Notably, a 3 × 1 subarray can support two polarizations—P pol. and N pol. Therefore, two signal lines supporting these two polarizations of the 3 × 1 subarray antenna were connected using the transmit/receive RF chain.

The size of the module, composed of two 3 × 1 subarrays, was determined by accounting for the productivity of the molding process and the efficiency of assembling it on metal ground. Furthermore, the 3 × 1 feed lines were created by cutting aluminum sheets of 100 μm thickness, which were then attached to the plastic fixture using specific melting structures, as shown in Fig. 6.

Fig. 7 shows the simulated S-parameters of the two 3 × 1 subarrays. S(N1,N1) refers to the S_{11} of the N pol. port, while S(P1,P1) denotes the S_{11} of the P pol. port. Furthermore, S(N1,N2) refers to the co pol. isolation between ports N1 and N2, while S(N1,P1) is the self-cross pol. isolation between ports N1 and P1. Finally, S(P1,N2) indicates the cross-pol. isolation between ports P1 and N2. The S_{11} of the two polarizations sat-

(a)

(b)

(c)

(d)
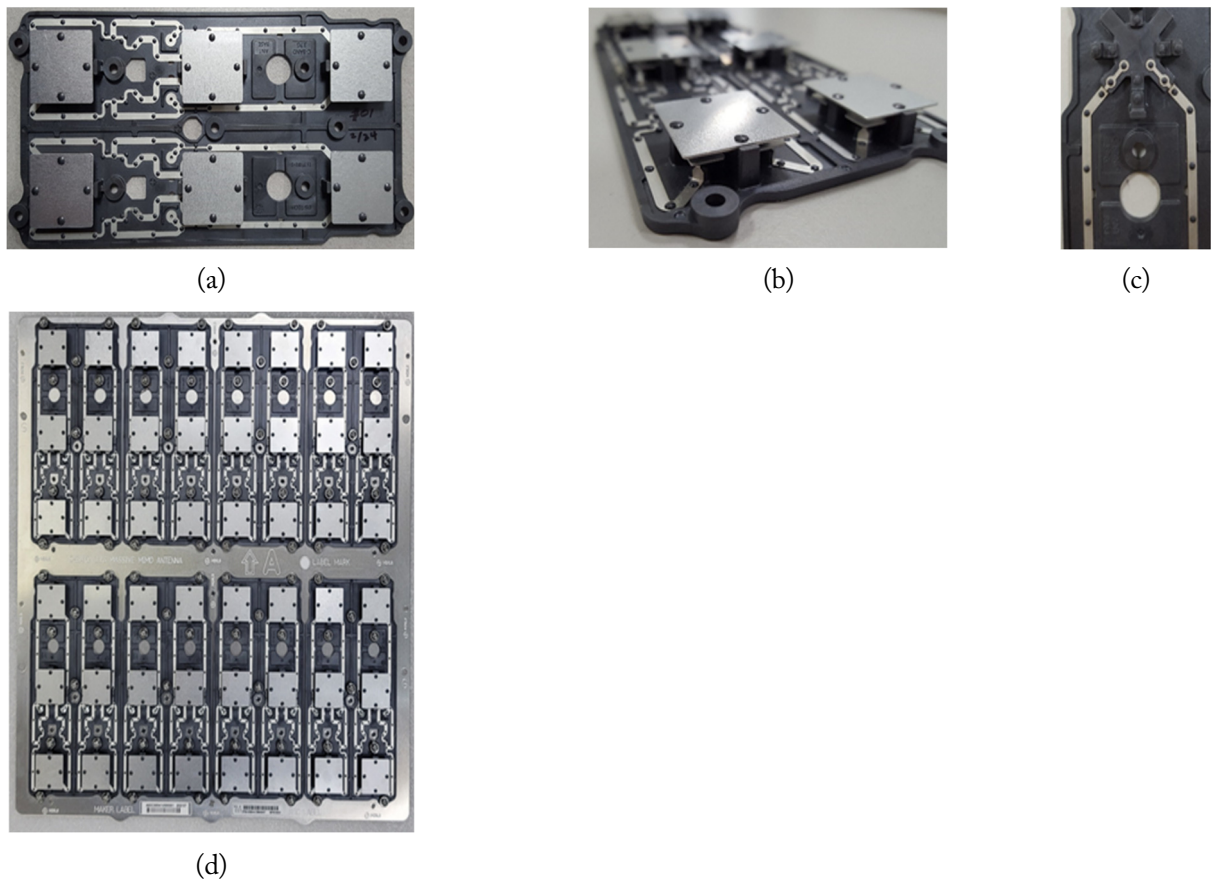
Fig. 6. Fabricated plastic molded antenna module: (a) top view of the two 3 × 1 subarrays, (b) side view of the subarray, (c) top view of the antenna element without the upper and lower patches, and (d) half of the total antenna array structure.
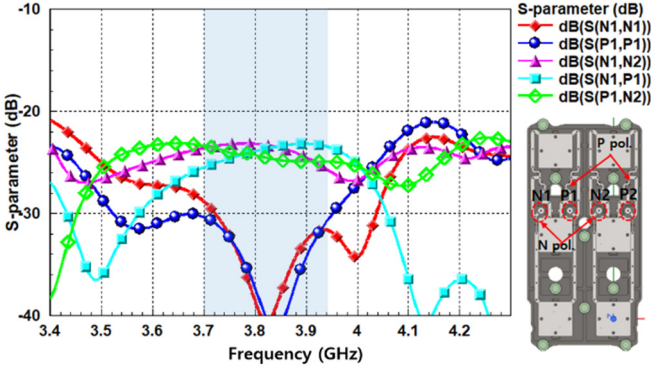
Fig. 7. Simulated *S*-parameters of the two 3 × 1 subarrays.
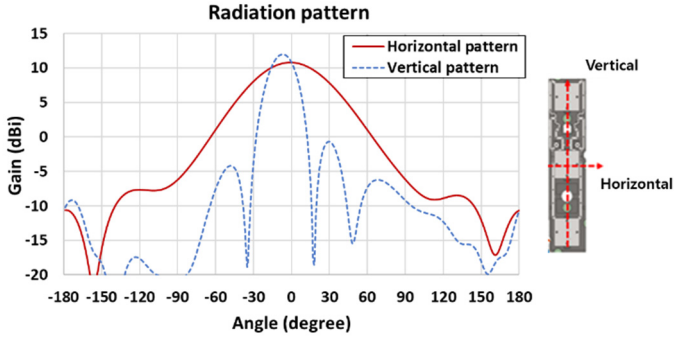
Fig. 8. Simulated radiation patterns of the 3 × 1 subarray antenna.

isfied the −20 dB specification and port isolation. Furthermore, polarization isolation between the two ports of the antennas was at least under −21 dB within the concerned frequency band. Notably, the broader impedance bandwidth achieved by the sub-array antenna compared to a single antenna can be attributed to the influence of the feeding structure.

Fig. 8 traces the simulated antenna patterns of the 3 × 1 subarray supporting P pol. Notably, the pattern of N pol. was found to be similar to that of P pol., since the feeding point was structurally symmetric. Furthermore, the 3 dB beamwidth of the horizontal pattern was approximately 61°, while the gain of

the subarray was 10.7 dBi. Similarly, the 3 dB beamwidth of the vertical pattern was 20° with a 6° fixed down-tilt angle, while the peak gain was 11.7 dBi. This indicates that the scanning range of the entire active antenna system can be accurately estimated from the subarray beam pattern.

III. RADIATION PATTERNS OF THE ACTIVE ANTENNA SYSTEM

Each input port of the subarray antenna was connected to beamforming integrated circuits (ICs). A user-specific beam was transmitted toward the individual receive antenna of the user through a beamforming weight vector, defined as a steering vector toward the user's direction in line-of-sight (LOS) conditions or a maximal ratio transmission vector in non-LOS environments. In LOS conditions, the array gain was observed to be equal to the number of subarrays. The maximum antenna gain of the user-specific beam can be expressed in dB as the sum of its array factor and the subarray gain. Notably, the array factor is usually proportional to the number of subarrays in an array, while the subarray gain is approximately proportional to the number of antenna elements within a subarray (3 × 1 subarray) and the spacing between adjacent subarrays (4 × 8 system). The antenna gain toward the boresight of the proposed active antenna system was estimated to be approximately 25.7 dBi when considering two factors—gains of the array factor (15 dB) and the subarray (10.7 dBi). Fig. 9 shows the simulated and measured patterns of the user-specific beam of the proposed active antenna system at boresight, exhibiting maximum gain in the azimuth and vertical directions at 3.7 GHz. The 3 dB beamwidth was approximately 12° in the azimuth direction and 5° in the vertical direction. Notably, the measured beam pattern and gain were similar to the simulation results obtained at boresight. The antenna efficiency was almost above 91%, including the feedline loss from a low-loss LCP-based substrate.

(a)

(b)

Fig. 9. Radiation patterns of the user-specific beam: (a) horizontal pattern and (b) vertical pattern.

The set-level, user-specific beam performance of the proposed active antenna system with maximum tilting range in the azimuth and elevation axes was measured, as shown in Fig. 10. The measured peak effective isotropic radiated power (EIRP) was 75.6 dBm, while the scanning 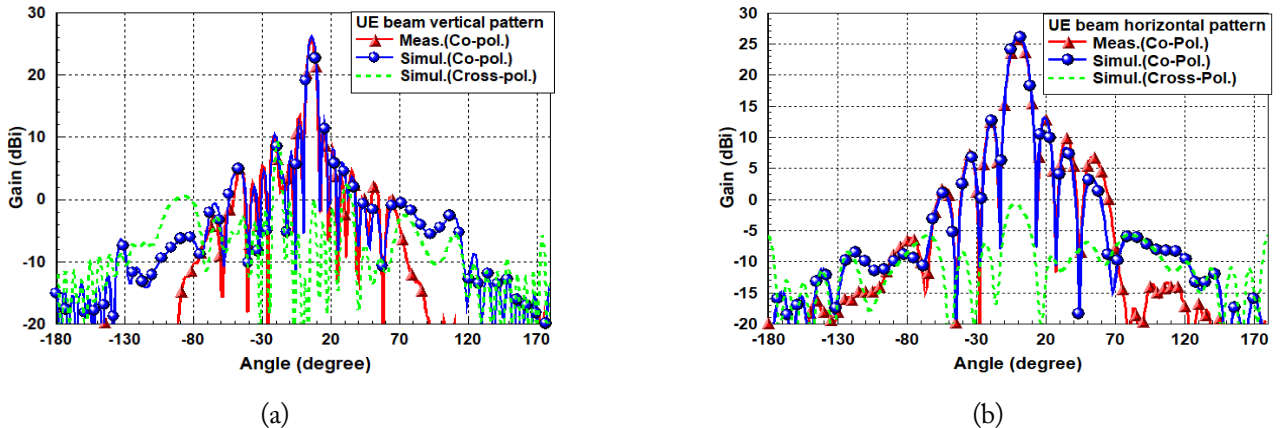range was 120° from −60° to 60° in the azimuth axis. The tilting range was approximately 20°—from +16° down-tilt angle to −4° up-tilt angle—along with the 6° fixed-tilt angle achieving maximum gain in the vertical axis. The cross-polarization ratio level—the ratio between co-polarization and cross-polarization—was 30.2 dB at boresight and 13.5 dB at the 60° scanning angle. Therefore, the beamforming performance of the proposed structure, including the performance of the system elements, such as antennas, RF transceivers, and other related functions, can be expected to satisfy the beamforming performance of commercial base stations.

Table 2 compares the performance of the antenna proposed in this paper with existing references [7–9, 15–18]. It is observed that the resonance frequency of the references is below 2 GHz, while their antennas were designed with a height of at least 17 mm. Additionally, while antennas designed for the 3.7 GHz band has a lower height compared to the proposed antenna, they still fail to reach a bandwidth as wide as that attained in this paper.

IV. Conclusion

This study investigated a novel low-cost antenna fabrication and assembly solution for large-scale AASs. The proposed antenna comprises over 96 antenna elements at 3.7 GHz, and involves repeatedly assembling an LCP-based plastic module using an attachable 3 × 1 feed line. In addition, a low-profile wideband antenna with stacked patch antennas was obtained, even with loose coupling between the upper and lower patch antennas, by perforating the inner patch antenna. Subsequently, the proposed structure was verified to satisfy a wide impedance bandwidth of 1.14 GHz within a height of 10 mm. Furthermore, set-level beamforming measurements of the active antenna system with 64-chain (4 × 8 array and two pol.) transceivers were verified, exhibiting a maximum EIRP of 75.5 dBm at boresight and a steering range of $< \pm 60°$ in the azimuth axis. Overall, the proposed solution can be considered a suitable candidate for use in commercial active antenna system-based base stations with large-scale arrays at 3.7 GHz.
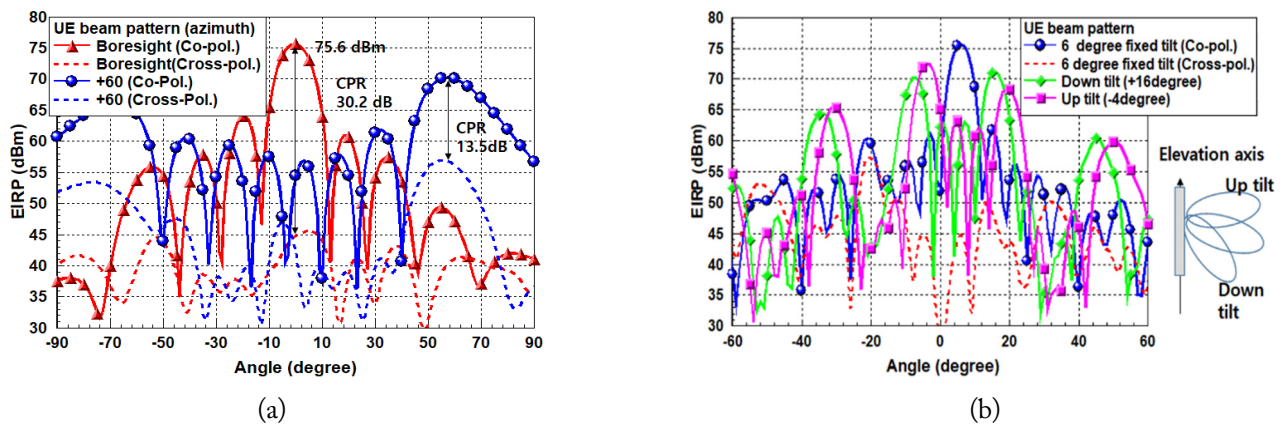
Fig. 10. Scanned patterns of the user-specific beam: (a) horizontal pattern (azimuth axis) and (b) vertical pattern (elevation axis).

Table 2. Comparison of the proposed antenna performance with that of existing references

	Antenna type	Frequency (GHz)	Height (mm)	Bandwidth (GHz)
Wong et al. [7]	L-probe single patch	1.8	17	0.43
Lai and Luk [8]	Meandering probe single patch	1.9	17.5	0.43
Guo et al. [9]	L-probe single patch	2.0	22.4	0.67
Zheng and Chu [15]	Loop-dipole	2.0	35	1.15
Nie et al. [16]	Slotted patch with shorting strips	2.0	40	1.18
Huang et al. [17]	Stacked patch	3.7	8.7	0.40
Gao et al. [18]	Slot patch	3.7	7.8	0.40
This work	L-probe stacked patch with hole	3.7	10	1.14

REFERENCES

[1] E. G. Larsson, O. Edfors, F. Tufvesson, and T. L. Marzetta, "Massive MIMO for next generation wireless systems," *IEEE Communications Magazine*, vol. 52, no. 2, pp. 186-195, 2014. https://doi.org/10.1109/MCOM.2014.6736761

[2] K. N. Poudel and W. Robertson, "Metamaterial inspired antenna design for massive MIMO, 5G communications system," in *Proceedings of 2017 USNC-URSI Radio Science Meeting (Joint with AP-S Symposium)*, San Diego, CA, USA, 2017, pp. 103-104. https://doi.org/10.1109/USNC-URSI.2017.8074918

[3] W. Roh, J. Y. Seol, J. Park, B. Lee, J. Lee, Y. Kim, J. Cho, K. Cheun, and F. Aryanfar, "Millimeter-wave beamforming as an enabling technology for 5G cellular communications: theoretical feasibility and prototype results," *IEEE Communications Magazine*, vol. 52, no. 2, pp. 106-113, 2014. https://doi.org/10.1109/MCOM.2014.6736750

[4] B. Q. Wu and K. M. Luk, "A broadband dual-polarized magneto-electric dipole antenna with simple feeds," *IEEE Antennas and Wireless Propagation Letters*, vol. 8, pp. 60-63, 2008. https://doi.org/10.1109/LAWP.2008.2011656

[5] Y. Gou, S. Yang, J. Li, and Z. Nie, "A compact dual-polarized printed dipole antenna with high isolation for wideband base station applications," *IEEE Transactions on Antennas and Propagation*, vol. 62, no. 8, pp. 4392-4395, 2014. https://doi.org/10.1109/TAP.2014.2327653

[6] Y. Cui, R. Li, and P. Wang, "A novel broadband planar antenna for 2G/3G/LTE base stations," *IEEE Transactions on Antennas and Propagation*, vol. 61, no. 5, pp. 2767-2774, 2013. https://doi.org/10.1109/TAP.2013.2244837

[7] H. Wong, K. L. Lau, and K. M. Luk, "Design of dual-polarized L-probe patch antenna arrays with high isolation," *IEEE Transactions on Antennas and Propagation*, vol. 52, no. 1, pp. 45-52, 2004. https://doi.org/10.1109/TAP.2003.822402

[8] H. W. Lai and K. M. Luk, "Dual polarized patch antenna fed by meandering probes," *IEEE Transactions on Antennas and Propagation*, vol. 55, no. 9, pp. 2625-2627, 2007. https://doi.org/10.1109/TAP.2007.904158

[9] Y. X. Guo, K. W. Khoo, and L. C. Ong, "Wideband dual-polarized patch antenna with broadband baluns," *IEEE Transactions on Antennas and Propagation*, vol. 55, no. 1, pp. 78-83, 2007. https://doi.org/10.1109/TAP.2006.888398

[10] I. Kim and B. Lee, "Wideband antenna for high-frequency 5G wireless communication," *Journal of Electromagnetic Engineering and Science*, vol. 22, no. 3, pp. 296-301, 2022. https://doi.org/10.26866/jees.2022.3.r.90

[11] J. Cho, T. H. Lim, Y. Kim, and H. Choo, "Design of a wideband printed patch dipole antenna with a balanced on-board feeding network," *Journal of Electromagnetic Engineering & Science*, vol. 22, no. 6, pp. 631-637, 2022. https://doi.org/10.26866/jees.2022.6.r.132

[12] K. Ding, Y. Wu, K. H. Wen, D. L. Wu, and J. F. Li, "A stacked patch antenna with broadband circular polarization and flat gains," *IEEE Access*, vol. 9, pp. 30275-30282, 2021. https://doi.org/10.1109/ACCESS.2021.3059948

[13] Z. Zhou, W. Li, J. Qian, W. Liu, Y. Wang, X. Zhang, et al., "Flexible liquid crystal polymer technologies from microwave to terahertz frequencies," *Molecules*, vol. 27, no. 4, article no. 1336, 2022. https://doi.org/10.3390/molecules27041336

[14] G. DeJean, R. Bairavasubramanian, D. Thompson, G. E. Ponchak, M. M. Tentzeris, and J. Papapolymerou, "Liquid crystal polymer (LCP): a new organic material for the development of multilayer dual-frequency/dual-polarization flexible antenna arrays," *IEEE Antennas and Wireless Propagation Letters*, vol. 4, pp. 22-26, 2006. https://doi.org/10.1109/LAWP.2004.841626

[15] D. Z. Zheng and Q. X. Chu, "A multimode wideband $\pm$ 45° dual-polarized antenna with embedded loops," *IEEE Antennas and Wireless Propagation Letters*, vol. 16, pp. 633-636, 2016. https://doi.org/10.1109/LAWP.2016.2594240

[16] L. Y. Nie, X. Q. Lin, Y. J. Chen, J. Zhang, B. Wang, Z. Q. Yang, and Y. Fan, "A low-profile coplanar dual-polarized and dual-band base station antenna array," *IEEE Transactions on Antennas and Propagation*, vol. 66, no. 12, pp. 6921-6929, 2018. https://doi.org/10.1109/TAP.2018.2869222

[17] W. Huang, Y. He, W. Li, L. Zhang, S. W. Wong, and Z. Zeng, "A low-profile dual-polarized wideband antenna for 5G massive MIMO base station," in *Proceedings of 2021 IEEE International Workshop on Electromagnetics: Applications and Student Innovation Competition (iWEM)*, Guangzhou, China, 2021, pp. 1-3. https://doi.org/10.1109/iWEM53379.2021.9790399

[18] X. Gao, L. Zhang, Y. He, L. Zhang, W. Li, S. W. Wong, and C. H. Liao, "A dual-polarized compact patch antenna for sub-6 GHz 5G base stations," in *Proceedings of 2020 IEEE Asia-Pacific Microwave Conference (APMC)*, Hong Kong, 2020, pp. 752-754. https://doi.org/10.1109/APMC47863.2020.9331429

Young Ju Lee

https://orcid.org/0000-0001-5004-8238

is currently the vice president of the Advanced Network Development Office at Doosan Corporation, South Korea, where he is involved in the research of mmWave antenna modules for 5G and advanced communications. From 2005 to 2018, he was a project leader with Samsung Electronics, South Korea, where he focused on 5G antenna systems in the sub-6 GHz and mmWave bands. His research interests include the design of beamforming array antennas for 5G communication systems, analysis of indoor and outdoor propagation for channel modeling, and mobile and base station antenna applications using electromagnetic wave technology. He received his doctorate in Electronics and Electrical Engineering from Pohang University of Science and Technology (POSTECH), Pohang, Korea, in 2005.

Jung-Yub Lee

https://orcid.org/0009-0006-2487-6033

is currently working with Samsung Electronics, where he is responsible for the research of antenna technologies for 5G communications. His research interests include the design of beamforming array antennas for various communication systems as well as mobile and base station applications using electromagnetic wave technology. He received his Ph.D. degree from the Department of Electrical Engineering at Seoul National University, Seoul, Korea, in 2007.

Seung-Ho Choi

https://orcid.org/0000-0001-9387-4855

received his Ph.D. degree from the School of Electrical Engineering at Korea University, Seoul, Korea, in 2018. He is currently working as an antenna engineer at Samsung Electronics, Korea. His research interests include sub-6 GHz antennas and phase shifters for 5G base stations.

Jae Hee Kim

https://orcid.org/0000-0003-2193-928X

received his B.S. degree in electrical engineering from Korea University, Seoul, Korea, in 2005, and his Ph.D. degree in electrical engineering from Pohang University of Science and Technology, Pohang, Korea, in 2010. From 2010 to 2012, he worked as a senior engineer with Samsung Electronics, Suwon, Korea. From 2012 to 2020, he was a senior researcher at the Korea Railroad Research Institute in Uiwang, South Korea. He is currently an associate professor at the School of Electrical, Electronics, and Communication Engineering, Korea University of Technology and Education, Cheonan, Korea. His research interests include the design and analysis of antennas and microwave components, and the development of wireless power transfer systems for railways.

Bum-Hee Lee

https://orcid.org/0009-0001-4971-5010

received his B.S. degree in radio wave engineering from Chungnam National University, Daejeon, Korea, in 2018. He is currently working as an antenna engineer at Samsung Electronics, Korea. His research interests include massive MIMO antenna arrays and sub-6 GHz antennas for 5G base stations.

Hybrid Topology with Reconfigurable Rectifier for Enable CC and CV Output Characteristics in Wireless Power Transfer Systems

Haibing Wen[1],* (ID) · Jiayuan Li[1] (ID) · Jiadong Yang[1] (ID) · Peng Wang[1] (ID) · Kehan Zhang[2] (ID) · Lei Yang[1] (ID) ·
Yaopeng Zhao[1] (ID) · Xiangqian Tong[1] (ID)

Abstract

To achieve simple and reliable conversion from constant current (CC) charging mode to constant voltage (CV) charging mode in wireless power transfer systems, this paper proposes a hybrid topology equipped with a reconfigurable rectifier. An AC switch is adapted to simultaneously realize the change from half-bridge rectification to full-bridge rectification and achieve the shift from a topology with capacitors in the series compensated primary and secondary sides to a topology with capacitors in the series compensated primary side and the inductor-capacitor-inductor (LCL) compensated secondary side. Notably, communication between the transmitter and receiver sides is not necessary in the proposed method. Furthermore, the zero phase angle characteristic is successfully maintained in both charging modes. The experimental results obtained using the 48 V/0.7 A experimental prototype, which was built to validate the relevant theoretical analysis, show that output current/voltage can be achieved in CC/CV charging mode independent of load resistance. Notably, the maximum power transfer efficiency of the system during the charging process reached 95.33%.

Key Words: Constant Current (CC), Constant Voltage (CV), Reconfigurable Rectifier, Wireless Power Transfer (WPT), Zero Phase Angle (ZPA).

I. INTRODUCTION

Wireless power transfer (WPT) technology has the potential to effectively enhance the freedom and security of a power supply approach. It has been widely used in electric vehicles, rail transit, implantable medical devices, industrial equipment, consumer electronics, power system monitoring equipment, and other fields [1–8]. In general, lithium-ion batteries have been chosen as the power source for several types of electrical equipment. To enhance the safety and efficiency of battery charging, a typical charging process can be divided into two stages—constant current (CC) charging mode and constant voltage (CV) charging mode [9]. Notably, during the charging process, the equivalent resistance of the battery undergoes significant changes. This requires the charging current (voltage) in the CC (CV) charging mode to be independent of load resistance. In addition, zero phase angle (ZPA) characteristics, which are integral to the efficient operation of the system, should be maintained throughout the charging cycle.

Currently, most reported technologies for realizing CC and CV charging in WPT systems can be classified into two types. The first type involves using CC and CV control methods based on compensation topology invariance, such as phase shifting control, DC-DC converter, and frequency modulation control, as proposed in [10–13]. The output current or voltage is controlled by adjusting the phase-shifting angle of the inverter or the rectifier [10]. However, this method is prone to causing hard on/off for the switch and increasing power loss. Although these problems can be avoided by introducing a DC-DC converter to regulate the output voltage and current on the transmitter and receiver sides [11], the introduction of passive components could lead to additional power loss and create issues related to volume and weight. Notably, CC and CV charging modes can be realized at two system frequencies when considering a fixed compensation topology, indicating frequency modulation control. For instance, when using a topology with capacitors in the series compensated primary and secondary sides (S-S topology), the system produces not only the characteristic CC output at the resonance frequency point, but also two CV output frequencies that are either higher or lower than the resonant frequency [12]. These same characteristics were observed for LCC-LCC topology [13]. However, the variation in mutual inductance between the transmitter coil and the receiver coil may affect the CC or CV operating frequency points of the system, in turn reducing its reliability. Moreover, communication is indispensable to the above methods. The delay or interruption in communication inevitably influences the output characteristics of the WPT system.

As for the second type, CC and CV charging modes can also be achieved by switching two different compensation topologies [9, 14–16]. When two different topologies exhibit CC and CV output characteristics at the same resonant frequency, the changing over of the charging mode is realized by switching one or more of the AC switches. For instance, Qu et al. [9] proposed hybrid topologies using either series-series (SS) and series-parallel (PS) compensation or parallel-series (PS) and parallel-parallel (PP) compensation to realize CC and CV charging modes, achieving conversion from CC to CV charging mode using AC switches. This topology involved one inductance and three additional AC switches. Furthermore, a hybrid inductive power transfer battery charger combining LCC-LCC and LCC-S topologies was presented in [17]. The LCC-LCC compensation topology was utilized to provide the configurable CC output, while the LCC-S compensation network was employed to realize the configurable CV output. Two extra power switches were used to change the operation mode. However, in the case of the charging mode transition from CC output to CV output, an inductor on the receiver side became redundant, causing additional power loss.

This paper proposes a novel hybrid topology consisting of a reconfigurable rectifier. An AC switch is employed to facilitate the switching of the rectifier operating modes and compensation topologies, and also to enable the system to switch from CC charging mode to CV charging mode. At the same time, the proposed method does not require communication between the transmitter and receiver sides, which is beneficial for the simple and reliable operation of WPT systems.

II. THEORETICAL ANALYSIS

1. A Hybrid WPT Topology with a Reconfigurable Rectifier

Fig. 1 presents the proposed WPT system with a reconfigurable rectifier, where S_1–S_4 denote four MOSFETs and D_1–D_4 are four diodes. L_1 and L_2 represent the inductance of the transmitter and receiver coils, respectively. Furthermore, C_1 is the compensation capacitor on the transmitter side, while C_2 and L_3 are the compensation capacitor and compensation inductance on the receiver side, respectively. C_r refers to the filter capacitor on the rectifier while R_L is the load resistance.

In addition, S is an AC switch composed of two anti-series connected MOSFETs on the receiver side, as shown in Fig. 2.

2. CC Charging Mode

The switch S not only controls the operating mode of the rectifier but also dominates the charging mode of the WPT system. The simplified circuit diagram of the system when S is turned off is depicted in Fig. 3, where the rectifier of the proposed WPT system works in the half-bridge rectifier (HBR) mode. The dotted line indicates the direction of the current flow on the receiver side. In HBR mode, C_1 and C_2 together form an S-S compensation network for the WPT system. Notably, the equivalent AC load of the HBR and battery load can be expressed as follows [18]:
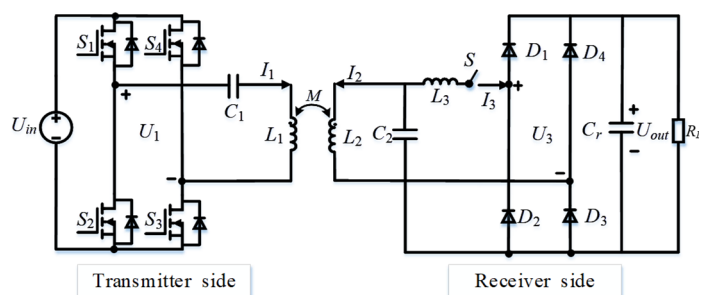

Fig. 1. The proposed WPT system with a reconfigurable rectifier.
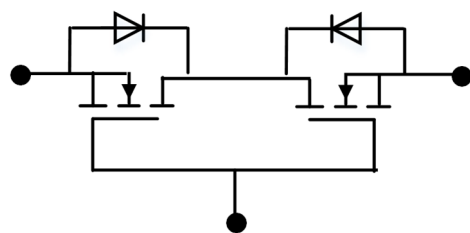

Fig. 2. Diagram of AC switch S.

$$R_{AC\_H} = \frac{2}{\pi^2} R_L. \tag{1}$$

Furthermore, according to the fundamental harmonic approximation method, the equivalent AC circuit of the HBR in Fig. 3 can be structured as shown in Fig. 4.

Subsequently, drawing on Kirchhoff voltage law (KVL), the following equation was obtained:

$$\begin{cases} \boldsymbol{U_1} = \left(j\omega L_1 + \dfrac{1}{j\omega C_1}\right)\boldsymbol{I_1} + j\omega M \boldsymbol{I_2} \\ 0 = -j\omega M \boldsymbol{I_1} + \left(j\omega L_2 + \dfrac{1}{j\omega C_3} + R_{AC\_H}\right)\boldsymbol{I_2} \end{cases} \tag{2}$$

When the operating frequency of the system becomes the resonant frequency—i.e., it is satisfied—the input current and output current can be expressed by drawing on Eq. (2), as follows:

$$\begin{cases} \boldsymbol{U_1} = \left(j\omega L_1 + \dfrac{1}{j\omega C_1}\right)\boldsymbol{I_1} + j\omega M \boldsymbol{I_2} \\ 0 = -j\omega M \boldsymbol{I_1} + \left(j\omega L_2 + \dfrac{1}{j\omega C_3} + R_{AC\_H}\right)\boldsymbol{I_2} \end{cases} \tag{3}$$
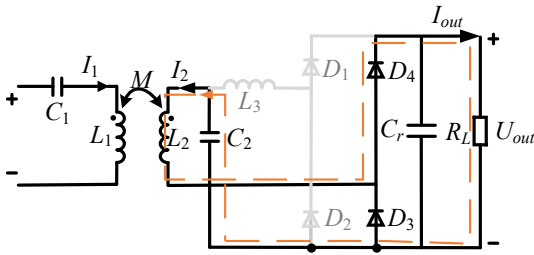
Fig. 3. HBR mode on the receiver side.
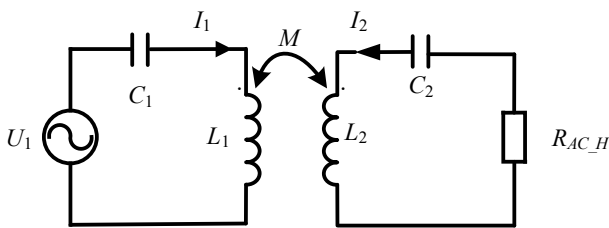
Fig. 4. Equivalent AC circuit of the HBR mode.

As evident in Eq. (3), since the output current is independent of load resistance in HBR mode, CC charging can be achieved. The input impedance of the WPT system in the HBR mode can be expressed as:

$$Z_{in} = \frac{\boldsymbol{U_1}}{\boldsymbol{I_1}} = \frac{(\omega M)^2}{R_{AC\_H}}. \tag{4}$$

Ultimately, based on Eq. (4), the ZPA operation in the CC charging mode was obtained.

3. CV Charging Mode

A simplified circuit diagram of the system when switch S is turned on is shown in Fig. 5. Notably, the rectifier of the proposed WPT system works in full-bridge rectifier (FBR) mode.

As shown in Fig. 5, when the rectifier operates in FBR mode, it performs equivalently to two HBRs connected parallelly, with the voltage of the battery determined by the higher value of $|V_{ao}|$ and $|V_{bo}|$[19]. When $|V_{ao}| > |V_{bo}|$, diode D_4 is clamped and D_3 is conducted. After the current flows through D_1 and the load from L_3, some of it flows through L_2 and back to L_3, while the other part flows back to L_3 from C_2. Notably, D_2 refers to the freewheeling diode, as shown in Fig. 6(a). Similarly, when $|V_{ao}| < |V_{bo}|$, diode D_1 is clamped and D_2 is turned off. As a result, the current flows through the load from D_4, where D_3 is the freewheeling diode, as shown in Fig. 6(b).

Subsequently, the equivalent AC circuit of the FBR mode can be structured the same way as shown in Fig. 7.

In Fig. 7, R_{AC_F1} and R_{AC_F2} vary with changes in the load voltage. The relationship between R_{AC_F1}, R_{AC_F2}, and R_L
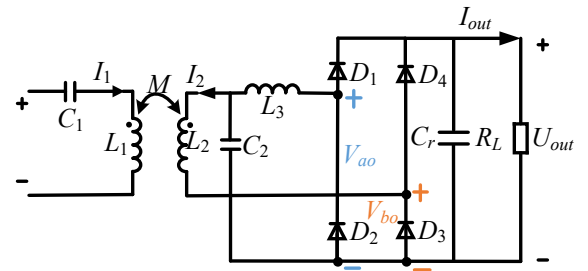
Fig. 5. FBR mode on the receiver side.
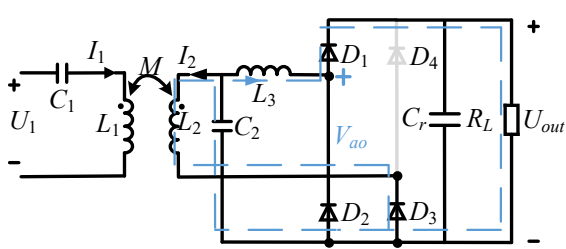
(a)
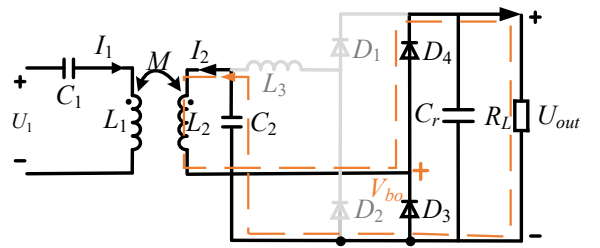
(b)

Fig. 6. Two operations of the FBR mode: (a) $|V_{ao}| > |V_{bo}|$ and (b) $|V_{ao}| < |V_{bo}|$.

can be expressed as follows [19]:

$$R_{AC\_F1}//R_{AC\_F2} = \frac{2}{\pi^2}R_L. \tag{5}$$

When the load voltage exceeds a certain rated value, the working mode of the system switches from Fig. 6(a)–6(b), with the equivalent AC circuit being the one depicted in Fig. 4. This may also be regarded as the branch disconnection of I_3 in Fig. 7, the detailed discussion for which has been presented in following section. Using KVL, the following equation was obtained:

$$\begin{cases} U_1 = \left(j\omega L_1 + \dfrac{1}{j\omega C_1}\right)I_1 + j\omega M I_2 \\ 0 = j\omega M I_1 + \left(j\omega L_2 + \dfrac{1}{j\omega C_2} + R_{AC\_F2}\right)I_2 + \dfrac{1}{j\omega C_2}I_3. \\ 0 = \dfrac{1}{j\omega C_3}I_2 + \left(j\omega L_3 + \dfrac{1}{j\omega C_2} + R_{AC\_F1}\right)I_3 \end{cases} \tag{6}$$

When the system operating frequency becomes the resonant frequency, i.e., $j\omega L_1 + 1/j\omega C_1 = j\omega L_2 + 1/j\omega C_2 = 0$ and $L_2 = L_3$ are established, the current flow through each inductor can be formulated by drawing on Eq. (6), as follows:

$$\begin{cases} I_1 = \dfrac{(\omega L_2)^2 + R_{AC\_F1}R_{AC\_F2}}{R_{AC\_F1}(\omega M)^2}U_1 \\ I_2 = \dfrac{1}{j\omega M}U_1 \\ I_3 = -\dfrac{L_2}{R_{AC\_F1}M}U_1 \end{cases} \tag{7}$$

Furthermore, the voltage of the equivalent AC load of the FBR and battery load V_{ao} and V_{bo} can be calculated as follows:

$$\begin{cases} V_{ao} = -\dfrac{L_2}{M}U_1 \\ V_{bo} = \dfrac{R_{AC\_F2}}{j\omega M}U_1 \end{cases} \tag{8}$$

Combining Eq. (8), it is evident that when $|V_{ao}| > |V_{bo}|$, CV charging mode can be achieved. In CV charging mode, the voltage across C_r does not change suddenly. Moreover, the input impedance in the FBR mode can be expressed as follows:
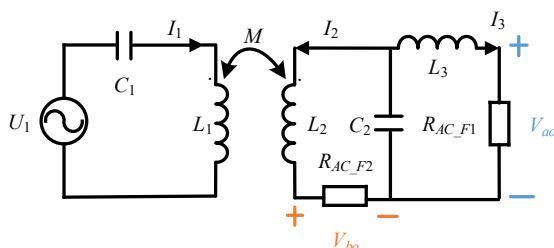
$$Z_{in} = \frac{U_1}{I_1} = \frac{R_{AC\_F1}(\omega M)^2}{(\omega L_2)^2 + R_{AC\_F1}R_{AC\_F2}}. \tag{9}$$

Furthermore, this study calculated the ZPA operations in CV charging mode using Eq. (9). However, as evident from Eq. (8), an increase in load resistance would cause $|V_{bo}| > |V_{ao}|$ to no longer hold true. In other words, when the load resistance value exceeds a critical value, the system would no longer operate in CV mode. In Eq. (8), assuming that V_{ao} is equal to V_{bo}, then $R_{AC\_F2} = \omega L_2$ can be obtained. Moreover, when $|V_{bo}| > |V_{ao}|$, the diodes D_1 and D_2 would be clamped. Subsequently, the state of the circuit will return to the FBR mode and its equivalent circuit model, as shown in Fig. 4, where $R_{AC\_F2} = R_{AC\_H}$. Drawing on the above discussion, the following conditions can be obtained using the following equation:

$$R_{L\_cr} = \frac{\pi^2 \omega L_2}{2}. \tag{10}$$

Notably, for WPT systems that operate in the standard frequency band for commercial use, the critical resistance R_{L_cr} usually exceeds several hundred ohms—a value that is difficult to reach when considering the internal resistance of the battery. Thus, a $|V_{bo}| > |V_{ao}|$ situation is not considered in the following discussions in this article.

A control flowchart of the proposed WPT system for CC/CV charging is presented in Fig. 8. When the process of charging begins, switch S remains turned off, during which the rectifier works in HBR mode and the WPT system works in CC charging mode. Subsequently, when the load voltage U_{out} is detected to be greater than the preset voltage U_{CV}, switch S is

Fig. 7. Equivalent AC circuit of the FBR mode.
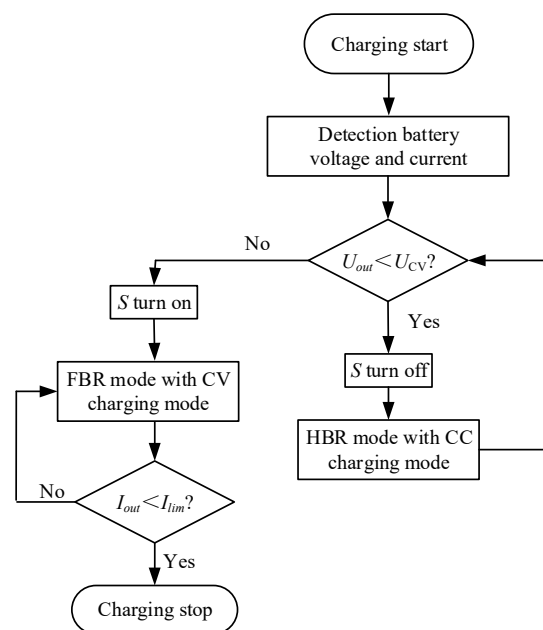
Fig. 8. Switching control flow chart of the proposed method.

turned on. As a result, the WPT system starts working in CV charging mode using FBR mode. Lastly, the charging process concludes when the load current is finally less than the preset current I_{lim}.

III. EXPERIMENTAL VALIDATION

To validate the feasibility and superiority of the theoretical analysis demonstrated in the previous section, a 48 V/0.7 A experimental prototype was designed and then fabricated, as shown in Fig. 9. The four MOSFETs are the GS66508B located on the inverter, while the four diodes used on the reconfigurable rectifier are IV1D12030U3. Notably, the variation in load resistance was simulated using an electronics load. Fig. 10 shows a photograph of the magnetic coupler of the transmitter coil, along with a ferrite black plate (PC40). Furthermore, the specific parameters are represented in Table 1. To ensure the accuracy of the compensation inductance L_3, it was given the same winding as the receiver coil and was placed at a considerable distance from the magnetic coupler.

At the beginning of the charging process, the system works in the CC charging mode. When battery resistance reaches 50% load condition, the system switches from CC charging mode to CV charging mode, and continues to maintain the CV charging mode until the end of the charging process.

As shown in Fig. 11, the fluctuation percentage of the charging current in CC charging mode is less than 1.6% (0.717–

0.705 A) while that of the charging voltage in CV charging mode is below 6.2% (48.21–51.42 V). This indicates that the proposed WPT system with a reconfigurable rectifier maintains agreeable CC/CV output characteristics throughout the charging process. Fig. 12 traces the waveforms of the input voltage U_1 and input current I_1 at different load conditions in the CC charging mode.

Fig. 12(a) and 12(b) show that changes in the load condition do not affect the input impedance angle between input voltage U_1 and input current I_1. Furthermore, the ZPA characteristics in the CC charging mode were verified. Fig. 13 presents the waveforms for load voltage U_{out} and load current I_{out} in the CC charging mode at the moment when the load resistance is switched from a 25% load condition to a 50% load condition.

It is evident that at the moment of load resistance switching, the load current re-attains its original value after a brief decrease, while the load voltage increases by half. A similar analysis was conducted for the CV charging mode, as shown in Figs. 14 and 15.

Furthermore, the ZPA characteristic in the CV charging mode was verified, the results of which are shown in Fig. 14. Notably, a change in load condition did not influence the input impedance angle between input voltage U_1 and input current I_1. Fig. 15 depicts the load voltage and load current waveforms in the CV charging mode on switching the load resistance from a 50% load condition to a 100% load condition. It is observed that the load current decreases by half, while the load voltage undergoes a slight change, only to subsequently return to a constant value.
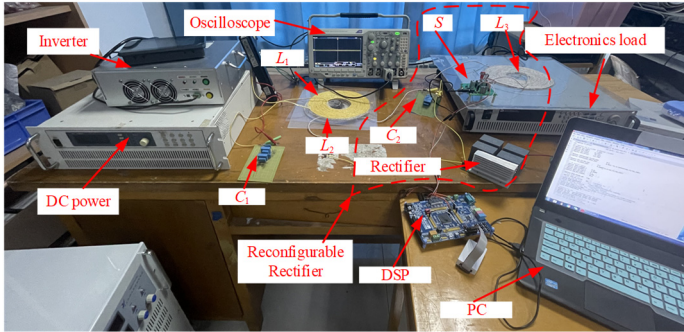
Fig. 9. Experimental prototype of the proposed WPT system.

Table 1. System specifications and their designed parameters

Parameter	Specification	Value
L_1	Inductance of transmitter coil	136.5 μH
L_2	Inductance of receiver coil	87.68 μH
L_3	Compensation inductance	88.43 μH
C_1	Compensation capacitor	25.67 nF
C_2	Compensation capacitor	40.67 nF
f	Operating frequency of system	85 kHz
M	Mutual inductance	35.7 μH
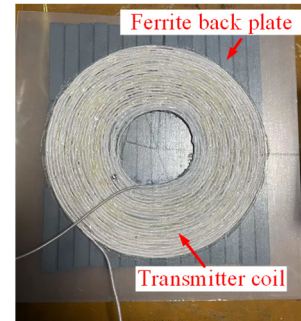
Fig. 10. Transmitter coil of the proposed WPT system.
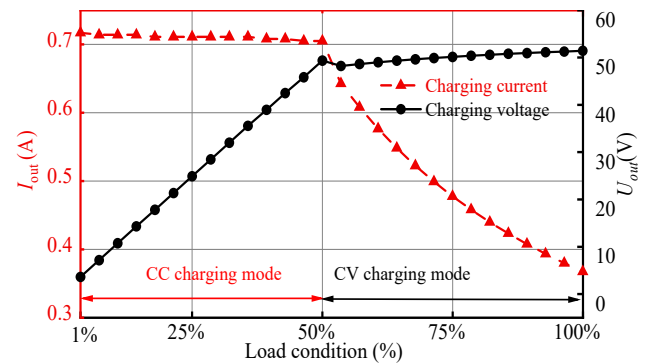
Fig. 11. Charging process of the proposed WPT system.

(a)

(b)
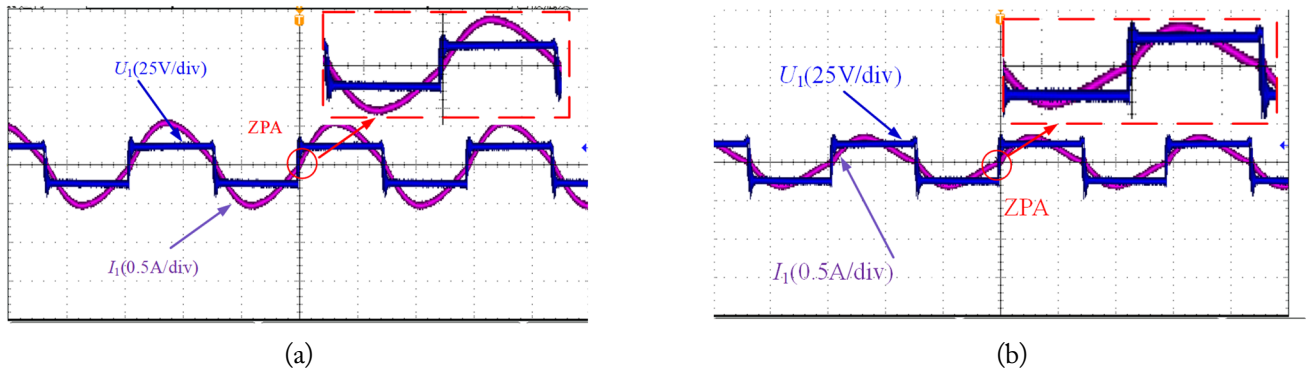
Fig. 12. Waveforms of input voltage U_1 and input current I_1 in CC charging mode: (a) 25% load condition and (b) 50% load condition.

As observed in Fig. 16, the power transfer efficiency of the entire charging process was successfully maintained above 86.23%. In the CC charging mode, the power transfer efficiency increased gradually with an increase in the load condition, with the maximum power transfer efficiency being 95.33%. Similar to the CC charging mode, the power transfer efficiency in the CV charging mode climbed from 88.76% to 94.28% with an increase in the load condition.

Table 2 provides an overview of a few of the typical methods currently used for implementing CC/CV charging modes, including their performance [9, 13, 20]. Compared to previous related studies, the method proposed in this paper offers marked improvements, such as fewer passive components and two charging modes achieved using only one AC switch at a fixed system frequency, which effectively reduced the difficulty of system control as well as system losses caused by the additional

introduction of devices.

Furthermore, all the controls were based on the secondary side, while the communication module could be avoided entirely. Hence, the proposed method is extremely suitable for scenarios in which communication between the primary and secondary sides is unstable, such as underwater or mine applications.
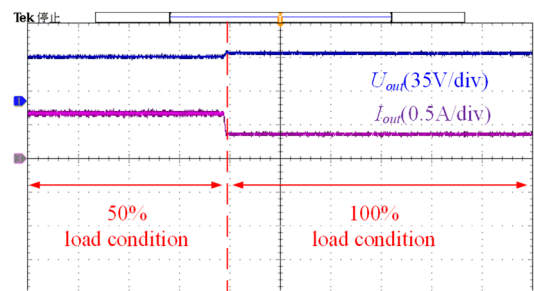
Fig. 15. Waveforms of load voltage and current at the moment of load resistance switching in CV mode.
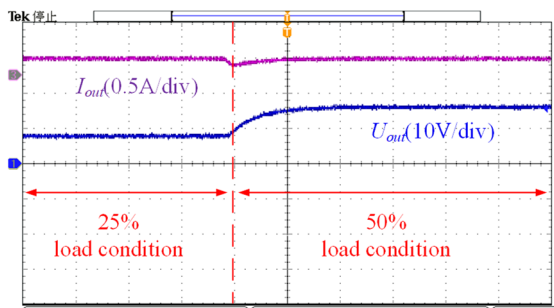
Fig. 13. Waveforms of load voltage and current at the moment of load resistance switching in CC mode.
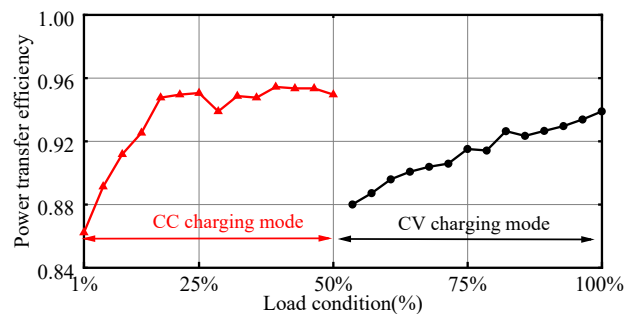
Fig. 16. Power transfer efficiency of the charging process.

(a)

(b)
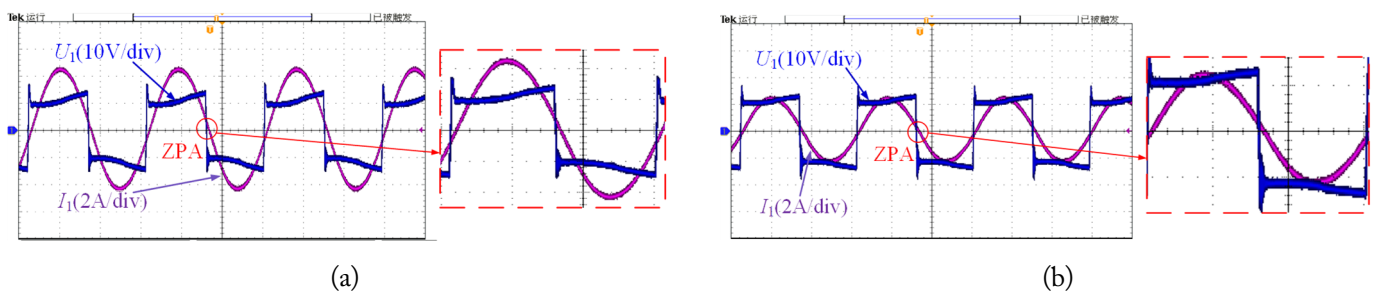
Fig. 14. Waveforms of input voltage U_1 and input current I_1 in CC charging mode: (a) 50% load condition and (b) 100% load condition.

Table 2. Comparison of the current work with previous related works

	Qu et al. [9]	Vu et al. [13]	Ji et al. [20]	This work
CC/CV switching method	Topology switching	Frequency switching	Topology switching	Topology switching
Total number of passive components	5	6	14	4
Communication	Yes	Yes	No	No
Total number of AC switches	3	0	1	1
Max DC-DC efficiency (%)	93.00	96.10	88.65	95.33

IV. CONCLUSION

This paper proposes a hybrid topology equipped with a reconfigurable rectifier for WPT systems. An AC switch is adapted to realize the change from the CC charging mode to the CV charging mode. When the switch is turned off, the rectifier operates in the HBR mode in conjunction with the S-S type compensation at the pre-stage, thus implementing the CC charging mode. In contrast, when the switch is turned on, the rectifier operates in the FBR mode, due to which the compensation structure of the system shifts to attain the S-LCL type, which then exhibits CV output characteristics. Notably, the ZPA condition could be maintained in both charging modes. In addition, the communication between the transmitter side and the receiver side could be eliminated in the proposed method. Furthermore, the experimental results show that fluctuations in charging current due to load condition changes in the CC charging mode can be maintained below 1.6%. For the CV charging mode, the fluctuations in charging voltage due to load resistance variation were less than 6.2%. Furthermore, during the charging cycle, power transfer efficiency was maintained above 86.23% throughout the process, with the maximum power transfer efficiency of the system reaching 95.33%. Overall, both the theoretical analysis and experimentation validate that the proposed hybrid WPT topology equipped with a reconfigurable rectifier exhibits agreeable CC/CV output characteristics throughout the charging process.

REFERENCES

[1] N. Ha-Van, H. Le-Huu, M. Thuy Le, K. Park, and C. Seo, "Free-positioning wireless power transfer using a 3D transmitting coil for portable devices," *Journal of Electromagnetic Engineering and Science*, vol. 20, no. 4, pp. 270-276, 2020. https://doi.org/10.26866/jees.2020.20.4.270

[2] A. U. Ibrahim, W. Zhong, and M. D. Xu, "A 50-kW three-channel wireless power transfer system with low stray magnetic field," *IEEE Transactions on Power Electronics*, vol. 36, no. 9, pp. 9941-9954, 2021. https://doi.org/10.1109/TPEL.2021.3064373

[3] M. Budhia, J. T. Boys, G. A. Covic, and C. Y. Huang, "Development of a single-sided flux magnetic coupler for electric vehicle IPT charging systems," *IEEE Transactions on Industrial Electronics*, vol. 60, no. 1, pp. 318-328, 2013. https://doi.org/10.1109/TIE.2011.2179274

[4] A. Alkasir, S. E. Abdollahi, S. Abdollahi, and P. Wheeler, "Analytical modeling of self and mutual inductances of DD coils in wireless power transfer applications," *Journal of Electromagnetic Engineering and Science*, vol. 22, no. 2, pp. 162-170, 2022. https://doi.org/10.26866/jees.2022.2.r.73

[5] C. Xiao, K. Wei, D. Cheng, and Y. Liu, "Wireless charging system considering eddy current in cardiac pacemaker shell: Theoretical modeling, experiments, and safety simulations," *IEEE Transactions on Industrial Electronics*, vol. 64, no. 5, pp. 3978-3988, 2017. https://doi.org/10.1109/TIE.2016.2645142

[6] J. Wang, H. Qu, B. Tao, C. Cai, Z. Lin, L. Xie, and F. Zhang, "Misalignment-tolerant integrated IPT systems for tram logistics robots featuring dual-purpose coupler," *IET Electric Power Applications*, vol. 14, no. 10, pp. 1984-1995, 2020. https://doi.org/10.1049/iet-epa.2020.0023

[7] Q. Zhu, M. Su, Y. Sun, W. Tang, and A. P. Hu, "Field orientation based on current amplitude and phase angle control for wireless power transfer," *IEEE Transactions on Industrial Electronics*, vol. 65, no. 6, pp. 4758-4770, 2018. https://doi.org/10.1109/TIE.2017.2767556

[8] G. Ning, K. Zhou, J. Liang, H. Wang, and M. Fu, "Reconfigurable and modular wireless charger based on dual-band design," *IEEE Transactions on Circuits Systems II: Express Briefs*, vol. 70, no. 9, pp. 3524-3528, 2023. https://doi.org/10.1109/TCSII.2023.3262245

[9] X. Qu, H. Han, S. C. Wong, K. T. Chi, and W. Chen, "Hybrid IPT topologies with constant current or constant voltage output for battery charging applications," *IEEE Transactions on Power Electronics*, vol. 30, no. 11, pp. 6329-6337, 2015. https://doi.org/10.1109/TPEL.2015.2396471

[10] C. S. Wang, O. H. Stielau, and G. A. Covic, "Design considerations for a contactless electric vehicle battery charger,"

IEEE Transactions on Industrial Electronics, vol. 52, no. 5, pp. 1308-1314, 2005. https://doi.org/10.1109/TIE.2005.855672

[11] M. Fu, H. Yin, X. Zhu, and C. Ma, "Analysis and tracking of optimal load in wireless power transfer systems," *IEEE Transactions on Power Electronics*, vol. 30, no. 7, pp. 3952-3963, 2015. https://doi.org/10.1109/TPEL.2014.2347071

[12] W. Zhang, S. Wong, C. K. Tse, and Q. Chen, "Load-independent duality of current and voltage outputs of a series or parallel compensated inductive power transfer converter with optimized efficiency," *IEEE Journal of Emerging and Selected Topics in Power Electronics*, vol. 3, no. 1, pp. 137-146, 2015. https://doi.org/10.1109/JESTPE.2014.2348558

[13] V. B. Vu, D. H. Tran, and W. Choi, "Implementation of the constant current and constant voltage charge of inductive power transfer systems with the double-sided LCC compensation topology for electric vehicle battery charge applications," *IEEE Transactions on Power Electronics*, vol. 33, no. 9, pp. 7398-7410, 2018. https://doi.org/10.1109/TPEL.2017.2766605

[14] J. H. Lu, W. J. Li, B. Li, and G. R. Zhu, "Variable compensation network for achieving constant current or voltage output in IPT system," in *Proceedings of the 2016 International Conference on Industrial Informatics–Computing Technology, Intelligent Technology, Industrial Information Integration (ICIICII)*, Wuhan, China, 2016, pp. 14-17. https://doi.org/10.1109/ICIICII.2016.0015

[15] C. Wang and J. Wang, "A hybrid LCC-SP compensation network with adjustable impedance angle used for single-stage wireless power transfer," *IEEE Transactions on Trans-portation Electrification*, vol. 9, no. 2, pp. 3452-3463, 2023. https://doi.org/10.1109/TTE.2022.3222869

[16] Y. Zhang, Z. Shen, W. Pan, H. Wang, Y. Wu, and X. Mao, "Constant current and constant voltage charging of wireless power transfer system based on three-coil structure," *IEEE Transactions on Industrial Electronics*, vol. 70, no. 1, pp. 1066-1070, 2023. https://doi.org/10.1109/TIE.2022.3150112

[17] D. Wang, X. Qu, Y. Yao, and P. Yang, "Hybrid inductive power transfer battery chargers for electric vehicle onboard charging with configurable charging profile," *IEEE Transactions on Intelligent Transportation Systems*, vol. 22, no. 1, pp. 592-599, 2021. https://doi.org/10.1109/TITS.2020.2976647

[18] S. Chen, Y. Chen, H. Li, N. Dung, R. Mai, Y. Tang, and J. S. Lai, "An operation mode selection method of dual side bridge converters for efficiency optimization in inductive power transfer," *IEEE Transactions on Power Electronics*, vol. 35, no. 10, pp. 9992-9997, 2020. https://doi.org/10.1109/TPEL.2020.2979769

[19] X. Li, H. Ma, S. Ren, J. Yi, S. Lu, and Q. Feng, "A novel LCL resonant converter with inherent CC-CV output for on-board chargers of plug-in electric vehicles," *IEEE Transactions on Power Electronics*, vol. 38, no. 4, pp. 4212-4217, 2023. https://doi.org/10.1109/TPEL.2022.3229025

[20] L. Ji, M. Zhang, B. Qian, and H. Sun, "A series of hybrid WPT systems with automatic switching between constant-current and constant-voltage modes on the secondary side," *IEEE Journal of Emerging and Selected Topics in Power Electronics*, vol. 11, no. 1, pp. 361-371, 2023. https://doi.org/10.1109/JESTPE.2022.3211253

Haibing Wen

https://orcid.org/0000-0003-1567-7172

received his B.S., M.S., and Ph.D. degrees from Northwestern Polytechnical University, Xi'an, China, in 2010, 2013, and 2021, respectively. Since 2021, he has been a full-time postdoctoral research fellow at the School of Electrical Engineering, Xi'an University of Technology, Xi'an, China. His research interests include wireless power transfer, electromagnetic shielding, and system optimization.

Jiayuan Li

https://orcid.org/0009-0004-7804-0931
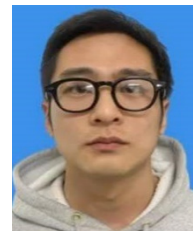
received his B.S. degree from Hunan University of Science and Technology, Xiangtan, China, in 2020. He is currently pursuing his M.S. degree at Xi'an University of Technology, Xi'an, China. His primary research interest is wireless power transfer.

Jiadong Yang

https://orcid.org/0009-0003-7828-5384
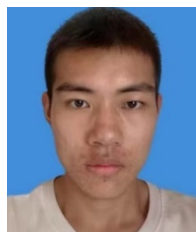
received his B.S. degree from Xi'an University of Posts & Telecommunications, Xi'an, China, in 2022. He is currently pursuing his M.S. degree at Xi'an University of Technology, Xi'an, China. His main research interest is wireless power transfer.

Lei Yang

https://orcid.org//0000-0002-4931-0486

received his B.S. degree from Information Engineering University, Zhengzhou, China, in 2011, and his M.S. and Ph.D. degrees from Northwestern Polytechnical University, Xi'an, Shaanxi, China, in 2014 and 2017, respectively. He is currently an associate professor at Xi'an University of Technology. His research interests include nonlinear control methods, wireless power transfer systems, and switched-capacitor converters.

Peng Wang

https://orcid.org/0009-0003-0078-7907

received his B.S. degree from Xi'an University of Technology, Xi'an, China, in 2021, where he is currently working toward his M.S. degree. His main research interest is wireless power transfer.

Yaopeng Zhao

https://orcid.org/0009-0009-5892-4998

received his B.S. and M.S. degrees from the School of Power and Energy at Xi'an Jiao Tong University, Xi'an, China, in 2010 and 2013, respectively. In 2021, he received his Ph.D. degree from the School of Microelectronics, Xidian University, Xi'an, China. He is currently an assistant professor at Xi'an University of Technology. His research interests include the design, packaging, and reliability testing of GaN power devices as well as applications pertaining to switching power supplies and inverters.

Kehan Zhang

https://orcid.org/0000-0001-7030-899X

received his B.S. and M.S. degrees in control theory and control engineering from Northwestern Polytechnical University, Xi'an, China, in 1993 and 1996, respectively. In 2000, he received his Ph.D. in control theory and control engineering from Xi'an Jiaotong University, Xi'an, China. He is currently a professor at Northwestern Polytechnical University. His research interests focus on DSP-based brushless DC motor control systems and wireless power transfer.

Xiangqian Tong

https://orcid.org/0000-0002-8833-1562

received his B.S. degree from Shaanxi Institute of Technology, Hanzhong, China, and his M.S. degree from Xi'an University of Technology, Xi'an, China, in 1983 and 1989, respectively. In 2006, he received his Ph.D. in electrical engineering from Xi'an Jiaotong University, Xi'an, China. He is currently a professor at Xi'an University of Technology. His research interests include the application of power electronics in power systems and the control of power quality.

Circularly Polarized Series Array and MIMO Application for Sub-Millimeter Wave/Terahertz Band

Thinh Tien Nguyen[1] (ID) · Dong Ho Kim[2] (ID) · Jung Han Choi[3] (ID) · Chang Won Jung[1,*] (ID)

Abstract

This article presents a compact, planar, and circularly polarized array antenna operating in the W-band (84.5–110 GHz), with all its prototypes fabricated using a low-cost, traditional, microwave printed circuit board composed of Rogers RT/duroid 5880 (ε_r = 2.2, tanδ = 0.009). The final design that was fabricated and measured was a 4 × 4 array antenna having an overall size of 9 mm × 20 mm × 0.254 mm that used series feeding to reduce its sidelobes. Measurements of the 4 × 4 patch antenna array showed approximately 6.9% 3-dB axial ratio bandwidth along with 15.2 dBi maximum right-hand circularly polarized (RHCP) antenna gain at 100 GHz. The array antenna yielded RHCP radiation characterized by a low profile, low cross-polarization levels (<–25 dB), low sidelobe levels ($\leq$–10 dB), and high radiation efficiency (>91%). Additionally, a two-port MIMO antenna system was investigated by considering side-by-side and front-to-front configurations, both of which achieved good isolation and considerable envelope correlation coefficient and diversity gain values. Therefore, the proposed series array and MIMO antennas can be reasonable candidates for 6G applications of the sub-THz band (100–110 GHz) in ultra-high-speed wireless and satellite communication systems.

Key Words: Array Antenna, Circular Polarization, Millimeter Wave, Patch Antenna, Terahertz Band.

I. INTRODUCTION

In recent years, research on applications of the sub-millimeter wave/terahertz frequency band (0.1–10 THz) has been gaining increasing attention, providing opportunities for the discovery of several promising applications. Specifically, the sub-THz band (0.1–1 THz), which has yet to be licensed for specific usage, is expected to play a significant role in future proposals for establishing wireless links with ultrahigh data rates (>100 Gbps), excellent dependability, and capacity for low-latency communications, since this band offers a broad atmospheric transmission window along with controllable losses [1].

However, the high path and molecular absorption losses related to THz frequencies, which affect the operation of wireless links, must first be addressed. To solve this issue in THz wireless and satellite communication systems, highly directional array antenna designs are essential [2].

Several array antennas with high gain and other desirable properties in the W-band (75–110 GHz) have already been proposed in the literature, including monopulse array [3–5], Yagi-like array [6], slot array [7], and low-temperature co-fired ceramic (LTCC) array antennas [8]. However, the construction of most of these antennas not only involves a high profile and high costs, but they also use linear polarization. The perfor-

mance of linearly polarized antennas often deteriorates due to polarization misalignment between transmitting and receiving antennas [9]. To overcome this challenge, circularly polarized (CP) antennas have been proposed. However, their bandwidth is narrow, their radiation efficiency often drops below 75% [3], and they involve high fabrication costs [8].

Fabrication capabilities have also significantly limited sub-THz antenna designs because wavelengths in the sub-THz band are relatively small. To address this, novel fabrication methods that use 3D printing, which reduces time and manufacturing costs, have been proposed. In spite of this, the performance of sub-THz antennas could not be significantly improved [3]. For example, LTCC technology, which yields high accuracy and low loss, is widely used in antenna-in-package technology. Chips can be integrated into an LTCC substrate through wire bonding or flip-chip interconnects [8]. However, LTCC materials have high fabrication costs, which largely depend on the desired number of crafting layers, and are time-consuming for sub-THz antennas. In contrast, antennas created by machining on printed circuit boards (PCB) [10] offer the benefits of low cost, lightweight design, and ease of fabrication.

Based on the above discussion, microstrip patch antennas [11, 12] emerge as a practicable solution for use in wireless and satellite communication systems because of their low profile and considerably lower fabrication time and cost. In this context, array antenna design can also be considered extremely important. Notably, the feed network design of array antennas [13–20] uses the series-fed technique and single-fed patches to reduce sidelobe levels (SLLs) and cross-polarization, thus achieving high gain.

Additionally, in terms of avoiding problems related to high data rates, which is a desirable feature in wireless communication since it enables the accommodation of more wireless services, multiple-input-multiple-output (MIMO) technology has gained increasing attention for its unique properties that offer increased channel capacity and improved reliability [21].

II. ANTENNA DEVELOPMENT PROCESS

This section describes the process of creating two orthogonal modes of resonance as diagonal modes to yield linear polarization along the direction of the two orthogonal modes of a truncated-corner square antenna. Notably, the operating frequency band and the feed point were chosen such that the two modes could be excited in the phase quadrature, leading to the formation of CP waves on implementing the antenna [13]. Furthermore, the robust development process from the 1 × 4 array antenna to the 4 × 4 array antenna is detailed in this section.

1. Analysis of the Array Factor of 1 × 4 Array Antenna

The configuration of the array antenna is depicted in Fig. 1.

Notably, the calculations of the theoretical dimensions w_p and l_p for the rectangular microstrip patch elements are provided in [13]. The substrate used for this structure is Rogers RT/duroid 5880 ($\varepsilon_r = 2.2$, $\tan\delta = 0.009$), with $h = 0.254$ mm.

Both the radiation patch and ground plane thicknesses were $t = 0.035$ mm. As shown in Fig. 1, the array antenna consists of four elements—the feed strip radiator and radiator positioned above the top substrate, the ground plane located beneath the bottom substrate, and two holes punched from the top to the bottom of the antenna. These holes are maintained in a fixed position between the connector, which is responsible for exciting the antenna and the PCB. Furthermore, the feedline signal head is slightly beveled to prevent contact between the antenna signal line and the connector ground. Numerical analysis of this antenna was conducted using the ANSYS High-Frequency Structure Simulator (HFSS). The design was thoroughly optimized before fabrication, the values of which are presented in Table 1. Moreover, the 1 × 4 array antenna, exhibiting a low SLL, was designed using the Dolph–Chebyshev distribution by adjusting the distance between adjoining single antenna elements. Notably, in the series-fed model of the patch array antenna, the spacing between single patches had to be optimized. Furthermore, because of the cumulative transmission characteristics of the preceding patches on the line, the transmission characteristics of the patches had to be accurately determined to achieve the desired amplitude and phase distribution of the radiating currents, along with the array. As shown in Fig. 1, the excitation amplitude of the linear microstrip array antenna is tuned using the distance between the single patches instead of the patch width. Fig. 2 clarifies the principle adhered to in this method, presenting the equivalent series circuit illustration with N antenna elements. The antenna elements are denoted using the radiation
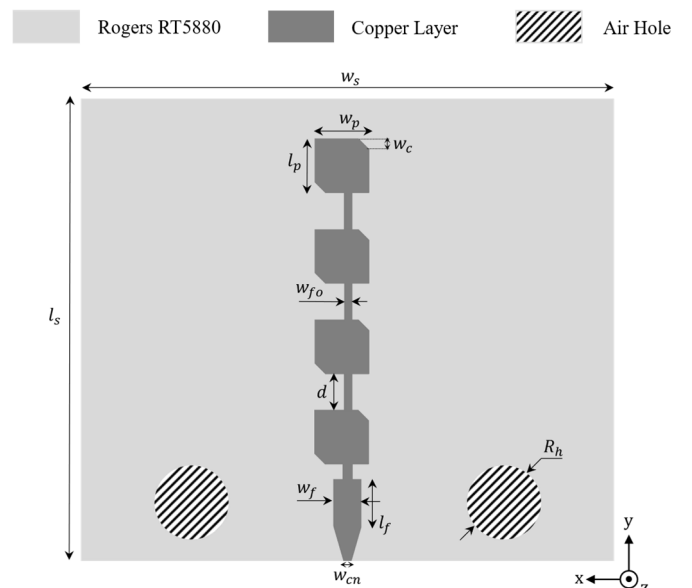

Fig. 1. Structure of the 1 × 4 array antenna.

Table 1. Optimized dimensions of the 1 × 4 array

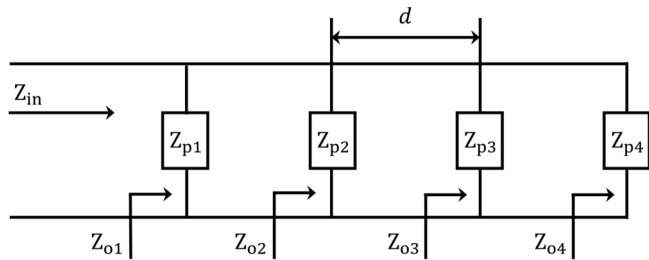| Parameter	Value (mm)
w_p	0.91
l_p	0.81
w_c	0.175
h	0.254
d	1.11
w_{f0}	0.125
w_f	0.75
l_f	1.5
R_b	0.825
w_{cn}	0.1
w_s	9
l_s	10

Fig. 2. Traditional structure of a 1 × 4 array antenna.

resistance Zp_i and their corresponding weights w_i, while the feedline's resistance caused by the patch elements is represented by Zo_i ($i = 1, 2, …, N$). The array factor (AF) can be determined using the following formula:

$$(AF)_{2N} = \sum_{i=1}^{N} w_i \cos(2nu) , \; u = \frac{kd\cos\theta}{2} = \frac{\pi d\cos\theta}{\lambda}. \quad (1)$$

For the proposed 1 × 4 array antenna, this study realized $N = 4$, from which the polynomial order constant was determined as $P = N - 1 = 3$, while the desired theoretical SLL value was 20 dB.

$$(AF)_4 = w_1 \cos(u) + w_2 \cos(3u). \quad (2)$$

On converting the SLL value from dB into an integer, the following equation was obtained:

$$R_o = 10^{SLL/20} = 10^{20/20} = 10. \quad (3)$$

To shorten and implement the result obtained in Eq. (3), the relations of the state between the cosine functions were utilized, as follows:

$$\cos(u) = \frac{z}{z_o}, \cos(3u) = 4\cos^3(u) - 3\cos(u). \quad (4)$$

With regard to the determination of the SLL value, parameter zo represents the magnitude of the SLL. Thus, the parameter z_o can be expressed as follows:

$$z_o = \cos\left(\frac{1}{P}cos^{-1}(R_o)\right) = \cos\left(\frac{1}{3}cos^{-1}(10)\right) = 1.54. \quad (5)$$

Using the equality between Eqs. (4) and (5), the above equation can be rewritten as follows:

$$(AF)_4 = (a_1 - 3a_2)\left(\frac{z}{z_o}\right) + 4a_2\left(\frac{z^3}{z_o^3}\right) = 4z^3 - 3z. \quad (6)$$

Ultimately, the AF of the linear array can be obtained using the following equation:

$$(AF)_4 = 1.736\cos(u) + \cos(3u). \quad (7)$$

Notably, the amplitude discrepancy among the radiation patch elements, which resulted in low SLLs, was found to be large. The theoretical ratio was 1:0.57, which was relatively difficult to reach due to the restricted variation range of resistance characteristics in terms of the distance of a single element. Therefore, this study realized the desired SLL values by changing the spacing between the single patches and maintaining an identical width for the radiating elements.

Furthermore, the gain of an array antenna (G_{Arr}) and that of a single antenna (G_S) can be related based on the following equation:

$$G_{Arr}(\theta,\varphi) = 2 \times (AF(\theta,\varphi))_{2N} + G_S(\theta,\varphi) \text{ (dB)}. \quad (8)$$

Therefore, using Eq. (8) at $d = 0.5\lambda$ and $\theta = 76°$, the theoretical array factor and theoretical gain of the 1 × 4 array antenna were achieved at 2 dB and 12 dBi, respectively.

As mentioned above, the spacing between the individual patches was optimized to achieve wide bandwidths for both the impedance and the 3-dB axial ratio (ARBW), while also maintaining the overall structural dimensions. To investigate this adjustment, the proposed prototype was examined by considering various values of d, as shown in Fig. 3. A significant increase in d resulted in a notable restriction of the –10 dB bandwidth, a reduction in the 3-dB ARBW, and a shift of the bandwidths toward lower frequencies. As observed in Fig. 3, the 1 × 4 array antenna with $d = 0.5\lambda$ results in a –10 dB bandwidth at 80–107.5 GHz (29.3%) and a 3-dB ARBW at 99.8–102.5 GHz (2.67%), while the corresponding bandwidths with $d = 0.6\lambda$ are 85–102.5 GHz (18.7%) and 97.5–99.8 GHz (2.3%), respectively. Ultimately, to obtain a wide bandwidth and improve the 3-dB ARBW, the optimal value of d was found to be 0.55λ, which achieved a –10 dB bandwidth of 83.2–105 GHz (23.2%) and a 3-dB ARBW of 98.2–102.1 GHz (3.9%).

2. *Analysis of 4 × 4 Array Antenna*

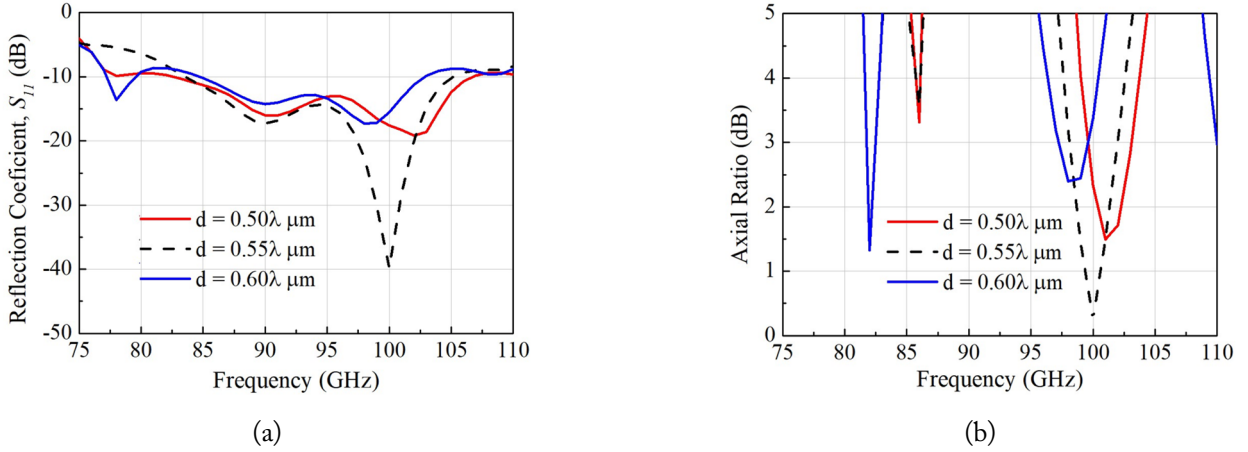The 4 × 4 array antenna proposed in this study was designed

Fig. 3. Simulated (a) $|S_{11}|$ and (b) axial ratio values of the 1 × 4 array antenna for various spacings between single elements (d).

to operate as a subarray for larger applications. Transitioning from the 1 × 4 array antenna described in Part 1, the proposed 4 × 4 array antenna was created using 1-to-4 power dividers. The geometry of the proposed 4 × 4 array antenna is illustrated in Fig. 4. The overall dimensions of the antenna were 9 mm × 20 mm × 0.254 mm (which is equal to $3\lambda_o \times 6.7\lambda_o \times 0.085\lambda_o$ at 100 GHz), with w_{s3} = 9 mm and l_{s3} = 20 mm. As observed in Fig. 4, the power divider bears a simple structure, using $\lambda/4$ impedance transformers of width w_{f1} = 0.085 mm, with T-junctions located where the energy separates into four identical 1 × 4 array antennas. In addition, since the radiation patches used in this structure were resonant, the input line to the patch could be matched.

Similar to the 1 × 4 array antenna, the spacing between the 1

× 4 array patches (d_2) was analyzed to choose a suitable value for achieving both wide impedance and 3-dB ARBW while retaining the configuration of the 1 × 4 array antenna. As a result, the proposed antenna was investigated by testing various values of d_2, the results of which are shown in Fig. 5. When the value of d_2 was increased to the threshold value, both the –10 dB impedance and 3-dB ARBW became slightly narrow and shifted to lower frequencies. Therefore, considering the results presented in Fig. 5, to ensure both wide –10 dB impedance and 3-dB ARBW, the optimal value of d_2 was found to be 0.6λ, which yielded corresponding bandwidths of 87.5–110 GHz (22.8%) and 98.3–104.8 GHz (6.5%).

Furthermore, to understand the generation of right-hand CP (RHCP) by the proposed antenna, changes in the surface current on top of the patch change at different phases were considered. First, as shown in Fig. 6, the current is displaced in the vertical direction at the 0° phase. In contrast, at the 90° phase, the current displaces in the opposite direction. This indicates that the current moves counterclockwise as the phase values increase, thus creating the RHCP wave [9]. In addition, it was observed that the current flow through each patch element gradually changed from the vertical to the horizontal direction at phase 0°. This confirms that the AR values at 100 GHz were mainly caused by the patch.

III. Measurement and Discussion

Fig. 7 shows a photograph of the antennas under test (AUTs) in a microwave anechoic chamber along with a magnified view of the proposed antennas fabricated using a machining process on the PCB. To assess radiation performance, a sub-THz planar far-field measuring setup was employed. The setup included a frequency extender (Oleson Microwave Labs. V10VNA2-T/R) in conjunction with a vector network analyzer (Agilent E8364B) to establish a Tx antenna system, as depicted in Fig. 7.
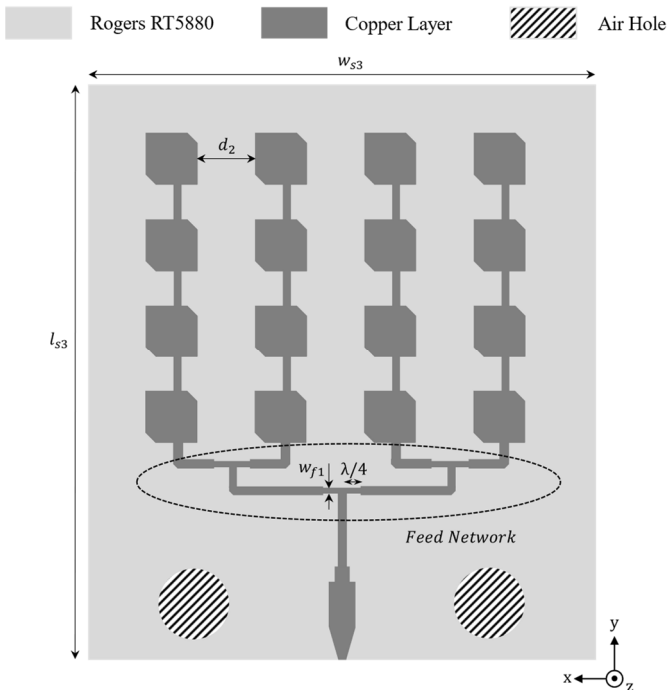
Fig. 4. Structure of the proposed 4 × 4 array antenna.

(a)

(b)
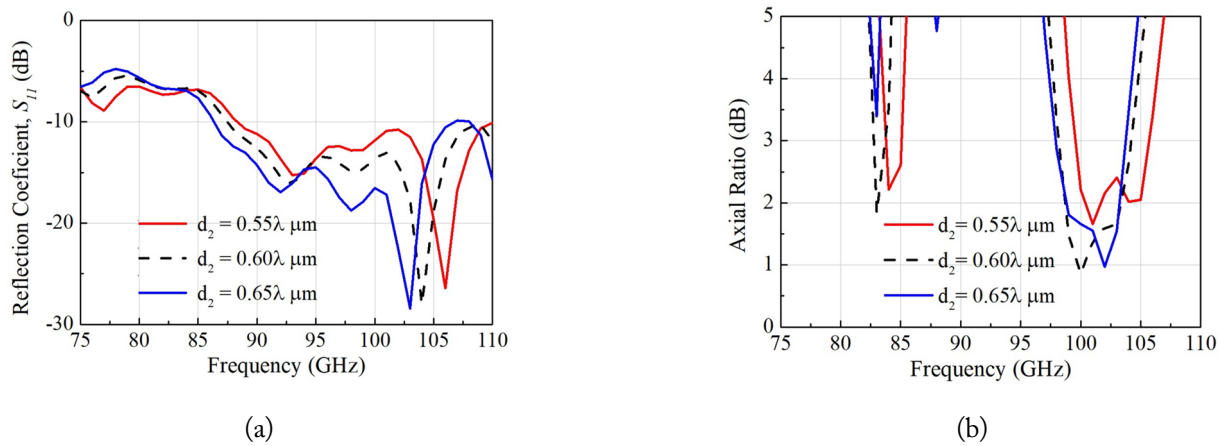
Fig. 5. Simulated (a) $|S_{11}|$ and (b) axial ratio values of the proposed 4 × 4 array antenna for various spacings between single patches (d_2).

(a)

(b)
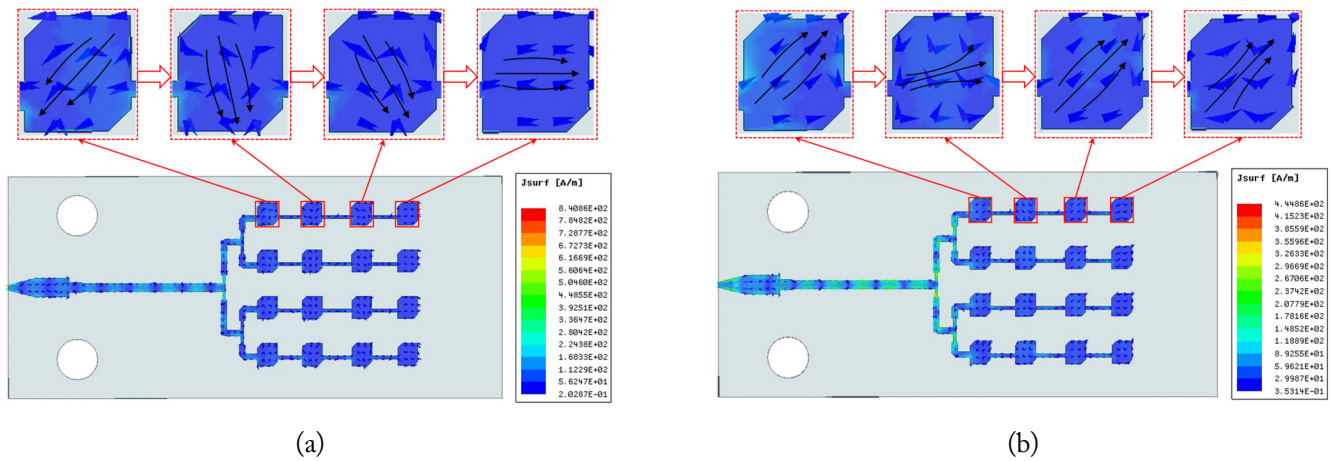
Fig. 6. Current distributions on top of the patch for different phases at 100 GHz: (a) 0° and (b) 90°.
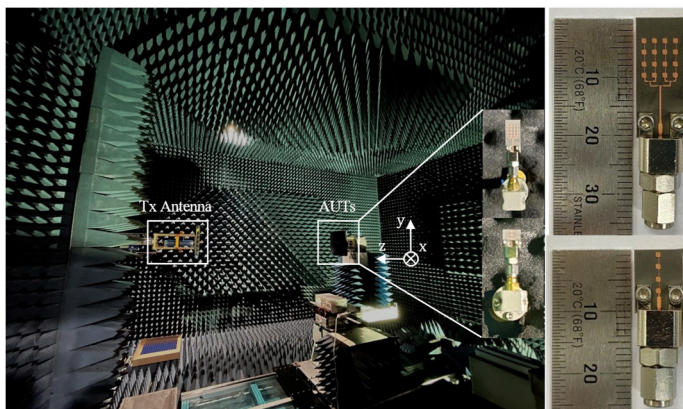
Fig. 7. Photograph of AUTs in a microwave anechoic chamber (left) and fabricated antennas (right).

The simulated and measured reflection coefficients of the 1 × 4 array antenna and the 4 × 4 array antenna are plotted in Fig. 8. Fig. 8(a) shows that the measured impedance bandwidth of the 1 × 4 array antenna at $|S_{11}|$ < –10 dB is 82.5–109 GHz (27.4%), whereas the simulated –10 dB impedance bandwidth is 83.2–105 GHz (23.2%). Meanwhile, the proposed 4 × 4 array anten-

na exhibits a measured –10 dB impedance bandwidth of 84.5–110 GHz (26.2%), while its simulated –10 dB impedance bandwidth is 87.5–110 GHz (22.8%), as shown in Fig. 8(b). Therefore, good agreement between the simulated and measured results was achieved. Although the measured results were slightly different from the simulated values, these deviations were primarily caused by the connection between the waveguide-to-coax adapter and the feedline of the antenna.

The measured and simulated normalized radiation patterns of the fabricated antennas at 100 GHz are depicted in Fig. 9. The measured radiation pattern exhibited RHCP along with a high front-to-back ratio (F/B) and broad high-power beamwidths (HPBWs) in the x–z and y–z planes. Furthermore, the measured cross-polarization levels were more than 20 dB below the main beam in the broadside direction at 100 GHz. In particular, the measured F/Bs were 25 dB and 34 dB, while the corresponding simulated values were 25.3 dB and 33.7 dB for both planes at 100 GHz, respectively. The HPBW simulated results approximated the measured results, which were slightly displaced at ±10 and ±1.50 for the x–z and y–z planes, respec-
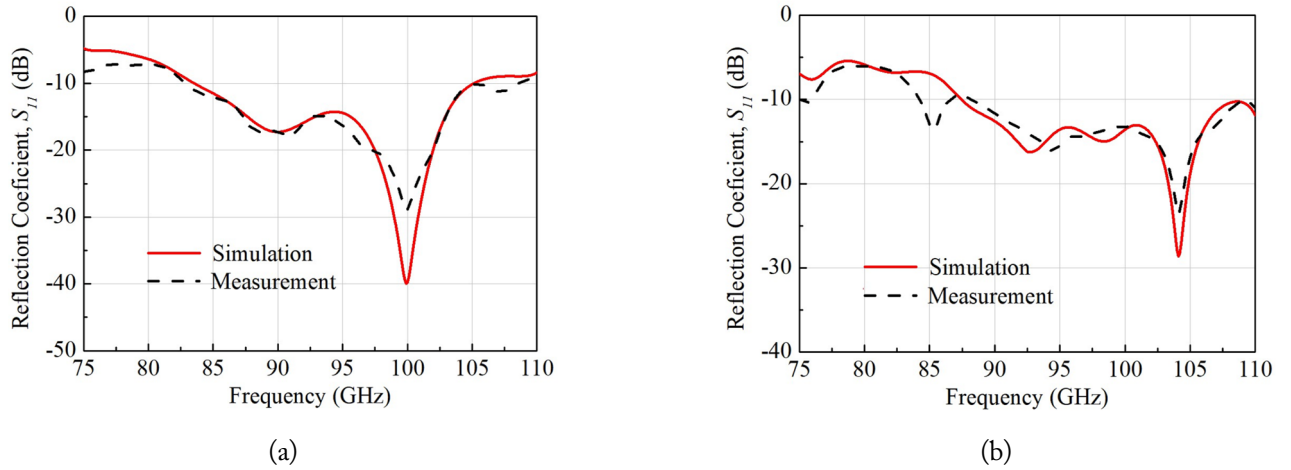
Fig. 8. Simulation and measurement of $|S_{11}|$ values of the proposed antennas: (a) 1 × 4 array antenna and (b) 4 × 4 array antenna.
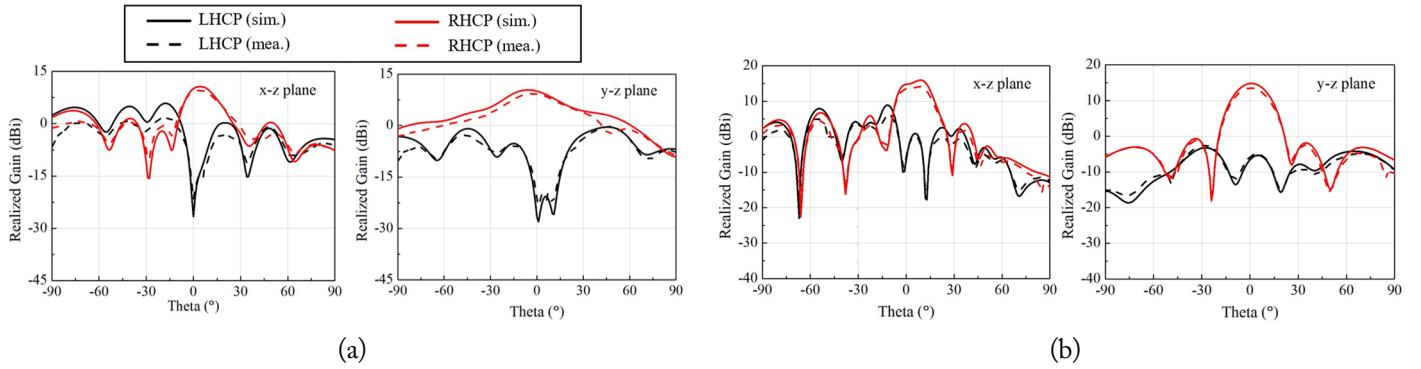
Fig. 9. Simulation and measurement results of the radiation pattern at 100 GHz for the (a) 1 × 4 array antenna and (b) 4 × 4 array antenna.

tively. With regard to the sidelobes, the measured SLL results differed only slightly from the simulated and theoretical SSL results. Notably, the SLL values of the 4 × 4 array antenna were relatively good ($\leq$–10 dB). The values of the specific parameters are mentioned in detail in Table 2.

The measurement and simulation results for the 1 × 4 array and 4 × 4 array antennas are provided in Fig. 10. For the antenna prototypes fabricated in this study—the 1 × 4 array and 4 × 4 array antennas—the measured 3-dB ARBWs were 97.7–102.1 GHz (4.4%) and 98.2–105.1 GHz (6.9%), whereas the simulated 3-dB ARBW were 98.2–102.1 GHz (3.9%) and 98.3–104.8 GHz (6.5%), respectively. Fig. 10 presents a comparison of the simulated and measured broadside gain values of the proposed antennas. The measured results show peak RHCP gains of 10.6 and 15.2 dBi, while the simulation results exhibit peak RHCP gains of 11.1 dBi, and 16 dBi for the 1 × 4 array and 4 × 4 array antennas, respectively.

Notably, the measured values exhibited slight discrepancies compared to the simulated and theoretical ones. These could be attributed to the precision of the fabrication process, unstable test fixture connection, part loss resulting from the thickness of the substrate that could have increased the loss caused by the antenna surface waves, and an unstable chamber environment.

Table 2 compares the principal characteristics of the proposed antenna with those of various recent sub-THz arrays operating in the W-band. Compared to previous works that fabricated antennas using a 3D printing process [3], the proposed antenna used a single layer and yielded significant improvements in radiation efficiency, HPBW, impedance, and 3-dB ARBW. For an antenna composed entirely of metal and fabricated using a machining process [4], the proposed antenna offers the advantages of a compact size, sufficient CP waves, and a significant improvement in HPBW and efficiency. Moreover, in contrast to the LTCC process, the proposed antenna bears a simple structure while also offering improvements in HPBW and impedance bandwidth, as well as a reduction in fabrication and material costs [8]. Although several antenna prototypes have been fabricated on PCB material by employing machining processes [5–7], the significance of the proposed array antenna lies in the fact that it obtained CP radiation and extended both the 3-dB AR and –10 dB impedance bandwidths. Furthermore, the measurement results demonstrate that the machining process on PCB not only reduced fabrication time and cost but also achieved high precision in fabrication.

Table 2. Comparison of the performance of recent antennas and proposed antennas operating in the W-band

Study	Size (λ_o^3)	−10 dB BW[a]	Pol./3-dB ARBW (%)	Peak gain (dBi)	Rad. efficiency (%)	# of elements	H-plane SLL (dB)	H-plane HPBW (°)	E-plane SLL (dB)	E-plane HPBW (°)	Ant. type	Fabrication technique
Tamayo-Dominguez et al. [3]	47×18.8×1.5	0.83% (93.2−94.8)	CP/0.83	27.8	70	−	−14	4	−15	5	Monopulse array	3D printing
Vosoogh et al. [4]	18.3×18.8×3	21.05% (85−105)	LP/−	30.5	70	16×16	−21	6	−16	4	Monopulse array	Machining
Cheng et al. [5]	41×39×0.16	3.2% (93−96)	LP/−	25.7	16.3	32×32	−8.3	3.23	−11.5	2.77	Monopulse array	PCB + Machining
Ghassemi et al. [6]	6.7×10×0.12	7.5% (94.2−101.8)	LP/−	18	90	4×4	−14	−	−11	−	Yagi-like array	PCB + Machining
Cheng et al. [7]	2.9×3.7×0.02	10.7% (75.9−84.5)	LP/−	11.1	38	4×4	−24	28	−13	20	Slot array	PCB + Machining
Cao et al. [8]	7.1×7.6×0.85	12.76% (88−100)	CP/10.1	22.8	N/A	8×8	−11	9	−11	12	LTCC array	LTCC
This work												
1×4 array	3×3.3×0.085	27.4% (82.5−109)	CP/4.4	10.6	92	1×4	−7	19	−17.3	36	Patch array	PCB + Machining
4×4 array	3×6.7×0.085	26.2% (84.5−110)	CP/6.9	15.2	91.5	4×4	−10	20	−15.6	21	Patch array	PCB + Machining

LP=linear polarization, CP=circular polarization.

[a]The number in parenthesis indicates the frequency range (GHz).
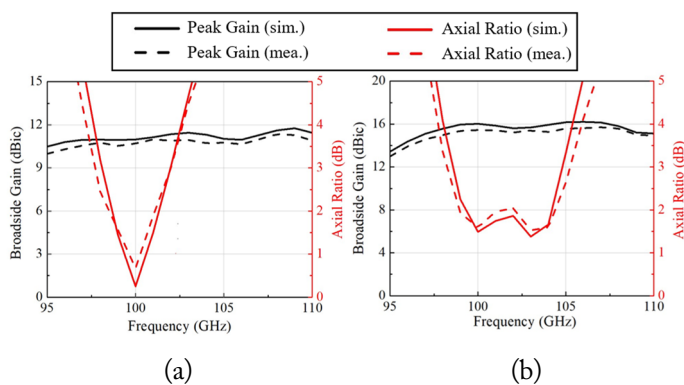
Fig. 10. Simulation and measurement results of the axial ratio and broadside gain values of the proposed antennas: (a) 1 × 4 array antenna and (b) 4 × 4 array antenna.

IV. MIMO ANTENNA SETUP

This section demonstrates the experiments conducted using MIMO antenna system configurations in the W-band. The arrangement of the two antennas depicted in Fig. 11 presents an orthogonal configuration along with a spacing dc. This orthogonal arrangement enabled polarization diversity and provided a means to minimize mutual coupling between distinct antenna components, thus eliminating the need for complex decoupling structures. Simulations of both the side-by-side and front-to-front configurations of the MIMO antenna were conducted. The total dimension of the board for both configurations was $L_{MIMO} \times W_{MIMO}$, which was equal to 20 mm × 20.5 mm and 38.2 mm × 9 mm, respectively.

Figs. 12 and 13 show the effects of the antenna element separation for both configurations by examining the impact of dc on antenna performance. On increasing dc from 4 mm to 6 mm, an enhancement in the isolation between elements was observed. Consequently, the optimal dc was determined to be 5 mm, which achieved a consistent reflection coefficient and favorable mutual coupling (<25 dB). This was established based on the experimental results obtained using the optimized dc value, which were consistent with the simulation results.
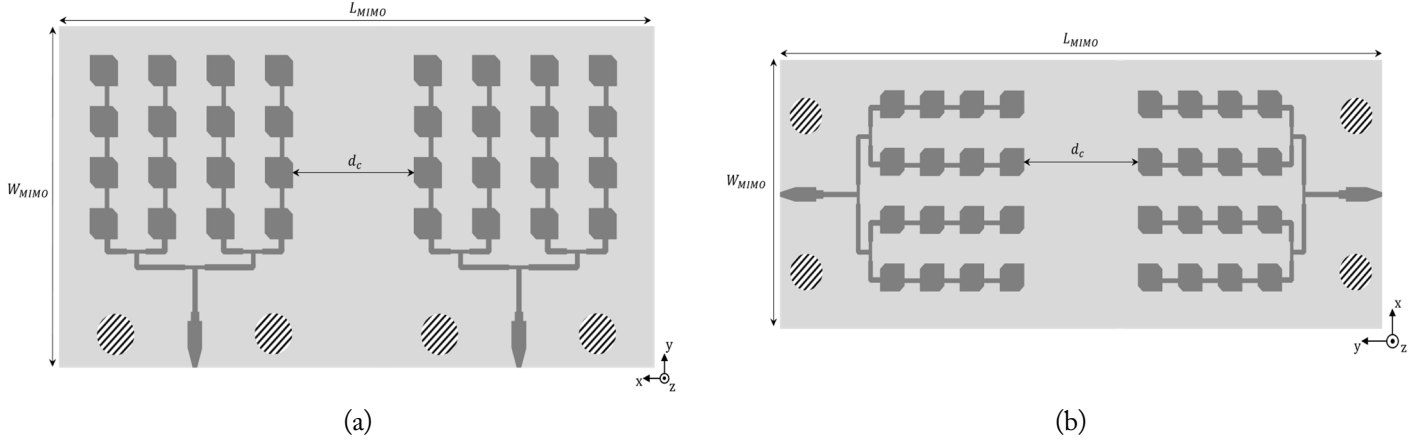
Fig. 11. Structure of the two-port MIMO antenna prototype for two distinct configurations: (a) side-by-side and (b) front-to-front.
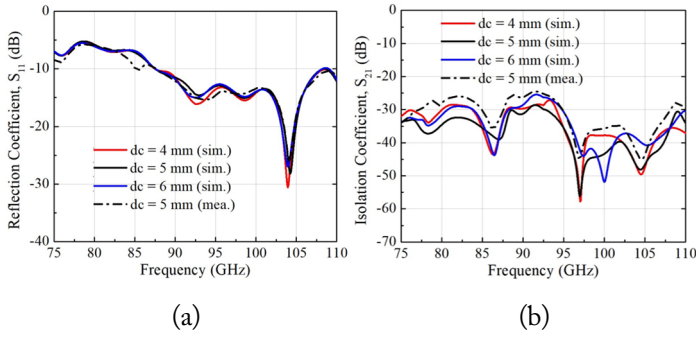
Fig. 12. Simulation and measurement result of the two-port MIMO antenna for the side-by-side configuration: (a) $|S_{11}|$ and (b) $|S_{21}|$.
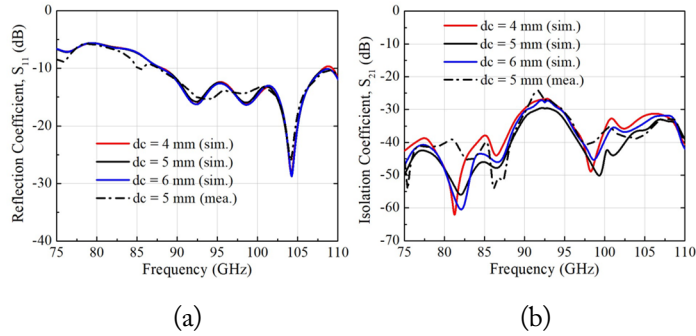
Fig. 13. Simulation and measurement result of the two-port MIMO antenna for the front-to-front configuration: (a) $|S_{11}|$ and (b) $|S_{21}|$.

Fig. 14. Simulated E-field of the two-port MIMO antenna system for side-by-side configuration at 100 GHz.
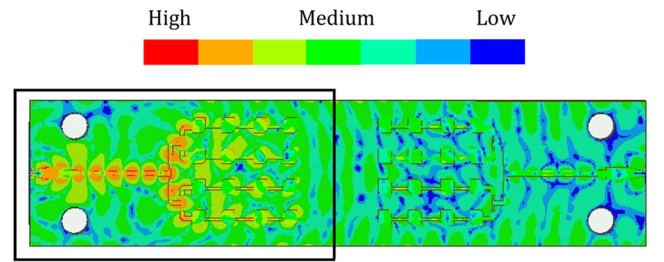
Fig. 15. Simulated E-field of the two-port MIMO antenna system for front-to-front configuration at 100 GHz.

Simulations of the E-field for the two ports of the MIMO antenna system are presented in Figs. 14 and 15. At 100 GHz, the E-field magnitude of the side-by-side configuration is observed as having collected around the patch elements and the notch of the feedline.

This indicates that all the elements in the antenna serve as radiation sources, resembling the front-to-front configuration. Furthermore, the field is primarily concentrated around the operated port with minimal E-field propagation to other ports, thereby affirming the high level of isolation between ports.

Fig. 16 plots the results of the simulated and measured radia-

tion patterns for both configurations at 100 GHz on arranging for antenna excitation at port 1 while simultaneously closing port 2 using a 50-load. The antenna pattern achieves a pencil pattern, while the radiation pattern of the MIMO antenna seems to change insignificantly compared to the proposed antenna. In particular, the measured performance achieves a peak gain of 14.8 dBi, while maintaining low SLLs (<-10 dB) and low cross-polarization (<-20 dB).

The diversity performance of the proposed MIMO antenna was examined by utilizing diverse performance metrics, including the envelope correlation coefficient (ECC) and diversity
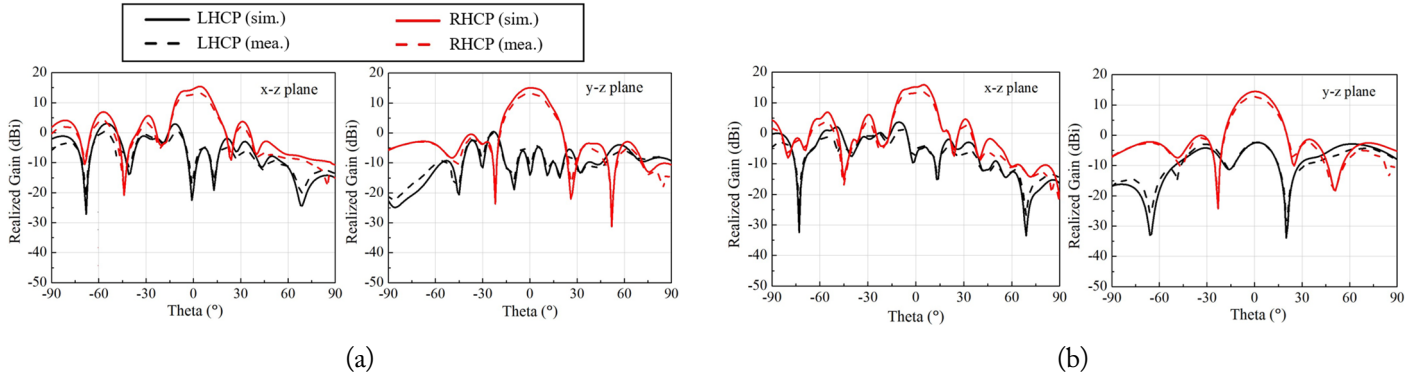
Fig. 16. Simulated and measured radiation patterns of the proposed two-port MIMO antenna at 100 GHz for both configurations: (a) side-by-side and (b) front-to-front.
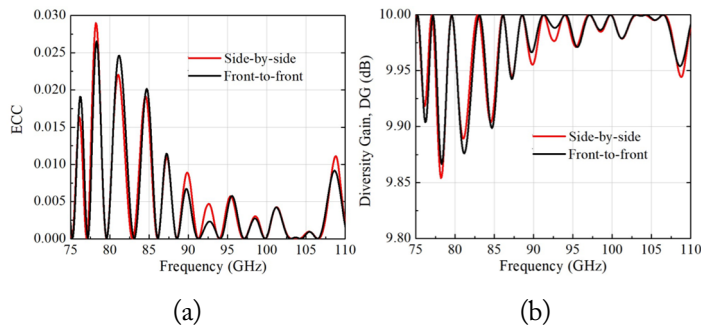
Fig. 17. Measured ECC and DG of the proposed two-port MIMO antenna for both configurations: (a) side-by-side and (b) front-to-front.

gain (DG). The ECC holds great importance in MIMO systems, as it quantifies the independence of antenna elements based on their characteristics. By employing the equation noted below, the ECC characteristics of each antenna element were derived by drawing on the complex simulated results [22]:

$$ECC = \frac{|S_{mm}^* S_{mn} + S_{mm}^* S_{nn}|}{(1 - |S_{mm}|^2 - |S_{mn}|^2) - (|S_{nm}|^2 - |S_{nn}|^2)^*}. \quad (9)$$

Fig. 17(a) illustrates the measured ECC results for the proposed two-port MIMO antenna, considering both scenarios. The simulations indicate ECC values below 0.0001 at 100 GHz.

To evaluate MIMO performance, the ECC and DG can be coupled using Eq. (10) [23], as noted below:

$$DG = 10 * \sqrt{1 - |ECC|}. \quad (10)$$

The results of the measured DG for both configurations are shown in Fig. 17(b) in terms of the frequency of the proposed MIMO antenna. The DG value is approximately 9.99 at 100 GHz, exhibiting excellent performance for both configurations.

V. Conclusion

This work presents a compact, wide impedance bandwidth, and high-gain array antenna for the W-band. A sequential evo-

lution from a 1 × 4 array antenna to a 4 × 4 array antenna was carried out. The 4 × 4 array antenna, with an overall size of 9 mm × 20 mm × 0.254 mm (approximately $3\lambda_o \times 6.7\lambda_o \times 0.085\lambda_o$ at 100 GHz), yielded a measured –10 dB bandwidth of 84.5–110 GHz (26.2%) and SLL peaks as low as –16 dB. The numerical and measurement results were found to be in feasible agreement. In addition, this is the first study to investigate configurations of the two-port MIMO antenna system for the W-band. Based on its superior characteristics, including a low profile, planar structure, wide operating bandwidth, stable RHCP radiation, low cross-polarization (<-25 dB), low SLLs (<-10 dB), and high radiation efficiency (>91%), and a reasonable fabrication method, the proposed 4 × 4 array and MIMO antennas can be considered appropriate candidates for 6G applications of the sub-THz band (100–110 GHz) in wireless and satellite communication systems.

References

[1] T. S. Rappaport, Y. Xing, O. Kanhere, S. Ju, A. Madanayake, S. Mandal, A. Alkhateeb, and G. C. Trichopoulos, "Wireless communications and applications above 100 GHz: Opportunities and challenges for 6G and beyond," *IEEE Access*, vol. 7, pp. 78729-78757, 2019. https://doi.org/10.1109/ACCESS.2019.2921522

[2] Y. He, Y. Chen, L. Zhang, S. W. Wong, and Z. N. Chen, "An overview of terahertz antennas," *China Communications*, vol. 17, no. 7, pp. 124-165, 2020. https://doi.org/10.23919/J.CC.2020.07.011

[3] A. Tamayo-Dominguez, J. M. Fernandez-Gonzalez, and M. Sierra-Castaner, "Monopulse radial line slot array antenna fed by a 3-D-printed cavity-ended modified butler matrix based on gap waveguide at 94 GHz," *IEEE Transactions on*

Antennas and Propagation, vol. 69, no. 8, pp. 4558-4568, 2021. https://doi.org/10.1109/TAP.2021.3060045

[4] A. Vosoogh, A. Haddadi, A. U. Zaman, J. Yang, H. Zirath, and A. A. Kishk, "W-band low-profile monopulse slot array antenna based on gap waveguide corporate-feed network," *IEEE Transactions on Antennas and Propagation*, vol. 66, no. 12, pp. 6997-7009, 2018. https://doi.org/10.1109/ TAP.2018.2874427

[5] Y. J. Cheng, W. Hong, and K. Wu, "94 GHz substrate integrated monopulse antenna array," *IEEE Transactions on Antennas and Propagation*, vol. 60, no. 1, pp. 121-129, 2012. https://doi.org/10.1109/TAP.2011.2167945

[6] N. Ghassemi, K. Wu, S. Claude, X. Zhang, and J. Bornemann, "Low-cost and high-efficient W-band substrate integrated waveguide antenna array made of printed circuit board process," *IEEE Transactions on Antennas and Propagation*, vol. 60, no. 3, pp. 1648-1653, 2012. https://doi.org/ 10.1109/TAP.2011.2180346

[7] S. Cheng, H. Yousef, and H. Kratz, "79 GHz slot antennas based on substrate integrated waveguides (SIW) in a flexible printed circuit board," *IEEE Transactions on Antennas and Propagation*, vol. 57, no. 1, pp. 64-71, 2009. https:// doi.org/10.1109/TAP.2008.2009708

[8] B. Cao, Y. Shi, and W. Feng, "W-band LTCC circularly polarized antenna array with mixed U-type substrate integrated waveguide and ridge gap waveguide feeding networks," *IEEE Antennas and Wireless Propagation Letters*, vol. 18, no. 11, pp. 2399-2403, 2019. https://doi.org/10.1109/ LAWP.2019.2917774

[9] S. S. Gao, Q. Luo, and F. Zhu, *Circularly Polarized Antennas*. Chichester, UK: John Wiley & Sons, 2014.

[10] I. Papapolymerou, R. F. Drayton, and L. P. Katehi, "Micromachined patch antennas," *IEEE Transactions on Antennas and Propagation*, vol. 46, no. 2, pp. 275-283, 1998. https://doi.org/10.1109/8.660973

[11] D. M. Pozar, "Microstrip antennas," *Proceedings of the IEEE*, vol. 80, no. 1, pp. 79-91, 1992. https://doi.org/10. 1109/5.119568

[12] D. K. Kong, J. Kim, D. Woo, and Y. J. Yoon, "Broadband modified proximity coupled patch antenna with cavity-backed configuration," *Journal of Electromagnetic Engineering and Science*, vol. 21, no. 1, pp. 8-14, 2021. https:// doi.org/10.26866/jees.2021.21.1.8

[13] D. M. Pozar and D. H. Schaubert, *Microstrip Antenna: The Analysis and Design of Microstrip Antennas and Arrays*. New York, NY: Institute of Electrical and Electronics Engineers, 1995.

[14] B. Jones, F. Chow, and A. Seeto, "The synthesis of shaped pat

terns with series-fed microstrip patch arrays," *IEEE Transactions on Antennas and Propagation*, vol. 30, no. 6, pp. 1206-1212, 1982. https://doi.org/10.1109/TAP.1982.1142963

[15] Y. B. Jung, I. Yeom, and C. W. Jung, "Centre-fed series array antenna for K-/Ka-band electromagnetic sensors," *IET Microwaves, Antennas & Propagation*, vol. 6, no. 5, pp. 588-593, 2012. https://doi.org/10.1049/iet-map.2011.0355

[16] Y. B. Jung, J. H. Choi, and C. W. Jung, "Low-cost K-band patch array antenna for high-sensitivity EM sensor," *IEEE Antennas and Wireless Propagation Letters*, vol. 9, pp. 982-985, 2010. https://doi.org/10.1109/LAWP.2010.2086423

[17] V. K. Kothapudi and V. Kumar, "Compact 1×2 and 2×2 dual polarized series-fed antenna array for X-band airborne synthetic aperture radar applications," *Journal of Electromagnetic Engineering and Science*, vol. 18, no. 2, pp. 117-128, 2018. https://doi.org/10.26866/jees.2018.18.2.117

[18] M. Fairouz and M. A. Saed, "A complete system of wireless power transfer using a circularly polarized retrodirective array," *Journal of Electromagnetic Engineering and Science*, vol. 20, no. 2, pp. 139-144, 2020. https://doi.org/10.26866/jees.2020.20.2.139

[19] V. K. Kothapudi, "SFCFOS uniform and Chebyshev amplitude distribution linear array antenna for K-band applications," *Journal of Electromagnetic Engineering and Science*, vol. 19, no. 1, pp. 64-70, 2019. https://doi.org/ 10.26866/jees.2019.19.1.64

[20] B. R. Shookooh, A. Monajati, and H. Khodabakhshi, "Theory, design, and implementation of a new family of ultra-wideband metamaterial microstrip array antennas based on fractal and Fibonacci geometric patterns," *Journal of Electromagnetic Engineering and Science*, vol. 20, no. 1, pp. 53-63, 2020. https://doi.org/10.26866/jees.2020.20.1.53

[21] M. A. Jensen and J. W. Wallace, "A review of antennas and propagation for MIMO wireless communications," *IEEE Transactions on Antennas and Propagation*, vol. 52, no. 11, pp. 2810-2824, 2004. https://doi.org/10.1109/TAP.2004.835272

[22] M. Hussain, S. Abbas, M. Alibakhshikenari, M. Dalarsson, and F. Falcone, "Circularly polarized wideband antenna for 5G millimeter wave application," in *Proceedings of 2022 IEEE International Symposium on Antennas and Propagation and USNC-URSI Radio Science Meeting (AP-S/URSI)*, Denver, CO, USA, 2022, pp. 830-831. https://doi.org/ 10.1109/AP-S/USNC-URSI47032.2022.9886807

[23] N. Sghaier, A. Belkadi, I. B. Hassine, L. Latrach, and A. Gharsallah, "Millimeter-wave dual-band MIMO antennas for 5G wireless applications," *Journal of Infrared, Millimeter, and Terahertz Waves*, vol. 44, pp. 297-312, 2023. https:// doi.org/10.1007/s10762-023-00914-5

Thinh Tien Nguyen

https://orcid.org/0000-0002-3166-1501

received his B.S. degree in electronics and telecommunications engineering from Hanoi University of Science and Technology (HUST), Vietnam, in 2021, and his M.S. degree in electrical engineering from the Seoul National University of Science and Technology, Seoul, South Korea, in 2023. He is currently an antenna engineer at Viettel High Tech (VHT), Hanoi, Vietnam. His current research interests include sub-THz antennas, frequency-selective surfaces, millimeter-wave applications, reflect/transmit-array antennas, and reconfigurable intelligent surfaces (RIS).

Jung Han Choi

https://orcid.org/0000-0002-2007-7238

received his B.S. and M.S. degrees in electrical engineering from Sogang University, Seoul, Korea, in 1999 and 2001, respectively, and a Dr.–Ing. degree from Technische Universität München, Munich, Germany, in 2004. From 2001 to 2004, he was a research scientist at the Institute for High-Frequency Engineering at Technische Universität München, Germany. During this time, he worked on high-speed device modeling and circuit development for high-speed optical communications. From 2005 to 2011, he worked at the Samsung Advanced Institute of Technology and the Samsung Digital Media & Communication Research Center, where he dealt with RF bio sensors, nano device modeling, and circuit design for millimeter wave applications, including 60 GHz CMOS. In 2011, he joined the Fraunhofer Institute (Heinrich-Hertz Institute), Berlin, Germany. His current research interests include active/passive device design and modeling, high-frequency circuit design, and metamaterials.

Dong Ho Kim

https://orcid.org/0000-0001-9136-8932

received his B.S. degree in electrical engineering from Yonsei University, South Korea, in 1997, and his M.S. and Ph.D. degrees in electrical engineering from the Korea Advanced Institute of Science and Technology (KAIST), South Korea, in 1999 and 2004, respectively. He worked at the 4G Wireless Technology Laboratory, Samsung Advanced Institute of Technology (SAIT), from 2004 to 2006, and the Mobile Communications Research Institute, Samsung Electronics, from 2006 to 2007. Since 2007, he has been working with the Department of Smart ICT Convergence Engineering, Seoul National University of Science and Technology (SeoulTech), South Korea. His current research interests include PHY/MAC design of 5G/6G mobile communication systems.

Chang Won Jung

https://orcid.org/0000-0002-8030-8093

received his B.S. degree in radio science and engineering from Kwangwoon University, Seoul, South Korea, in 1997, and his M.S. degree in electrical engineering from the University of Southern California, Los Angeles, CA, USA, in 2001. In 2005, he received his Ph.D. in electrical engineering and computer science from the University of California at Irvine, Irvine, CA, USA. He was a research engineer in the Wireless Communication Department, LG Information and Telecommunication, Seoul, South Korea, from 1997 to 1999. From 2005 to 2008, he was a senior research engineer at the Communication Laboratory, Samsung Advanced Institute of Technology, Suwon, South Korea. He joined Seoul National University of Science and Technology, Seoul, Korea, as a professor at the Graduate School of Nano IT Design Technology in 2008. Since 2022, he has been a professor in the Department of Semiconductor Engineering at the same institution. His current research interests include antennas for multi-mode multi-band communication systems, multifunctional reconfigurable antennas, electromagnetic interference, millimeter-wave applications, optically transparent electrodes, and wireless power transfer for energy harvesting.

Design of Magnetic Coupling Mechanism with Different Primary and Secondary Coils for Maximum Output Power

Zhongyu Dai[1] (ID) · Wenxi Peng[2] · Yake Tang[3] · Haoran Xu[4] · Huihui Wang[1] · Yanhu Zhai[1] ·
Ming Xue[1] (ID) · Xian Zhang[1,*] (ID)

Abstract

Output power is an important performance metric related to static or quasi-static wireless power transfer (WPT). As an important component of WPT, the electrical parameters of a magnetic coupling mechanism (MCM) are directly related to its output characteristics. Notably, an optimal WPT design is largely based on MCMs using the same primary and secondary coils. However, in some scenarios involving limited space, the physical structure and electrical parameters of the coils cannot be kept completely consistent. Based on the influence of physical parameters on coupling performance and system characteristics, an optimal design method for MCMs using different primary and secondary coils to ensure maximum output power is proposed. The best receiving coil within a limited space that achieves maximum power at a specific location was selected. Experiments were conducted, with the corresponding results verifying the correctness of theoretical and simulation analyses, as well as the effectiveness of the proposed method.

Key Words: Coils, Magnetic Coupling Mechanism (MCM), Output Power, Wireless Power Transfer (WPT).

I. INTRODUCTION

The continuous consumption of fossil fuels has made environmental problems, such as global warming, increasingly prominent. To address these circumstances, replacing petrol vehicles with electric vehicles (EVs) has become a strategic policy adopted by many countries [1–4]. Driven by the promotion of policies and incentives, the number of EVs has sharply increased. However, the widespread applications of EVs require proper solutions to their charging problems. Charging stations are the most common power replenishment equipment for EVs. However, manual operations are required in the charging process, posing risks pertaining to poor contact and electric shock on rainy days, among others [5, 6].

Wireless power transfer (WPT) offers a new solution for charging EVs [7, 8]. In WPT, the electromagnetic field is used as the medium for non-contact power transmission, thus eliminating safety issues such as sparks and electric shock. Combined with intelligent identification and control, manual operation during EV

charging can be entirely eliminated [9, 10] and completely unmanned operations can be achieved. The modular structure of WPT allows for embedded installations that do not require additional land, which is extremely beneficial for urban planning. WPT offers numerous advantages in the field of EV charging and, therefore, has received increasing attention in recent years [11, 12].

Extensive research and exploration has been conducted on WPT for EVs, mainly with regard to the converter and magnetic coupling mechanism (MCM) [13–15]. Converter technology is relatively mature, with a general efficiency higher than 95% or even 98% [16, 17]. The design of MCM can be divided into two parts—the compensation topology and the coil structure [18, 19]. The three most common forms of compensation topologies are series and parallel compensation, which are the basic compensation topologies [20, 21], and LCC compensation, which is representative of a new compensation topology for meeting specific performance demands [14, 22]. Furthermore, a unipolar Q-type coil is the most widely used structure prevalent in MCMs [23, 24]. However, to meet the high power requirements at close distance for EVs, the use of DD-type coil has been proposed [25, 26], since it comprises two-directional magnetic fields on one side, due to which it is also known as the bipolar coil.

In published research on WPT for EV charging, the optimization of transmission performance and structural parameters has usually been based on the identical structure of the MCM, which uses the same primary and secondary coils. However, in practical applications, EV wireless charging can be significantly affected by the characteristics of WPT and the application environment. For instance:

1) Placing the transmitter on the ground in EV wireless charging makes it easy to achieve a unified design, but the volume of the EV receiver may be limited.
2) The ground clearance of different EVs varies. Therefore, diverse kinds of EVs need to be optimized and designed under various transmission distances to achieve better performance.
3) Different batteries have varying characteristics. Therefore, to determine the optimal receiver, EV wireless charging needs to be adjusted according to the properties of the batteries.

Compared to fuel-based vehicles, EVs are at a disadvantage with regard to their power replenishment time. Addressing this issue would require greater output power from WPT to shorten the charging time [4, 11, 27]. Therefore, to build a unified transmitter, a targeted design should be developed for receivers of different EVs to achieve maximum power. The traditional optimal method for achieving maximum output power using the same coils is no longer applicable. Therefore, in this study, a design method for the MCM that employs heterogeneous primary and secondary coils is proposed. The size of the receiving coil, the transmission distance, and the load differences are com-

prehensively examined to achieve maximum output power at a fixed distance within a limited design space.

II. THEORETICAL ANALYSIS

1. Transmission Performance of WPT

In an LC resonant circuit, the frequency f of voltage and current are not affected by the ideal resonant frequency $f_0 = 1/\sqrt{LC}$, which always remains the same as the frequency f_{source} of the source. The difference in frequency $\Delta f = |f_0 - f_{source}|$ between the LC and the source only affects the equivalent impedance $X_{LC} = 2\pi f_{source}L - 1/2\pi f_{source}C$. In WPT, LC resonance, which is composed of coil inductance and compensation capacitance, exhibits the same characteristics. The simplified equivalent circuit for WPT using a series-series (SS) compensation topology is shown in Fig. 1. Notably, $R_t = R_S + R_{l1}$ and $R_r = R_L + R_{l2}$ refer to the total resistance of the primary and secondary sides, $X_t = \omega L_1 - 1/\omega C_1$ and $X_r = \omega L_2 - 1/\omega C_2$ denote the total reactance, and $X_M = \omega M$ is the mutual inductance reactance. Notably, Kirchhoff's voltage law proposes the following equation:

$$\begin{bmatrix} \dot{U}_S \\ o \end{bmatrix} = \begin{bmatrix} R_t + jX_t & -jX_M \\ -jX_M & R_r + jX_r \end{bmatrix} \begin{bmatrix} \dot{I}_t \\ \dot{I}_r \end{bmatrix}, \tag{1}$$

where current $\dot{I}_t$ and $\dot{I}_r$ of the primary and second sides, respectively, can be formulated as follows:

$$\begin{cases} \dot{I}_t = \dfrac{[AR_r + BX_r + j(AX_r - BR_r)]\dot{U}_S}{A^2 + B^2} \\ \dot{I}_r = \dfrac{(jA + B)X_M\dot{U}_S}{A^2 + B^2} \end{cases} \tag{2}$$

where $A = R_tR_r + X_M^2 - X_tX_r$, $B = R_tX_r + R_rX_t$.
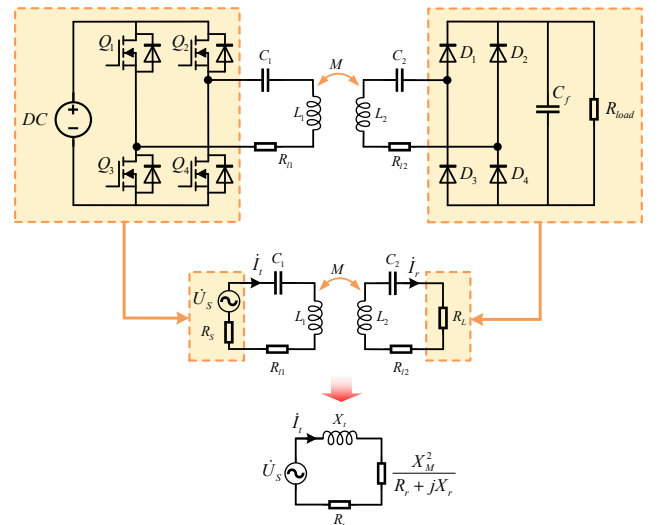

Fig. 1. Equivalent circuit of WPT with SS compensation topology.

Furthermore, the input power P_{in}, output power P_{out}, and transmission efficiency η can be expressed as follows:

$$P_{in} = \text{Re} \left[\dot{U}_S \dot{I}_t^* \right] = \frac{(AR_r + BX_r)U_S^2}{A^2 + B^2} \tag{3}$$

$$P_{out} = I_r^2 R_L = \frac{X_M^2 U_S^2 R_L}{A^2 + B^2} \tag{4}$$

$$\eta = \frac{P_{out}}{P_{in}} = \frac{X_M^2 R_L}{AR_r + BX_r} \tag{5}$$

where U_s and I_r are the modulus values of $\dot{U}_S$ and $\dot{I}_r$.

Based on Eq. (5), the variation in transmission performance with regard to mutual inductance was obtained, as shown in Fig. 2. It is noted that the larger the mutual inductance reactance X_M, the higher the transmission efficiency η. In other words, an increasing mutual inductance M or resonant frequency f can improve η. Furthermore, when output power P_{out} attains its maximum value, X_M must satisfy the following equation:

$$X_M^2 = \sqrt{(R_t^2 + X_t^2)(R_r^2 + X_r^2)} = |Z_t||Z_r|, \tag{6}$$

where $|Z_t| = \sqrt{R_t^2 + X_t^2}$ and $|Z_r| = \sqrt{R_r^2 + X_r^2}$ are the amplitudes of the primary and secondary impedances.

Moreover, for WPT with determined physical parameters, a unique value of mutual inductance M that maximizes the output power is usually considered. The maximum output is

$$P_{out \cdot max} = \frac{U_S^2 R_L}{2|Z_t||Z_r| + 2(R_t R_r - X_t X_r)} \tag{7}$$

When the primary and secondary sides of the MCM have the same resonant frequency, which is the same as that of the source, the ideal resonant state is achieved, $X_t = X_r = 0$. Therefore, Eqs. (6) and (7) can be simplified as follows:
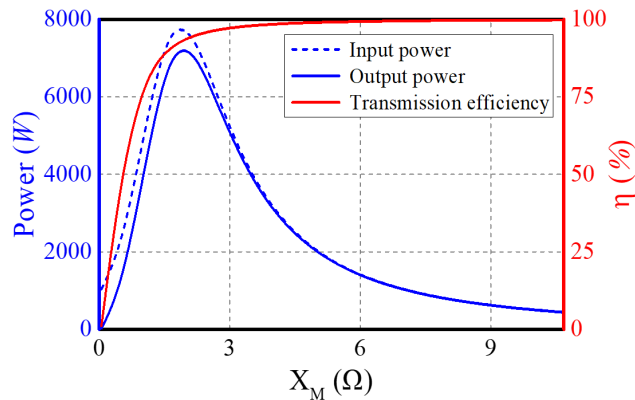
Fig. 2. Relationship between transmission performance and mutual inductance.

$$\begin{cases} X_M^2 = R_t R_r \\ P_{out \cdot max} = \dfrac{U_S^2 R_L}{4 R_t R_r.} \end{cases} \tag{8}$$

2. Maximum Output Power of the MCM

For an MCM characterized by different primary and secondary coils, the most significant electrical parameter characteristics are the unequal inductances L_1 and L_2. To meet resonance conditions, it may be assumed that the compensating capacitances and inductances satisfy $L_1 C_1 = L_2 C_2$. On determining the structural parameters of the transmitting coil and the resonance frequency f, Eqs. (6) and (7) indicate that the maximum output power is restricted by the secondary impedance X_r and the mutual inductance reactance X_M.

Notably, when the frequency f_{source} of the source is equal to the ideal resonant frequency f_0, $X_t = X_r = 0$ and $Z_t = R_t$, $Z_r = R_r$. Fig. 3 shows the impact of mutual inductance reactance X_M and receiver resistance R_r on the performance of equivalent circuit, where R_r is positively correlated and X_M is negatively correlated with input power P_{in}. Furthermore, when either R_r or X_M is kept constant, the output power P_{out} will initially increase and then decrease with an increase R_r or X_M. As for the transmission efficiency η, as shown in Fig. 3(c), it increases continuously with an increase in X_M or a decrease in R_r, indicating an opposite trend as that of P_{in}.

If the frequency f_{source} of the source is not equal to the ideal resonant frequency f_0, $X_t / L_1 = X_r / L_2 \neq 0$. Assuming $f_{source} = f_0 + \Delta f$, the receiver impedance Z_r cannot be considered purely resistive. Fig. 4 depicts the impact of mutual inductance reactance X_M and receiver resistance R_r on the performance of WPT under non-ideal resonant conditions. Notably, the variation trend of the output power P_{out} and transmission efficiency η is the same as that shown in Fig. 3(b) and 3(c). However, the maximum output power $P_{out \cdot max}$ is reduced. This indicates that the power difference in $P_{out \cdot max}$ is related to the frequency difference Δf—the greater the Δf, the greater the reduction in $P_{out \cdot max}$. Furthermore, the input power P_{in} in Fig. 4(a) is different from that in Fig. 3(a). This variation is the same as that of P_{out} under non-ideal resonant conditions—increasing initially to then decrease with an increase in X_M or R_r.

Based on the output power estimations shown in Figs. 3 and 4, a unique mutual inductance reactance X_M is observed, which achieves the maximum output power $P_{out \cdot max}$ for any receiver impedance Z_r, thus satisfying Eq. (6). Furthermore, $X_M = \omega M$ is influenced by mutual inductance M and angular frequency ω. The primary and secondary impedances—$Z_t = R_t + j\omega L_t + 1/j\omega C_t$ and $Z_r = R_r + j\omega L_r + 1/j\omega C_r$—are influenced by coil resistances R_{AC}, self-inductances L, and angular frequency ω. Moreover, M, R_{AC}, and L are found to be closely related to the physical parameters and the relative spatial
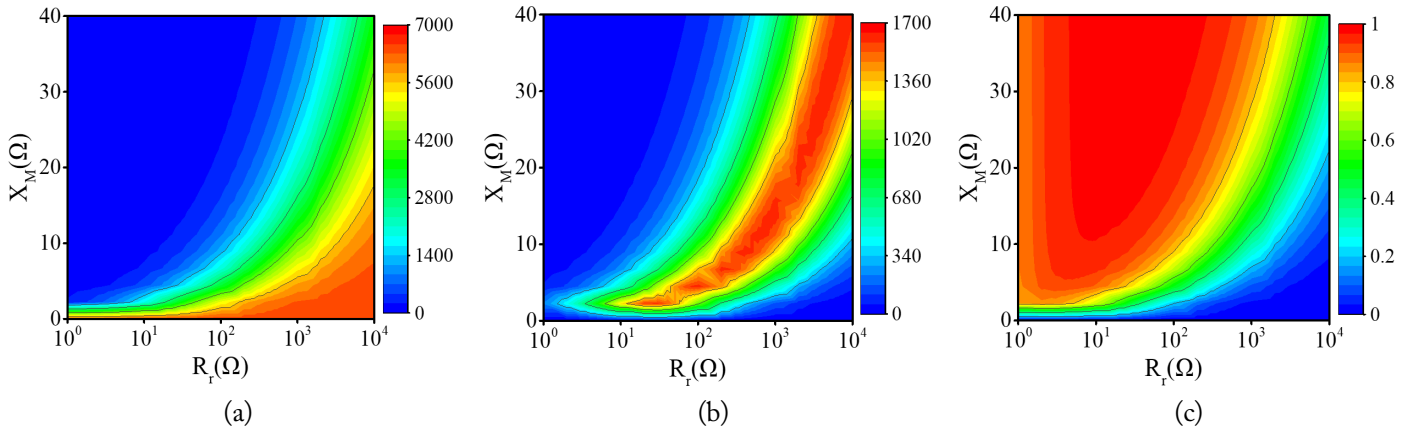
Fig. 3. Influence of mutual inductance reactance X_M and receiver resistance R_r on performance under ideal resonant conditions: (a) input power P_{in}, (b) output power P_{out}, and (c) transmission efficiency η.
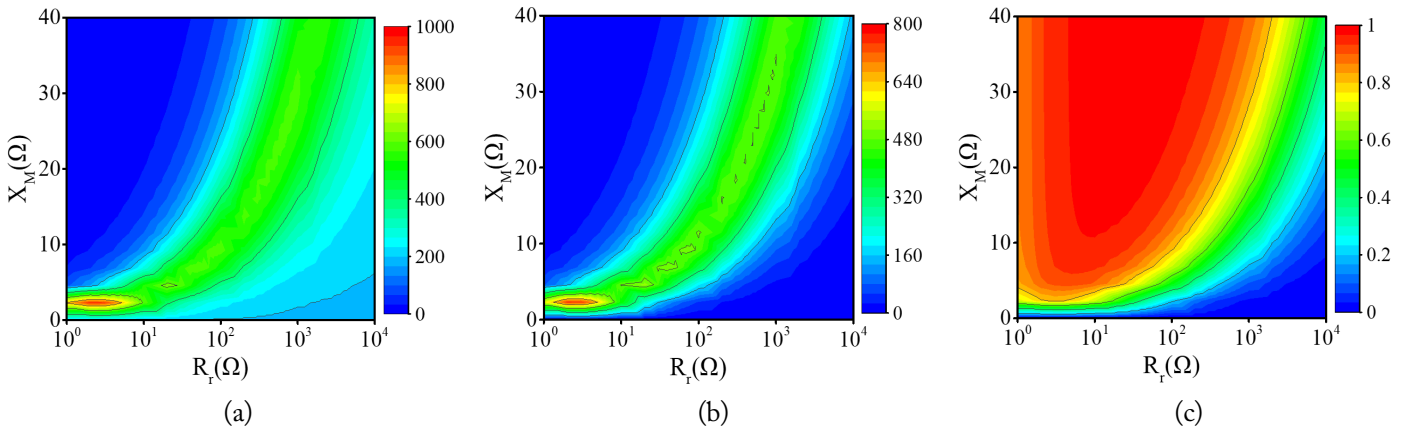
Fig. 4. Influence of mutual inductance reactance X_M and receiver resistance R_r on performance under non-ideal resonant conditions: (a) input power P_{in}, (b) output power P_{out}, and (c) transmission efficiency η.

position of the coils. Notably, during static WPT, the relative spatial position of the coils usually remains constant. This paper takes advantage of the effects of the physical parameters of coils on their electrical characteristics to optimize their structure and maximize their output power.

III. ELECTRICAL PARAMETERS OF THE MCM

For the MCMs used for EVs, electromagnetic shielding is usually implemented to reduce electromagnetic leakage and improve transmission performance, as shown in Fig. 5(a). Notably, the influence of electromagnetic shielding on the electrical parameters of coils does not change the impact of its physical parameters on self-inductance or mutual inductance [28, 29]. In other words, the difference in electrical parameters between two typical MCMs, as shown in Fig. 5, is mainly reflected in the relative magnetic permeability μ. To simplify the analysis process, this study considers an MCM without electromagnetic shielding, as shown in Fig. 5(b), as an example.

To achieve maximum output power within a limited design space, appropriate parameters and structure of the MCM need to be selected and optimized based on the application scenario. Therefore, the mutual inductance and impedance were adjusted to satisfy Eq. (6). For a typical MCM without electromagnetic shielding, as depicted in Fig. 6, the optimization of its physical parameters involves (i) both its transmitting and receiving coils, and (ii) either the transmitting or receiving coil. In the case of EV wireless charging, the transmitting coil can be flexibly designed, but the receiving coil is limited by the size of the EV chassis, which indi-
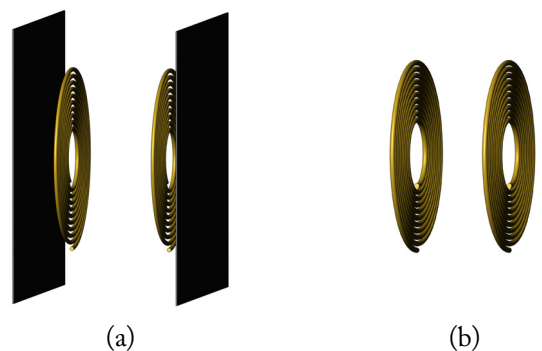
Fig. 5. A typical MCM with two coils: (a) with electromagnetic shielding and (b) without electromagnetic shielding.
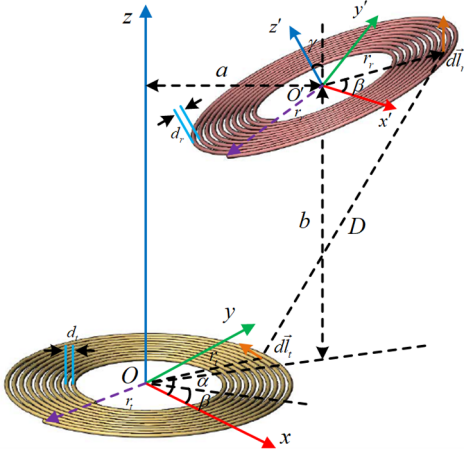
Fig. 6. A typical MCM without electromagnetic shielding.

cates that Situation (ii) applies in this particular context. Therefore, the current paper selected this situation as an example for optimizing the MCM. Subsequently, the transmitting coil and the relative spatial position were fixed, while the receiving coil was designed within a limited space to obtain the maximum output power.

1. Mutual Inductance

Mutual inductance refers to the ratio of the magnetic flux linking any coil to the current-producing magnetic flux in the other coil. For two parallel single-turn circular coils [30], the mutual inductance can be expressed as follows:

$$M_{ij}(RC_i, RC_j, D_{i,j}) = \frac{2\mu_0}{\alpha_{ij}}\sqrt{RC_i RC_j}, \tag{9}$$

where $\alpha_{ij} = 2\sqrt{RC_i RC_j / [(RC_i + RC_j)^2 + D_{ij}^2]}$, μ_0 is the permeability of vacuum, RC_i and RC_j are the radii of the two single-turn coils, and D_{ij} is the center-to-center distance of the two single coils. Furthermore, $P(\alpha_{ij})$ and $Q(\alpha_{ij})$ are the complete elliptic integrals of the first and second kinds, respectively.

Notably, a multi-turn coil can be considered equivalent to some single-turn coils with a continuously varying radius. Furthermore, since the coil radius RC is usually much larger than the wire radius r, the effect of r can be ignored. Therefore, the equivalent radius of the ith single-turn coil from the center can be formulated as $RC_i \approx RC_0 + (i-1)d$, where d is the pitch. Notably, all single-turn coils have the same center. Furthermore, the distance $D_{t,r}$ between the center of the transmitting coil and the receiving coil also remains constant. Assuming that the turns of the transmitting and receiving coils are N_t and N_r, the mutual inductance of MCM can be represented as follows:

$$M = \sum_{t=1}^{N_t}\sum_{r=1}^{N_r} M_{t,r}(RC_t, RC_r, D_{t,r}). \tag{10}$$

Mutual inductance is influenced by multiple factors, which can be divided into two categories—the physical parameters of the coils, including the pitch d_t, d_r, turns N_t, N_r, outer radii RC_t, and RC_r, and the relative spatial position parameters $D_{t,r}$, also known as spatial parameters of the MCM, including the vertical spacing b, horizontal offset a, and tilt angle γ. In static WPT, spatial parameters, usually regarded as known parameters in an optimal design, can be obtained through measurement and prediction.

To carry out an in-depth emamination of the influence of physical parameters on mutual inductance, a simulation model was employed in this study. According to the symmetry characteristics and magnetic field distribution of the MCMs, the transmitting and receiving coils have the same effect on mutual inductance. Therefore, in the simulation, only the parameters of the receiving coil were changed. Furthermore, to eliminate the influence of specific parameter values, the physical and electrical parameters were synchronously normalized, the function for which can be defined as follows:

$$\chi = \frac{\varsigma}{\varsigma_{av}}, \tag{11}$$

where ς_{av} represents the mean value of each parameter within the change range.

The outer radius RC_r, turns N_r, pitch d_r, and the mutual inductance M were synchronously normalized based on Eq. (11), the results of which are shown in Fig. 7. The slopes of the curves in Fig. 7 represent the strength of the influence of physical parameters on mutual inductance. A positive slope indicates an active impact, while slopes less than 0 indicate a negative correlation. In other words, the greater the absolute value of the slope, the more significant the effect. According to the variations of the curves observed in Fig. 7, it is evident that RC_r and N_r are positively correlated with M, while d_r is negatively correlated. Furthermore, the slopes corresponding to RC_r and d_r are approximately constant, indicating a linear correlation between RC_r, d_r, and M. It is further observed that as N_r increases, the rate of change of M decreases continuously. This may be attributed to the fact that when N_r increases while RC_r and d_r are constant, the increased RC gradually starts to decline, as a result of which the influence of N_r on M will continue to weaken.

From Fig. 7, it is evident that changing the transmitting coil does not affect the impact of the receiving coil on mutual inductance. Therefore, when a single-sided coil is optimized, the parameters of the other side can be considered known. Overall, the influence of the physical parameters of a single-sided coil on mutual inductance M can be expressed as

$$M = x_1(RC_r, N_r, d_r). \tag{12}$$

2. Self-Inductive

Mutual inductance is defined as the ratio of the magnetic flux linking one coil to the current-producing magnetic flux in the same coil [31, 32]. Its corresponding equation can be presented as:

$$L(RC_i, r_i) = \mu_0 RC_i \left[\ln \left(\frac{8RC_i}{r_i} \right) - 2 \right], \tag{13}$$

where, RC_i is the radius of the single-turn coil and r_i is the radius of the wire.

All equivalent single-turn coils have the same center—$D_{t,r} = 0$. The self-inductance of a coil with N_r turns can be formulated as:

$$L = \sum_{r=1}^{N} L(RC_r, r) + \sum_{t=1}^{N} \sum_{rl, r+t}^{N} M_{t,r}(RC_t, RC_r, D_{t,r} = 0). \tag{14}$$

According to Eq. (14), self-inductance is mainly influenced by its own turns N_r, radius RC_r, pitch distance d_r, and wire radius r_r. Therefore, during coil design, r_r is usually determined based on electrical parameters, such as current and voltage. Only N_r, RC_r, and d_r are the optimal targets for the coil structure. The results processed using Eq. (11) are presented in Fig. 8, which shows that the changes in the curves are similar to those shown in Fig. 7. The radius RC_r and turns N_r are positively correlated with self-inductance L_r, while the pitch d_r is

negatively correlated with the same. Furthermore, RC_r and d_r are linearly correlated with L_r. Notably, RC_r and N_r correspond to a larger curve slope, meaning that these parameters have a more obvious influence on L_r.

Therefore, the self-inductance of a coil is constrained only by its own physical parameters, which can be expressed as:

$$L = x_2(RC_r, N_r, d_r). \tag{15}$$

3. Resistance

The AC losses of an MCM comprise ohmic losses and radiation losses [7]. Ohmic losses dominate in the low-frequency range, while radiation losses become prevalent at high frequencies. For EV wireless charging, the resonant frequency generally remains between 80 kHz and 100 kHz, thus falling in the low-frequency range. Therefore, in this case, radiation losses can be neglected. As a result, only ohmic resistance was considered in this experiment, which can be expressed as follows:

$$R_{AC} = \sqrt{\frac{\mu_0 \omega}{2\sigma}} \frac{l}{4\pi r} = \sqrt{\frac{\mu_0 \omega}{2\sigma}} \frac{2R - (N-1)d}{8\pi r} N, \tag{16}$$

refers to the pitch, ω denotes angular frequency, and σ indicates conductivity.

According to Eq (16), the AC resistance R_{AC} is influenced by the operating parameters (angular frequency ω), wire material (conductivity σ, wire radius r), and structure parameters (radius
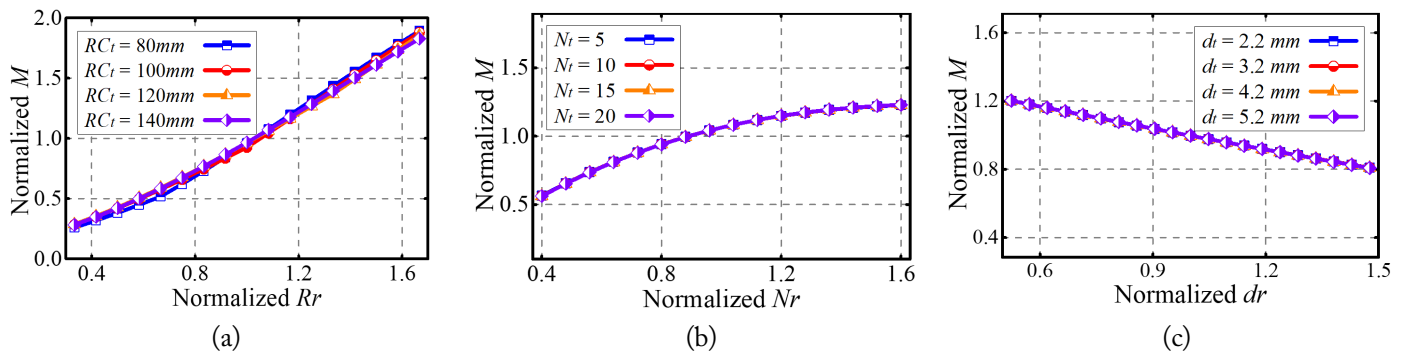

Fig. 7. Influence of physical parameters on mutual inductance: (a) outer radius, (b) turns, and (c) pitch.
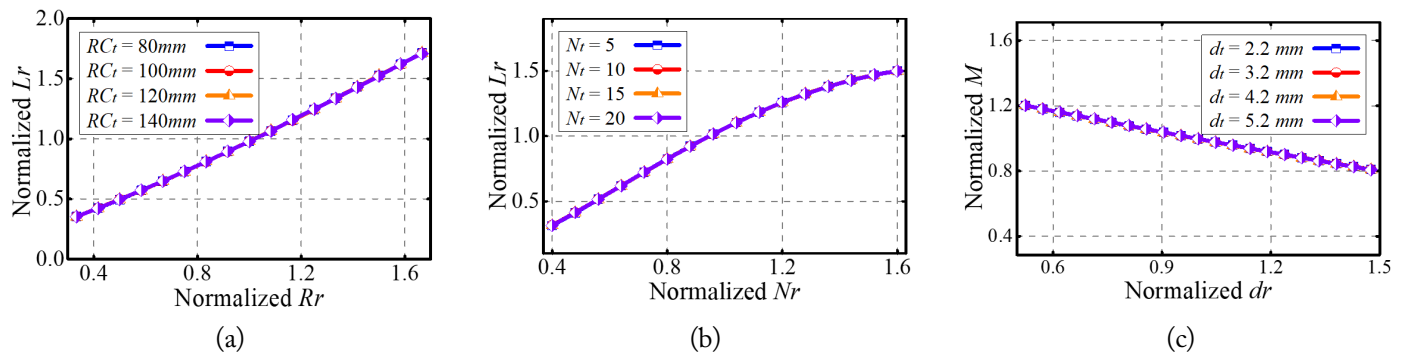

Fig. 8. Influence of physical parameters on self-inductance: (a) outer radius, (b) turns, and (c) pitch.
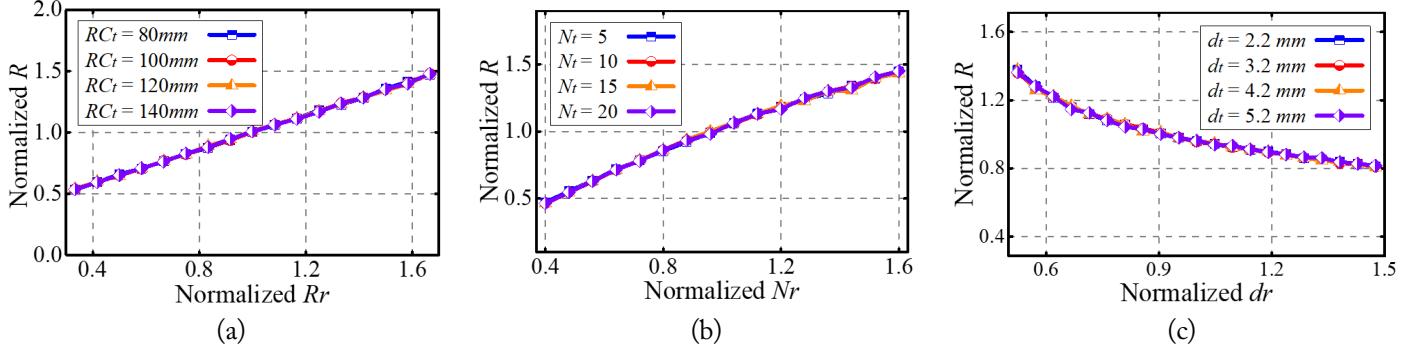
Fig. 9. Influence of physical parameters on AC resistance: (a) outer radius, (b) turns, and (c) pitch.

RC, turns N, pitch d). Therefore, the proposed design focused on structure parameters. The impact of physical parameters on AC resistance R_{AC} is demonstrated in Fig. 9.

Notably, the curves shown in Fig. 9 were also normalized. The influence of physical parameters on AC resistance R_{AC} is consistent with the overall trend shown in Figs. 7 and 8. The outer radius RC_r and turns N_r are linearly positively correlated with R_{AC}, while pitch d_r is negatively correlated. Essentially, it is observed that an increase in RC_r and N will lengthen the total length of wire l, while the increase in d_r will shorten it. Furthermore, Litz wire is usually used in WPT, as it can effectively mitigate the skin effect and proximity effect. There exists a linear relationship between physical parameters and R_{AC}. It is only when d_r is very small that it will exhibit a reduced skin effect. In other words, R_{AC} gradually decreases and eventually stabilizes with an increases of d_r.

AC resistance R_{AC} is also restricted by radius RC_r, turns N_r, and pitch d_r, which can be expressed as follows:

$$R_{AC} = x_3(RC_r, N_r, d_r). \qquad (17)$$

Overall, based on the effects of physical parameters on electrical parameters, Figs. 7–9 show that the outer radius RC_r, turns N_r, and pitch d_r have an almost similar influence on mutual inductance M, self-inductance L, and AC resistance R_{AC}.

IV. OPTIMIZATION OF THE MCM

1. Influence of Resonance Frequency

Based on the theories demonstrated above, resonance frequency f is another crucial factor that affects the maximum output power $P_{out·max}$. Eq. (6) clearly shows that f influences $P_{out·max}$, primary impedance Z_t, secondary impedance Z_r, and mutual inductance reactance X_M. The impact of f and mutual inductance M on transmission performance, based on Eqs. (3)–(5), are shown in Fig. 10, where the black dashed line corresponds to the ideal resonant frequency f_0. The area to its right represents the under-compensation area, where the primary reactance X_t and secondary reactance X_r are inductive. Moreover, input power P_{in} and output power P_{out} have the same variations. When frequency f reaches close to f_0, the maximum output power $P_{out·max}$ is achieved, while the corresponding mutual inductance M is the smallest. Furthermore, as f increases, the required M for $P_{out·max}$ increases along with it. This is because when f deviates from f_0, $X_t/L_1 = X_r/L_2 \neq 0$. This means that the larger the deviation, the larger the X_t and X_r. Since the modulus of the primary and secondary impedances $|Z_t|$ and $|Z_r|$ are also larger, a larger X_M was required. In addition, for the transmission efficiency η in Fig. 10(c), the higher the M, the higher the η. Therefore, η is also affected by f. A small M results in a
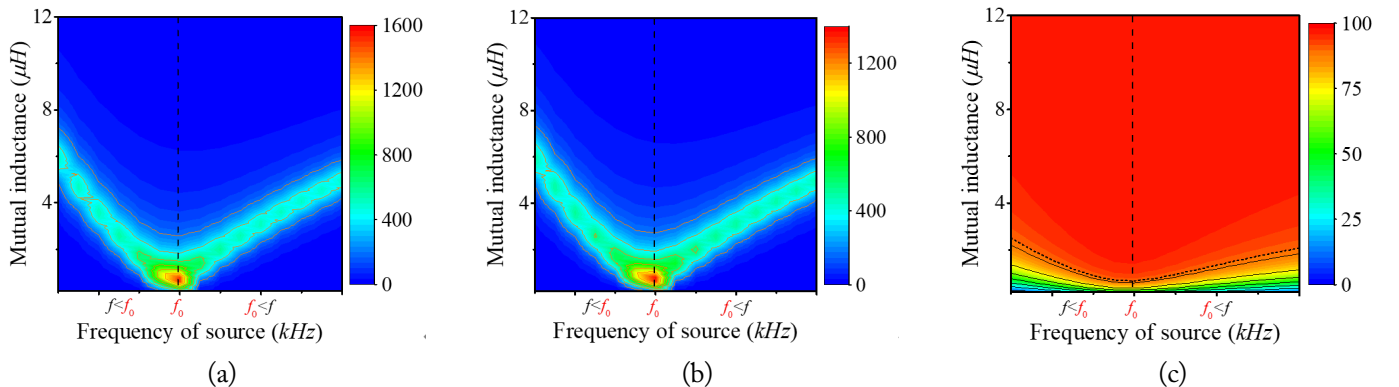

Fig. 10. The transmission performance varying with the mutual inductance and frequency: (a) input power (W), (b) output power (W), and (c) transmission efficiency (%).

higher f and lower η. At f_0, the required M is at its minimum. This is also why both the primary and secondary sides of an MCM should work in a resonant state as much as possible.

2. Design of the Receiving Coil

The design process for the receiving coil to obtain the maximum output power $P_{out \cdot max}$ is shown in Fig. 11. First, the wire radius r, load R_l, and resonance frequency f were determined based on the requirements of EV wireless charging. In a single-sided restricted MCM, the physical parameters of a transmitting coil and its relative spatial position are known conditions. Furthermore, self-inductance L_t and resistance R_{l1} of the transmitting coil were determined using Eqs. (15) and (17). For this purpose, the primary and secondary coils with similar or identical structures and parameters were considered the most favorable. Notably, for a restricted receiving coil, the radius RC_r should be as close as possible to that of the transmitting coil. Moreover, since the resistance of coils is usually small, R_{l1} is generally higher than the resistance of the source and the compensation capacitor. Therefore, it is included in Z_t. However, resistance R_{l2} of the receiving coil is usually ignored. Additionally, to reduce losses, the influence of the skin effect should be weakened as much as possible. The optimal pitch d_r was selected based on f. Subsequently, based on Eq. (6), the optimal impedance X_M was calculated. The outer radius RC_r, turns N_r, and pitch d_r of the receiving coil were selected using Eqs. (12), (15), and (17).

When both the primary and secondary sides of an MCM are in ideal resonance, $X_t = X_r = 0$, $Z_t = R_t$, and $Z_r = R_r$. The effect of self-inductance L_r of the receiving coil can be ignored, since it only needs to satisfy Eq. (6). In such a case, the turns of the receiving coil can be calculated without accounting for Eq. (15). As shown in Fig. 4, when the resonance frequency f deviates from the ideal value—that is, when it is in non-ideal resonance—an optimal mutual inductance M is present. Therefore, the effects of the self-inductances of both the transmitting and receiving coils must be accounted for in the design process shown in Fig. 11.

Requirements for wireless charging and limitations on design space

1. Determine wire radius, frequency, load, etc.
2. Determine the self-inductance, resistance, etc. of transmitting coil according to (15) and (17).
3. Determine the outer radius of receiving coil based on the limited space.

Determine the optimal pitch range of the receiving coil, whether the internal resistance of coils is included, etc.

Calculate the optimal mutual inductance (or mutual inductance) based on equation (6).

Calculate the optimal radius, turns, and pitch according to (12), (15), and (17), and design the optimal coil structure.

Fig. 11. Design flow of an optimal receiving coil.

V. EXPERIMENTS

Four coils were wound with 0.1 mm × 500 Litz wire, maintaining a pitch of 5 mm. One of the coils was a transmitting coil, while the other three were receiving coils. The representative symbols and corresponding structures are listed in Table 1, while the physical and electrical parameters of the four coils are shown in Table 2. Excluding the reserved length of the wire, the total lengths of the four coils were 250π cm, 176π cm, 210π cm, and 240π cm. The ratio of wire length to AC resistance was approximately equal, consistent with the theoretical derivation in Eq. (16). Furthermore, the ratio of self-inductance to the number of turns was closely aligned with the law depicted in Fig. 8(b). Notably, the SS compensation topology was selected. Coils and corresponding compensation capacitors together formed the

Table 1. Symbols and their means and structures

Symbol	TC	RC1	RC2	RC3
Means	Transmitting coil	Receiving coil 1	Receiving coil 1	Receiving coil 3
Structure				
Wire length of coil (cm)	250π	176π	210π	240π
Optimal transmission distance (cm)	–	25	27	28

transmitter and the different receivers, ultimately generating different MCMs. The representative symbols and meanings of the transmitter, receivers, and MCMs are presented in Table 3.

The resonant frequency was selected as 85 kHz. A vector analyzer (TH2826) was employed to perform the impedance characteristics. The sweep frequency range was 50 kHz–150 kHz. Notably, compensation capacitances of the transmitter and receivers were adjusted to meet the reactance X of 0 in frequency $f = 85$ kHz. Fig. 12 traces the variations in X and resistance R with f. It is evident that X increases continuously with an increase in f, changing from negative (capacitive) to positive (inductive). Notably, compensation capacitor banks are composed of standard capacitors (with certain errors). Table 2 presents the actual compensation capacitances calculated. Due to the parasitic capacitances of the coils, the actual compensation capacitances were slightly lower than those calculated based on resonance. Furthermore, the resistances of the transmitter and receivers were approximately the sum of those of the coils and the corresponding capacitors.

This study constructed three MCMs, as shown in Table 3. Fig. 13 presents the variation in mutual inductance M with transmission distance D when the transmitting and receiving coils face each other. It is observed that as D increases, M continues to decrease—first fast and then slow. Furthermore, the more turns the receiving coil has, the greater the M of the MCM that it forms. This result is consistent with the theoretical analysis, thus verifying that in a limited space (that is, the

radius of coils remains unchanged), the adjustment of turns can ensure that the same M at different D.

Under ideal resonant conditions, the load R_L remained constant, but the transmission distances D of the MCMs changed (essentially, the change in mutual inductance M in Fig. 13). Furthermore, Fig. 14 shows the variations in output power P_{out} and transmission efficiency η with the transmission distance D. It is evident that the trends of all three MCMs are the same. As D increases, P_{out} increases at first and then declines. η shows a continuous downward trend. Furthermore, the more the turns of the receiving coil, the greater the η. All three MCMs achieved maximum P_{out} at η of around 50%. However, the optimal D corresponding to the maximum P_{out} was different—25 cm, 27 cm, and 28 cm for the three MCMs.

To achieve maximum output power P_{out}, Eq. (6) had to be met. At ideal resonance frequency f_0, the primary impedance Z_t refers to the sum of the resistances of the coil and compensation capacitor, which showed almost no change. Meanwhile, the secondary impedance Z_r includes the resistances of the coil, compensation capacitor, and load. Usually, the resistance R_L of a load is significantly greater than that of the receiver, with Z_r being approximately equal to R_L. Notably, the transmission distances D corresponding to the three images are found to be 25 cm, 27 cm, and 28 cm, representing the optimal D corresponding to the different MCMs. The three curves in Fig. 15 correspond to the P_{out} and η of the three MCMs. Their variations are almost identical to Fig. 14. As R_L increases, P_{out} increases at first and then decreases, while η shows a continuous decreas-

Table 2. Physical and electrical parameters of MCM

	TC	RC1	RC2	RC3
Radius (mm)	150	130	130	130
Turns	10	8	10	12
Pitch (mm)	5	5	5	5
Self-inductive (µH)	38.55	22.61	30.27	37.52
Compensation capacitor (nF)	88.68	153.86	113.88	92.71

Table 3. Symbols and their means

Symbol	Means
TX, RX1, RX2, RX3	TC, RC1, RC2, RC3 and their corresponding compensation capacitances
MCM1	MCM composed of TX and RX1
MCM2	MCM composed of TX and RX2
MCM3	MCM composed of TX and RX3
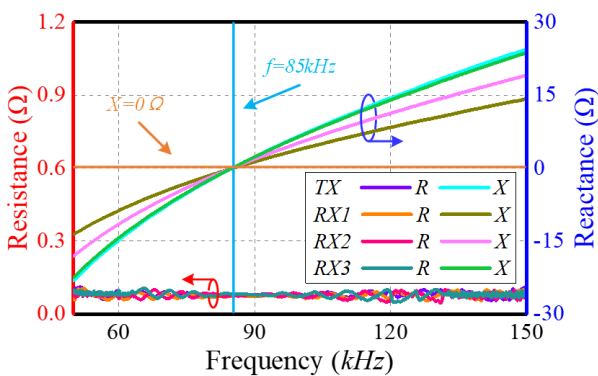
Fig. 12. The impedance and resistance varying with frequency.
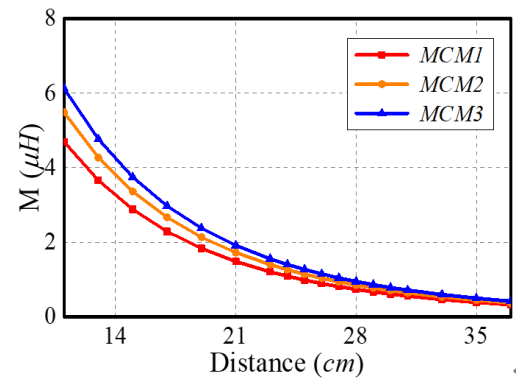
Fig. 13. Mutual inductance varying with transmission distance.
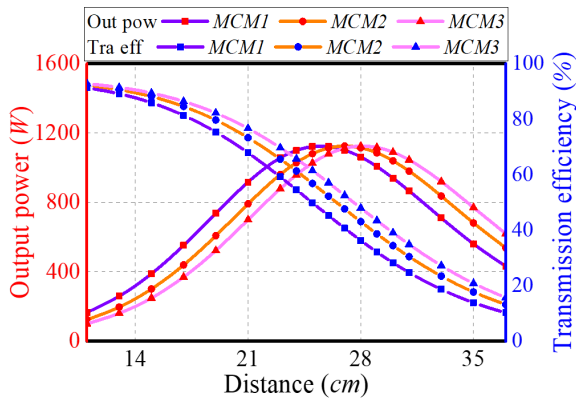
Fig. 14. Variations in output power and transmission efficiency with transmission distance.

ing trend. Furthermore, the more the turns of the receiving coil, the greater the corresponding optimal R_L. Also, the farther the D, the smaller the corresponding optimal R_L. Moreover, the three pictures shown in Fig. 15 indicate that the MCMs corresponding to the maximum P_{out} are *MCM1*, *MCM2*, and *MCM3*. This implies that the change in R_L does not affect the optimal D corresponding to the different MCMs.

Under non-ideal resonance conditions, frequency f tends to have an impact on mutual inductance reactance X_M, primary

impedance Z_t and secondary impedance Z_r. In theory, as long as Eq. (6) is satisfied, WPT can extract the maximum output power P_{out}. Fig. 16 presents the variation in output power P_{out} and transmission efficiency η with f when the mutual inductance M and load R_L are constant. Notably, the transmission distances D corresponding to three images remains 25 cm, 27 cm, and 28 cm. However, as f increases, P_{out} and η first show an increasing trend that ultimately becomes a decreasing trend. The maximum values are achieved around the ideal resonant frequency $f = f_0$. However, the rate of change in P_{out} is considerably higher than η. Notably, similar to the influence of R_L on the maximum P_{out}, f does not influence the optimal D corresponding to the different MCMs.

In obtaining the above experimental results using different MCMs, the transmitting coil remained the same. The outer radiuses of the receiving coils were also the same. Furthermore, even when the transmission distance D, load R_L, and frequency f changed, there was always an optimal MCM that was able to obtain the maximum output power $P_{out \cdot max}$. The only variable for this optimal MCM was the turns N_r of receiving coil. This result verifies the feasibility of taking recourse to the adjustment of turns to achieve maximum output power for MCMs with different primary and secondary coils at a specific position.
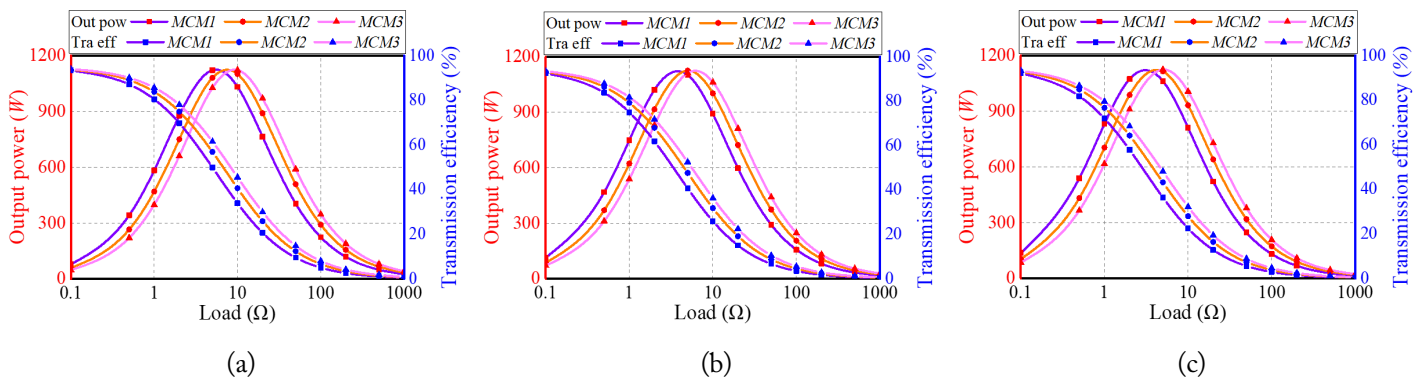

Fig. 15. Output power and transmission efficiency varying with load: (a) transmission distance is 25 cm, (b) transmission distance is 27 cm, and (c) transmission distance is 28 cm.
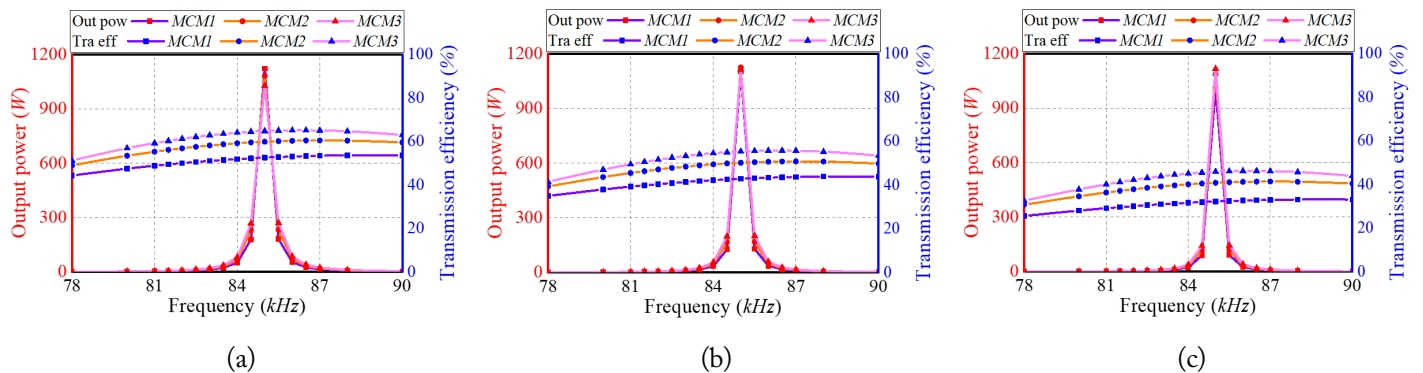

Fig. 16. Variations in output power and transmission efficiency with frequency: (a) transmission distance of 25 cm, (b) transmission distance of 27 cm, and (c) transmission distance of 28 cm.

VI. CONCLUSION

This paper presents an optimal design method for achieving the maximum output power from MCMs using different primary and secondary coils. Detailed analyses were conducted on the impact and variation of the physical parameters on the electrical characteristics. Considering a confined space, the maximum power output for a specific transmission distance was achieved by optimizing the structural parameters of the coil. A design process for this optimal coil was also summarized. Three different MCMs were built, and relevant experiments were conducted on a 1 kW experiment platform. The differences between the best mutual inductances corresponding to the maximum output power were verified at different transmission distances, loads, and resonance frequencies. Notably, the results were found to be consistent with those of the simulations and theories, thus verifying the feasibility of the proposed optimal method.

REFERENCES

[1] Z. Dai and J. Wang, "A dual-frequency WPT based on multilayer self-decoupled compact coil and dual CLCL hybrid compensation topology," *IEEE Transactions on Power Electronics*, vol. 37, no. 11, pp. 13955-13965, 2022. https://doi.org/10.1109/TPEL.2022.3183861

[2] K. Shi, C. Tang, H. Long, X. Lv, Z. Wang, and X. Li, "Power fluctuation suppression method for EV dynamic wireless charging system based on integrated magnetic coupler," *IEEE Transactions on Power Electronics*, vol. 37, no. 1, pp. 1118-1131, 2022. https://doi.org/10.1109/TPEL.2021.3097504

[3] A. Ahmad, M. S. Alam and R. Chabaan, "A comprehensive review of wireless charging technologies for electric vehicles," *IEEE Transactions on Transportation Electrification*, vol. 4, no. 1, pp. 38-63, 2018. https://doi.org/10.1109/TTE.2017.2771619

[4] Y. Zhang, Y. Wu, Z. Shen, W. Pan, H. Wang, J. Dong, X. Mao, and X. Liu, "Integration of onboard charger and wireless charging system for electric vehicles with shared coupler, compensation, and rectifier," *IEEE Transactions on Industrial Electronics*, vol. 70, no. 7, pp. 7511-7514, 2023. https://doi.org/10.1109/TIE.2022.3204857

[5] O. N. Nezamuddin, C. L. Nicholas, and E. C. dos Santos, "The problem of electric vehicle charging: state-of-the-art and an innovative solution," *IEEE Transactions on Intelligent Transportation Systems*, vol. 23, no. 5, pp. 4663-4673, 2022. https://doi.org/10.1109/TITS.2020.3048728

[6] D. Patil, M. K. McDonough, J. M. Miller, B. Fahimi, and P. T. Balsara, "Wireless power transfer for vehicular applications: overview and challenges," *IEEE Transactions on Transportation Electrification*, vol. 4, no. 1, pp. 3-37, 2018. https://doi.org/10.1109/TTE.2017.2780627

[7] A. Kurs, A. Karalis, R. Moffatt, J. D. Joannopoulos, P. Fisher, and M. Soljacic, "Wireless power transfer via strongly coupled magnetic resonances," *Science*, vol. 317, no. 5834, pp. 83-86, 2007. https://doi.org/10.1126/science.1143254

[8] W. Xiong, Q. Yu, Z. Liu, L. Zhao, Q. Zhu, and M. Su, "A detuning-repeater-based dynamic wireless charging system with quasi-constant output power and reduced inverter count," *IEEE Transactions on Power Electronics*, vol. 38, no. 1, pp. 1336-1347, 2023. https://doi.org/10.1109/TPEL.2022.3204054

[9] H. Feng, A. Dayerizadeh, and S. M. Lukic, "A coupling-insensitive X-type IPT system for high position tolerance," *IEEE Transactions on Industrial Electronics*, vol. 68, no. 8, pp. 6917-6926, 2021. https://doi.org/10.1109/TIE.2020.3000116

[10] P. S. Subudhi, S. Padmanaban, F. Blaabjerg, and D. P. Kothari, "Design and implementation of a PV-fed grid-integrated wireless electric vehicle battery charger present in a residential environment," *IEEE Journal of Emerging and Selected Topics in Industrial Electronics*, vol. 4, no. 1, pp. 78-86, 2023. https://doi.org/10.1109/JESTIE.2022.3195087

[11] F. Grazian, T. B. Soeiro, and P. Bauer, "Voltage/current doubler converter for an efficient wireless charging of electric vehicles with 400-V and 800-V battery voltages," *IEEE Transactions on Industrial Electronics*, vol. 70, no. 8, pp. 7891-7903, 2023. https://doi.org/10.1109/TIE.2022.3208582

[12] Z. Dai, J. Wang, M. Long, H. Huang, and M. Sun, "Magnetic shielding structure optimization design for wireless power transmission coil," *AIP Advances*, vol. 7, article no. 095013, 2017. https://doi.org/10.1063/1.4990775

[13] Z. Dai, J. Wang, H. Zhou, and H. Huang, "A review on the recent development in the design and optimization of magnetic coupling mechanism of wireless power transmission," *IEEE Systems Journal*, vol. 14, no. 3, pp. 4368-4381, 2020. https://doi.org/10.1109/JSYST.2020.3004201

[14] F. Wang, W. Zhang, L. Ye, J. Guo, K. Liu, and H. T. Do, "A design method to implement ZVS for electric vehicle wireless charging system with double-side LCC compensation," *IEEE Journal of Emerging and Selected Topics in Power Electronics*, vol. 9, no. 3, pp. 3791-3801, 2021. https://doi.org/10.1109/JESTPE.2020.3012614

[15] K. Lee and S. H. Chae, "Comparative study of achievable efficiency between three- and four-coil wireless power

transfer systems," *IEEE Journal of Emerging and Selected Topics in Power Electronics*, vol. 10, no. 2, pp. 2138-2146, 2022. https://doi.org/10.1109/JESTPE.2021.3072733

[16] W. V. Wang, D. J. Thrimawithana, and M. Neuburger, "An Si MOSFET-based high-power wireless EV charger with a wide ZVS operating range," *IEEE Transactions on Power Electronics*, vol. 36, no. 10, pp. 11163-11173, 2021. https://doi.org/10.1109/TPEL.2021.3071516

[17] J. Tang, T. Na, and Q. Zhang, "A novel full-bridge step density modulation for wireless power transfer systems," *IEEE Transactions on Power Electronics*, vol. 38, no. 1, pp. 41-45, 2023. https://doi.org/10.1109/TPEL.2022.3200759

[18] Z. Dai, W. Peng, Z. Wang, M. Li, Y. Zhou, R. Wang, T. Chen, X. Zhang, and J. Wang, "Reconfigurable receiver with adaptive output voltage for wireless power transfer," *IEEE Transactions on Circuits and Systems I: Regular Papers*, vol. 71, no. 1, pp. 454-462, 2024. https://doi.org/10.1109/TCSI.2023.3326839

[19] Z. Dai, X. Zhang, T. Liu, C. Pei, T. Chen, R. Dou, and J. Wang, "Magnetic coupling mechanism with omnidirectional magnetic shielding for wireless power transfer," *IEEE Transactions on Electromagnetic Compatibility*, vol. 65, no. 5, pp. 1565-1574, 2023. https://doi.org/10.1109/TEMC.2023.3266089

[20] M. Ishihara, K. Umetani, and E. Hiraki, "Strategy of topology selection based on quasi-duality between series–series and series–parallel topologies of resonant inductive coupling wireless power transfer systems," *IEEE Transactions on Power Electronics*, vol. 35, no. 7, pp. 6785-6798, 2020. https://doi.org/10.1109/TPEL.2019.2956732

[21] Z. Dai, J. Wang, M. Long, and H. Huang, "A Witricity-based high-power device for wireless charging of electric vehicles," *Energies*, vol. 10, no. 3, article no. 323, 2017. https://doi.org/10.3390/en10030323

[22] G. Ke, Q. Chen, L. Xu, X. Ren, and Z. Zhang, "Analysis and optimization of a double-sided S-LCC hybrid converter for high misalignment tolerance," *IEEE Transactions on Industrial Electronics*, vol. 68, no. 6, pp. 4870-4881, 2021. https://doi.org/10.1109/TIE.2020.2988215

[23] G. Rituraj and P. Kumar, "A new magnetic structure of unipolar rectangular coils in WPT systems to minimize the ferrite volume while maintaining maximum coupling," *IEEE Transactions on Circuits and Systems II: Express Briefs*, vol. 68, no. 6, pp. 2072-2076, 2021. https://doi.org/10.1109/TCSII.2020.3044585

[24] G. Rituraj, B. K. Kushwaha, and P. Kumar, "A unipolar coil arrangement method for improving the coupling coefficient without ferrite material in wireless power transfer systems," *IEEE Transactions on Transportation Electrification*, vol. 6, no. 2, pp. 497-509, 2020. https://doi.org/10.1109/TTE.2020.2994091

[25] Z. Luo, X. Wei, M. G. S. Pearce, and G. A. Covic, "Multi-objective optimization of inductive power transfer double-D pads for electric vehicles," *IEEE Transactions on Power Electronics*, vol. 36, no. 5, pp. 5135-5146, 2021. https://doi.org/10.1109/TPEL.2020.3029789

[26] M. Mohammad, O. C. Onar, V. P. Galigekere, G. J. Su, and J. Wilkins, "Magnetic shield design for the double-d coil-based wireless charging system," *IEEE Transactions on Power Electronics*, vol. 37, no. 12, pp. 15740-15752, 2022. https://doi.org/10.1109/TPEL.2022.3191911

[27] A. U. Ibrahim, W. Zhong, and M. D. Xu, "A 50-kW three-channel wireless power transfer system with low stray magnetic field," *IEEE Transactions on Power Electronics*, vol. 36, no. 9, pp. 9941-9954, 2021. https://doi.org/10.1109/TPEL.2021.3064373

[28] J. Yi, P. Yang, Z. Li, P. Kong, and J. Li, "Mutual inductance calculation of circular coils for an arbitrary position with a finite magnetic core in wireless power transfer systems," *IEEE Transactions on Transportation Electrification*, vol. 9, no. 1, pp. 1950-1959, 2023. https://doi.org/10.1109/TTE.2022.3187953

[29] Y. P. Su, X. Liu, and S. Y. Hui, "Extended theory on the inductance calculation of planar spiral windings including the effect of double-layer electromagnetic shield," *IEEE Transactions on Power Electronics*, vol. 23, no. 4, pp. 2052-2061, 2008. https://doi.org/10.1109/TPEL.2008.924824

[30] C. M. Zierhofer and E. S. Hochmair, "Geometric approach for coupling enhancement of magnetically coupled coils," *IEEE Transactions on Biomedical Engineering*, vol. 43, no. 7, pp. 708-714, 1996. https://doi.org/10.1109/10.503178

[31] Q. Ke, W. Luo, G. Yan, and K. Yang, "Analytical model and optimized design of power transmitting coil for inductively coupled endoscope robot," *IEEE Transactions on Biomedical Engineering*, vol. 63, no. 4, pp. 694-706, 2016. https://doi.org/10.1109/TBME.2015.2469137

[32] A. K. RamRakhyani, S. Mirabbasi, and M. Chiao, "Design and optimization of resonance-based efficient wireless power delivery systems for biomedical implants," *IEEE Transactions on Biomedical Circuits and Systems*, vol. 5, no. 1, pp. 48-63, 2011. https://doi.org/10.1109/TBCAS.2010.2072782

Zhongyu Dai

https://orcid.org/0000-0002-4574-405X

received his B.S. and Ph.D. degrees in electrical engineering from the School of Electrical Engineering and Automation, Wuhan University, Wuhan, P. R. China, in 2014 and 2020, respectively. After this, he joined the School of Power and Mechanical Engineering as a postdoctoral researcher. He is currently an associate professor in the School of Electrical Engineering at Hebei University of Technology. His main research interests include wireless power transmission technology and its applications, and condition monitoring of smart grids.

Huihui Wang

received her B.S. degree in electrical engineering from Shandong Agricultural Engineering University. She is currently working toward her M.E. degree in electrical engineering from Hebei University of Technology, Tianjin, China. Her research interests include wireless power transfer and its industrial applications.

Wenxi Peng

received his B.S. degree in electrical engineering from Wuhan University, Wuhan, P. R. China, in 2014. He then joined the State Grid Sichuan Ultra High Voltage Company, where he worked in the field of relay protection. He is currently the leader of the substation maintenance team at State Grid Sichuan Ultra High Voltage Company, as well as a skilled craftsman and young talent recommended by the State Grid Sichuan Electric Power Company. His main research interests include relay protection, professional management, and plan management.

Yanhu Zhai

received his B.S. degree in electrical engineering from Shijiazhuang Tiedao University. He is currently working toward his M.E. degree in electrical engineering at Hebei University of Technology, Tianjin, China. His main research interests are wireless power transmission technology and its applications.
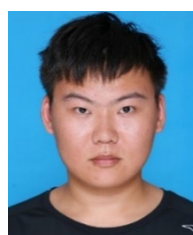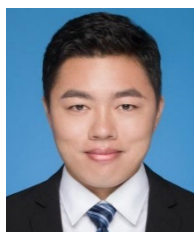
Yake Tang

received his B.S. and M.S. degrees in electrical engineering from the School of Electrical Engineering and Automation, Wuhan University, Wuhan, P. R. China, in 2015 and 2017, respectively. He is currently an intermediate engineer at the Henan Electric Power Company Economy Research Institute. His main research interests include the design and research of transmission lines.

Ming Xue

https://orcid.org/0000-0001-6153-9761

received his B.S. and M.S. degrees from Tianjin Polytechnic University, Tianjin, China, in 2011 and 2014. In 2022, he received his Ph.D. degree in electrical engineering from the Hebei University of Technology, Tianjin, China. He is currently an associate professor with the School of Electrical Engineering, Hebei University of Technology, Tianjin. His current research interest include wireless power transfer technology and its application.

Haoran Xu
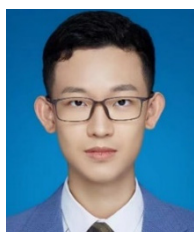
is currently working toward his M.E. degree in electrical engineering and automation from Donghua University. His main research interests include the engineering electromagnetic field and power electronics technology.

Xian Zhang

https://orcid.org/0000-0002-0925-9831

received his M.E. and Ph.D. degrees in electrical engineering from Hebei University of Technology, Tianjin, China, in 2009 and 2012, respectively. He is currently a professor at Hebei University of Technology, Tianjin, China. He is the director of the China Electrotechnical Society and the secretary-general of the National Specialized Committee on Wireless Power Transmission Technology. His research interests encompass intelligent high-power wireless power transmission technology, measurement of three-dimensional electromagnetic fields, and numerical calculations of modern engineering electromagnetic fields.

Performance Evaluation of Spaceborne Bistatic SAR Systems

Suk-Jin Kim[1] (ID) · Seong Joo Maeng[2] (ID) · Jung-Hwan Lim[2] (ID) · Jae Wook Lee[2,*] (ID) ·
Taek-Kyung Lee[2] (ID) · Woo Kyung Lee[2] (ID)

Abstract

In this paper, the performances of spaceborne bistatic synthetic aperture radar (SAR) systems are evaluated and compared with those of the conventional monostatic SAR system. Drawing on information on the altitude of satellites and the pulse repetition frequency of the system, the distance between the satellites carrying the transmitter and the receiver is first determined to then obtain the maximum observable width by overlapping the blind ranges. The performances of the bistatic SAR for two satellites at the same altitude moving parallel to each other at the same speed are evaluated, and the results are compared with those obtained from a monostatic SAR system located at left or right end of the baseline. The resolutions, noise equivalent sigma zero, and ambiguities of the bistatic SAR are evaluated based on the windows between blind incident angles of a timing diagram. Subsequently, the most ap-propriate window is determined by comparing the evaluated performances of the bistatic SAR.

Key Words: Ambiguity, Baseline, Bistatic SAR, NESZ, Resolution, Timing Diagram.

I. INTRODUCTION

Unlike an imaging system that captures images using optics, the synthetic aperture radar (SAR) system acquires images by directing radio waves at a target and then measuring the reflected signal. This means that it is free from the influence of environmental conditions, such as bad weather, clouds, and dust, and observations are possible regardless of the time of the day [1].

Among the many ways available for operating SARs, most studies have been conducted on the monostatic mode, which operates using only one satellite platform because of its easy control and low complexity of geometry analysis [2]. However, since the monostatic mode operates by using only one satellite

platform, limitations related to SAR system performance and related geometric problems often arise as a result of inflexible platform operation [3].

In this context, bistatic SAR systems have gained significant military and civilian attention in recent years. It has enhanced the capability of remote sensing missions in the areas of anti-jamming, covert instrument detection, and configuration flexibility [4, 5]. In addition, it exhibits better performance than monostatic SAR systems for several pertinent variables, such as signal-to-noise ratio (SNR) and spatial resolution, by appropriately utilizing the bistatic platform structure [6]. Because of these advantages, several SAR missions, such as TanDEM-X by the German Aerospace Centre—a high-resolution X-band

SAR using phase array technology—and RADARSAT-2/3 developed by the Canada Center for Remote Sensing, have been conducted to investigate the bistatic SAR mode [7, 8].

One of the major interests of these SAR missions has been analyzing performances, such as those of resolution, noise-equivalent sigma zero (NESZ), and range/azimuth ambiguity. Since the performance of a SAR system greatly influences the quality of the images obtained from SAR sensors, studies analyzing SAR performance have been actively conducted. With regard to the monostatic mode, considerable effort has been directed at improving image quality by analyzing the ambiguities of the SAR system [9, 10]. Furthermore, an appropriate quad-pol SAR was designed by drawing on a performance analysis of antenna characteristics [11].

In the performance analysis of bistatic SAR systems, the separation of the transmitter and receiver means that additional considerations must be made based on the geometric configurations of the system. In the literature, the performance analysis of bistatic SAR has included investigations into SNR, resolution, and NESZ in spaceborne–airborne and inter-spaceborne operating environments [6, 12]. Spaceborne bistatic SAR is primarily operated in a repeat-pass scenario along one path, which offers an advantage in interferometry processing, since two satellites repeatedly investigate the same path [12]. However, various configurations of the bistatic SAR system must be explored to improve performance by adjusting the positional relationship and direction of progress to ultimately meet the goal of each SAR mission.

The performance of bistatic SAR systems is highly affected by their geometry and the scenario of operation. In spaceborne SAR environments, parallel trajectory configurations [13], in which two satellites are operated parallelly at the same altitude and speed, offer the advantages of reduced geometric and radial distortion as well as pointing and timing synchronization [2]. Notably, the optimum geometric configuration of a parallel trajectory can be designed by conducting a performance analysis of bistatic SAR systems. In a parallel trajectory bistatic SAR system, the baseline—the distance between two satellites—must be carefully determined from a timing diagram. In particular, both the arrival time of signals received through a direct path and the path reflected onto the Earth's surface must be accounted for in the timing diagram to attain the optimum design.

In this paper, the baseline of the bistatic spaceborne SAR system is first determined to identify the largest observation area from a timing diagram of the two satellites flying parallelly at the same altitude and speed. The resolution, NESZ, range ambiguity-to-signal ratio (RASR), and azimuth ambiguity-to-signal ratio (AASR) performances of the SAR system are investigated using the determined geometric configurations. After selecting the optimum observation area from the calculation results, a comparison of the results for the forward and back-ward operations of the transmission/reception satellites operating in the monostatic mode is conducted to determine the operation scenario offering better results.

II. BASELINE DETERMINATION IN BISTATIC SAR

Fig. 1 shows the configuration of a spaceborne, parallel trajectory, bistatic SAR system where the transmitting and receiving satellites move in a parallel flight path at the same altitude and speed. In bistatic operations, the transmitter is assumed to be at Trajectory 1 and the receiver at Trajectory 2. For comparison, a monostatic SAR mode was also assumed to operate at Trajectory 1 or 2. In Fig. 1, the distance between the two satellites or the baseline is denoted by B, the altitude of the satellites is H, and the look angle at the transmitter is represented as θ_L. Notably, the transmission/reception satellites were synchronized and operated in simultaneous transmission mode. Notably, for a given pulse repetition frequency (PRF), the bistatic SAR in Fig. 1 bears the blind look angle at which the return signals travel along path $r_T + r_R$ to reach the satellite during transmission.

In spaceborne bistatic SAR systems, two additional signals reach the receiver [14]. One is the direct signal from the transmitter to the receiver through baseline B. The other is the common plane specular echo reflected by the Earth's surface between the two satellite trajectories along path length $2r_s$.

In Fig. 2, the timing diagram of a spaceborne bistatic SAR is displayed for $H = 500$ km and $B = 200$ km. The red stripes represent the blind look angle, while the blue and green stripes are the footprints of the direct signal and the common plane specular echo, respectively. The direct signal and the specular echo disturb the sensing of return signals from the observation
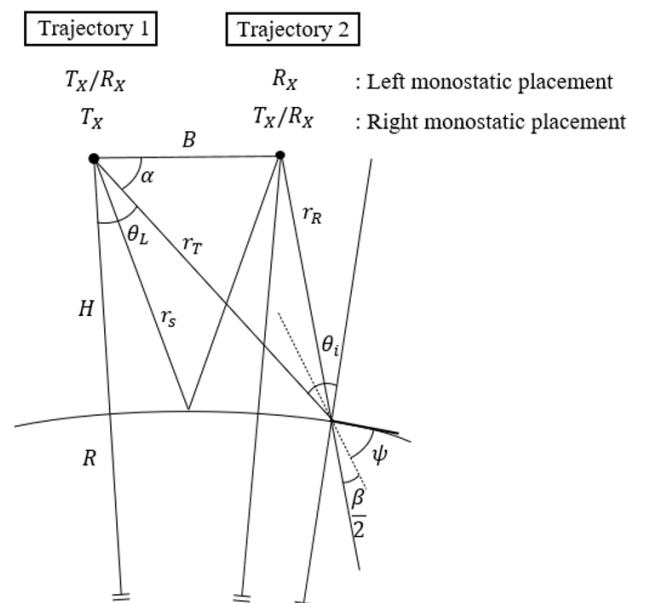

Fig. 1. Geometric cross-section of the bistatic SAR.

area. Therefore, for a fixed PRF, swath widths are limited only to the look angles that do not correspond to the blind angles and are not disturbed by the direct signal and specular echo. As shown in Fig. 2, for a PRF of 14,400 Hz, the observable area for the bistatic SAR is quite narrow for $B = 200$ km. Furthermore, the frequency of the PRF range is slightly higher than expected. This may be attributed to the antenna used in the simulation in this study, which was manufactured by the authors in their own laboratory, with dimensions of 1.5 m width and length in a parabola configuration [15]. Notably, the PRF should be high enough to be high enough to avoid ambiguity.

To obtain the widest swath width, the stripes of the direct signal and specular echo must overlap with those of the blind angle. Although Fig. 2 indicates that an overlap of three stripes is not realizable for all PRFs, this can be achieved by adjusting the baseline of a specific PRF. To identify the proper baseline and PRF for a given H, this study took recourse to forbidden arrival times, expressed as Eqs. (1)–(3), where T is the pulse repetition interval (PRI) of the transmitted signal and l, m, and n are the integers including zero.

In particular, $t_D(l)$ and $t_E(m)$ are the forbidden arrival times resulting from the direct signal and the specular echo, respectively, while $t_B(n)$ is the forbidden time for transmission. If three forbidden arrival times occur at the same time, the forbidden look angle can be minimized.

$$t_D(l) = \frac{B}{c} + lT, \quad (1)$$

$$t_E(m) = \frac{2r_s}{c} + mT, \quad (2)$$

$$t_B(n) = nT. \quad (3)$$

For a specific PRF, the baselines satisfying $t_D = t_E$ can be easily estimated. However, the t_B might not always coincide with the other two since it is quantized by the PRI. For instance, in Fig. 2, it can be observed that for B = 200 km, the t_D coincides with t_E at PRF = 14,300 Hz, but t_B has different values. Fig. 3(a) displays the arrival times when the baseline changes for PRF = 14,300 Hz. The t_D(blue) and t_E(green) are coincident for $B = 175$ km and 200 km, but the t_B does not coincide for both baselines. Therefore, to find the accurate PRF and baseline at which three arrival times coincide simultaneously, repeated calculations are necessary. As the PRF changed, the baselines satisfying $t_D = t_E$ were first identified, and then their coincidence with t_B was checked. After conducting iterations of the above process, the proper PRF and baseline at which the three signals arrived simultaneously were identified. For PRF = 14,400 Hz, Fig. 3(b) shows that $t_D = t_E$ for B = 182 km and 208 km, but the arrival times of the three signals collapse into the same instance only for $B = 208$ km.

The timing diagram for the baseline of 208 km is presented in Fig. 4. It is observed that when the PRF is 14,400 Hz, the stripes for the direct and specular echo merge into those of the

Fig. 2. Timing diagram of a bistatic SAR system ($B = 200$ km).
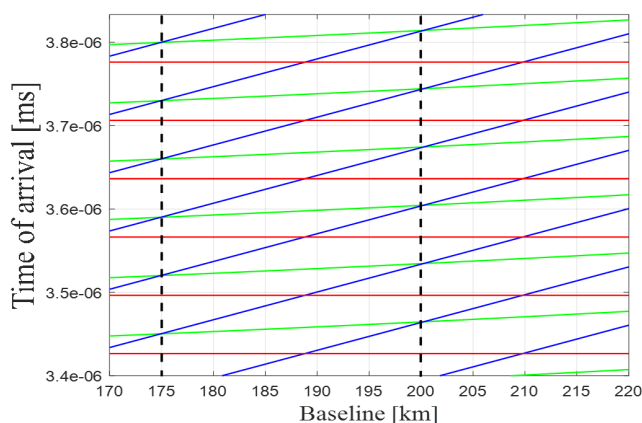
(a)
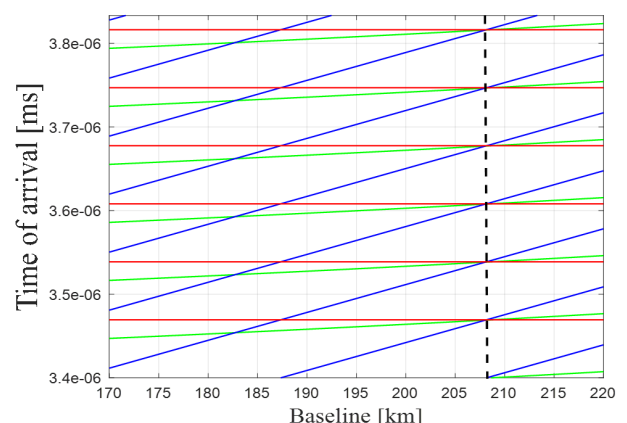
(b)

Fig. 3. The forbidden arrival times t_D(blue), t_E(green), and t_B(red) vs. the baseline: (a) PRF = 14,300 Hz and (b) PRF = 14,500 Hz.

blind look angle at incidence angles of 27.9°, 31°, and 34°. Subsequently, three observation areas with maximum swath width were achieved for three incidence angle ranges—from 28.8° to 30.2°, from 31.8° to 32.9°, and from 34.2° to 35.2°.

III. Bistatic SAR System Performance Evaluation

In Section II, SAR system parameters were selected using the timing diagram, with the baseline being 208 km, the PRF being 14,400 Hz, and the three incidence angle ranges being 29° to 29.8°, 31.8° to 32.9°, and 34.2° to 35.2°. The performance of the bistatic SAR system was analyzed in terms of relevant performance variables, such as ambiguity ratio, NESZ, and resolution, as was the case with the monostatic mode.

However, unlike the monostatic mode, the bistatic mode operates using two satellites—one set to be only a receiver and the other set to operate in the monostatic mode (operates both Tx and Rx). As a result, the system parameters, such as incidence angle and slant range, changed depending on the location of the monostatic satellite. Since such changes affect the performance of the SAR system, a performance analysis was conducted by classifying the monostatic satellites into cases in which a satellite is set to be in the monostatic mode. As shown in Fig. 1, this study divided the signal trajectory into two parts—the left monostatic placement and the right monostatic placement. Notably, since the position of the satellite remained unchanged, it did not affect the timing variables. For both cases, the performance of the bistatic SAR system was analyzed, and each performance was compared based on the monostatic operating position.

1. Ambiguity-to-Signal Ratio

The ambiguity-to-signal ratio comprises the RASR and the AASR, representing the ratio of undesired signals to the desired SAR signal. The RASR can be calculated using the transmission/reception gain $G_t(\theta)/G_r(\theta)$; , the transmission/reception slant range r_T/r_R, the bistatic angle β, the aspect angle ψ, and

the angle at which the ambiguity signal occurs in the range direction angle θ_A. In particular, bistatic RASR can be expressed as in [13, 16]. Notably, when receiving the n-th signal, the ambiguity ratio can be calculated using the ratio of the n-th received signal to the other signals.

$$RASR_{bi} = \frac{\sum_{n \neq 0} \dfrac{G_t(\theta_A(n)) G_r(\theta_A(n))}{r_T r_R \sqrt{r_R^2 + r_T^2}\,(n) \cos\left(\dfrac{\beta(n)}{2}\right) \cos(\psi(n))}}{\dfrac{G_t(\theta_A(0)) G_r(\theta_A(0))}{r_T r_R \sqrt{r_R^2 + r_T^2}(0) \cos\left(\dfrac{\beta(0)}{2}\right) \cos(\psi(0))}}. \tag{4}$$

Unlike the monostatic mode, the bistatic RASR reflected parameters such as the transmit/receive gain (G_t/G_r), the bistatic angle (β), the aspect angle (ψ), and the transmit/receive slant range (r_T/r_R) caused by the separation of the transceiver. When the PRF reached 14,400 Hz, the baseline with the maximum swath width was assumed to be 208 km. It was also assumed that the two satellites maintained the same speed at an altitude of 500 km, as well as the same baseline and fly parallel, and that both were operating in stripmap mode.

Fig. 5 shows the bistatic RASR performance results with regard to the baseline. As the right-side satellite (receiver only) approaches the left-side satellite (monostatic mode), the performance tends toward being similar to the monostatic mode, and it ultimately matches the monostatic RASR when the baseline reaches 0 km. Fig. 6 shows the results of the RASR for the three observation areas obtained from the bistatic timing diagram. In the bistatic mode, the incidence angles 28.8° to 30.2°, 31.8° to 32.9°, and 34.2° to 35.2° achieve a minimum RASR of −47 dB, −41 dB, and −33 dB, respectively. Furthermore, as the incidence angle increases, the slant range with the target becomes longer, leading to the increased reception of undesired signals and ultimately resulting in increased range direction am-
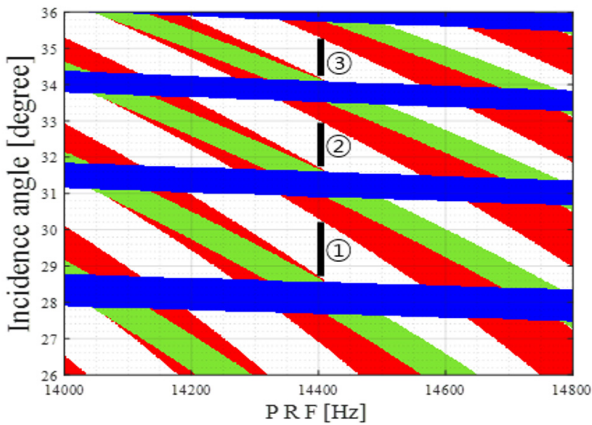

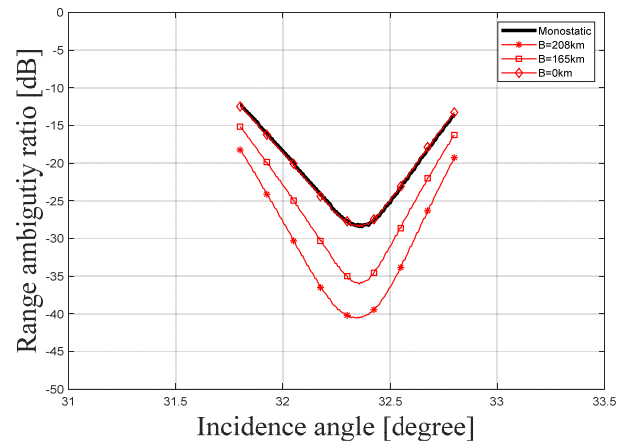Fig. 4. Timing diagram of the proposed bistatic SAR at $B = 208$ km.

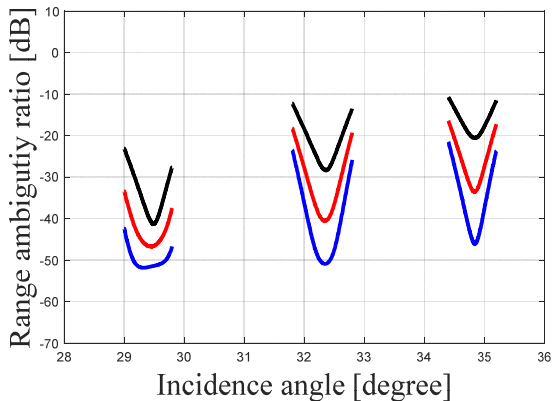Fig. 5. Comparison of bistatic RASR performance.

Fig. 6. Range ambiguity ratio according to incidence angle ($B = 208$ km).

biguity signals. Notably, in the monostatic mode, the left arrangement for the three observation areas attained a minimum RASR of −41.3 dB, −28.4 dB, and −20.5 dB. Notably, the right arrangement received fewer ambiguity signals because it was located close to the target, so it exhibited the best range ambiguity performance.

Unlike the monostatic mode, the AASR in the bistatic mode reflected the gains attained on transmission and reception, which can be expressed as follows:

$$AASR_{bi} = \frac{\sum_{n \neq 0} \int_{PB} G_t(\theta_{AZ}(n)) G_r(\theta_{AZ}(n)) d\theta_{AZ}(n)}{\int_{PB} G_t(\theta_{AZ}(0)) G_r(\theta_{AZ}(0)) d\theta_{AZ}(0)}, \quad (5)$$

where θ_{AZ} is the azimuth angle.

Fig. 7 depicts the bistatic AASR based on the baseline. Similar to the RASR simulation, as the right side of the satellite gets closer to the left satellite, the AASR tends to respond in the same way as the monostatic AASR did, ultimately matching the monostatic AASR when the baseline reaches 0 km. Fig. 8 shows the results of the AASR for the three observation regions obtained from the bistatic timing diagram. In the bistatic mode, the AASR was found to be −28 dB, with the left and right monostatic placements being −22 dB and −31 dB, respectively. Notably, since AASR is affected by changes in the azimuth pattern near the angle at which the azimuth signal occurs, no significant change was observed for any of the cases, even when the incidence angle changed. Furthermore, since the distance from the target was lesser for the right arrangement than for the left arrangement in the monostatic mode, the former attained a large azimuth angle. For this reason, the AASR of the right arrangement achieved a lower value, as it received the signal from the small sidelobe of the antenna pattern.

2. Resolution

Similar to the monostatic mode, the bistatic SAR system resolution depends on the bandwidth of the antenna. However, in contrast to the monostatic mode, the bistatic mode considers

the bistatic angle and aspect angle reflecting the positional relationship between two satellites instead of the incidence angle in the range direction, as considered by the monostatic mode.

$$\rho_{bi_{gr}} \cong \frac{c}{2 W \cos\left(\frac{\beta}{2}\right) \cos(\psi)}, \quad (6)$$

$$\beta = \sin^{-1}\left(\frac{B}{r_R} \sin\alpha\right). \quad (7)$$

Variations in the bistatic angle were directly affected by the baseline. Notably, the bistatic angle is often used as the angle that replaces the incidence angle in the bistatic SAR, as shown in Eq. (7). Fig. 9 presents the bistatic angle in terms of the angle of incidence when the baseline is fixed at 208 km.

As shown in Fig. 10, the bistatic mode has a resolution of 6 m or less when the incidence angle is 30.4° or more. This indicates that the required performance is satisfied only for the observation areas in Cases 2 and 3 of Fig. 4. Furthermore, in the case of the monostatic mode, the ground range resolution was quite large in the forward arrangement (right placement), since the incidence
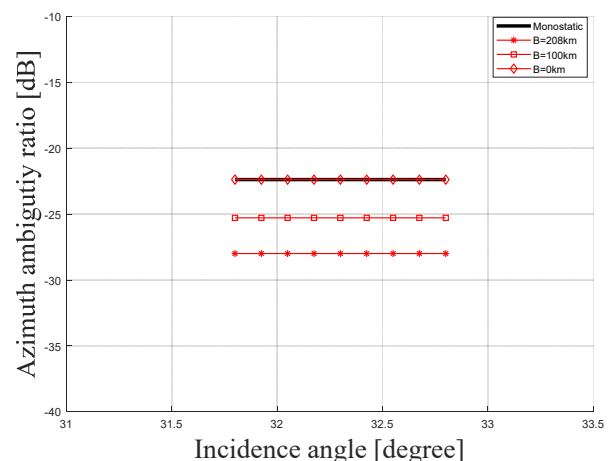

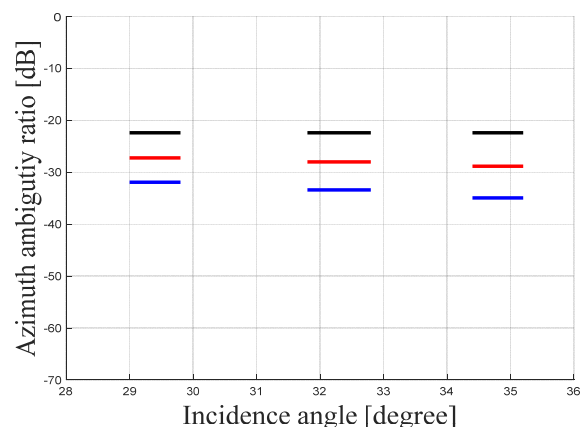Fig. 7. Comparison of bistatic AASR performance.

Fig. 8. Azimuth ambiguity ratio according to incidence angle ($B = 208$ km).
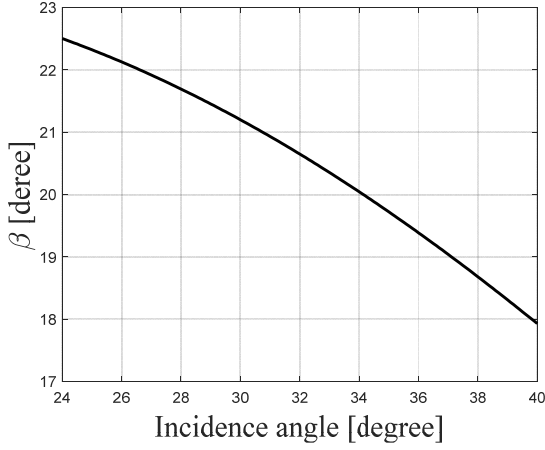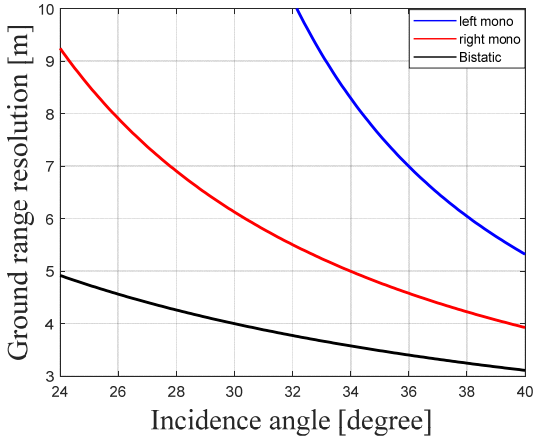
Fig. 9. Bistatic angle.

Fig. 10. Ground range resolution.

angle decreased significantly compared to the backward arrangement (left placement), while the resolution value increased significantly in the process of reflecting the ground range of the SAR. In addition, as the incidence angle increased, the $\sin(\theta_i)$ and $\cos(\beta/2)\cos(\psi)$ terms also increased, as a result of which improvements in the ground range resolution performances of both monostatic and bistatic SAR were observed.

The bistatic azimuth resolution expressed in Eq. (8) reflects the ratio of the slant range of the transmitter to the slant range of the receiver [3], with L_T being the size of the transmission satellite antenna.

$$\rho_{bi_a} = L_T \frac{r_R}{r_R + r_T}. \tag{8}$$

The results obtained by comparing the azimuth resolution performances of the monostatic SAR and bistatic SAR using Eq. (5) are shown in Fig. 11. It is observed that the bistatic SAR satisfies the required performance for all incidence angles and maintains the same azimuth resolution regardless of the location of the monostatic SAR. Furthermore, r_T is larger than r_R, which means that the bistatic azimuth resolution performs bet-

ter than its counterpart. It is further observed that as the incidence angle increases, r_T becomes longer and the azimuth resolution value becomes lower.

The NESZ, an indicator of sensitivity performance, investigates the new variables arising from a bistatic SAR system operating two satellites—the distance between the two satellites and the gain of each transmitting/receiving antenna. Here, P_t is the transmission power, G_T is the transmission antenna gain, G_R is the reception antenna gain, λ is the wavelength, k the Boltzmann constant, V_s is the satellite speed, τ is the pulse width, T_0 is the thermal noise, NF is the constant noise, BW is the transmission bandwidth, and L_t is the system's total loss.

$$N_t = (kT_0)(NF)(BW)L_t, \tag{9}$$

$$NESZ_{bi} = \frac{4(4\pi)^3 r_T r_R \sqrt{r_R^2 + r_T^2} V_s \cos\left(\frac{\beta}{2}\right)\cos(\psi) N_t}{\lambda^3 G_T G_R c\tau P_T(PRF)}. \tag{10}$$

The slant range of the two satellites was obtained from $r_T r_R \sqrt{r_R^2 + r_T^2}$, while their ground range was estimated using $\cos\left(\frac{\beta}{2}\right)\cos(\psi)$. Because the radiation center axes of the two satellites were different, the transmission gain and reception gain were separately calculated to account for this difference. Fig. 12 shows the NESZ calculation results for the three observation areas obtained using the bistatic timing diagram.

All three bistatic modes achieved a value of −20 dB or less. Moreover, in the case of the monostatic satellite, the slant range of the transmitter was large—about 1 dB larger than that of the bistatic mode. In contrast, since the slant range was short in the bistatic mode, its sensitivity performance was better.

IV. Conclusion

This paper analyzed the performance of a bistatic SAR system for two parallelly flying satellites, as well as the performance
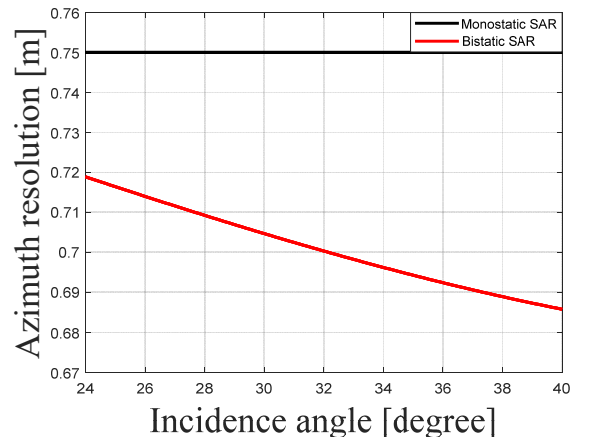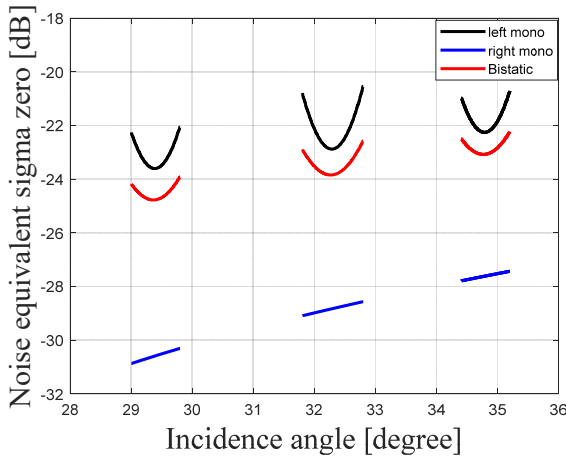

Fig. 11. Azimuth resolution.

Fig. 12. NESZ.

Table 1. Monostatic mode SAR system performance

Mode	Monostatic	
	Backward	Forward
Ground range resolution (m)	<5.8	<10.1
Azimuth resolution (m)	0.75	0.75
NESZ (dB)	<−22	<−28.2
RASR (dB)	<−10.2	<−22
AASR (dB)	<−21	<−34

Table 2. Bistatic mode SAR system performance

Mode	Bistatic
Ground range resolution (m)	<9.2
Azimuth resolution (m)	<0.72
NESZ (dB)	<−23.8
RASR (dB)	<−16.5
AASR (dB)	<−26.46

achieved utilizing a monostatic mode satellite operating in backward and forward directions. In the case of the bistatic mode, when the PRF was 14,400 Hz, a baseline of 208 km was set to guarantee the maximum swath width of the SAR system.

Furthermore, the observation area was divided into three separate cases for performance analysis. The results showed a ground range resolution of less than 6 m for Cases 2 and 3 of Fig. 4, while the azimuth resolution of all cases met the targeted performance. In addition, while the NESZ and RASR of all cases satisfied the expected performance, the AASR produced satisfactory results only for Cases 1 and 2.

Since Case 2 satisfied the targeted value for all performance indicators, its values were determined as bistatic SAR system parameters. Therefore, for the monostatic operation, a performance analysis was performed only on the observation area pertaining to Case 2, as it was determined as the bistatic SAR system. Furthermore, in the case of ground range resolution, the performance of the backward arrangement was 5.8 m—significantly better than the 10.1 m of the forward arrangement. The azimuth resolution exhibited similar performance. In the case of NESZ, the forward arrangement was observed to be better, at −28.2 dB, due to its close slant range and small incidence angle. Although the RASR differed significantly from the targeted performance at −10.2 dB in the backward placement, its performance remained below −22 dB in the case of the forward placement, thus satisfying the target performance. Furthermore, AASR satisfied the expected performance in both cases. Overall, when using an SAR system that meets the target performance of 10 m or less for range resolution, a forward arrangement that exhibits overall good performance with regard to the indicators should be selected, while a backward arrangement should be preferred in cases where more precise performance is allowed for range direction ambiguity. These results confirm that when setting up a bistatic SAR system, the ground range resolution deteriorates with a decrease in the receiver's

distance from the target, but the ASR tends to improve. Furthermore, optimized variables can be set based on a comparison of the bistatic and monostatic performances in this paper.

REFERENCES

[1] A. Currie and M. A. Brown, "Wide-swath SAR," *IEE Proceedings F (Radar and Signal Processing)*, vol. 139, no. 2, pp. 122-135, 1992. https://doi.org/10.1049/ip-f-2.1992.0016

[2] A. Y. Nashashibi and F. T. Ulaby, "Bistatic SAR imaging: a novel approach using a stationary receiver," in *Proceedings of 2007 IEEE International Geoscience and Remote Sensing Symposium*, Barcelona, Spain, 2007, pp. 125-128. https://doi.org/10.1109/IGARSS.2007.4422745

[3] A. Moccia and A. Renga, "Spatial resolution of bistatic synthetic aperture radar: impact of acquisition geometry on imaging performance," *IEEE Transactions on Geoscience and Remote Sensing*, vol. 49, no. 10, pp. 3487-3503, 2011. https://doi.org/10.1109/TGRS.2011.2115250

[4] M. Lyu and C. Gao, "Study of bistatic angle's impact on imaging performance in bistatic RCS measurement," in *Proceedings of 2016 International Conference on Identification, Information and Knowledge in the Internet of Things (IIKI)*, Beijing, China, 2016, pp. 449-452. https://doi.org/10.1109/IIKI.2016.105

[5] H. Xie, D. An, X. Huang, and Z. Zhou, "Research on spatial resolution of one-stationary bistatic ultrahigh frequency ul-

trawidebeam–ultrawideband SAR based on scattering target wavenumber domain support," *IEEE Journal of Selected Topics in Applied Earth Observations and Remote Sensing*, vol. 8, no. 4, pp. 1782-1798, 2015. https://doi.org/10.1109/JSTARS.2015.2414412

[6] M. Rodriguez-Cassola, S. V. Baumgartner, G. Krieger, and A. Moreira, "Bistatic TerraSAR-X/F-SAR spaceborne–airborne SAR experiment: description, data processing, and results," *IEEE Transactions on Geoscience and Remote Sensing*, vol. 48, no. 2, pp. 781-794, 2010. https://doi.org/10.1109/TGRS.2009.2029984

[7] M. Rodriguez-Cassola, P. Prats, D. Schulze, N. Tous-Ramon, U. Steinbrecher, L. Marotti, et al., "First bistatic spaceborne SAR experiments with TanDEM-X," *IEEE Geoscience and Remote Sensing Letters*, vol. 9, no. 1, pp. 33-37, 2012. https://doi.org/10.1109/LGRS.2011.2158984

[8] P. F. Lee and K. James, "The RADARSAT-2/3 topographic mission," in *Proceedings of IEEE 2001 International Geoscience and Remote Sensing Symposium (IGARSS): Scanning the Present and Resolving the Future (Cat. No. 01CH37217)*, Sydney, Australia, 2001, pp. 499-501. https://doi.org/10.1109/IGARSS.2001.976202

[9] A. M. Guarnieri, "Adaptive removal of azimuth ambiguities in SAR images," *IEEE Transactions on Geoscience and Remote Sensing*, vol. 43, no. 3, pp. 625-633, 2005. https://doi.org/10.1109/TGRS.2004.842476

[10] S. S. Yoon, J. W. Lee, T. K. Lee, and D. W. Yi, "Parameter selection procedure of parabolic reflector antenna for the optimum synthetic aperture radar performances," *Journal of Electromagnetic Engineering and Science*, vol. 13, no. 4, pp. 251-258, 2013. https://doi.org/10.5515/JKIEES.2013.13.4.251

[11] J. H. Lim, J. W. Lee, T. K. Lee, H. C. Lee, S. G. Lee, S. B. Ryu, and S. S. Yoon, "Performance evaluation of a modified Sweep-SAR mode for quad-pol application in SAR systems," *Journal of Electromagnetic Engineering and Science*, vol. 20, no. 3, pp. 199-206, 2020. https://doi.org/10.26866/jees.2020.20.3.199

[12] J. L. Bueso-Bello, M. Martone, P. Prats-Iraola, and B. Brautigam, "First characterization and performance evaluation of bistatic TanDEM-X experimental products," *IEEE Journal of Selected Topics in Applied Earth Observations and Remote Sensing*, vol. 9, no. 3, pp. 1058-1071, 2016. https://doi.org/10.1109/JSTARS.2015.2430454

[13] M. Cherniakov, *Bistatic Radar: Emerging Technology*. Chichester, UK: John Wiley & Sons, 2008.

[14] F. Bordoni, M. Younis, M. Rodriguez-Cassola, P. Prats-Iraola, P. Lopez-Dekker, and G. Krieger, "SAOCOM-CS SAR imaging performance evaluation in large baseline bistatic configuration," in *Proceedings of 2015 IEEE International Geoscience and Remote Sensing Symposium (IGARSS)*, Milan, Italy, 2015, pp. 2107-2110. https://doi.org/10.1109/IGARSS.2015.7326218

[15] S. Lee, S. J. Jo, J. H. Lim, S. S. Yoon, J. Y. Kim, T. K. Lee, J. W. Lee, and J. H. Ro, "Design and implementation of lightweight antenna for small satellite SAR with feeder strut," *The Journal of Korean Institute of Electromagnetic Engineering and Science*, vol. 31, no. 9, pp. 758-769, 2020. https://doi.org/10.5515/KJKIEES.2020.31.9.758

[16] J. H. Lim, J. W. Lee, and T. K. Lee, "Cross-pol pattern effects of parabolic reflector antennas on the performance of spaceborne quad-pol SAR systems," *Journal of Electromagnetic Engineering and Science*, vol. 21, no. 3, pp. 218-227, 2021. https://doi.org/10.26866/jees.2021.3.r.29
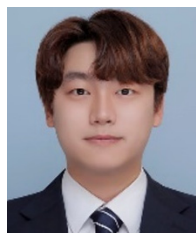
Suk-Jin Kim

https://orcid.org/0000-0001-9028-9503

received his B.S. and M.S. degrees in electronics and information engineering from Korea Aerospace University, Goyang, Korea, in 2020 and 2022, respectively. He is currently a junior researcher in Technical Development Team 3 at Genmixtech. His current research interests include satellite communications and radar antennas, spaceborne SAR systems, and antenna design and analysis.

Seong Joo Maeng

https://orcid.org/0009-0001-9641-8940

received his B.S. degree in electronics and information engineering from Korea Aerospace University, Goyang, Korea, in 2019. He is currently working toward his M.S. degree at the Microwave and Millimeter-wave Solution Laboratory (MMSL) of Korea Aerospace University. His main research interests are satellite communications, spaceborne SAR systems, and SAR signal processing.

Jung-Hwan Lim

https://orcid.org/0000-0003-0325-2775

received his B.S. and M.S. degrees in electronics and information engineering from Korea Aerospace University (KAU), Goyang, Korea, in 2018 and 2020, respectively. He is currently working toward a Ph.D. degree at the Microwave and Millimeter-Wave Solution Laboratory of KAU. His current research interests include satellite communications/radar antennas, spaceborne SAR systems, and EMI/EMC.

Jae Wook Lee

https://orcid.org/0000-0003-2903-5904

received his B.S. degree in electronic engineering from Hanyang University, Seoul, Korea, in 1992, and his M.S. and Ph.D. degrees in electrical engineering, with a specialization in electromagnetics, from the Korea Advanced Institute of Science and Technology, Daejeon, Korea, in 1994 and 1998, respectively. From 1998 to 2004, he was a senior member of the Advanced Radio Technology Department, Radio and Broadcasting Research Laboratory, Electronics and Telecommunications Research Institute, Daejeon. In 2004, he joined the faculty of Korea Aerospace University, Goyang, Korea, where he is currently a professor at the School of Electronics and Information Engineering. His current research interests include high-power amplifier design, computational electromagnetics, electromagnetic interference/electromagnetic compatibility analysis on printed circuit boards, satellite antennas, and spaceborne SAR systems.

Taek-Kyung Lee

https://orcid.org/0000-0002-2577-2037

received his B.S. degree in electronic engineering from Korea University, Seoul, Korea, in 1983, and his M.S. and Ph.D. degrees in electrical engineering from the Korea Advanced Institute of Science and Technology (KAIST), Daejeon, Korea, in 1985 and 1990, respectively. From 1990 to 1991, he was a postdoctoral fellow at the University of Texas at Austin, TX, USA, under a grant from the Korea Science and Engineering Foundation. From 1991 to 1992, he was a research scientist at KAIST. In 1992, he joined the faculty of Korea Aerospace University (KAU), Goyang, Korea. He was an associate visiting research professor at the University of Illinois at Urbana–Champaign, IL, USA, from 2001 to 2002. From 2006 to 2007, he was chairman of the School of Electronics, Information, and Computer Engineering at KAU. He was also the director of the Aerospace and Aviation Electronics Research Center at KAU from 2011 to 2013. He was also the chairman of the Radar Technical Group, Korean Institute of Electromagnetic Engineering and Science, Seoul, from 2012 to 2013, and served as the president of the institute in 2014. He is currently a professor emeritus in the School of Electronics and Information Engineering at KAU. His current research interests include computational electromagnetics, antennas, microwave passive circuits, satellite antennas and spaceborne SAR systems, and air surveillance systems.

Woo-Kyung Lee

https://orcid.org/0000-0003-2092-2048

received his B.Sc. and M.Sc. degrees from the Korea Advanced Institute of Science and Technology (KAIST), Seoul, Korea, in 1990 and 1994, and his Ph.D. degree from the University College London, United Kingdom, in 2000, all in electrical engineering. From 1999 to 2002, he worked as a research professor at SaTReC, KAIST, where he was involved in developing communication and antenna systems for small satellite systems. From 2003 to 2004, he worked at the Samsung Advanced Institute of Technology, conducting research on UWBs, antennas, and communication systems. In 2004, he joined the Electrical Engineering and Avionics Department at Korea Aerospace University, Seoul, Korea, where he currently works as a professor. His research interests are communication and radar system design, spaceborne antenna development, image processing, and electronic countermeasure techniques.

Novel CPW-Fed Gamma-Shaped Circularly Polarized Slot Antenna for UWB Applications

Junmo Choi[1,a] (ID) · Youngkyun Oh[2,b] (ID) · Jaehoon Choi[1,c] (ID) · Kyung-Young Jung[1,*,d] (ID)

Abstract

In recent years, ultra-wideband (UWB) technology has garnered significant attention for enabling exceptional precision in applications, such as positioning and radar systems. This letter presents a novel coplanar waveguide-fed circularly polarized slot antenna specifically designed for UWB applications. The proposed antenna incorporates innovative elements, including an asymmetric ground equipped with gamma-shaped slits for circular polarization and a gamma-shaped monopole to enhance reflection coefficients. The overall size of the proposed antenna is 18 mm × 18 mm × 1.2 mm ($0.37\lambda_0 \times 0.37\lambda_0 \times 0.02\lambda_0$). The measurement results demonstrate a reflection coefficient that is consistently below −10 dB from 6.10 GHz to 10 GHz, and an axial ratio below 3 dB from 5.70 GHz to 8.50 GHz. Furthermore, the radiation patterns closely match the simulation results. Additionally, this study analyzes antenna and system fidelity factors using time-domain analysis.

Key Words: UWB, Circular Polarization, CPW-Fed Antenna, Time-Domain Analysis.

I. INTRODUCTION

In recent years, ultra-wideband (UWB) technology has garnered significant attention owing to its remarkable capability for delivering high-resolution and precise positioning performance across a multitude of domains, including indoor positioning and radar systems [1]. UWB technology not only achieves centimeter-level precision through precise signal travel time measurements but also adeptly manages multipath propagation, thereby enhancing overall accuracy [2].

Circularly polarized (CP) antennas play a critical role in UWB applications by effectively preserving signal quality and mitigating multipath interference [3–5]. Notably, coplanar waveguide (CPW)-fed slot antennas can be seamlessly integrated into printed circuit boards (PCBs), thus facilitating the seamless infusion of UWB technology into diverse electronic devices [6]. In the context of CPW-fed slot antennas, various approaches have been proposed in the literature to produce CP characteristics. For example, one study achieved CP characteristics by employing symmetrical ground along with two inverse L-shaped ground strips [7].

This work proposes a novel CPW-fed CP slot antenna designed for UWB applications. In contrast to the approach employed in [7], the proposed antenna integrates a gamma-shaped monopole surrounded by an asymmetric ground equipped with gamma-shaped slits to achieve CP characteristics. Furthermore,

this work investigates antenna and system fidelity factors to evaluate UWB pulse distortion, which is a critical aspect in the realm of UWB technology [8].

II. DESIGN AND MEASUREMENT

Fig. 1 illustrates the design and fabrication steps involved in creating the proposed antenna, including its final dimensions (unit: mm). All antennas were designed on an 18 mm × 18 mm FR4 substrate (ε_r = 4.4, tanδ = 0.02, h = 1.2 mm) and were excited by the CPW transmission line using a 50-Ω SMA connector.

Fig. 2 displays the reflection coefficient and axial ratio (AR) for each design step. The blue box represents the target operating frequency range (6.24–8.24 GHz) corresponding to UWB channels 5, 6, 8, and 9, with Ant.1 being a linearly polarized slot antenna designed for comparison purposes. To achieve circular polarization, Ant.2 incorporated asymmetric slots and a CPW ground, as shown in Fig. 1(b). However, its AR remained above 3 dB within the 6.66–9.33 GHz range, thus failing to meet the target frequencies. To address this issue, in Ant.3, gamma-shaped slits were added to the slot. Ant.3 achieved an AR below 3 dB within the 6.31–8.14 GHz band. Furthermore, to optimize the reflection coefficient and AR, the monopole shape was modified into a gamma shape in Ant.4. Consequently, the simulated reflection coefficients of the proposed antenna were found to be below −10 dB within the 5.74–9.18 GHz range, while the simulated AR was below 3 dB in the 6.14–8.52 GHz range, thus meeting the desired operating frequencies. Finally, the measured reflection coefficients of the proposed antenna remained below −10 dB above 6.10 GHz, while the measured

AR was below 3 dB in the 5.70–8.50 GHz range, thus aligning with the target operating frequencies. The disparities between the measurement and simulation outcomes may be ascribed to inaccuracies stemming from fabrication and measurement procedures.

Fig. 3 illustrates the current distribution in the proposed antenna at 7.3 GHz. It is evident that the proposed antenna exhibits right-handed circular polarization (RHCP) characteristics in the +z direction and left-handed circular polarization (LHCP) characteristics in the −z direction.

Furthermore, Fig. 4 depicts the radiation pattern of the proposed antenna in the xz- and yz-planes at two specific frequencies (6.9 GHz and 7.6 GHz) within the target UWB channel. The measured RHCP and LHCP radiation patterns are observed to be in close agreement with the simulation results of both planes. The simulated peak realized gains are recorded at 2.69 dBic and 3.77 dBic at 6.9 GHz and 7.6 GHz, respectively, while the measured peak realized gains are slightly higher, measuring 2.85 dBic and 4.02 dBic at 6.9 GHz and 7.6 GHz, respectively.

III. TIME-DOMAIN ANALYSIS

This section analyzes the performance of the proposed antenna in the time domain using the CST electromagnetic simulator. The fidelity factors were computed by comparing the in-

Fig. 3. Current distribution of the proposed antenna at 7.3 GHz: (a) 0°, (b) 90°, (c) 180°, and (d) 270°.
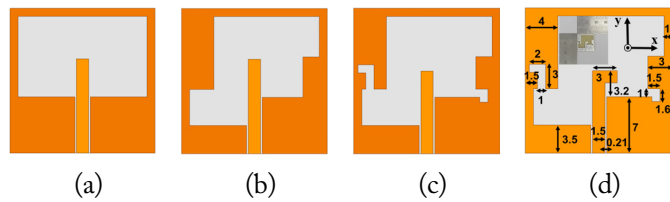

Fig. 1. Design and fabrication steps of the antennas: (a) Ant.1, (b) Ant.2, (c) Ant.3, and (d) Ant.4 (proposed).

Fig. 2. (a) Reflection coefficient and (b) axial ratio.
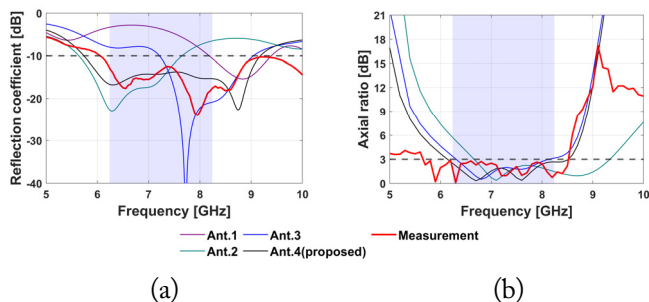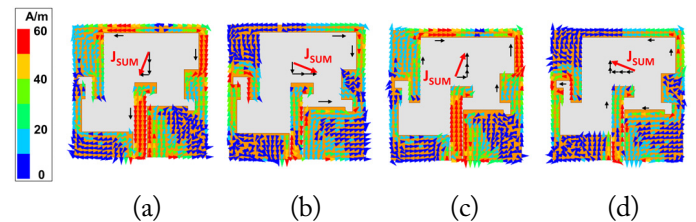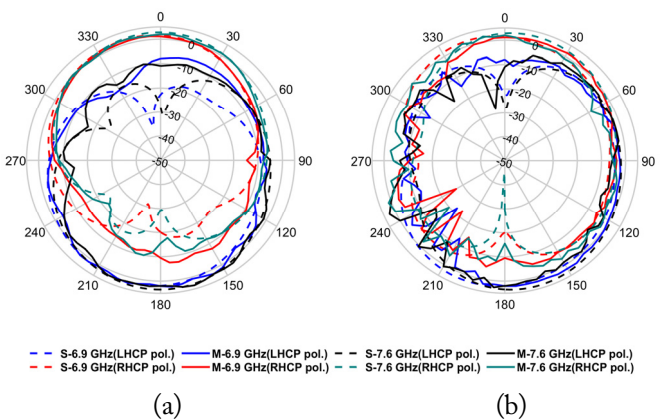

Fig. 4. Radiation pattern of the proposed antenna: (a) xz-plane and (b) yz-plane.

put pulse with the radiated E-fields. Furthermore, to investigate circular polarization attributes, this study conducted a cross-correlation analysis involving the input pulse and both the phi and theta components of radiated E-fields.

Fig. 5 illustrates the antenna fidelity factor (AFF) in both planes, considering both phi and theta polarizations. In the *xz*-plane, the AFF exceeds 0.9 for all angles in both polarizations. Meanwhile, in the *yz*-plane, the AFF is greater than 0.8 for all angles in the phi polarization, whereas it exceeds 0.8 for all angles in the theta polarization except for 270°, where the factor is valued at 0.70. This relatively low AFF at 270° may be attributed to significant fluctuations in gain across the operating frequency range.

Fig. 6 presents the normalized transmitted and received pulse signals, which were utilized to evaluate the system fidelity factor (SFF). For this purpose, two identical proposed antennas with a separation of 500 mm in both face-to-face and side-by-side configurations were arranged. The SFFs for the side-by-side and face-to-face setups were 92.5% and 98.4%, respectively.

IV. CONCLUSION

This letter introduces a novel CPW-fed CP slot antenna specifically designed for UWB applications. This antenna features innovative design elements, including an asymmetric ground equipped with gamma-shaped slits to achieve circular polarization and a gamma-shaped monopole to enhance reflection coefficients. Meticulous design optimization enables the proposed antenna to demonstrate consistent performance within the de-

sired operating frequency range, which also aligns with UWB channels. The time-domain analysis shows good antenna fidelity, while the radiation patterns closely match the simulation results. Therefore, the proposed antenna exhibits great promise for UWB applications, in turn contributing to advancements in wireless communication and positioning technology.

REFERENCES

[1] S. Park and K. Y. Jung, "Novel compact UWB planar monopole antenna using a ribbon-shaped slot," *IEEE Access*, vol. 10, pp. 61951-61959, 2022. https://doi.org/10.1109/ACCESS.2022.3182443

[2] R. J. Fontana, "Recent system applications of short-pulse ultra-wideband (UWB) technology," *IEEE Transactions on Microwave Theory and Techniques*, vol. 52, no. 9, pp. 2087-2104, 2004. https://doi.org/10.1109/TMTT.2004.834186

[3] R. Xu, Z. Shen, and S. S. Gao, "Compact-size ultra-wideband circularly polarized antenna with stable gain and radiation pattern," *IEEE Transactions on Antennas and Propagation*, vol. 70, no. 2, pp. 943-952, 2021.

[4] S. Park and K. Y. Jung, "Design of a circularly-polarized UHF antenna for partial discharge detection," *IEEE Access*, vol. 8, pp. 81644-81650, 2020. https://doi.org/10.1109/ACCESS.2020.2991158

[5] J. Lee, J. Cho, J. Choi, H. Choo, and K. Y. Jung, "Design of a miniaturized spiral antenna for partial discharge detection system," *Microwave and Optical Technology Letters*, vol. 60, no. 1, pp. 75-78, 2018. https://doi.org/10.1002/mop.30916

[6] I. C. Deng, Q. X. Ke, R. J. Lin, and Y. T. King, "A circular CPW-fed slot antenna resonated by the circular loop for broadband circularly polarized radiation," *Microwave and Optical Technology Letters*, vol. 50, no. 5, pp. 1423-1426, 2008. https://doi.org/10.1002/mop.23359

[7] Y. Zehforoosh and S. Mirzaei, "CPW-fed circularly polarized slot antenna with elliptical-shaped patch for UWB applications," *Journal of Communication Engineering*, vol. 6, no. 2, pp. 151-162, 2017. https://doi.org/10.22070/jce.2017.2342.1042

[8] G. Quintero, J. F. Zurcher, and A. K. Skrivervik, "System fidelity factor: a new method for comparing UWB antennas," *IEEE Transactions on Antennas and Propagation*, vol. 59, no. 7, pp. 2502-2512, 2011. https://doi.org/10.1109/TAP.2011.2152322
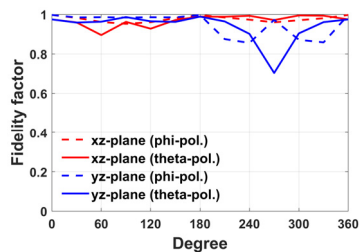
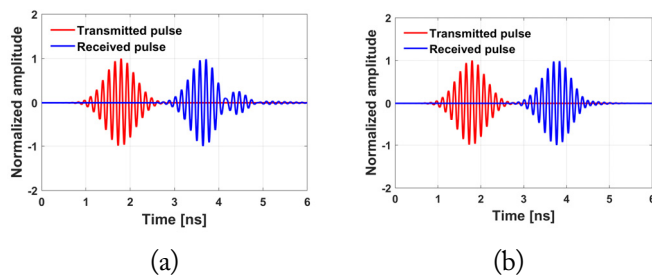Fig. 5. Antenna fidelity factor of the proposed antenna.

(a)   (b)

Fig. 6. Normalized transmitted and received pulse signals in the time domain: (a) side-by-side configuration and (b) face-to-face configuration.

JEES Journal of Electromagnetic Engineering and Science

Instructions for Authors

Journal of Electromagnetic Engineering and Science (*J. Electromagn. Eng. Sci.*; *JEES*) is an official English journal of the Korean Institute of Electromagnetic and Engineering Science (KIEES). The objective of *JEES* is to publish academic as well as industrial research results and foundings on electromagnetic engineering and science. The journal covers all aspects of researches and technology related to electromagnetics: Electromagnetic Compatibility/Electromagnetic Interference, Microwave and Millimeter-Wave Engineering, Antenna and Propagation, Electromagnetic Theory, Wireless Communication, Lightwave and Electro-Optics, Materials and Components, Software Defined Radar, Radar, Bioelectromagnetics, and etc.

I. Copyright and Creative Commons Attribution Licensing

The copyright and the transfer rights of the digital content of published papers and the journal is owned by the KIEES. All published materials are also assigned a Creative Commons Attribution License (http://creativecommons.org/licebses/by-nc/4.0/). The journal accepts manuscripts for consideration with the understanding that the manuscript has not been published previously and is not currently under consideration for publication elsewhere, and in addition, that the authors (or their employer, if it holds the copyright) are authorizing the transfer of the copyright to the Institute when the manuscript is submitted. Author should check the copyright transfer conditions and forms at http://www.jees.kr.

II. Research and Publication Ethics

Research published in JEES (Journal of Electromagnetic Engineering and Science) must have followed institutional, national, and international guidelines.

It is necessary to agree upon standards of the expected ethical behaviors for all parties involved in the act of publishing: the author, the journal editor, the blind peer reviewer and the publisher.

Our policies on research and publication ethics are based on the Committee on Publication Ethics (COPE) Guidelines.
(http://publicationethics.org/resources/code-conduct)

For further details, please refer to the Research Publication Ethics of the Korean Institute of Electromagnetic and Science (KIEES).
(https://www.jees.kr/authors/ethics.php)

III. Submission of Manuscripts

Authors are expected to be members of the KIEES except for some special cases approved by the Editorial Board of KIEES. All manuscripts should be submitted electronically through the online submission and review site (https://mc03.manuscriptcentral.com/jees). For the first submission, you may be required to create an account on the submission site. A manuscript can be submitted at any time of the year. When submitting a manuscript, authors need to make sure that their

manuscripts do not provide any of their identities such as authors' names and affiliations as the review is double-blinded. More detailed submission instruction is available in the upper right corner of the submission site. All manuscripts submitted to the Journal must comply with the instruction and the standard format of the Journal. Otherwise, it will result in return of the manuscript and possible delay in publication. For assistance, please contact us via e-mail (admin-jees@kiees.or.kr).

IV. Peer Review Process

 The manuscript will be forwarded to three reviewers selected for their expertise in the field of the submitted manuscript. The acceptance criteria for all papers are based on the quality and originality of the research and its clinical and scientific significance. During the review process, the author is often asked to expand, rewrite, or clearly explain the specific contents of his/her paper. It is not uncommon that an author is asked to provide another draft with the suggested changes for further review. A revised manuscript should be submitted to the homepage within a month from the date on which any change of the manuscript is requested to the author. Once a manuscript has received the final approval of the reviewers and Editor-in-Chief, the author will be notified and asked to prepare the manuscript for final publication and to possibly complete an additional information form.

V. Publication Type

 The papers are classified into five categories.

Regular Paper should be an original work that contributes to the academic interests of the KIEES members with technical values. The paper should also be written within 12 pages with A4 size including figures, charts, and tables (The main body of text consists of two columns).

Letter consists of reports of preliminary results or short reports on completed work that are of current interest to many researchers in the field. Comments on material previously published in the journal, suggestions for new directions, and errata could be included. Their length must be less than 3 pages (with a two-column format) including paper title, author affiliation, reference, etc.

Review Paper will be published by direct submission as well as from invited experts. In both cases, the work will be subject to editorial review. Review papers should critically review topics not only to inform the reader of the background, but also to communicate the state of the art and outstanding research problems.

Technical Report is on innovative technical achievements of interest to the community and usually a report of an extensive series of measurements. Report is often involving display in the form of tables or graphs, with text describing the conditions and procedures of measurement.

Editorial is a brief report of research findings adequate for the journal's scope and of particular interest to the community.

VI. Manuscript Preparation

 All manuscripts must be written in MS-Word and adhere to the following guidelines:

1. A cover of each paper manuscript should include a title, authors' names (main author and co-authors), author's organizations, contact information (e-mail and phone number), and the author's area of expertise.
2. The first page of a main text should only contain title, abstract with a length of about 150 words, and key words with around five words.
3. The contents of the manuscript should be arranged in the order of abstract, main text, acknowledgments, references, and appendix.

4. The numbers corresponding to chapters in the manuscript should be written in Roman numerals (I, II, III, IV…) and the numbers corresponding to sections should be written in Arabic numerals (1, 2, 3, 4…).

5. Equation numbers should be given in Arabic numerals enclosed in parentheses on the right-hand margin. They should be cited in the text as, for example Eq. (1) or Eqs. (1)-(3).

6. All tables should be numbered consecutively with Arabic numerals. They should be referred to in the text and should be numbered according to their order of mention in the text. In addition, all tables should, not only list all abbreviations in the table in footnotes at the end, but also have a title that is concise and describes the table's contents. Vertical lines are not used. The table should be self-explanatory and supplement, not duplicate, the text. If the table or any data therein have been published, a footnote to the table must give permission information to the original source. The structure should be clear, with simple column headings giving all units. A table should not exceed one page when printed. Use lowercase letters in superscripts [a,b,c…] for special remarks.

7. All figures should be of high quality meeting with the publishing requirement with legible symbols and legends. In preparing the figures, authors should consider a size reduction during the printing process to have acceptable line clarity and character sizes. Use only figures that are necessary to illustrate the meaning of the text. Figures must be black and white of high contrast. All figures should be referred to in the text as, for example, Fig. 1, Fig. 2(a), or Figs. 1-3.

8. Only those references cited in the text should be listed in the references. Authors are responsible for the accuracy and completeness of their references and the correct text citations. In the text the reference should be numbered in bracket in ascending order (e.g., [1, 3], or [4-6]; Lee [2] and Kim and Park [5]; Jang et al. [7]). In case of the paper title, only the first letter is to be capitalized. However, in case of journal and book titles, the first letter of each word should be capitalized and all of the letters should be italicized. If available, please include full DOI links in your reference list. See the example below.

Books

[1] F. Giannini and G. Leuzzi, *Nonlinear Microwave Circuit Design.* NewYork, NY: John Wiley & Sons Inc., 2004.

Journals

[2] H. Ahn and B. Kim, "Equivalent transmission-line sections for very high impedances and their application to branch-line hybrids with very weak coupling power," Journal of Electromagnetic Engineering and Science, vol. 9, no. 2, pp. 85-97, 2009. https://doi.org/10.5515/JKIEES.2009.9.2.085

Report

[3] E. E. Reber, R. L. Michell, and C. J. Carter, "Oxygen absorption in the earth's atmosphere," Aerospace Corp., Los Angeles, CA, Tech. Rep. TR-0200 (4230-46)-3, Nov. 1988.

Conference Proceedings

[4] S. P. Bingulac, "On the compatibility of adaptive controllers," in *Proceedings of the 4th Annual Allerton Conference on Circuit and System Theory*, NewYork, pp. 8-16, 1994.

Papers Presented at Conferences

[5] J. G. Kreifeldt, "An analysis of surface-detected EMG as an amplitude-modulated noise," presented at the 8th International Conference on Medical and Biological Engineering, Chicago, IL, 1969.

[6] J. Arrillaga and B. Giessner, "Limitation of short-circuit levels by means of HVDC links," presented at the IEEE Summer Power Meeting, Los Angeles, CA, Jul. 1990.

Theses (M.S.) and Dissertations (Ph.D.)

[7] N. Kawasaki, "Parametric study of thermal and chemical nonequilibrium nozzle flow," M.S. thesis, Department of Electronic Engineering, Osaka University, Osaka, Japan, 1993.

[8] J. O. Williams, "Narrow-band analyzer," Ph.D. dissertation, Department of Electronic Engineering, Harvard University, Cambridge, MA, 1993.

Standards

[9] *IEEE Criteria for Class IE Electric Systems*, IEEE Standard 308, 1969.

Online Sources

[10] R. Bartle, "Early MUD History," Nov. 1990; www.ludd.luth.se/aber/mud-history.html.

9. When citing any paper published in JEES, it should be indicated the name of the journal as *Journal of Electromagnetic Engineering and Science* or *J. Electromagn. Eng. Sci.*

10. Acknowledgment, if needed, appears before the reference. Sponsorship or financial support acknowledgment should be included here.

11. Unit and Abbreviation: If the authors describe length, height, weight, and volume, they should use standard metric units. Temperature should be given in degrees Celsius. All other units should follow the International System of Units (SI). All units must be preceded by one space except percentages (%) and temperatures (°C).

 Abbreviations must be used as an aid to the reader, rather than as a convenience of the author, and therefore their use should be limited. Generally, abbreviations that are used less than 3 times in the text, including tables and figure legends, should be avoided. Standard SI abbreviations are recommended. Other common abbreviations are as follows (the same abbreviations are used for plural forms): h (hour), min (minute), s (second), d (day), wk (week), mo (month), y (year), L (liter), mL (milliliter), μL (microliter), g (gram), kg (kilogram), mg (milligram), μg (microgram), ng (nanogram), pg (picogram), *g* (gravity; not g), nm (nanometer), μm (micrometer), mV (millivolt), mA (milliampere), mW (milliwatt), C (coulomb), μF (microfarad), mH (millihenry), n (samplesize), SD (standard deviation of the mean), and SE (standard error of the mean).

VII. Accepted Manuscript

 Once the review process has been completed with a decision of acceptance, the final manuscript accommodating all of the reviewers' comments should be submitted along with photos of the authors and their brief biographies (including major research areas). The accepted papers will be published, in principle, in the order of initially submitted dates subject to decision of the Editorial Board.

1. Page Proofs

 Authors will be given an opportunity to review the laser printed version of their manuscripts before printing. One set of page proofs in PDF format will be sent by e-mail to the corresponding author. The review should be solely dedicated to detecting typographical errors.

2. Publishing Charge

 The publishing charge for general publishing is KRW 450,000 (US$450) for up to the first 6 pages. For 7 to 8 pages, an extra charge of KRW 120,000 (US$120) per page, and for 9 pages or more, an extra charge of KRW 160,000 (US$160) per page. Furthermore, the KIEES charges extra KRW 100,000 (US$100) for the paper acknowledging a financial support from an institution, in addition to the above mentioned page charge. Twenty reprints without a cover will be supplied without an additional charge.

Contact Us

Editorial office of the Korean Institute of Electromagnetic Engineering and Science
217, Saechang-ro, Yongsan-gu, Seoul, 04376, Korea
Tel: +82-2-337-9666/332-9665 Fax: +82-2-6390-7550
http://www.jees.kr, E-mail: admin-jees@kiees.or.kr

Call for Papers

2024 KIEES Summer Conference

21(Wed.) – 24(Sat.) August 2024

ALPENSIA Resort Pyeongchang, Gangwon-do, Republic of Korea

Important Dates

Paper Submission Deadline	Acceptance Notification	Early Bird Registration
28 June (Fri.)	**10 July (Wed.)**	**24 June (Mon.) ~ 8 August (Thu.)**

General Session ▸ Special Session ▸ English Session ▸ Excellent Papers ▸ Undergraduate Student Paper Competition ▸ KIEES Journals

Suggested Topics

- EMI/EMC/EMP
- EM Components and Materials
- IoT & Sensor Network
- Biomedical Applications
- EM Measurement
- Emerging Technologies (5G-Adv/6G, AI, Deep learning, etc.)
- EM Theory & Computational EM
- Radio Wave Propagation & Scattering
- Radar & Remote Sensing
- Satellite and Cosmic Radio Waves
- Wireless Power Transfer & Energy Harvesting
- Microwave/mmWave Passive Circuits
- Antenna Theory & Design
- CR/SDR
- Wireless Communication Systems
- Electronic Warfare & EM Security
- Microwave/mmWave Active Circuits
- THz/Optical Systems & Components
- EM Bio-effects & EMF
- Radio & Broadcasting Policies/Standards
- Broadcasting Technologies/Applications

Paper Template and Submission Procedures

- Online submission at: https://conf.kiees.or.kr
- Template: 1pages of A4 size (in Korean or English)
- Submitted your file through KIEES website (or Click the button '논문접수 하러가기')
- Presentation: The preference for oral or poster presentation should be indicated during the submission process, however the final decision on the presentation format may be subject to change

※ For detailed information, please refer to the conference website

Excellent papers and JKIEES Journal Submission Procedures

- Excellent papers: Both manuscript (1-2 pages) and front page must be submitted
- JKIEES Journals: Both manuscript 1pages and 4pages review paper must be submitted

Additional Information

- Some of the selected excellent papers will be awarded at the event venue
- Please contact the conference secretariat for more information on organizing sessions.

KIEES office (Secretariat)

Tel. +82-2-337-9666   E-mail : kees@kiees.or.kr   Website: https://www.kiees..or.kr

Korean Institute of Electromagnetic Engineering and Science

1st Call for Papers

isap2024.org

ISAP 2024

2024 International Symposium on Antennas and Propagation

November 5 / Tue. ~ 8 / Fri. , 2024

Songdo Convensia, Incheon, Republic of Korea

The 29th International Symposium on Antennas and Propagation (ISAP 2024) will be held on November 5~8, 2024, at Songdo Convensia, Incheon, Republic of Korea. We are pleased to host an excellent forum for academic and industrial participants at all career stages worldwide. We also convince ISAP 2024 must be a perfect opportunity to exchange new technical/scientific achievements, demonstrate state-of-the-art technology, and establish and strengthen professional cooperation networks in antennas, propagation, electromagnetic wave theory, and related fields. We, the Local Organizing Committee of ISAP 2024, are delighted that ISAP will be held again in Republic of Korea after 2005 (Seoul), 2011 (Jeju), and 2018 (Busan). We hope you will enjoy the Symposium in Incheon, the city of unique tourism resources.

IMPORTANT DATES

Paper Submission Deadline
May 31, 2024

Notification of Acceptance
July 26, 2024

Early-bird Registration
September 20, 2024

CONFERENCE TOPICS

A. Antennas
Antenna Theory and Design
Small Antennas and RF Sensors
Antennas for Mobile, and V2X Applications
Broadband and Multi-band Antennas
Active, In-package, and On-chip Antennas
Adaptive and Reconfigurable Antennas
Additive Manufacturing
Array Antennas
Reflectarrays and Transmitarrays
Antenna Measurements
Millimeter-wave, THz, and Optical Antennas
HF/VHF Antennas
Reflector, Lens, and Radomes
Antennas with Periodic Structures
Other Antenna-related Topics

C. Electromagnetic-wave Theory
Electromagnetic Theory
Computational and Numerical Techniques
Scattering, Diffraction, and RCS
Inverse and Imaging Techniques
Metamaterials, Metasurfaces, and Artificial Materials
Periodic Structures
Nano-electromagnetics
Other EM Theory-related Topics

B. Propagation
Propagation Theory and Models
Millimeter-wave, THz, and Optical Propagation
Machine-to-machine/Infrastructure Propagation
Channel Sounding and Channel Estimation
Radar, DOA, Localization, and Sensing
Propagation for Vehicular Communications
Terrestrial, Earth-space, and Ionospheric Propagation
Propagation Measurement Techniques
Other Propagation-related Topics

D. AP-related Topics
Passive and Active Components
Reconfigurable Intelligent Surfaces
Antenna Systems for Mobile(5G, B5G, and 6G) Communications
MIMO, Diversity, and Their Applications
Broadcasting and Receiving Technologies
Wireless Power Transfer Technologies
Wearable Device Networks and Medical Applications
Sensor Networks and Adhoc Systems
RFID and Applications
EMC/EMI Technologies
Satellite and Military Applications
Machine Learning and Artificial Intelligence
Other AP-related Topics

Organized by KIEES

Technically Co-Sponsored by
IEICE Communications Society · A/Ps · IEEE · A/Ps · Seoul Chapter · Φ · U.R.S.I. · IEIE · KICS · EurAAP · EuCAP · AMTA

Supported by
KOREA TOURISM ORGANIZATION 한국관광공사 · Incheon Metropolitan City · Incheon Tourism Organization

PREPARATION OF PAPERS

Only original papers are solicited that have not been presented previously and that describe new contributions in the area suggested in the Conference Topics. Each author is requested to prepare a 2-page camera-ready paper in 2-column and written in English, including all texts, references, figures and photographs. Please refer to the paper preparation instruction via the ISAP 2024 Website (www.isap2024.org).

SUBMISSION OF PAPERS

An online paper submission window will be opened in ISAP 2024 website. Submitted papers will be assessed in a single acceptance/rejection review process. Presented papers will be submitted to IEEE Xplore® if the authors choose submission to Xplore during the final submission process. Compliance with the IEEE format and publication standards is mandatory in this case.

INCHEON

Incheon is a major port city of Korea and home to the Incheon International Airport. As a free economic zone, Incheon plays a pivotal role in logistics, business, and leisure sports in Northeast Asia. The Songdo international business district of Incheon specializes in international finance, trade, and the knowledge-based industry.

ORGANIZING COMMITTEE As January 9, 2024

Honorary Chairs
Hyo Joon Eom (KAIST)
Young-Ki Cho (Kyungpook National Univ.)
Jaehoon Choi (Hanyang Univ.)

General Chair
Young Joong Yoon (Yonsei Univ.)

General Vice-Chairs
Ikmo Park (Ajou Univ.)
Jin-Seob Kang (KRISS)

Local Advisory Committee
Choon-Sik Cho (Korea Aerospace Univ.)
Bomson Lee (Kyung Hee Univ.)
Jeong-Hae Lee (Hongik Univ.)
Kyeong-Sik Min (Korea Maritime and Ocean Univ.)
Sangwook Nam (Seoul National Univ.)
Seong-Ook Park (KAIST)
Jong-Gwan Yook (Yonsei Univ.)

Technical Program Committee Chair
Dongho Kim (Sejong Univ.)

Technical Program Committee Vice-Chairs
Sungjoon Lim (Chung-Ang Univ.)
Byung-Wook Min (Yonsei Univ.)

Finance Chairs
Franklin Bien (UNIST)
Keum Cheol Hwang (Sungkyunkwan Univ.)

Publication and Publicity Chairs
Gangil Byun (UNIST)
Sanghoek Kim (Kyung Hee Univ.)

Exhibition Chair
Jungsuek Oh (Seoul National Univ.)
Wang-Sang Lee (Gyeongsang National Univ.)

Local Arrangement Chair
Sun K. Hong (Soongsil Univ.)

Short Course Chair
Sangkil Kim (Pusan National Univ.)

Special Session Chair
Wonbin Hong (POSTECH)

Award Chair
Sangjo Choi (Kyoungpook National Univ.)

General Secretaries
Jae-Young Chung (SeoulTech)
Ick-Jae Yoon (Chungnam National Univ.)

APMC 2025

2025 ASIA-PACIFIC MICROWAVE CONFERENCE

Nov 4 (Tue) - 7 (Fri), 2025

Jeju Island, Korea

Welcome to APMC 2025

The 37th Asia-Pacific Microwave Conference (APMC) will be held on November 4-7 in Jeju, Korea. Since the first conference held in 1986, APMC has been serving as the largest microwave event of its kind in the Asia-Pacific region for nearly 40 years. We are pleased to host APMC again back in Korea after the three past meetings held in Korea (1985, 2003, 2013).

We firmly believe APMC 2025 will serve as a perfect opportunity for researchers from both academia and industry to exchange new technical and scientific achievements in the frequency ranges of microwave, millimeter-wave, terahertz, and beyond. It will also contribute to promoting solid networks between participants from all over the world. We hope you will visit and enjoy APMC 2025 in the beautiful island of Jeju.

Organizer KIEES Korean Institute of Electromagnetic Engineering and Science

Technical Sponsors IEEE · MTT-S MHz to THz Community · AP-S · EuMA European Microwave Association

Organizing Committee

Honorary Chairs
Jung-Woong Ra (KAIST)
Hyuckjae Lee (KAIST)
Dong-Chul Park (Chungnam National Univ.)

Advisory Committee
Jin-Koo Rhee (Dongguk Univ.)
Bumman Kim (POSTECH)
Sangwon Yun (Sogang Univ.)
Hai-Young Lee (Ajou Univ.)
Songcheol Hong (KAIST)

General Chair
Jae-Sung Rieh (Korea Univ.)

Vice Chairs
Young-Chul Park (Hankuk Univ. of Foreign Studies)
Hyunchol Shin (Kwangwoon Univ.)

Technical Program Committee Chair
Moon-Que Lee (Univ. of Seoul)

Technical Program Committee Co-Chairs
Young-jin Kim (Korea Aerospace Univ.)
Hosung Choo (Hongik Univ.)

Tutorial/Workshop Committee Chairs
Ho-Jin Song (POSTECH)
Wonbin Hong (POSTECH)

Finance Committee Chairs
Sanggeun Jeon (Korea Univ.)
Seungyoung Ahn (KAIST)

Publication Committee Chairs
Eunmi Choi (UNIST)
Byung-Wook Min (Yonsei Univ.)

Publicity Committee Chairs
Woo-Jin Byun (ETRI)
Jae-Young Chung (Seoul Tech)

Local Arrangement Committee Chairs
Hyunchul Ku (Konkuk Univ.)
Dong-Su Kim (KETI)

Exhibition Committee Chairs
Sung Ho Wang (Nemesis)
Yongshik Lee (Yonsei Univ.)

Award Committee Chairs
Jong Won Yu (KAIST)
Jong-Ryul Yang (Konkuk Univ.)

Secretaries
Jungsuek Oh (Seoul National Univ.)
Youngwook Kim (Sogang Univ.)

Jeju Island, Globally Recognized for Its Natural Wonders!

Jeju is the foremost island in Korea in terms of size and unique climate. The island province consists of Jeju and its adjacent islands. Geographically, its relative isolation from the mainland resulted in a unique dialect and lifestyle of its own. The natural beauty of Mt. Hallasan and the surrounding sea make Jeju an ideal resort island. In recent years, Jeju has been awarded multiple times by global organizations. The island contains the natural World Heritage Site Jeju Volcanic Island and Lava Tubes. Jeju Island is UNESCO's only triple-crown winner for World Natural Heritage, Global Geopark, and Biosphere Reserve. It is also renowned for its beautiful, pristine environment and has been designated as one of the New 7 Wonders of Nature. With the 21st century's arrival, Jeju City is transforming itself into irreplaceable tourist area.

AUTHOR CHECKLIST

Title : _____

General

☐ This paper has not been and will not be published in any other journal.

☐ This paper follows the format of the KIEES paper submission guideline, is less than 12 pages long, including figures and tables (3 pages for a letter), and has a two-column layout.

☐ This paper includes a cover page, an abstract, keywords, main text, appendix, and references in the correct order. Each page has a consecutive page number.

Cover page

☐ The cover page includes the title, authors, affiliation of all authors, identifier of the corresponding author, and provides contact information for the corresponding author (phone number, e-mail address, and mobile number).

Abstract and key words

☐ An abstract is provided and is less than 500 words long.

☐ Fewer than 5 keywords are provided.

Main text

☐ The reference number is written next to the quote.

☐ The chapter numbers are written in Roman numerals (I, II, III, IV…) and subheading numbers are written in Arabic numerals (1, 2, 3, 4…).

References

☐ Sufficient Korean as well as international literature is referenced in the paper.

☐ Only the references used in the main text are included in the reference list and these are numbered according to their order of appearance.

☐ All reference citations follow the correct format indicated in the submission regulations.

Figures and tables

☐ For the figures and tables, the first letter of the very first word is capitalized.

☐ All figure legends include both a title and a detailed explanation to help in understanding what the figure depicts.

☐ All tables are self-explanatory and do not repeat the content from figures or sources included in the main text.

* Check each box after confirming that the statement is true.

The authors of this paper have confirmed the above items, following the paper submission regulations of *the Korean Institute of Electromagnetic Engineering and Science (KIEES)*, and are requesting publication of this paper.

_____/_____/ 2024

Representative author: _____ (signature)